



University
of Glasgow

Mordue, Christopher William (2022) *Modelling, quantifying and attenuating multi-material thermal bend in atomic force microscopy cantilevers*. PhD thesis.

<https://theses.gla.ac.uk/83293/>

Copyright and moral rights for this work are retained by the author

A copy can be downloaded for personal non-commercial research or study, without prior permission or charge

This work cannot be reproduced or quoted extensively from without first obtaining permission in writing from the author

The content must not be changed in any way or sold commercially in any format or medium without the formal permission of the author

When referring to this work, full bibliographic details including the author, title, awarding institution and date of the thesis must be given

Enlighten: Theses

<https://theses.gla.ac.uk/>
research-enlighten@glasgow.ac.uk



University
of Glasgow

DOCTORAL THESIS

Modelling, Quantifying and Attenuating Multi-Material Thermal Bend in Atomic Force Microscopy Cantilevers

Author:

Christopher William MORDUE

First Supervisor:

Dr P. S. DOBSON

Second Supervisor:

Professor J.M.R. WEAVER

*A thesis submitted in fulfilment of the requirements
for the degree of Doctor of Philosophy at the*

The University of Glasgow
James Watt School of Engineering

8th July, 2022

Declaration of Authorship

I, Christopher William MORDUE, declare that this thesis titled, “Modelling, Quantifying and Attenuating Multi-Material Thermal Bend in Atomic Force Microscopy Cantilevers” and the work presented in it are my own. I confirm that:

- This work was done wholly or mainly while in candidature for a research degree at this University.
- Where any part of this thesis has previously been submitted for a degree or any other qualification at this University or any other institution, this has been clearly stated.
- Where I have consulted the published work of others, this is always clearly attributed.
- Where I have quoted from the work of others, the source is always given. With the exception of such quotations, this thesis is entirely my own work.
- I have acknowledged all main sources of help.
- Where the thesis is based on work done by myself jointly with others, I have made clear exactly what was done by others and what I have contributed myself.

Signed:

Date: 08/07/2022

“The prize is in the pleasure of finding the thing out, the kick in the discovery, the observation that other people use it. Those are the real things, the honours are unreal to me.”

Richard Feynman

THE UNIVERSITY OF GLASGOW

Abstract

James Watt School of Engineering

Modelling, Quantifying and Attenuating Multi-Material Thermal Bend in Atomic Force Microscopy Cantilevers

by Christopher William MORDUE

Atomic Force Microscopy (AFM) is a technique that generates images of surfaces with a resolution down to the atomic scale through the use of a micro-cantilever. Like many machines that operate at such a scale, it is prone to thermal drift which can result in imaging artefacts. This body of work comprehensively explores the micro-cantilever's contribution to this phenomenon, particularly in the situation where the cantilever is constructed from two materials (typically an insulator and metal). This work made use of a specific type of AFM called Scanning Thermal Microscopy (SThM), that provided simultaneous temperature and deflection quantification. Modelling demonstrated that an AFM tip can deflect up-to 166 nm/K when out-of-contact resulting in variable and erroneous measurement of deflection and topography in AFM. The latter is a highly unique insight and is a consequence of AFM's commonly employed optical lever system that measures cantilever rotation (rather than deflection) at the laser spot focused on the cantilever. The AFM converts this signal into tip-deflection, using a tip-force defined sensitivity factor, meaning the tip deflection measurement is indirect. This thermal induced deflection was similarly modelled in standard contact-mode AFM cantilevers, emphasising its widespread occurrence. With AFM cantilever tips in-contact with surfaces and so their degrees of freedom limited, all cantilevers were theoretically predicted to deflect like a bridge when undergoing a temperature change. This manifested as a humped deflection profile along each cantilever's length. As a result, this provided the conclusion that an AFM can interpret thermal induced deflection either positively or negatively depending on the longitudinal position of the optical lever's laser.

Both out-of-contact and in-contact experimental measurements on SThM cantilevers showed that AFM systems employing optical lever set-ups do have variable and inherently incorrect responses to thermal induced cantilever deflection. This was also seen for commercial contact-mode AFM cantilevers. Measured deflection profiles of all cantilevers when in-contact agreed with models, demonstrating inconsistent AFM measured deflection direction depending on laser location on the cantilever. This provides clear evidence of a new phenomenon not previously documented. Contact AFM scans were employed to confirm this effect's direct impact on topographic scans with images of the same area varying positively or negatively over a 600 nm range for 2 K of temperature change. For a technique that measures sub-nanometre features, this is a significant artefact. However, with the humped cantilever deflection profile seen in-contact, it offers a point-of-inflexion where very little thermal bending induced tip-deflection would be measured by the optical lever. Measurements demonstrated an improvement of up-to 97.7 % when the laser was focused at this position on the cantilever. This presents a useful technique to mitigate thermal bending artefacts in-contact AFM scan modes, although cantilever bend itself remains present.

To address this latter aspect, a simple solution was explored, where the native metal is counteracted by another metal on the backside of the cantilever. Using SThM cantilevers to study this, up-to 99 % reduction in thermal bend induced deflection of the cantilever is possible. New SThM cantilevers with evaporated aluminium on their backside to counteract the native gold were fabricated and showed complete attenuation of thermal bending for laser locations along the whole cantilever length when out-of-contact and in-contact. These were further improved by fabrication of modified SThM cantilevers with gold patterning that better complement the planar aluminium deposition to further improve the effect not only longitudinally, but also laterally in their deflection. This translated into in-contact AFM scans showing variation of only 10s nm for 2 K of temperature change in contrast to 100s nm without any design alteration. These findings were mirrored in commercial, contact-mode AFM cantilevers with a similar trend of pronounced insensitivity to thermal bending when out and in-contact with surfaces, translating into greatly reduced scan artefacts.

Acknowledgements

No significant body of work is constructed alone, with it being a collection of ideas, application and motivation. This is no different. I would first like to thank my parents for always encouraging me and providing constant support. I would never have gotten close to performing a doctorate without their help. Beyond this, I owe a huge amount to my supervisor, Dr Phil Dobson. Through his encouragement for independent thought and application, he made me a better engineer and researcher. His instrumental guidance made this work as much a product of his, as it is mine. Additionally, his advice was always in parallel with informal conversations that made me feel welcome at first and later an equal. Moreover, I would like to thank the following people/groups:

- **Professor Jonathan Weaver:** While wise and immensely helpful throughout the project, I would also like to thank you for being a great guy to chat to and exchange ridiculous ideas with. Furthermore, you provided the technical bedrock for my work and I can not thank you enough for that.
- **Rory Lambert:** At the start of the PhD, you were incredible at answering my numerous questions and were integral in providing great knowledge and understanding to jettison my work from the beginning. You were also a great colleague and friend so thank you so much.
- **David Atkins:** My partner in crime throughout the PhD. Without your help and company, my work would not have been half as good, or half as fun.
- **Lukas Avilovas:** A man who always helped me out when I asked and was great to chat anything and everything with, thank you!
- **Hao Xu:** Incredibly kind and thoughtful, cheers for being you and a great office neighbour.
- **Ravish Rajkumar:** A top man who helped me at the start with SThM fabrication and gave me a plethora of ideas to go off.

- **Sara Dow:** I owe you so much for your help, giving me those secret tips to help me fabricate my probes at the end, alongside were a good friend into the bargain. Thank you!
- **University Staff:** I would like to extend a great amount of gratitude to all staff, particularly those in the JWNC and Rankine Level 7 labs, for providing a great environment to explore and learn.
- **Engineering and Physical Sciences Research Council:** Thank you for providing the resources to perform this body of work and all the support.
- **Eve:** Last but not least, thank you Eve. You listened to all my ramblings and provided unquantifiable support throughout. I would not have had the same energy and drive without your unwavering presence at my side.

Contents

Declaration of Authorship	i
Abstract	iii
Acknowledgements	v
1 Introduction	1
1.1 Research Focus	1
1.2 Project Structure	2
1.3 Research Goals	3
2 Literature Review	4
2.1 Atomic Force Microscopy	4
2.1.1 Operating Principle	4
2.1.2 Classification	6
2.1.3 Development	7
2.1.4 Deflection Detection Systems	9
2.1.5 Interaction Forces	14
2.2 Thermal Drift & Bending in AFM	16
2.2.1 AFM Cantilever Thermal Bending	17
2.2.2 Thermal Actuation of Micro-Cantilevers	18
2.2.3 Modelling Thermal Bending	20
2.2.3.1 Thermal Bend Equations	20
2.2.3.2 Solid Mechanics Theory	22
2.2.3.3 Principle of Superposition	23
2.2.3.4 End-Force Equations	25
2.3 Scanning Thermal Microscopy	27

2.3.1	Operating Principles	27
2.3.2	Development	29
2.4	Fabrication	34
2.4.1	Lithography	34
2.4.1.1	Mask Based - Photolithography	35
2.4.1.2	Direct Write - Electron Beam Lithography	36
2.4.2	Etching	38
2.4.2.1	Wet Etching	38
2.4.2.2	Dry Etching	40
2.4.3	Deposition	41
2.4.3.1	Physical Vapour Deposition (PVD)	42
2.4.3.2	Chemical Vapour Deposition (CVD)	43
3	Research Method	45
3.1	Modelling	45
3.1.1	FDM Model	46
3.1.1.1	Thermal Bend Equations	46
3.1.1.2	Solid Mechanics Theory	48
3.1.1.3	End-Force Equations	51
3.1.1.4	FDM Model Generation	52
3.1.2	FEA Model	55
3.2	Experimental Quantification	57
3.2.1	Measurement Approach & Tools	58
3.2.1.1	Deflection Measurement	58
3.2.1.2	Temperature Measurement	58
3.2.2	Out-of-Contact	63
3.2.2.1	Direct Deflection Quantification	64
3.2.2.2	AFM Interpretation Experiments	66
3.2.3	In-Contact	69
3.2.3.1	Self-Heating Experiment	71
3.2.3.2	Microheater Experiment	72
3.3	Thermal Bend Attenuation	75

3.3.1	Fabrication	76
3.3.1.1	Lithography	76
3.3.1.2	Etching	78
3.3.1.3	Deposition	80
4	Mechanical & Thermal Bend Modelling of AFM Cantilevers	82
4.1	SThM Cantilevers	82
4.1.1	Material Properties	83
4.1.1.1	Mechanical	83
4.1.1.2	Thermal	89
4.1.2	Construction	91
4.1.3	Out-of-Contact	92
4.1.3.1	Boundary Conditions	93
4.1.3.2	Mechanical Modelling	95
4.1.3.3	Thermal Bend Modelling	108
4.1.4	In-Contact	123
4.1.4.1	Boundary Conditions	124
4.1.4.2	Thermal Bend Modelling	136
4.2	Non-Thermal AFM Cantilever Modelling	143
4.2.1	Out-of-Contact	143
4.2.2	In-Contact	148
5	Experimental Quantification of Thermal Bending in AFM Cantilevers	152
5.1	SThM Cantilevers	152
5.1.1	Out-of-Contact	152
5.1.1.1	Direct Deflection Quantification	153
5.1.1.2	AFM Interpretation Experiments	157
5.1.2	In-Contact	163
5.1.2.1	Self-Heating Experiment	163
5.1.2.2	Microheater Experiment	167
5.2	Non-Thermal AFM Cantilevers	172
5.2.1	Out-of-Contact	172
5.2.2	In-Contact	176

6 Attenuation of Thermal Bending in AFM Cantilevers	187
6.1 Objective & Approach	187
6.2 SThM Cantilevers	189
6.2.1 Potential Solutions	190
6.2.1.1 Lower CTE & Young's Modulus Wire Material	191
6.2.1.2 SiO _x on Coating-Side	193
6.2.1.3 Wider Coating Position	196
6.2.1.4 Backside Deposited Metal	197
6.2.2 Chosen Solution - Backside Deposited Metal	200
6.2.2.1 Modelling	201
6.2.2.2 Feasibility Study	213
6.2.3 Design Study	226
6.2.3.1 Method	227
6.2.3.2 Results	235
6.2.4 Summary	247
6.3 Non-Thermal AFM Cantilevers	248
6.3.1 Current Market Solutions	248
6.3.2 Backside Deposited Metal Solution	250
6.3.2.1 Modelling	251
6.3.3 Design Study	252
6.3.3.1 Method	252
6.3.3.2 Results	253
7 Conclusion & Future Work	258
7.1 Conclusion	258
7.2 Future Work	260
A Supplementary Modelling Work	262
A.1 FDM Model	262
A.1.1 Grooved Cantilever's	262
A.1.1.1 Simplified Cross-Section	262
A.1.1.2 Complex Cross-Section	264

<i>Contents</i>	xi
B Supplementary Experimental Quantification Work	265
B.1 PT-100 Equations	265
C Supplementary Attenuation Work	266
C.1 Normal vs. Thin-Wide SThM Cantilever Work	266
D SThM Fabrication Process Sheet	269
Bibliography	272

List of Figures

1.1	UofG SThM probe	1
2.1	Basic AFM Operation Diagram	5
2.2	Microscopy Vertical Resolution Ranges	6
2.3	Original STM Operational Diagram	8
2.4	Optical Lever Diagram	10
2.5	Optical Lever Rotation & Vertical Displacement Change	12
2.6	Example of a Voltage-distance Curve for an AFM Cantilever Under Ambient Air Conditions	14
2.7	Example of Drift in an AFM Image	17
2.8	Thermal Bending in Cantilevers	18
2.9	A Diagram by V. Pini et al. depicting a Photothermally Actuated Cantilever (Using the EX Laser) in a Fluid [71]	19
2.10	Example of an Electro-Thermally Acuated Cantilever with a Integrated Piezoresistor for deflection Measurement at its base for (a) $7 \mu\text{m} \times 2 \mu\text{m}$ and (b) $23 \mu\text{m} \times 6 \mu\text{m}$ [72]	20
2.11	Principle of Superposition Diagram where L, M, θ, δ are the Lengths, Bending Moments, Rotations and Vertical Displacements Respectively	24
2.12	A.Majumdar SThM Design Diagram	30
2.13	SEM Image of Single Wollaston Wire Probe	31
2.14	Two & Four Terminal Resistive SThM SEM Images [49]	32
2.15	Grooved Resistive SThM Probe SEM Images & Graphic [114]	33
2.16	SEM Image of a KNT-SThM-1an Probe	33
2.17	Diagram of Photolithography Exposure & Development	35
2.18	Diagram of an Electron Beam Lithography (EBL) System	37
2.19	Simplified Diagram of a Wet Etch Kit	39

2.20	Diagram of a Parallel Plate RIE System	41
2.21	Simplified Electron-Beam Evaporation Tool Diagram based on Plassys II & IV in JWNC	43
2.22	Simplified Diagram of a LPCVD System	44
3.1	Diagram of the Transformed Section & Second Moment of Area Appre- ciation for Single Au Coating	47
3.2	Scaled Side-View of a SThM Cantilever With Slender Beam Ratio	49
3.3	Example of a Fractured, Half SThM Probe Drawing to Generate Elements	53
3.4	FEA - SThM Cantilever Constructed with Hexagonal Elemental Mesh . .	56
3.5	Fabricated SThM Tip Compared to FEA's Tip Simplifications	57
3.6	Bruker Contour GT-X 3D Optical Microscope Utilised in Project [139] . .	60
3.7	Digital Instruments Dimension 3100 AFM Employed in Project	61
3.8	Wheatstone Bridge Employed in SThM - Simplified Circuit Diagram . .	62
3.9	Equipment Employed for Determining SThM Probe's TCR	62
3.10	3D Topographic Image Produced by the Bruker Contour Interferometer	65
3.11	Direct Deflection Quantification Experimental Set-up	66
3.12	AFM Interpretation Experiments - 1st Experiment: AFM & Interferom- eter Set-ups (left-to-right)	68
3.13	AFM Interpretation Experiments - 2nd Experiment: AFM Set-up	69
3.14	Image of Microheater Fabricated by P. S. Dobson et al. [153], Whereby Line Scans Were Performed Along the X-X Line	71
3.15	Self-Heating Experiment: AFM & Interferometer Set-ups	73
3.16	SUSS Mask Aligner MA6 in the JWNC [139]	77
3.17	Raith's EBPG 5200 in the JWNC [139]	78
3.18	Wet Etch Kit in the JWNC [139]	79
3.19	Oxford Instruments RIE 80+ in the JWNC [139]	80
3.20	Plassys Tools in the JWNC [139]	81
4.1	Engineering Drawing of Flat SThM Cantilever Design	92
4.2	FBD of an AFM Cantilever OC	93
4.3	SThM Cantilever OC Heat Transfer Diagram	94
4.4	FDM - Flat SThM 100 nN End-Force Displacement Profile	97

4.5	FDM - Flat SThM 100 nN End-Force Displacement Profile	98
4.6	FEA - Vertical Deflection of a SThM Cantilever with 100 nN Tip Force Applied Vertically	100
4.7	FDM - Sensitivity Analysis of SiN _x Young's Modulus (180-280 GPa) and Thickness (375-425 nm) vs Spring Constant	101
4.8	FDM - Sensitivity Analysis of Au Young's Modulus (30-90 GPa) and Thickness (130-170 nm) vs Spring Constant	101
4.9	FDM - Flat SThM Theoretical InvOLS vs Longitudinal Position	102
4.10	Aerial SEM Image of a Grooved SThM Cantilever	103
4.11	Grooved SThM Cross-Section Diagram	104
4.12	Grooved SThM Cross-Section Diagram With Proportional Key Dimensions For Ideal NA Position	105
4.13	Grooved SThM Cross-Section Diagram with Angled Side-Wall	107
4.14	FEA - Flat SThM Cantilever 10 K Uniform Thermal Bending OC	110
4.15	FDM - Flat SThM Uniform Temperature Thermal Bend Vertical Deflection Profile	112
4.16	FDM - Flat SThM Uniform Temperature Thermal Bend Rotation Profile	112
4.17	FDM - Flat SThM Theoretical AFM Interpretation of Uniform Temperature Thermal Bend	113
4.18	Flat SThM Cantilever's Self-Heating Temperature Distributions With Average Tip Sensor Temperature Change	115
4.19	Flat SThM Cantilever's Self-Heating Vertical Deflection Profiles With Tip Deflection	115
4.20	Grooved Cantilever Cross-Section Layer Separation Diagram	116
4.21	FEA: Theoretically Ideal 75 μm Long Groove Cantilever Undergoing 10 K Uniform Thermal Bending	117
4.22	Grooved Cantilever FEA Model Length Study: 75 μm & 600 μm Long 10 K Temperature Change	120
4.23	Grooved Cantilever Length Study - Centreline Deflection Profiles	121
4.24	SThM Cantilever Tip DOF Diagram	124
4.25	Flat SThM Voltage-distance Curve on Polished Silicon	126
4.26	SThM Friction Loop on Polished Silicon Surface	129

4.27	Tilting a Reflective Surface Method Experiment - Change in Horizontal Voltage vs Mirror's Angle	129
4.28	Friction Loop Demonstrating Stick and Slip of a SThM Cantilever	132
4.29	Roller Tip Boundary Condition on a Cantilever	134
4.30	FEA: Flat SThM Cantilever Thermal Bending (10 K) with Roller Tip BC .	137
4.31	FEA - Flat SThM Cantilever Thermal Bending with Roller Tip BC Deflection Profile	138
4.32	FEA - Flat SThM Cantilever Thermal Bending with Roller Tip BC Rotation Profile	138
4.33	FEA - Theoretical AFM Interpretation According to FDM Theoretical InvOLS	139
4.34	FEA - Diagram of the Temperature BCs Imposed Along the SThM Cantilever	140
4.35	Longitudinal Temperature Distributions for SThM Cantilever's for Self-Heating	141
4.36	FEA - Self-Heating Induced IC Thermal Bending Vertical Deflection	142
4.37	Optical Images of Non-Thermal AFM Cantilevers	144
4.38	FDM OC - Non-Thermal Cantilevers Vertical Deflection Profiles	145
4.39	FDM OC - Non-Thermal Cantilevers Rotation Profiles	146
4.40	FDM OC - Non-Thermal Cantilevers Theoretical AFM Interpretation Profiles	147
4.41	FEA IC - Non-Thermal Cantilevers Vertical Deflection	148
4.42	FEA IC - Non-Thermal Cantilevers Rotation	149
4.43	FEA IC - Non-Thermal Cantilevers Theoretical AFM Interpretation	150
5.1	Interferometer Image of a Flat SThM Cantilever with Annotated Scale Bar	153
5.2	Flat SThM Cantilever's Uniform Temperature Induced Thermal Deflection 133 μm Along	154
5.3	Flat SThM Cantilever's Uniform Temperature Thermal Bend Deflection Profile	155
5.4	Grooved SThM Cantilever's Thermal Deflection Gradient's at 75 μm Along	156

5.5	AFM's Interpretation of OC Thermal Bending - 1st Experiment	160
5.6	AFM's Interpretation Profile of OC Thermal Bending - 2nd Experiment with Graphic Depiction of Optical Lever Laser	162
5.7	SThM Self-Heating Experiment - Interferometer OC & IC Deflection Profiles	164
5.8	Self-Heating Experiment - AFM OC & IC Deflection Profiles	165
5.9	Microheater Experiment - Flat SThM Cantilever With Annotated Laser Locations	167
5.10	Microheater Experiment - Flat SThM OC & IC Deflection Profiles	168
5.11	Image of Microheater Fabricated by P. S. Dobson et al [153], whereby line scans were performed along the X-X line	170
5.12	Microheater Experiment - Temperature Change Line Scans Measured by the SThM Probe	170
5.13	Microheater Experiment - Topography Line Scans for a SThM Probe	171
5.14	Non-Thermal AFM Cantilevers - OC Thermal Bend Deflection Profiles Measured by an Interferometer	173
5.15	Non-Thermal AFM Cantilevers - OC Thermal Bend Deflection Profiles Measured by an AFM	174
5.16	Optical Images of Non-Thermal Cantilevers' Microheater Experiment Locations	177
5.17	Non-Thermal AFM Cantilevers - Microheater Experiment - OC Thermal Bend Deflection Profiles	178
5.18	Non-Thermal AFM Cantilevers - Microheater Experiment - IC Thermal Bend Deflection Profiles	179
5.19	Non-Thermal AFM Cantilevers - Microheater Experiment - IC Thermal Bend Deflection Profiles With Normalised Length	181
5.20	MLCT-B AFM Line Scan Across X-X Line on Microheater	182
5.21	Annotated Microheater Image of Scanned Area	182
5.22	MLCT-B Full AFM Scan - Tip Laser Position	183
5.23	MLCT-B Full AFM Scan - Base Laser Position	184
5.24	MLCT-B Full AFM Scan - Middle Laser Position	185

6.1	Grooved SThM Cross-Section Diagram	190
6.2	Cross-Section of a Flat SThM Cantilever with SiO _x	194
6.3	FDM Model - SiO _x Thickness vs. Spring Constant	195
6.4	FDM Model - SiO _x Thickness vs. Thermal Bend Induced Tip Deflection	195
6.5	Coating Lateral Positioning Graphic	197
6.6	FDM - Backside Metal Preliminary Study of Al & Au Thickness vs. Vertical Tip Deflection due to Thermal Bending	199
6.7	FDM Model - Backside Metal Study of Al Thickness vs. Vertical Tip Deflection due to Thermal Bending with Updated Material Properties	203
6.8	FDM Model - Thermal Bend Vertical Deflection Profile for 73 & 89 nm Al & Au Backside Coating's Resepectively for flat SThM	204
6.9	FEA Model - Al (73nm) SThM Thermal Bending Induced Vertical Deflection from 10 K Temperature Change	204
6.10	FEA Model - Al (81nm) SThM Thermal Bending Induced Vertical Deflection from 10 K Temperature Change	205
6.11	FEA Model - Al (81 nm) SThM Thermal Bend Induced Centreline Deflection Profile	206
6.12	FEA Model - Al (77nm) SThM Thermal Bend Induced Centreline Deflection Profile with no Wide Mirror Section	207
6.13	New SThM Cantilever Designs - FEA Longitudinal Profiles	209
6.14	New SThM Cantilever Designs - FEA Lateral Profiles	209
6.15	FEA Wire Study - Thermal Bend (10 K) Outputs Images for OC (left) & IC (right) for Designs (1) Wide Position Wire; (2) Middle Position Wire; (3) Narrow Position Wire; (4) Wide & Thin Wire	210
6.16	FEA Wire Study - Thermal Bending Centreline Profiles for Designs (1) Wide Position Wire; (2) Middle Position Wire; (3) Narrow Position Wire; (4) Wide & Thin Wire	212
6.17	Preliminary Feasibility Study - Probe Thermal Bending Deflection Profiles	215
6.18	Feasibility Study - Cantilever Thermal Bending Deflection Percentage Change 90 μ m Along	216
6.19	Feasibility Study - Change in Ambient Profiles/Curvature	217

6.20	Feasibility Study - Cantilever Thermal Bending Deflection Percentage Change 90 μm Along With Dummy Ti Data	219
6.21	Feasibility Study - Cantilever Thermal Bend Gradients 90 μm Along with Varying Al Thicknesses	220
6.22	Feasibility Study - Dummy Ti Cantilever's Change in Ambient Profiles/Curvature	221
6.23	Feasibility Study - Probe 5 Microheater OC & IC Profiles vs Normal Flat SThM	223
6.24	Feasibility Study - Probe 5 Microheater Line Scan's vs Normal Flat SThM	225
6.25	Feasibility Study - Probe 6 Microheater Line Scan's vs Normal Flat SThM	225
6.26	New SThM Designs L-Edit Images (Dimensions Shown in μm)	229
6.27	SEM Image of Narrow Wire Design Post Wire Definition (Step 62) with the Etch Cut Highlighted	230
6.28	Image of a 3" SThM Probe Wafer Prior to Release	230
6.29	SEM Images of all SThM Probe Designs Fabricated: (a) Narrow; (b) Middle; (c) Wide; (d) Thin-Wide	231
6.30	Interferometer - Longitudinal Thermal Bend Profiles of New SThM Cantilever Designs	235
6.31	Interferometer - Lateral Thermal Bend Profiles 90 μm Along New SThM Cantilever Designs	237
6.32	Interferometer - Longitudinal Thermal Bend Profiles of New SThM Cantilever Designs with Backside Deposition Solution (Al)	239
6.33	Interferometer - Longitudinal Change in Thermal Bend Profiles & Percentage Change of New SThM Cantilever Designs with Backside Deposition Solution (Al)	240
6.34	Interferometer - Lateral Thermal Bend Profiles of New SThM Cantilever Designs with Backside Deposition Solution (Al)	241
6.35	AFM - Peltier Induced Uniform Temperature Profile of Thin-Wide SThM (Al = 80 nm) Design with Previous SThM Cantilever Comparisons	243
6.36	AFM - Microheater OC vs IC Experiment with Varying Laser Lateral Location on Thin-Wide (Al = 80 nm) Design	244
6.37	Microheater IC Experiment - All SThM Cantilever Design Comparison	245

6.38 Thin-Wide (Al = 80 nm) - Microheater Line Scan Contrast to Old SThM Design Without Al	247
6.39 FEA - Deflection Output for Example of Commercial Solution with Partial Au Coverage Near Tip	249
6.40 FEA - Deflection Output for Example of Commercial Solution with Partial Au Coverage Midway Along Cantilever	250
6.41 FEA - Vertical Deflection from 10 K Uniform Temperature Change in MLCT-B Cantilever with 44 nm of Al on the Underside	251
6.42 FEA - Vertical Deflection Centreline Profile Normalised to per Kelvin for MLCT-B Cantilever with 44 nm of Al on the Underside	252
6.43 Interferometer - MLCT-B Peltier Induced Thermal Bend Profiles	253
6.44 AFM - MLCT-B Peltier Induced Thermal Bend Profiles	254
6.45 AFM - MLCT-B Microheater OC Induced Thermal Bend Profiles	255
6.46 AFM - MLCT-B Microheater IC Induced Thermal Bend Profiles	255
6.47 AFM Line Scan - MLCT-B Topography Change	257
C.1 Normal vs. Thin-Wide SThM Au Designs - Key Cross-Section Areas (μm^2)	266
C.2 Thermal-Resistive Model - Thermal Resistance Along Cantilever Graph	267
C.3 Thermal-Resistive Model - Temperature Change Along Cantilever Graph	268
D.0 SThM Fabrication Process Sheet	271

List of Tables

2.1	SThM Mechanism Classifications [92], [109], [110]	29
3.1	Cantilever Deflection Measurement Tools: Benefits & Drawbacks	59
4.1	SThM Materials - Poisson's Ratio Literature Values	85
4.2	SThM Materials - Young's Modulus Literature Values	86
4.3	SThM Materials - Linear Coefficient of Thermal Expansion Literature Values	89
4.4	Flat SThM Model Comparison for an End-Force	99
4.5	SThM Model Comparison for Uniform Temperature Thermal Bending	110
4.6	Flat SThM Models Lateral Position Comparison for Uniform Temperature Thermal Bending 90 μm Along Cantilever	111
4.7	Groove Depth vs. Cantilever Length Preliminary Study	118
4.8	Grooved Cantilever Length Study	119
4.9	FEA: Additional Self-Heating Material Properties	141
4.10	Non-Thermal AFM Probe Details	144
6.1	SThM Potential Wire Material Properties	192
6.2	SThM Potential Wire Material Mechanical & Thermal Bend Results	193
6.3	Wider Coating Position Study Data	197
6.4	Potential SThM Backside Metals	198
6.5	Relevant Aluminium Mechanical & Thermal Properties	201
6.6	Final Design Exploration FEA Study	208
6.7	Feasibility Study - Spring Constants & Resistances	215
6.8	Attenuation Design Study - Different Designs	227

Nomenclature

ACRONYMS & INITIALISMS

AFM	Atomic Force Microscopy
SThM	Scanning Thermal Microscopy
SPM	Scanning Probe Microscopy
STM	Scanning Tunnelling Microscopy
OBD	Optical Beam Deflection
InvOLS	Inverse Optical Lever Sensitivity
FDM	Finite Difference Method
RTD	Resistance Temperature Detector
EF	End Force
SNR	Signal-to- Noise- Ratio
FEA	Finite Element Analysis
JWNC	James Watt Nanofabrication Centre
CTE	Coefficient of Thermal Expansion
OC	Out of Contact
IC	In Contact
F-d	Force-distance
DOF	Degree Of Freedom
FBD	Free Body Diagram
POI	Point Of Inflexion
BC	Boundary Condition
EBL	Electron Beam Lithography
PVD	Physical Vapour Deposition
CVD	Chemical Vapour Deposition
LPCVD	Low Pressure Chemical Vapour Deposition

PECVD	Plasma Enhanced Chemical Vapour Deposition
RIE	Reactive Ion Etching
CES	Cambridge Engineering Selector
KNT	Kelvin Nano Technology
PNP-DB	Pyrex- Nitride Probe Diving Board
MLCT	<i>Unknown</i>
SEM	Scanning Electron Microscope
TCR	Temperature Coefficient of Resistance

SYMBOLS

ELEMENTS/CHEMICALS

Si	Silicon
SiN _x	Silicon Nitride
SiO _x	Silicon Oxide
Au	gold
Al	aluminium
Pd	Palladium
Pt	Platinum
W	Tungsten
O	Oxygen
C	Carbon
Cl	Chlorine
F	Fluorine
H	Hydrogen
NiCr	Nickel-Chromium
TMAH	Tetramethylammonium Hydroxide

MISCELLANEOUS

δ	Deflection
F	Force
M	Moment

E	Young's Modulus
α	Coefficient of Thermal Expansion
ν	Poisson's Ratio
z	Vertical
y	Lateral
x	Longitudinal
L	Length
w	Width
t	Thickness
T	Temperature
c	Uniform Strain Component
t_b	Bending Axis
h	Layer Height
K	Curvature
I	Second Moment of Area
x_{NA}	Neutral Axis
n	Modular Ratio
k	Spring Constant
s_θ	Torsional Sensitivity
D	Dimension
$c_{\delta:\theta}$	Conversion Coefficient of Deflection to Rotation
θ	Rotation
μ_s	Static Friction
φ	Angle

1. Introduction

1.1 Research Focus

Temperature change is an inevitable consideration for scientists and engineers in a world above absolute zero. The effects of which are often ignored, but in many physical scenarios this should not be the case. Therefore, understanding temperature's influence(s) in systems is a necessity. This body of work aimed to achieve this for the crucial component in Atomic Force Microscopy (AFM), the cantilever. This type of microscope generates topographic images of surfaces down to atomic scale by monitoring the deflection of a micro-cantilever attached to a sharp tip that is raster scanned across the surface [1]. It has been previously documented and well established that temperature change can cause displacement in AFM systems, resulting in topographic

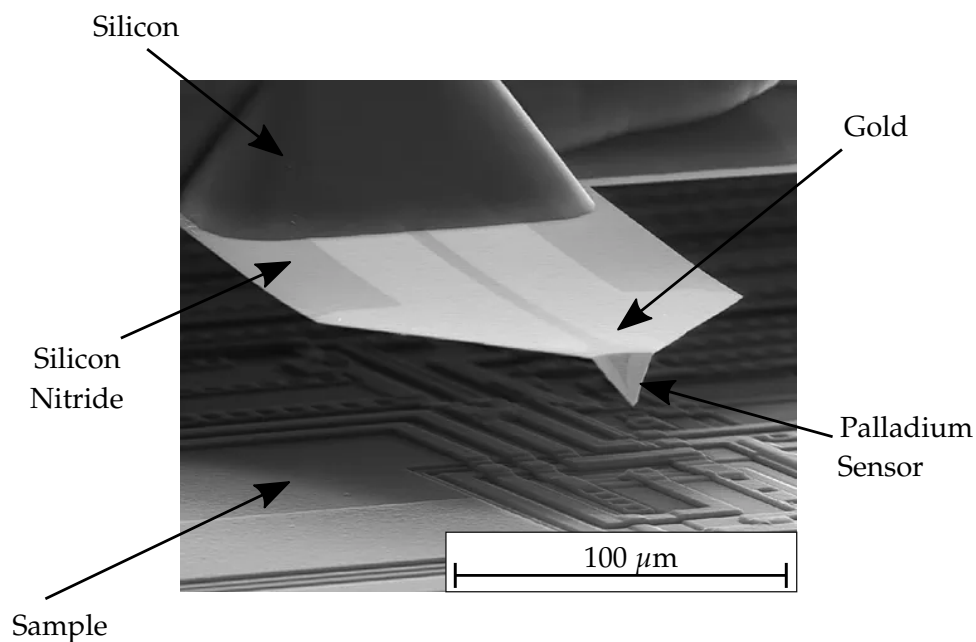


FIGURE 1.1: SThM Probe Fabricated at The University of Glasgow [2]

artefacts to present in their images (ubiquitously known as Thermal Drift) [3]. However, the research to-date has not provided a comprehensive analysis of temperature changes' exact influence on the key component of the AFM cantilever, alongside its instrument's interpretation of these changes. To fill this void, this work aimed to model, quantify and provide solutions that reduce the effects of temperature induced cantilever deflection and its translation to topography. To achieve this, Scanning Thermal Microscopy (SThM) cantilevers (as seen in Fig. 1.1) were employed due to their simultaneous and accurate measurement of cantilever temperature and deflection. Furthermore, with its significant metallisation and application to variable temperature environments, it is greatly beneficial to understand and reduce thermal bending in their specific design alongside AFM cantilevers in general.

1.2 Project Structure

As eluded to above, the project was broken into three sections, whereby SThM cantilevers were the initial vehicle for exploration followed by more ubiquitous, non-thermal AFM cantilevers. These sections, described below, were performed in the following respective order:

- **Modelling** - Utilising theoretical modelling through Finite Element and Finite Different Methods. This aimed to increase understanding, compare to experimental results and, once validated, be used as design tools for later attenuation work.
- **Experimental Quantification** - Performing experiments to provide real-world figures for temperature induced bending, deflection and topography that could be contrasted to theoretical models. Once sound experimental procedure had been established, they were employed to quantify the effectiveness of future thermal bend attenuation designs and solutions.
- **Attenuation** - Retaining and extending the knowledge and understanding acquired in the previous two sections, effort was applied to reduce the effect of

temperature induced bending, deflection and topographic artefacts. This involved proposing practice and design changes that were implemented and demonstrated through fabrication of new AFM cantilevers.

1.3 Research Goals

- Develop theoretical models that predict the Mechanical and thermal bend behaviour of AFM cantilevers, with a specific appreciation for SThM cantilevers.
- Quantify thermal bending in multi-material AFM and SThM cantilevers for out-of-contact and in-contact applications.
- Compare experimental results to models and theory of AFM operation.
- In-depth Mechanical and thermal bend analysis of SThM cantilevers.
- Extract practice improvements based upon developed knowledge and understanding from modelling and experimental quantification work.
- Design, model and fabricate new designs for attenuating thermal bending in SThM and non-thermal AFM cantilevers.
- Demonstrate new designs through experimental quantification and AFM operation.

2. Literature Review

In this section, literature pertaining to AFM was initially reviewed with a particular focus on the most common techniques employed. Moreover, particular concentration was given to the deflection measurement that influences topographic interpretation due to its fundamental role in AFM. This was followed by an exploration of the work to-date on thermal bending alongside an appreciation of the SThM cantilevers employed in this body of work. Beyond this, common fabrication techniques utilised to manufacture SThM and AFM cantilevers were elucidated.

2.1 Atomic Force Microscopy

Microscopy is defined as a technique that enables the ability to view objects outwith the resolution of the human eye [4]. Within this broad definition, there are many different types of microscope that fall into four main categories: Optical, Scanning Electron, Transmission Electron and Scanning Probe. Each with their unique operating principle, resolution and traits. Regarding Scanning Probe Microscopy (SPM), as the name suggests, it involves scanning a probe across a surface to produce high resolution images of a surface. Operating in such a manner, AFM is one of the main types of SPM with its exact operating principle expanded below.

2.1.1 Operating Principle

AFM functions by generating point-by-point topographic measurements of surfaces down to the micro, nano and even atomic-scale [1]. It operates by bringing a micro-cantilever with a sharp tip towards a sample's surface and raster scanning it whilst

monitoring its deflection. The latter is then connected to a feedback system that maintains a constant cantilever deflection and so force between the tip and surface throughout the scan. As a result, the outputted response to the cantilever's deflection is the sample topography that is used to build up an image. A diagram depicting such an AFM system can be seen in Fig. 2.1.

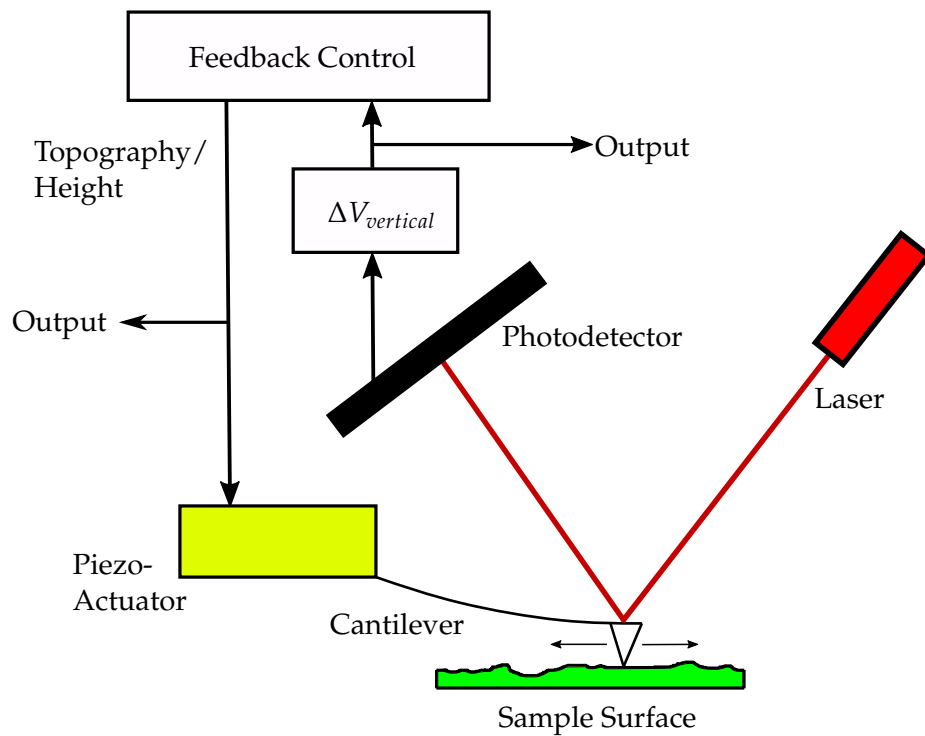


FIGURE 2.1: *Basic AFM Operation Diagram*

To achieve the above operation, the majority of AFMs utilise the following key components: cantilever, deflection detection system, stage, piezoelectric transducers and electronic feedback control [4]. The exact techniques/technology utilised in these components has changed over the years, alongside additional functionality to their basic role. For example, over time multiple scan modes have been developed changing the type of mechanical interaction with the surface. The main difference being the extent of tip contact and/or proximity to the sample surface during scanning. Regarding this, some tips are brought in direct contact with the surface and a constant cantilever deflection (and so tip-force) maintained. However, others are oscillated near the surface and by sustaining a constant oscillation amplitude, a consistent tip-sample interaction and force is generated. Hence, even with these different scan modes, the general measurement principle of a maintained tip-force is sustained which employs

one common instrument for their deflection detection system: the optical lever [1], [5]. This shall be elucidated later in this chapter due to its ubiquitous nature and obvious impact on the measurement of the sample topography. However, the classification and development of AFM will first be explored.

2.1.2 Classification

Placement and categorisation of AFM in the world of metrology allows appreciation of its relative ability and objective as a technique. Specifically, as the name suggests, AFM can measure forces involved at the atomic-scale and so can output Angstrom level spatial resolution. Therefore, it is one of the highest resolution microscopy techniques to date. A diagram depicting SPM and AFM's position in the world of microscopy based on resolution can be seen in Fig. 2.2.

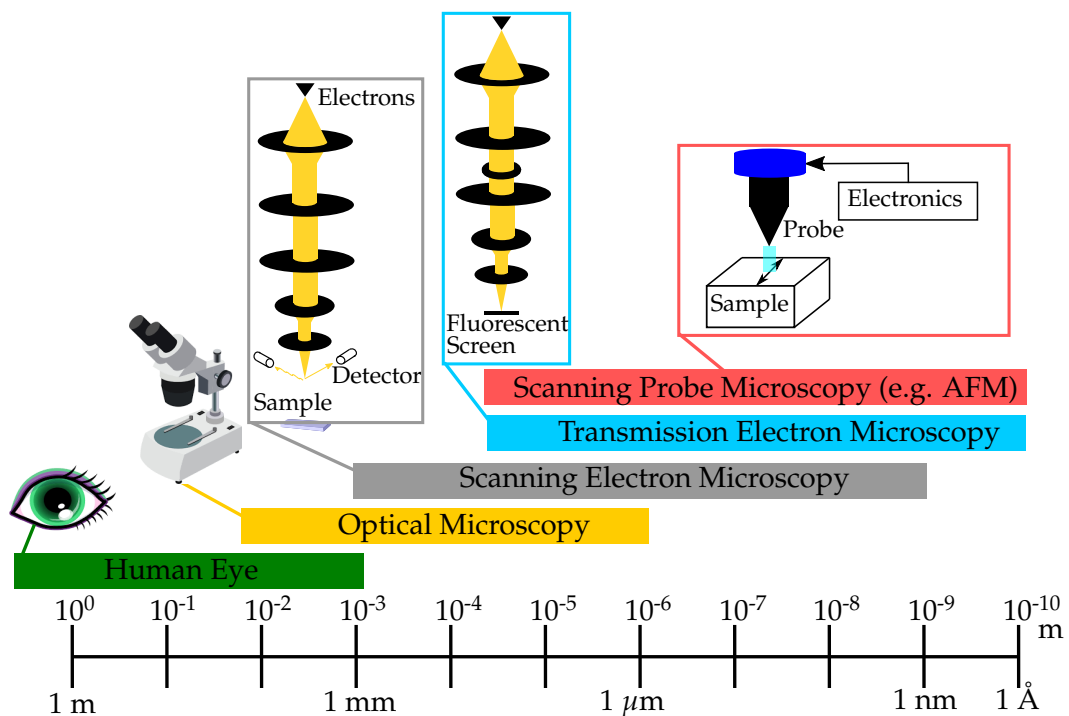


FIGURE 2.2: Microscopy Vertical Resolution Ranges

In AFM, there are sub-classifications based upon different criteria. The most obvious is the type of scan mode, where there are three main approaches based upon the extent they mechanically interact with the surface [1]:

1. **Contact** - Scanning the surface while the tip is in contact with it; typically indicated through snap-in of the tip. Changes in the measured cantilever deflection

infer the tip-force and a feedback loop response is used to generate a topography signal.

2. **Tapping/Intermittent/Oscillating Contact** - The cantilever is oscillated at a desired frequency (typically the cantilever's resonance frequency) and scanned across the surface where the tip makes intermittent contact with it. Changes in the nature of this oscillation such as its amplitude, phase or frequency then infer the force and with a feedback loop outputs a topography signal.
3. **Non-Contact/Close-Contact** - Similar to Intermittent Contact, but instead the cantilever tip does not make contact with the surface and stays within the attractive force regime of the surface forces (explained in greater detail in Section 2.1.5).

Each mode has different benefits and drawbacks with one key one being the degree of tip and sample wear alongside their Signal-to-Noise Ratio (SNR). However, these can change based upon another sub-classification of AFM: its additional functionality. The extent of this list is vast, but some of the main types are Lateral Force; Force Spectroscopy; Kelvin Probe Force; SThM and Magnetic Force to name but a few. The reason for this large number of varying AFM functionalities is due to the flexible operating principle and set-up that a basic AFM instrument provides [1]. How this came to pass is key and is explored below.

2.1.3 Development

The origins of AFM go as far back as 1929 by G. Schmalz [6], whom constructed a profiler that measured surface topography by monitoring the movement of a cantilever whose tip interacted with it. Surprisingly similar to current AFM designs for just under a century ago, it utilised an optical lever arrangement to measure cantilever movement. However, it lacked the ability to control the mechanical interaction with the surface. This lack of control caused damage to the cantilever tip and/or the sample. A solution was developed by R. Young in 1972 [7] that demonstrated a massive leap towards modern day AFMs. He developed a non-contact profiler that measured the electron field emission current between the profiler tip and surface to maintain a constant distance. Connected to an electronic feedback system, the required change

in height that was actuated using a piezoelectric ceramic, would output the sample topography.

The next major breakthrough came once mechanical stability of instrumentation was improved to such an extent that instead of the field emission being measured, the quantum phenomenon of electron tunnelling was possible [1]. Developed by G. Binnig and H. Rohrer et al. and first demonstrated in 1982 [8], this allowed a far more sensitive measurement of surface-tip distance and so a far greater resolution of topography. Named the Scanning Tunnelling Microscope (STM), it utilised piezoelectric actuation and electronic feedback to control the probe and output topography. An operation diagram of this is depicted in Fig. 2.3. STM's ability was further demonstrated in multiple subsequent papers: verification of 0.65 nm step heights in Gallium Arsenide ($\bar{1}\bar{1}\bar{1}$) facets [9]; articulation of its ability relative to other microscopy techniques [10] and demonstrating Si(111) atomic arrangement [11].

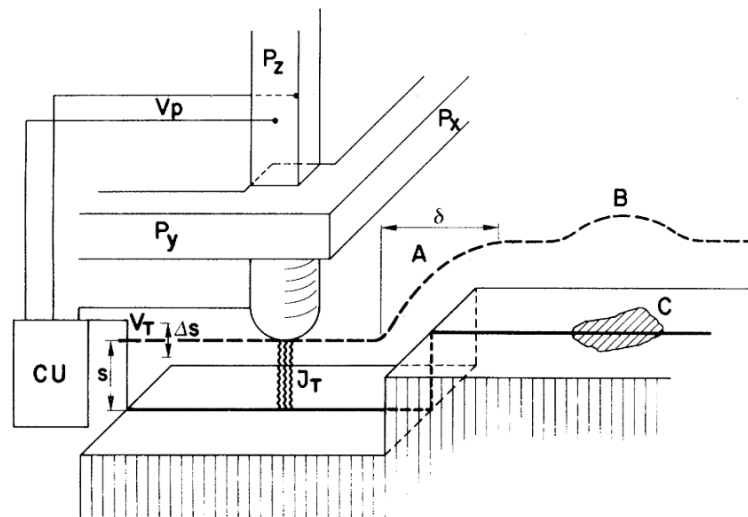


FIGURE 2.3: Original STM Operational Diagram [8]: P_i - Piezoactuators translate tip along axis i ; CU - Control Unit produces the required piezo-voltage (V_p) constant tunnel current (J_T) at a set voltage (V_T); s - Tunnel junction distance with Δs depicting the change due to piezo-actuation. The dashed line represents the subsequent profile generated by the STM with key features at A, B and C of the step and contamination and work function respectively

Building upon all of this, G. Binnig took the principle of controlling the mechanical interaction with the scanned surface further by measuring a spring's elastic deformation instead of a tip-sample tunnelling current [12]. This utilised the same tunnelling phenomenon, but to measure a cantilever's deflection that acted as a spring. As a result of this different measure of tip-sample interaction, it permitted controlled contact

scanning of non-conductive samples with very high force sensitivity down to 10^{-18} N. Scanning over a Al_2O_3 surface and using a diamond tipped Gold (Au) foil cantilever, a vertical and lateral resolution of less than 0.1 nm and 3 nm respectively was achieved. Hence, a general purpose device of sub-nanometre resolution that interfaced with atomic forces was demonstrated. As a result, many other academics explored the principle of this force microscope and applied various techniques/components to its operation including: Si based lithography of cantilevers [13]; optical lever for the force measurement [14] and additional scanning modes such as tapping [15]. Furthermore, due to AFM's flexible nature, additional functionality of the probe tip was realised: localised electrical charge deposition and imaging [16]; measurement of dielectric constants [17]; quantification of thermal properties [18] and measurement of sub-surface features [19] to name a few. These probes of which have been further tweaked and optimised over the years along with continued application development. Today, AFM is ubiquitously used in academic science and engineering contexts with its vast array of functionality resulting in a broad range of applications and roles. Therefore, with this clear understanding of AFMs context and development history, specifics of its modern design features that this project heavily utilised and analysed are explored below.

2.1.4 Deflection Detection Systems

One key feature of all AFMs, as highlighted in Section 2.1.1, is its method for detecting cantilever deflection. Through the measurement of a cantilever's deflection, tip-sample interaction force is inferred and can be maintained allowing for a reliable surface image to be generated. Therefore, it could be argued to be the most crucial component in an AFM alongside the cantilever. With such a function, there are many different types of deflection detection systems used in AFM:

- **Optical Lever/Optical Beam Deflection (OBD) Method**

This involves reflecting a laser off an AFM cantilever and onto a photodetector that outputs the reflected laser spot position. Changes to this position are directly related to alteration in cantilever orientation due to tip force. With calibration, this provides a measurement of tip deflection and hence tip-sample force [1][14]. A diagram depicting this can be seen in Fig. 2.4.

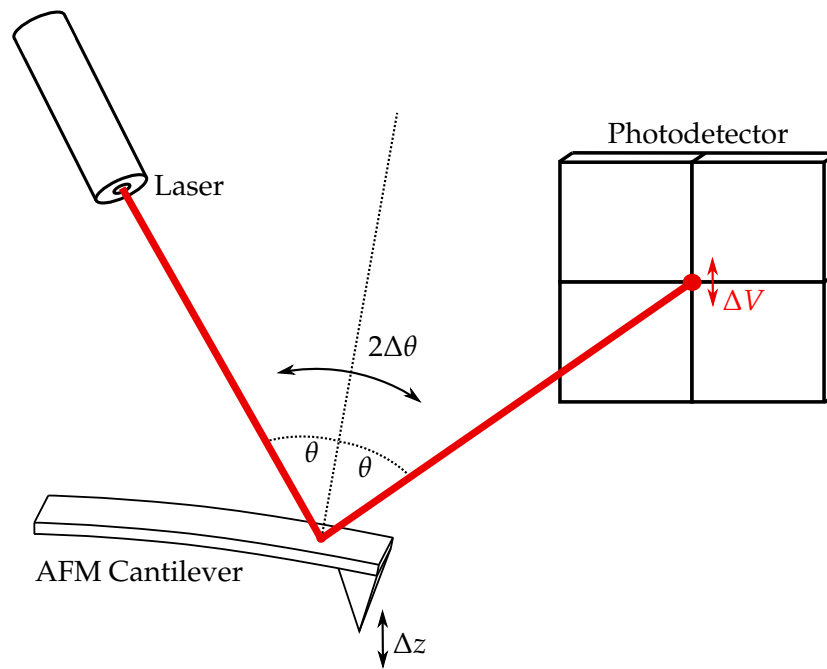


FIGURE 2.4: Optical Lever Diagram

- **Interferometry**

Based upon the interference of light, a beam of laser light is split with one beam reflecting off the cantilever and the other off a stationary reference mirror. With movement of the cantilever due to tip-force, the distance travelled by one of these laser beams changes. This alters the interference pattern created when the two laser beams are recombined, resulting in a direct measurement of cantilever deflection and interpretation of the tip force [20][21].

- **Scanning Tunnelling**

Utilising the distance sensitive quantum phenomenon of electron tunnelling between the AFM cantilever and an electrode located above it, a direct measurement of cantilever deflection is possible [12]. This can then be linked and calibrated to tip force.

- **Crystal Oscillator**

Utilising the principle of piezoelectricity, an alternating current can be used to cause a piezoelectric tuning fork to vibrate constantly. With an AFM tip attached to it, the vibration changes when it experiences a force at its tip and so provides a method of tip force measurement with calibration [22][23].

- **Capacitive Detection**

The change in capacitance between two separated, parallel, metallic plates can render measurement of the distance between the two. Hence, placing a plate on the cantilever and another above it permits direct deflection and force measurement of the tip [24].

- **Piezoresistance**

Applying microfabrication techniques, AFM cantilevers can be constructed with a piezoresistive sensor on its body. This produces a change in electrical resistance due to applied stress and subsequent strain to the cantilever from a tip force and with calibration, the tip deflection and force can be determined [25].

As it can be seen, there is no shortage of methods for determining tip deflection and force; all requiring sound determination of the AFM cantilever spring constant. All of these approaches have their benefits and drawbacks for topographic measurement and other functions. However, the most ubiquitous approach is the optical lever. This is due to its excellent SNR [26]; few and common components; simple overall design [27] and compatibility with a wide range of cantilevers that only need to reflect enough of the laser onto the photodetector. Therefore, due to its prevalence in AFM systems, greater depth of its operating principle is reviewed and elucidated below.

Optical Lever

As previously highlighted, this technique directly measures the change in cantilever orientation that manifests in displacement of the reflected laser spot on the photodetector [14]. Also called the optical beam deflection method (OBD), a diagram depicting its operating principle can be seen in Fig. 2.4 where the laser spot is focused on the cantilever (frequently aligned manually by the user). As graphically demonstrated, the change in rotation at the laser spot's position on the AFM cantilever is directly measured. However, direct vertical displacement of the cantilever also contributes to the measurement in accordance to the following equation determined by T. Tsang [28] that appreciates both this and rotation's contribution to the output:

$$\Delta d = 2L\Delta\theta + 2\Delta z \sin\theta \quad (2.1)$$

where Δd , L , θ , Δz are the displacement on the photodetector, laser path length between the cantilever and the photodetector, laser's angle of incidence on the cantilever and change in cantilever vertical displacement respectively. A graphical representation of the above equation can be seen in Fig. 2.5 for both rotation's and vertical displacement's contribution to the measured displacement on the photodetector. A

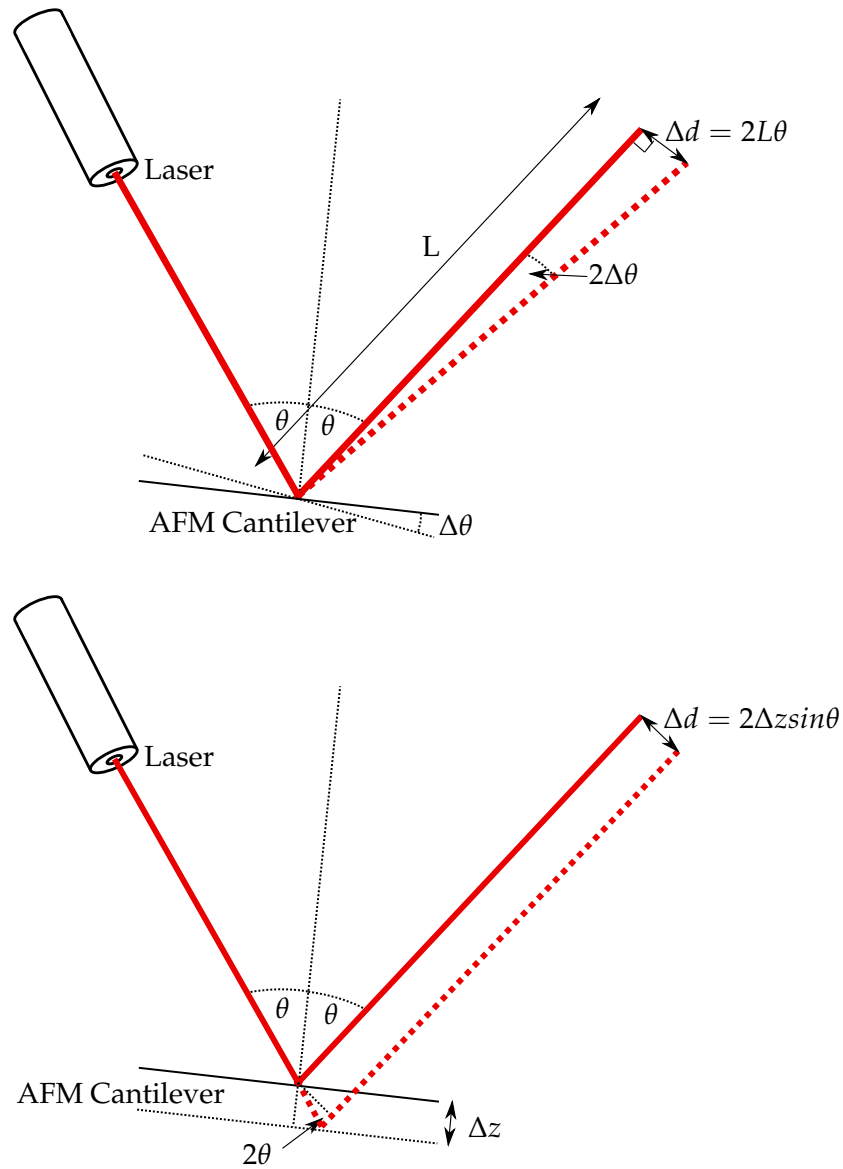


FIGURE 2.5: Optical Lever Rotation & Vertical Displacement Change

brief analysis of this equation demonstrates that as long as the path length between the cantilever and the photodetector (L) is appreciable (for most AFM systems this will be greater than a centimetre), then the rotation will dominate the displacement on the detector. This is reinforced by C. N. Jones et al. [29] who demonstrated 2,000 times greater displacement of the laser on the photodetector from rotation relative to vertical

deflection of the cantilever tip. Although this assumed a linear relation between tip-deflection and photodetector displacement meaning the cantilever acted like a rigid lever arm, this is still an accurate approximation. Hence, vertical displacement will be approaching a negligible contribution with cantilever rotation providing the major influence on the laser spot's displacement on the photodetector in typical AFM set-ups.

Moving towards the exact construction of the photodetector, they are typically made up of four-quadrant photodiodes [5]. These photodiodes output an electrical current dependent on light absorption due to the photoelectric effect, which is subsequently converted into voltage [4]. These voltages then undergo different mathematical operations such as the subtraction of the bottom two photodiodes from the top to output vertical motion of the reflected spot [1]. Hence, cantilever rotation along various planes is possible. This photodiode output is subsequently converted into deflection by determining the Inverse Optical Lever Sensitivity (InvOLS) [30], also termed the deflection sensitivity [31] or sensitivity factor [4]. This is typically determined by driving the cantilever into a hard surface and measuring the vertical photodetector voltage change as a function of piezoactuator's displacement while the tip and surface are in-contact. The latter is then divided by the former as depicted mathematically below:

$$InvOLS = \frac{\delta_{piezo}}{V_{vert}} \quad (2.2)$$

where δ_{piezo} and V_{vert} are the piezoactuator displacement and photodetector's vertical voltage change respectively. This can be seen visually in the Voltage-distance curve in Fig. 2.6. In this scenario, it is assumed the piezoactuator is rigidly connected to the cantilever tip and so their displacements are equal. Therefore, once contact is made with the surface and the piezoactuator is driving the tip into the surface, the cantilever will displace equally and oppositely according to Newton's Third Law. The latter is due to the far greater relative stiffness of the sample to the cantilever resulting in negligible deformation of the sample and tip causing only deflection of the cantilever in the low force range of AFM operation. Thus, a complete cantilever deflection measurement is possible. It should be noted that this calibration procedure is not isolated to the optical lever set-up and is utilised for the other deflection detection systems such as

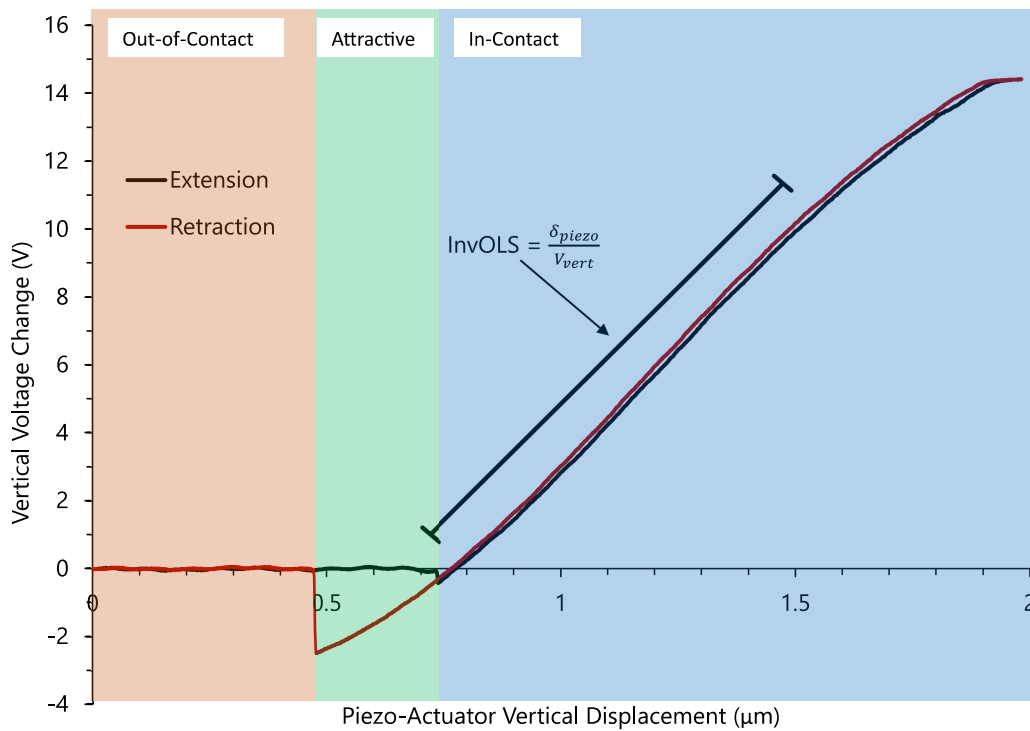


FIGURE 2.6: Example of a Voltage-distance Curve for an AFM Cantilever Under Ambient Air Conditions

piezoresistive [32]. In addition, there are other methods for determining the InvOLS such as the non-contact thermal method that utilises the cantilevers spring constant (e.g. obtained through the Sader method [33]) and measures the voltage noise density to ascertain the InvOLS [4]. However, this is far less well known and employed.

2.1.5 Interaction Forces

Most of this review has focused on AFM instrumentation, but the actual forces it interacts with have not been considered in detail. However, it is important to not only appreciate these forces to anticipate their magnitudes during operation, but also how these forces effect the AFM's cantilever. The most common tool employed to understand the forces an AFM tip experience are through Force-distance (F-d) curves. These appear similar to the plot seen in Fig. 2.6, but with the InvOLS (already known) and the cantilever spring constant utilised to convert vertical voltage signal to Newtons on the y-axis. Hence, F-d curves are the same as that seen in Fig. 2.6, but with a coefficient applied to the y-axis. In this figure, the attractive regime (the region where forces pull the tip towards the sample causing a negative force) can be seen coming into play just before initiating contact (the green to blue region transition) and conversely when

losing contact (green to orange region transition). These forces include Van der Waal (London dispersion and Casimir forces); electrostatic (ionic and hydrogen bonds); capillary forces; water meniscus [34]; quantum mechanical (covalent and metallic bonds) and ion correlation [3]. The magnitude of each varies dependent of the tip-sample interaction conditions along with that of the surrounding ambient environment. For example, when immersed in a liquid, Van der Waal forces tend to be reduced and its influence on F-d curves less pronounced [4]. Moving closer to the sample, a snap-in effect occurs which typically prompts engagement. Beyond this, repulsive forces are more prominent causing typically a linear increase between vertical position and voltage/force (i.e. the InvOLS). These repulsive forces include electrostatic (Coulombic forces;) quantum mechanical (steric and Born repulsion); solvation (hydration and structural forces) and entropic (thermal fluctuation and protrusion forces) [3]. When the y-axis magnitude becomes positive (or the approach voltage/force is exceeded), then the repulsive forces are greater than attractive ones causing an equal and opposite positive force on the cantilever. As a result of these two directions of force, whenever the tip is in-contact with the surface, it has a strong mechanical connection in the vertical axis. Therefore, when AFM maintains a constant balance of these forces, it should output a consistent topographic image of the scanned surface.

In addition to these forces having an influence over the vertical direction in AFM operation, they have an effect over the horizontal plane of the sample (lateral and longitudinal). This is due to the cantilever scanning along the horizontal plane which can result in twisting/displacement of the cantilever in some imaging modes due to friction. This friction measurement is dependent on the sample and tip material; tip geometry; roughness; applied force (normal force); scan speed and other operational conditions during scanning [3]. Hence, a complex and variable horizontal condition and so set of forces occur for each AFM scan. With this better appreciation of AFM and its cantilevers, Thermal Drift and Bending's influence on this system can be reviewed.

2.2 Thermal Drift & Bending in AFM

In AFM, Thermal Drift is the common term for temperature change over time resulting in material movement that effects images or microscope operation [3]. It is generally regarded as the main source of drift in AFM images [35]. Thermal Drift has mostly been attributed to the coefficient of thermal expansion (CTE) in the materials utilised in the AFM [36]. With this understanding, various papers have quantified the phenomenon using different methods and focused on different components of the AFM. Some have measured Thermal Drift in different AFM design's which have been attributed to their varied metrological chain lengths [37], while some specifically measured the contribution from cantilevers alone [36], [38]. Whichever the source, its general manifestation is widely accepted to be due to ambient temperature change that causes displacement in the AFM instrument, typically producing gradual movement in topographic features, as seen in Fig. 2.7. This figure is a general example and does not account for potential concentrated temperature changes from the laser, probe or sample. Regarding the latter points, changes in the laser position, laser source-cantilever distance, laser power or optical properties of the immediate sample area [39] can change the cantilever temperature and hence effect measurement. For example, J. Spiece et al. demonstrated 0.5 K of temperature change over 30 minutes of scanning in one instance [40]. In addition to quantifying the problem, effort has been put towards attenuating and removing the effects of Thermal Drift and Bending. This includes thermally compensated stages [41], improved scanning/processing techniques [42]–[45], structurally compensated/altered cantilevers [46], [47] and minimising the extent of the reflective coating [38]. However, as suggested by this project's scope, sound quantification of the problem was still lacking, especially regarding one of the most mechanically and thermally sensitive components in the AFM, the cantilever itself. Hence, the following section shall articulate the relevant literature pertaining to the influences of temperature change on the displacement/deflection of AFM cantilevers.

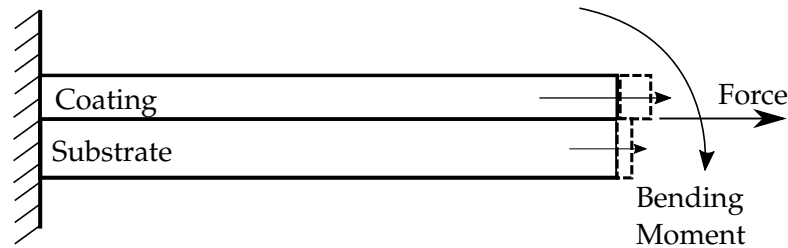


FIGURE 2.7: *Example of Drift in an AFM Image* [37]

2.2.1 AFM Cantilever Thermal Bending

Not all AFM cantilevers are made equal with different materials, shapes and geometries. However, many of them are constructed from two layered materials, one providing the mechanical cantilever structure, while the other a reflective coating for the laser in the optical lever system [48]. Moreover, some cantilevers require an electrically conductive wire along their length for various functions such as thermometry [49], Conductive-AFM [50], Kelvin Probe Force Microscopy [51] and self-sensing [52]. Hence, this layered structure is common and unavoidable in some cases. With such a construction and use in AFM, Thermal Drift of the cantilevers is dominated by thermal bending or the Bimetallic Effect [48]. S. Timoshenko was one of the first to document this general phenomenon in 1925 [53], whereby he explained it occurs due to the two materials being strongly adhered together and possessing different CTE's. As a result, during temperature change, each material displaces by different magnitudes, producing different strains and axial forces along the cantilever length. This disparity in displacement and force generates a bending moment towards the material with the lower CTE. This moment subsequently produces a vertical deflection. A diagram visualising this can be seen in Fig. 2.8 with the coating possessing a CTE greater than the substrate.

This phenomenon is best documented in bimetallic strips, bi-metal thermostats and bimorphs with many applications such as in toasters, kettles, irons, electrical switches and circuit breakers [54]. Hence, when structures that are similarly constructed from two layered materials with dissimilar CTE's, as in the case of many AFM

FIGURE 2.8: *Thermal Bending in Cantilevers*

cantilevers, a similar behaviour occurs. In AFM, the vertical deflection occurs along the same axis as topography resulting in direct Thermal Drift being generated in images. First documented and demonstrated by M. Radmacher in 1995 [36], he showed that both annealing and removing the metal layer vastly reduced displacement of the cantilever due to temperature change in an AFM system. This was further supported by L. Wenzler [38] who showed a similar attenuation in displacement from a reduction in metal coating. In addition, one paper demonstrated that the common MLCT-C probe displaced by 315 nm/K [55]. As a result of this research, many commercial manufacturers of AFM probes have developed cantilevers with no metal coating or a reduced coating [56], [57]. However, apart from this reduction in metal or balancing the materials axial forces and bending moments [58], little has been achieved in understanding how thermal bending is exactly interpreted in the AFM's optical lever system.

2.2.2 Thermal Actuation of Micro-Cantilevers

With the knowledge of thermal bending occurring in micro-cantilevers, many authors and technologies have harnessed it for actuating MEMS cantilevers. The exact application of these is highly varied with some used to extract waste heat in both macro and micro systems [59], [60]; actuation in scanning fiber endoscopy [61]; general micro-cantilever actuation [62] and AFM cantilever actuation [63]–[76]. The number of devices that have been theorised and fabricated is significant, highlighting the effective simplicity of this form of actuation. Looking further into its employment for AFM cantilevers, there are multiple different thermal sources that have been employed and are hence described:

- **Photothermal:**

Typically employing a laser, photons of light are directed onto an AFM cantilever which are absorbed causing excitation of the cantilever material and temperature increase. Through the multi-layered structure of the cantilever, thermal bending and actuation is induced. Furthermore, pulsing of these photons can be utilised to cause an oscillating motion to enable dynamic scan modes in AFM [63]. One key merit of this approach is the isolated heating and actuation that minimises spurious peaks in the spectra associated with other techniques [71], [74], [76], [77]. As a result, this renders it especially good for dynamic scanning modes when the cantilever is submerged in liquid such as in Fig. 2.9.

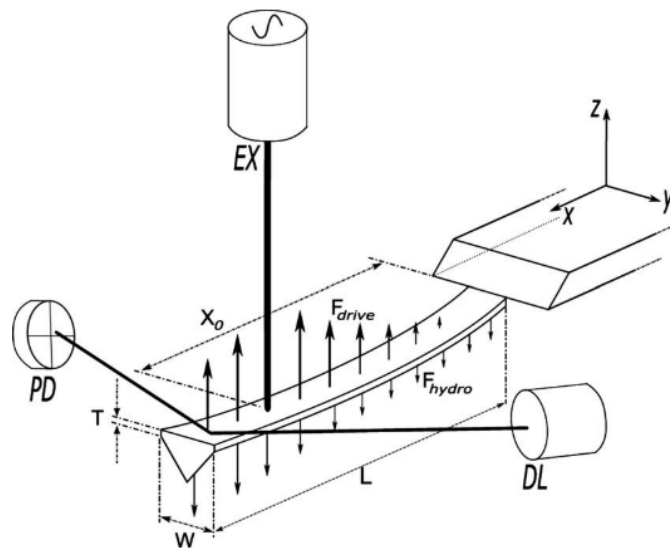


FIGURE 2.9: A Diagram by V. Pini et al. depicting a Photothermally Actuated Cantilever (Using the EX Laser) in a Fluid [71]

- **Electro-Thermal:**

This employs a heater (e.g. resistive heater) powered through an electrical current that is located on or near the cantilever. This induces temperature change of the multi-material cantilever resulting in thermal bending. Hence, actuation can be controlled through the heater's electrical input. Moreover, many of these devices employ a piezoresistive sensor for the deflection measurement [65]–[69], [72], [73], [75]. An example of this can be seen in Fig. 2.10.

From all of the above, it is apparent that there are many examples whereby thermal actuation has been harnessed with it being a very common technique in AFM.

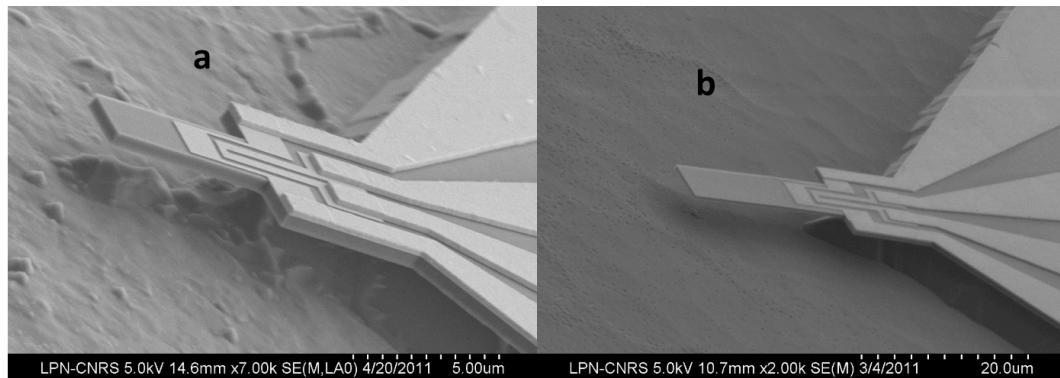


FIGURE 2.10: Example of an Electro-Thermally Actuated Cantilever with a Integrated Piezoresistor for deflection Measurement at its base for (a) $7\ \mu\text{m} \times 2\ \mu\text{m}$ and (b) $23\ \mu\text{m} \times 6\ \mu\text{m}$ [72]

However, all the above methods of actuation are predominantly to induce dynamic AFM scanning and not for contact mode operation meaning this is an area little explored. With the literature highlighted, the next step was to research the appropriate modelling techniques for the thermal bend phenomenon.

2.2.3 Modelling Thermal Bending

2.2.3.1 Thermal Bend Equations

In pursuit of increased understanding, theoretical work on modelling thermal bending in cantilevers was explored. Thermal bending for structures with thin-films was first documented by G. Stoney in 1909 [78]. He described and connected the stress experienced by a substrate due to thin film deposition with its curvature through mathematical relation and experimentation. This allowed imparted stress from thin films to be linked and quantified to curvature and displacement in structures. Therefore, thin films which impart a stress with a change in curvature (such as from a change in temperature) can be theoretically and experimentally appreciated. Acting as the foundation, many authors have tweaked and evolved G. Stoney's initial formula and applied it to different imparted stresses and structures. Some important developments were performed by W. Riethmuller and W. Beneche in 1988 [79] alongside W. H. Chu in 1993 [80] that altered G. Stoney's equations and demonstrated their application for micro-cantilevers constructed from two materials. W. H. Chu articulated the subsequent mathematical relation explicitly with very good agreement to experiments for

cantilever curvature (K):

$$K = \frac{6w_s w_c E_s E_c t_s t_c (t_s + t_c) (\alpha_c - \alpha_s) \Delta T}{w_s^2 E_s^2 t_s^4 + w_c^2 E_c^2 t_c^4 + 2w_s w_c E_s E_c t_s t_c (2t_s^2 + 3t_s t_c + 2t_c^2)} \quad (2.3)$$

where E , w , t , α , T denote the Young's Modulus, width, thickness, CTE and temperature respectively alongside the subscripts s and c representing the substrate and coating respectively. Many other authors have followed this or very similar mathematical derivation methods for cantilever and plate type structures [81]–[84]. From these, C. Hsueh in 2002 [82] provided a comprehensive derivation of elastic deformation of multi-layered structures due to stresses imparted from a mismatch in material layers CTE. This allows more than two layers to be appreciated while undergoing a temperature change alongside external bending moments. This is subsequently shown below for the curvature and contributing equations:

$$c = \frac{(E_s t_s \alpha_s + \sum_{i=1}^n E_i t_i \alpha_i) \Delta T}{E_s t_s + \sum_{i=1}^n E_i t_i} \quad (2.4)$$

$$t_b = \frac{-E_s t_s^2 + \sum_{i=1}^n E_i t_i (2h_{u,i-1} + t_i)}{2(E_s t_s + \sum_{i=1}^n E_i t_i)} \quad (2.5)$$

$$K = \frac{3[E_s t_s^2 (c - \alpha \Delta T) - \sum_{i=1}^n E_i t_i (c - \alpha_i \Delta T) (2h_{u,i-1} + t_i)] + 6M}{E_s t_s^2 (2t_s + 3t_b) + \sum_{i=1}^n E_i t_i [6h_{u,i-1}^2 + 6h_{u,i-1} t_i + 2t_i^2 - 3t_b (2h_{u,i-1} + t_i)]} \quad (2.6)$$

where c , t_b , h_u and M denote the uniform strain component, bending axis (the cantilever's cross-section line where zero moment and strain occurs), layer height from the substrate topside and bending moment. However, different widths between the substrate and coatings are not appreciated in the above equations, unlike in Equation 2.3. Although, as it derives the curvature, it can be translated into displacements and rotations, depending on the solid mechanics theory.

In addition to the above equations, there is literature pertaining to altering the above depending on the relative thickness of the coating and its mechanical contribution to the cantilever structure. First derived for piezoelectric bimorphs by A. Li et al. [85], they demonstrated an equation to determine its flexural rigidity. With the understanding in general beam theory that flexural rigidity equals the Young's Modulus multiplied by the second moment of area, J. W. Yi et al. subsequently showed that for these non-homogeneous cantilevers the effective modulus can be determined [86].

This is shown below:

$$E_{eff} = \frac{E_s^2 a^4 + E_c^2 b^4 + 2E_s E_c ab(2a^2 + 2b^2 + 3ab)}{E_s a + E_c b} \quad (2.7)$$

where $a = \frac{t_s}{t_s+t_c}$ and $b = \frac{t_c}{t_s+t_c}$. This aimed to provide a more realistic representation of the Young's Modulus or the stiffness of the bimorph. This was determined to be applicable in the scenario where the coating provides a significant thickness and so changes the mechanical and thermal bend response of the bimorph [83]. Hence, if there is a relatively thick coating on the substrate, then using the effective modulus may provide a more accurate representation of the subsequent deflection of the structure. However, like in Equation 2.6, this does not account for different widths between the substrate and coating. Moreover, no clear thickness ratio is articulated in these pieces of literature, with J. W. Yi utilising the effective modulus for a structure with a 1:3 ratio between the coating and substrate thickness respectively [86].

Overall, this literature provides a sound basis of theoretical appreciation for thermal bending that has been experimentally validated for multi-material cantilever structures at the micro-scale. Hence, it should be possible to be model thermal induced deflection in AFM cantilevers by employing a similar approach.

2.2.3.2 Solid Mechanics Theory

The next area required to be explored was how the thermal bend equation for curvature (Eq. 2.6) can be converted into deflection and rotation, i.e. its solid mechanics theory. Regarding cantilevers, Euler-Bernoulli Beam Theory is highly applicable. This is a well-known theory and documented to accurately describe slender beams [87]. The definition of beams being structures that bear loads across/perpendicular to their longitudinal axis [88] which is the case for AFM cantilevers. The key assumptions of this theory are [89]:

1. Vertical displacements of the cross-section are small and equal to the deflection of the beam axis (this axis being coincidental to the cross-section's centroid)
2. Lateral displacement is zero

3. The cross-section is normal to the beam axis and remains plane and orthogonal to the beam axis after deformation (i.e. no shear deformation occurs)

Therefore, a key aspect of the above is that significant deflection does not occur that changes the cross-section. Moreover, the theory applies to all stimuli of deflection, for example concentrated and distributed forces. In addition to the above, the theory allows beams to be simplified into 1D structures [89]. However, this simplification may not be the case if the beams are regarded as plates (i.e. if wide relative to their length). Such structures would require to be modelled in 2-Dimensions, allowing three degrees of freedom at each node. However, even if not completely appropriate or desired as a governing theory for the deflections of such structures, modifications of the Euler-Bernoulli Beam Theory can provide some appreciation for plate like beams. This can be performed utilising the Biaxial Young's Modulus instead of the Young's Modulus [81]. This partially accounts for the stress and strain experienced across the width by appreciating the stiffness across the width and not assuming it is infinitely stiff. The equation for its determination can be seen below, where the Poisson's ratio describes the relation between the principle directions (x, y, z):

$$E_{biaxial} = \frac{E}{1 - \nu} \quad (2.8)$$

2.2.3.3 Principle of Superposition

Following the above, the literature pertaining to the use of the above equations and theoretical approaches in FDM models was explored. One method that permits this is based on the principle of superposition [88]. The concept of which is that the deflection of a beam from multiple different loads when acting simultaneously can be reproduced by superposing the deflections produced by the same loads acting individually. The reason this superposing is possible is due to the linear nature of the differential equations pertaining to the deflection curve in the beams, i.e. the quantity to be computed is a linear function of the load. This is valid in cantilevers for stresses, strains, bending moments and deflections due to non-excessive forces. For deflection determination, three conditions must apply: (1) Hookes law holds true for the material during load application; (2) deflections and rotations are small; (3) deflections

do not change the action of a load applied. The above applies to AFM cantilevers alongside thermal bending as long as the temperature change is not large enough to induce gross magnitudes of deflection and/or material phase transition. This is due to it resulting in significant change in the cantilever shape, properties and stiffness that would alter the response to thermal bending alongside other loads, such as from an end-force. With this assumption, the cantilever can then be broken down into theoretically infinite elements and nodes along its length with the load applied to each and summation of the deflections and rotations. A visualisation of this can be seen in a simple two element example in Fig. 2.11.

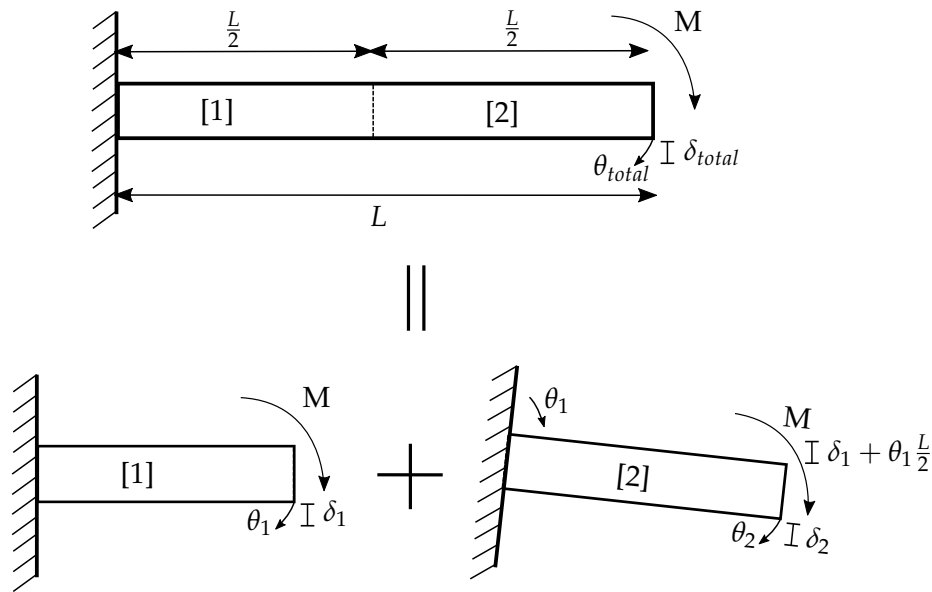


FIGURE 2.11: *Principle of Superposition Diagram where L , M , θ , δ are the Lengths, Bending Moments, Rotations and Vertical Displacements Respectively*

As the load is applied to each element individually, they can contain a different cross-sections or moment of inertia (beams with varying cross-sectioning are commonly termed nonprismatic beams [88]). This means cantilevers with varying widths, thicknesses and materials can be appreciated. Hence, a method for soundly accounting for multiple, simultaneous loads such as from thermal bending is possible as well as appreciating different cross-sectional geometry along the length of a cantilever. This

mathematically translates into the following set of relations:

$$\begin{aligned}\delta_{e,\theta_{e-1}} &= \sum_{e=1}^e L_e \tan(\theta_{e-1}) \\ \delta_{e,total} &= \sum_{e=1}^e \delta_e + \delta_{e,\theta_{e-1}} \\ \delta_{TOTAL} &= \sum_{e=1}^e \delta_{e,total}\end{aligned}\tag{2.9}$$

where $\delta_{e,\theta_{e-1}}$, $\delta_{e,total}$, δ_{TOTAL} are the vertical deflections in each element due to rotations from preceding elements, total vertical deflection in each element due to load & rotation and the total structure's vertical deflection from all the elements respectively. In addition, if the rotation is small, then the small angle approximation is possible rendering $\tan(\theta_{e-1}) \approx \theta_{e-1}$. Application of these equations simply requires substitution of the load producing vertical deflection and rotation equations alongside the element length.

2.2.3.4 End-Force Equations

The final tool required from literature to fully model thermal bending in AFM is an ability to theoretically interpret a typical AFM system. In an actual AFM system, this is performed by applying the InvOLS that is based upon the force imparted by the surface at the cantilever tip (i.e. end-force). Therefore, this needs to be modelled to generate a theoretical InvOLS that can be applied to the thermal bend equations outputs for a complete model. The previously elaborated Euler-Bernoulli Beam Theory is completely applicable to end-forces (EF) in micro-cantilevers and hence an EF for a constant cross-section cantilever can be mathematically determined as such [88]:

$$\text{Cantilever's with an EF: } \quad \delta_{z,max} = \frac{FL^3}{3EI} \quad \theta = \frac{FL^2}{2EI} \tag{2.10}$$

where F , L , I are the EF, cantilever length and second moment of area respectively. Assuming a simple, homogeneous rectangular cross section the latter is simply $I = \frac{wt^3}{12}$. However, one additional equation is required alongside the above for an FDM model. As demonstrated by J. Gere [88], as you translate along the cantilever length, the moment applied by the EF changes. For example, the closer the cantilever element

to the EF, the lower the bending moment imparted. As a result, the Coupled-End-Moment equations are required to model an EF using FDM:

$$\text{Cantilever's with a Coupled-End-Moment: } \delta_{z,max} = \frac{ML^2}{2EI} \quad \theta = \frac{ML}{EI} \quad (2.11)$$

Alongside the above, complex shapes with multiple materials can have their second moment of area's determined through two methods: Parallel Axis Theorem and Transformed-Section Method [88]. The former permits complex cross-sections to be determined and can be mathematically represented as such:

$$x_{NA} = \frac{\sum_{i=1}^n x_{NA,i} A_i}{\sum_{i=1}^n A_i} \quad (2.12)$$

$$I_{x,i} = I_{x_c,i} + Ay_{NA,i}^2 \quad (2.13)$$

$$I_{Total} = \sum_{i=1}^n I_{x,i}$$

where A and z_{NA} represent the section's area and z-distance (i.e. vertical) from the sections neutral axis (NA) to the overall cross-section's NA respectively. However, there are potentially multiple materials that need to be appreciated in the above equations. This is where the Transformed-Section Method is applicable: it allows one material to be transformed into another through the modular ratio, whereby the NA must be located at the same position as it was before (i.e. the ratio can not alter a geometry that effects the NA). Hence, the modular ratio is applied to material sections widths allowing conversion into a homogeneous cross-section. The modular ratio is expressed mathematically as such:

$$n_c = \frac{E_c}{E_s} \quad (2.14)$$

Hence, the above provides a literature tool-kit to determine the theoretical deflection and rotation due to EFs and temperature changes in multi-material, complex and variable cross-section cantilever structures.

2.3 Scanning Thermal Microscopy

With the two above key topics reviewed, to fully explore thermal bending in AFM cantilevers, it was determined that both the temperature and displacement of the cantilever should be measured. SThM cantilevers allow simultaneous measurement of both and so were employed throughout this work. Therefore, their operating principles are expanded below, followed by the key developments over the years that have resulted in modern day SThM devices.

2.3.1 Operating Principles

As a type of AFM, SThM utilises a probe that is scanned across a surface whilst monitoring the tip-sample force. This is performed simultaneous with thermal measurement and so produces a spatial and thermal image of the scanned surface. The spatial resolution, as previously articulated for AFM, can be down to the atomic scale with the thermal resolution potentially approaching 0.01 K [90], [91]. However, these are dependent upon the cantilever geometry, tip shape and thermal measurement technique. The latter being a key variable and influences how they are operated. Broadly, there are four key mechanisms for temperature measurement: thermovoltage, electrical resistance, fluorescence and thermal expansion [92]. Each of which have a pronounced temperature dependent mechanism and so permit temperature quantification. Each are briefly explained below:

- **Thermovoltage**

This is based upon the thermoelectric effect that generates a voltage with temperature between two dissimilar electrodes in-contact with each other. The electrodes can be either located between the tip and sample, such as in tunnelling thermometry [93]–[96], or formed at the tip of the cantilever itself, for example in thermocouples [97]–[100] or Schottky Diode Probes with a Thermal Sensor [100], [101].

- **Electrical Resistance**

Exploiting the relation of electrical properties and temperature within conductors, measurement and heat generation in AFM tips is possible. This involves a

resistive element (typically a noble metal such as Palladium or Platinum) whose electrical resistance changes with the phonons limiting electron flow that is related to temperature change. Temperature and resistance then have a positive correlation in most materials with the Wollaston Wire Probe being the first demonstrated [102]. By passing differing currents through such a probe, it is possible to also use it as a localised heat source thanks to Joule heating of the tip. However, some cantilevers do not have a metallic resistive element and use semiconductor material to generate heat for thermomechanical actuation, thermal analysis, data storage or nanolithography. The first probe of this form was developed by IBM using doped Si [103].

- **Fluorescence**

Employing the highly temperature dependence of fluorescence, temperature can be quantified by monitoring the emitted intensity. The latter is proportional to the population of excited states related to temperature, whereby Bose-Einstein statistics can connect these when the material is under thermal equilibrium. Therefore, SThM probes have been constructed through the placement of a fluorescent particle on an AFM tip [104], [105].

- **Thermal Expansion**

This technique utilises the connection of temperature with the expansion of a material or materials that the AFM cantilever is constructed from. The vast majority of materials expand when temperature increases which is captured through its CTE. Therefore, how the cantilevers material displaces is directly correlated to temperature change. Cantilevers employing this phenomenon have taken various forms that either use thermoacoustic such as in a Scanning-Joule Expansion Microscope [106] or AFM-Infrared [107]. However, some cantilevers are made from two materials and use the Bimetallic effect or thermal bending [108].

From the above, it can be seen that there are many different types of SThM probes that can measure temperature either qualitatively or quantitatively through a variety of mechanisms. These are organised in Table 2.1 for a clear overview. However, one

key aspect is how these all came about and developed. This is subsequently expanded in the following section.

TABLE 2.1: *SThM Mechanism Classifications* [92], [109], [110]

Classification	Sub-Classifications
Fluorescence	Fluorescent-Particle-based Probes
Thermal Expansion	Bimorph Sensors; Scanning Joule Expansion Microscopy; AFM-IR Technique
Thermovoltage	Tunnelling Thermometry; Point Contact Thermocouple Method; Thermocouple Probes with Thermal Sensor; Schottky Diode Probes with Thermal Sensor
Electrical Resistive Change	Metallic Probes; Doped Si Probes
Other	Thermal Radiation Scanning Tunnelling Microscopy

2.3.2 Development

A technique that maps topography alongside thermal properties in a SPM [1], SThM was first demonstrated by Williams and Wickramasinghe in 1986 [18]. They developed a non-contact, high resolution profiler that utilised a thermocouple at its tip to measure heat flow to control the gap between the tip and sample. This employed an electronic feedback system similar to G. Binnig and H. Rohrer's STM in 1982. Not directly employed for quantification of thermal properties at the nano-scale, it did demonstrate the ability to do so at a high resolution. Hence, an explosion of probes focusing on thermal measurements occurred: Tunnelling Thermometry (1989) [93], Kelvin Probe Force (1991) [51] and Scanning Thermal Conduction (1992) [94] microscopes. The former utilised thermal measurement (using a thermocouple generated between the tip and sample) to determine the degree of absorption of light due to the sample and so determine its chemical make-up. The latter two were based on the concept of temperature change inducing a shift in the electrochemical potential difference between a metallic tip and sample. All three techniques required a conductive sample and so restricted their capability for thermal property measurement. However, it did not take long to overcome this. In 1993 A. Majumdar exhibited an AFM system

with a thermocouple tip formed from two different metal wires that met to produce the tip apex [111]. A diagram showing this arrangement can be seen in Figure 2.12. This was an important step as it demonstrated simultaneous thermal and topographic measurement in the flexible AFM system. Therefore, electrically insulating samples could be scanned [91]. However, there were problems such as the sensor deforming that effected its reproducibility. Following this, R. Pylkki et al. invented the Wollaston Wire Probe in 1994 that demonstrated a leap in thermal and topographic performance [102]. Constructed from a thin wire of Platinum/Rhodium in a v-shape to create a tip, changes in electrical resistance of the wire due to temperature enabled its measurement. A Scanning Electron Microscope (SEM) image of this can be seen in Figure 2.13. With spatial resolution down to 100 nm, it is still utilised to this day due to great sample compatibility, high temperature coefficient of resistance, high endurance and fast response time. However, its large thermally active area prevents high spatial-thermal resolution.

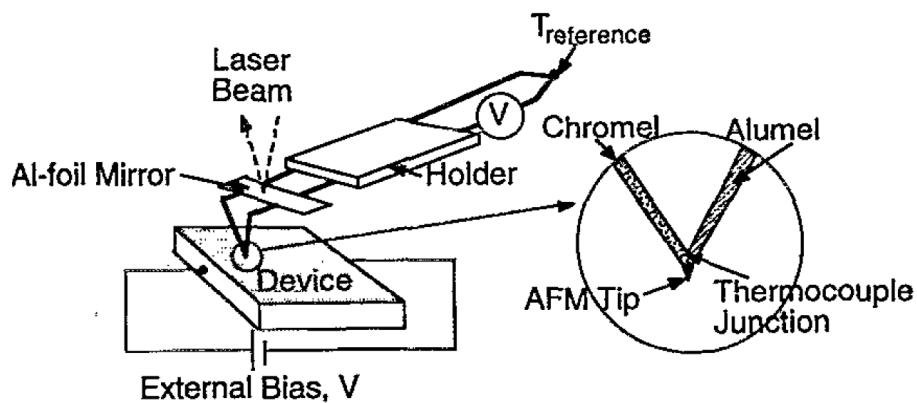


FIGURE 2.12: A.Majumdar SThM Design Diagram [111]

Through micro/nanofabrication techniques, sharper tips were produced to enhance spatial resolution, thermal response time and thermal sensitivity [112]. Hence, subsequent probes were fabricated by G. Mills et al. in 1998 [97] that were focused on batch fabrication as opposed to individual craftsmanship. Structurally constructed from Silicon Nitride (SiN_x), these utilised a thermocouple made from thin Au and Palladium (Pd) depositions at its tip for thermal measurement. Specifically, it used Electron Beam Lithography (EBL) for this tip definition permitting reproducible thermocouple tips with a radius of 50 nm. This enabled commercial production and distribution of SThM probes. However, these thin thermocouples did not demonstrate

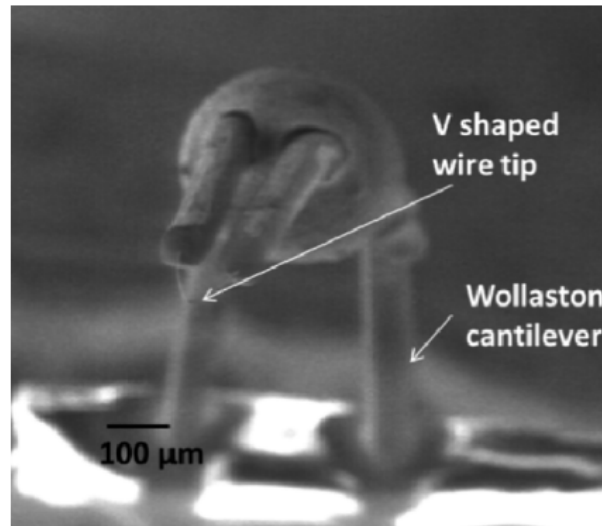


FIGURE 2.13: *Scanning Electron Microscopy Image of a Wollaston Wire Probe [92]*

the same sensitivity as their bulk form, as well as suffered from non-linear thermal response and difficulty maintaining a constant temperature cold junction (especially over hot samples producing large thermal energy). With these drawbacks, a new probe based upon the change in electrical resistance with temperature was batch fabricated by P. S. Dobson et al. [49]. Similarly batch fabricated to G. Mills et al., they were constructed from SiN_x with a Pd resistor at the tip. Two different types were constructed of a two and four terminal configuration for the electrical resistance measurement of the Pd which can be seen in Figure 2.14. The former is a more standard SThM design, while the latter allowed localised tip resistance measurements that removed wire resistance and any changes that occur to them on its thermal measurements. Irrespective of design, the probe demonstrated excellent characteristics due to the resistive thermal sensor's linear thermal response, enabling simpler calibration. Moreover, additional design tweaks to the original G. Mills et al. design were performed. This included a longer tip to increase cantilever and sample distance and so reduce air conduction artefacts alongside reducing spring constant rendering the quality factor immaterial. However, some caveats to this design were apparent. Utilising the change in electrical resistance due to temperature change of a Pd sensor, it is susceptible to Joule heating occurring during thermometry, effecting the thermal measurement. This is due to the sensor requiring an electrical current for resistance and thermal measurement. However, research by Y. Ge [113] realised that this could

be rendered negligible by reduction to a current less than 0.2 mA. Further develop-

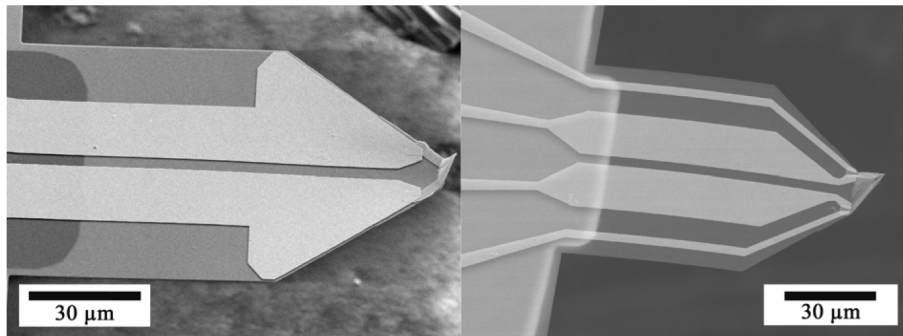


FIGURE 2.14: *Two & Four Terminal Resistive SThM SEM Images [49]*

ments were made to the SThM probes fabricated by P. S. Dobson et al. with a change in the shape of the probe. This involved ribbed/grooved cantilevers by Y. Zhang et al. [114] as seen in Figure 2.15. This design aimed to attenuate thermal bending to permit hotter samples to be interrogated alongside more accurate topographic measurement.

Outwith the above commercial SThM design, alternative SThM probes were fabricated such as the Point Contact Thermocouple probe in 2010 by S. Sadat et al. [115] and novel SThM resistive tips by P. Janus [116] alongside a number of others. Furthermore, developments and research employed on these existing SThM probes was performed [39], [114], [117]–[120]. However, the batch fabricated probe developed by G. Mills and P. S. Dobson et al. that is fabricated by Kelvin Nanotechnology (KNT) at the James Watt Nanofabrication Centre (JWNC) [2] is a well used and common one in the academic and commercial SThM communities due to the following attributes:

- Ability for perform passive (thermometry) and active mode (thermometry and heat source) SThM measurements [109]
- Relatively good topographic imaging for SThM
- Greater conformity between probes and so standardisation and reproducibility of application
- Demonstration of sound calibration [121]

The two main types of probe manufactured by KNT over the years are the KNT-SThM-1an (also named VITA-XX-GLA-1) and KNT-SThM-2an probes. The former employs a two terminal design for resistive interrogation of a Pd (thickness of 45 nm) sensor that was connected through Au wires (145 nm), all deposited on a SiN_x cantilever

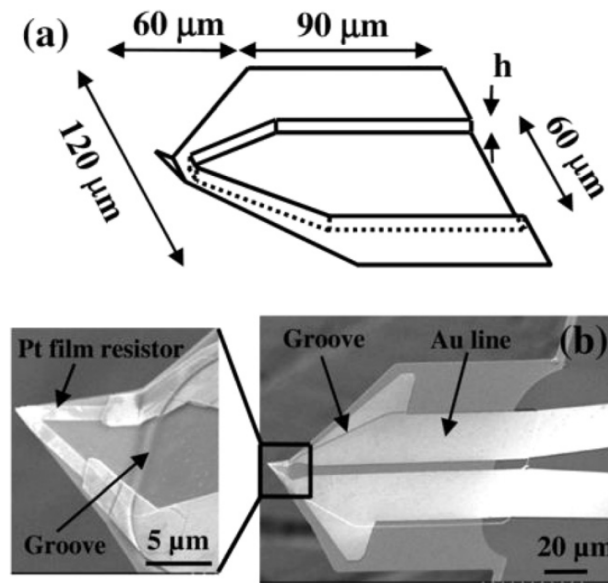


FIGURE 2.15: *Grooved Resistive SThM Probe SEM Images & Graphic [114]*

(400 nm). A view of this can be seen in Figure 2.16. However, the KNT-SThM-2an probes use the ribbed/grooved design [114] that aimed to mitigate thermal bending, but were unsuccessful in completely attenuating this.

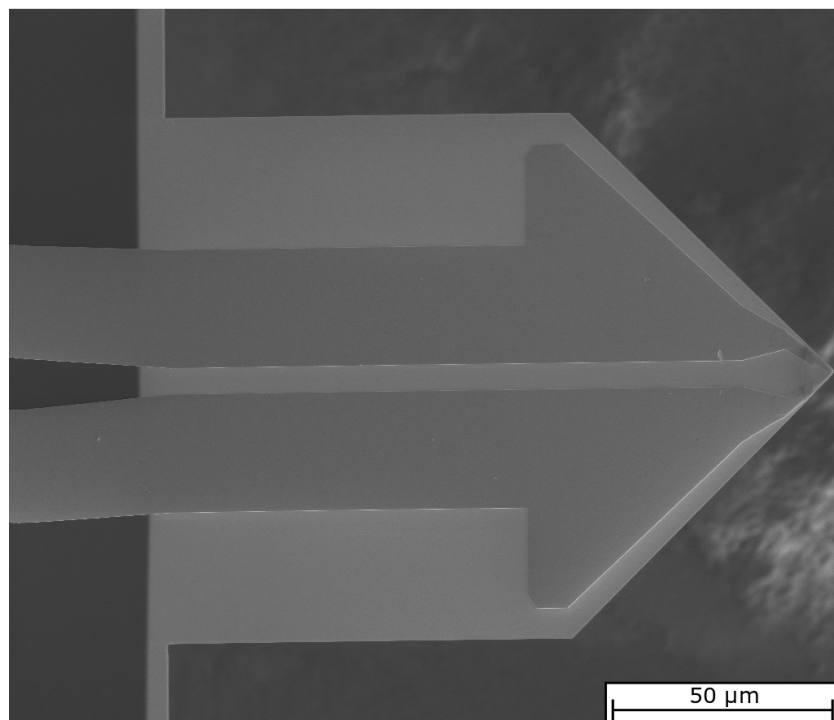


FIGURE 2.16: *SEM Image of a KNT-SThM-1an Probe*

2.4 Fabrication

With all the literature reviewed for AFM, SThM and thermal bending, the final component to be explored was the main fabrication techniques appropriate to AFM and SThM probe manufacture. This was required to inform on the constraints imposed by probe fabrication on their design alongside how to manufacture new probes within this project. Therefore, any design improvements proposed such as to attenuate thermal bending could subsequently be conceived and fabricated. As with most micro-sized devices, the majority of AFM probes utilise three main processes in their fabrication: Lithography (patterning), Etching (removing material) and Deposition (adding material). Each shall be expanded below.

2.4.1 Lithography

Lithography can be defined literally from its Greek origins with "lithos" and "gràphein" meaning stone and write respectively which dates back to 1796 to Aloys Senedelder who first invented the process based upon the repellent nature of oil and water on stone to produce images [122], [123]. It has changed and developed a lot since this humble beginning, whereby a significant modern day application is to generate micro and nano-metre scale patterns within the semiconductor industry. Within this area, there are various techniques to generate patterns at this resolution. The two main types of which are mask based or direct-write lithography [124]. However, it is not just confined to these where there are Scanning Probe based and Nanoimprint Lithography, but these are rarely employed in AFM fabrication. Mask based and direct-write lithography predominantly utilise radiation to expose photosensitive materials that are spun on samples to produce an exposed pattern. When the latter occurs, the photosensitive material (typically a polymer called photoresist) reacts to the radiation to change its solubility [123]. Once this has occurred, it can be subject to a chemical called a developer that removes the exposed/unexposed photoresist leaving the desired pattern. This can then be processed further to either remove (etch) or add (deposit) materials in the form of the defined pattern. With this general definition, the two main types of lithography in mask-based and direct-write can be further elaborated below.

2.4.1.1 Mask Based - Photolithography

Within mask based lithography, the most common and relevant form to batch fabrication of any micro-sized device such as AFM, is Photolithography. This employs Ultra-Violet (UV) radiation to expose samples through a quartz mask with a chromium defined pattern [123]. This can achieve resolutions down to 100 nm [123]. A visualisation of this can be seen in Fig. 2.17, whereby the follow on process of either increasing or decreasing the photoresist's solubility and developing the pattern can be seen. This exposure can be performed either in contact, close proximity or projected. The former being with the mask and photoresist making contact during exposure, where the latter two with a close and large gap between them. With this technique, there are a num-

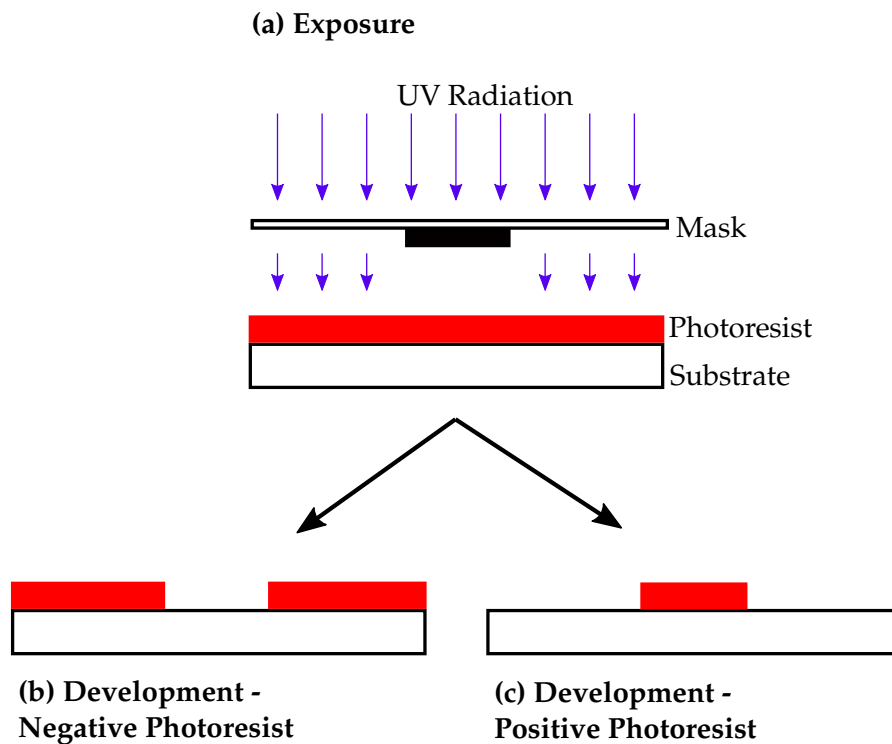


FIGURE 2.17: *Diagram of Photolithography Exposure & Development*

ber of traits it possesses enabling it to be popular in microfabrication. The main one being able to expose all the patterns simultaneously and so reducing exposure and production time. This major benefit is the reason for its employment in batch fabrication of devices, such as AFM, as it allows the definition of multiple probes on a single substrate.

2.4.1.2 Direct Write - Electron Beam Lithography

The other main type of lithography is direct-write techniques such as Electron Beam Lithography (EBL). Although less employed in batch fabrication, this allows for high resolution features to be written that are especially crucial for more bespoke AFM probes or very sharp tips [114], [125]–[130]. Focusing on EBL as a common type of the direct-write technique, it involves focusing a beam of electrons that exposes the photoresist and through displacing the beam, a pattern can be written. Due to electron's wavelength being four or five orders of magnitude less than for example UV light, it can generate very high resolution patterns down to sub-10 nm [131]. This resolution and exposure (also called dose) is controlled through the beam current, spot size, dwell time (i.e. time the beam lingers over a region) and beam-step-size to define a wide range of patterns [132]. As a result, it can produce varied and very high resolution patterns. However, it can not expose the whole pattern simultaneously like in Photolithography and only through individual pixel exposure from displacement of the beam spot to define the pattern. A diagram illustrating an EBL system can be seen in Fig. 2.18. As a result of the operating principle, it typically takes a lot longer to define the pattern than Photolithography, but renders far greater resolution definition and typically more precise alignment.

Before proceeding on with literature pertaining to processes that exploit this patterning to define features, alignment should be focused on as this is a major aspect in EBL and a major benefit of it. Due to EBL using a beam of electrons, it can utilise this for imaging purposes like an SEM (the first EBL system was in-fact a modified SEM [132]). Therefore, they can image regions and identify features whereby these can be used to align the beam and accurately define the pattern relative to this. These features are typically called markers with the most ubiquitous being crosses. The markers can be broadly placed into two categories of global and local markers. The former is used to correct for placement and rotation of the sample/wafer where crosses typically have a line width of 2-6 μm and 100-200 μm in length/height. However, they do not have to be crosses whereby alternatives include L-shaped [133], squares and even more advanced shapes/patterns such as Sierpinsky carpet pattern and Penrose tiles

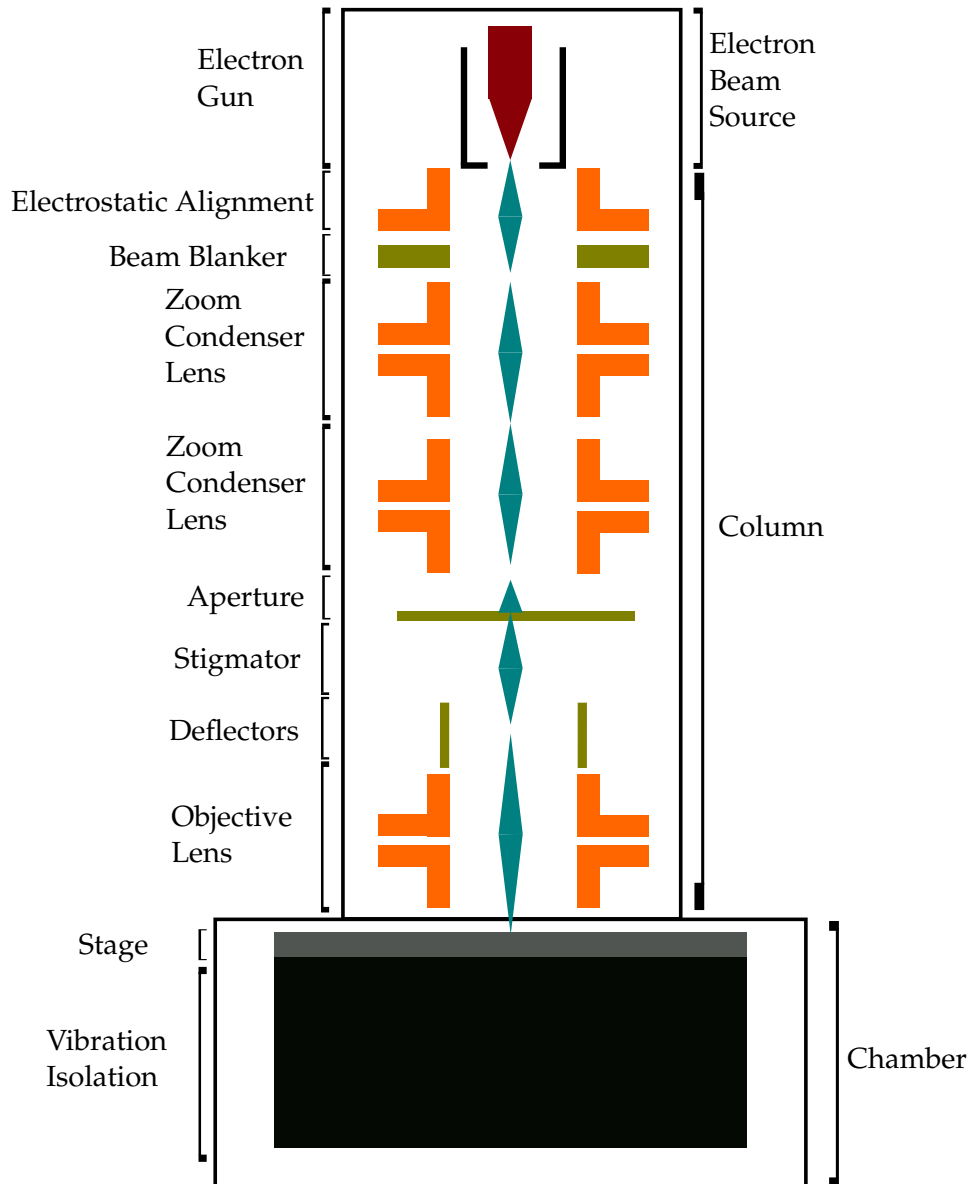


FIGURE 2.18: *Diagram of an Electron Beam Lithography (EBL) System*

[134]. Regarding local markers, these can be useful for multiple purposes: compensate for mechanical/Thermal Drift for pattern definitions over a long period of time and provide diagnostic information on displacement over time/location [132]. Moreover, with accounting for potential drift they can ensure a fine tolerance for writing a pattern in the desired location when it is nearby the local marker (e.g. hundreds of microns). Although these two marker types are separate, they can utilise the same marker on the sample (e.g. cross, square) for their specific categories purpose. Furthermore, these markers on the sample that the EBL aligns to can be defined either through deposition (typically a metal) or etching. Employment depends on a number

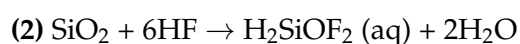
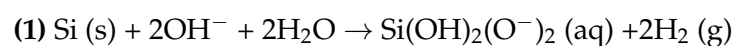
of factors such as the overall process steps (e.g. if a metal is used to define the markers, then no etches that would remove that metal are possible), required resolution, facility process capabilities and ease. Overall, these markers permit EBL to have a very fine tolerance in pattern location coupled with the electron beam providing sub-10 nm resolution enabling a very powerful lithography technique.

2.4.2 Etching

With lithography providing an ability to create patterned areas defined by photoresist, the sample can be processed according to this. One of two key processes employed to take advantage of this in micro/nano-fabrication is etching. This is the simple process of removing material. However, there are many different ways this can be achieved, with the two main classifications of Wet and Dry Etching [135]. The former refers to subjecting the patterned sample to a liquid that chemically reacts with it (called an etchant) to remove selective or multiple materials on it. The latter however utilises gaseous based methods such as plasma (i.e a dry fluid and hence the name) to remove the materials either through chemical and/or mechanical agitation. Each type will be further explored below.

2.4.2.1 Wet Etching

This technique employs chemical reaction of an etchant with material(s) to remove it from the sample. Generally, this exploits two types of chemical reaction involving either a metal or insulator, whereby the former involves electron transfer while the latter is an acid-baser reaction [123]. Common examples employed in Si based devices are:



Furthermore, this type of etch is typically isotropic meaning it etches uniformly causing spherical or rounded profiles. As a result, it can struggle to define fine features. However, this is not always the case such as for Hydroxide based etches of Si. One example being reaction (1) above which generates a 54.7° angled etch to the flat due to

its ability to etch the {111} plane more than the other crystalline planes [136]. Alongside this, how this etchant is exposed to the sample varies with the three main types being bath (submersion in a bath of the etchant), spray (spraying the etchant onto the sample) or single-wafer processing (spraying the etchant but singled sided). Using the former as a example, typical equipment include a vessel (e.g. Quartz, Teflon) with heating and temperature control. A simplified graphical depiction of such a set-up can be seen in Fig. 2.19. In addition, temperature control is a common feature due to elevated temperature typically altering the reaction and etch rate [137]. However, as a

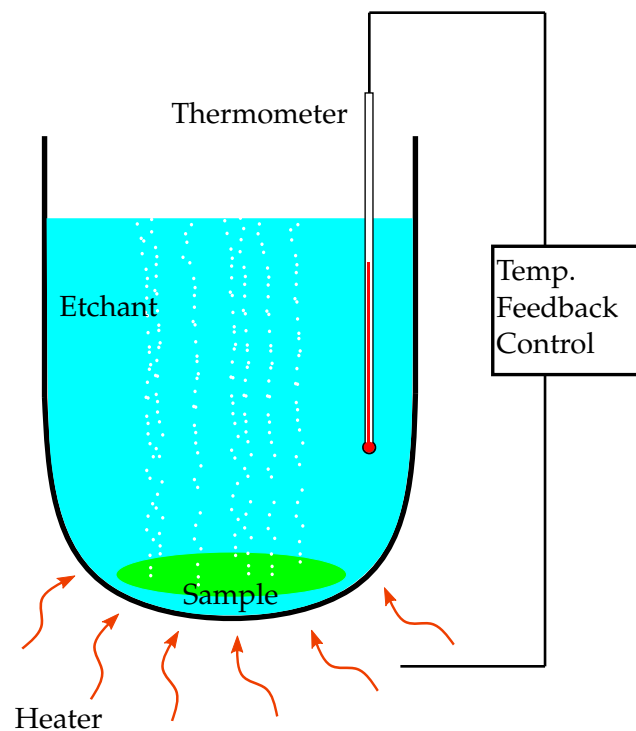


FIGURE 2.19: *Simplified Diagram of a Wet Etch Kit*

result, it requires sound and ideally uniform temperature control to ensure consistent etch rates. Additionally, most wet etches are controlled through time of exposure to the etchant and so a consistent etch rate is required for more accurate magnitudes of the material to be removed in the process making it highly dependent on the chemical concentration and temperature control. As a result, wet etching can be challenging to produce consistent etch depths, but has the ability to produce unique etches and remove a significant magnitude of material while being relatively low in its initial capital expenditure [137].

2.4.2.2 Dry Etching

Moving onto dry etching, this involves the removal of material from a surface using gases or plasma which do not wet the surface (hence the name) [124]. This can utilise chemical reaction and/or physical sputtering to remove materials from a sample. The former is similar to wet etching, while the latter involves ions that accelerate to the sample surface and through transfer of momentum, remove particles on the surface. Many dry etch techniques involve the employment of plasma etchant which is typically formed by the presence of gas(es) between two electrodes that has a certain frequency in the flow of electrons. These electrons cause dissociation in the gas to turn it into a plasma containing reactive species such as ions (positively and/or negatively charged), radicals/neutrals, electrons and photons [138]. One of the most popular dry etch techniques is Reactive Ion Etching (RIE) and is employed in the fabrication of many micro/nano sized devices such as AFM cantilevers. This utilises both chemical and physical aspects to etch the surface typically in a synergistic fashion. The former utilises the reactive species while the latter uses ions to physically bombard the sample surface. The ions bombard the surface due to the electrons greater mobility than ions in the plasma and the lower plate (which the sample is on) being connected to a blocking capacitor. Hence a build-up of negative charge occurs that the positive ions are attracted and accelerate towards to physically etch the sample surface. As a result of these two mechanisms and ability to control them, it is very popular in academic and industrial sectors. One example of an RIE system can be seen in Fig. 2.20 for a parallel plate configuration with a shower head gas delivery, whereby one plate acts as an anode and the other a cathode. In this example, the sample to be etched is located on top of the lower plate. With this basic understanding, the following etches are examples employed in RIE:

Hexafluoroethane (C₂F₆) Etch of Silicon Nitride & Silicon Dioxide:

A non-selective etch of SiN_x and SiO_x with a similar etch rate for both to produce a vertical sidewall [139].

Trifluoromethane and Oxygen Etch of Silicon Nitride:

A selective etch of SiN_x over SiO_x and Si (approx. 2:1 and 10:1 respectively) which generates vertical and smooth sidewalls of SiN_x [139].

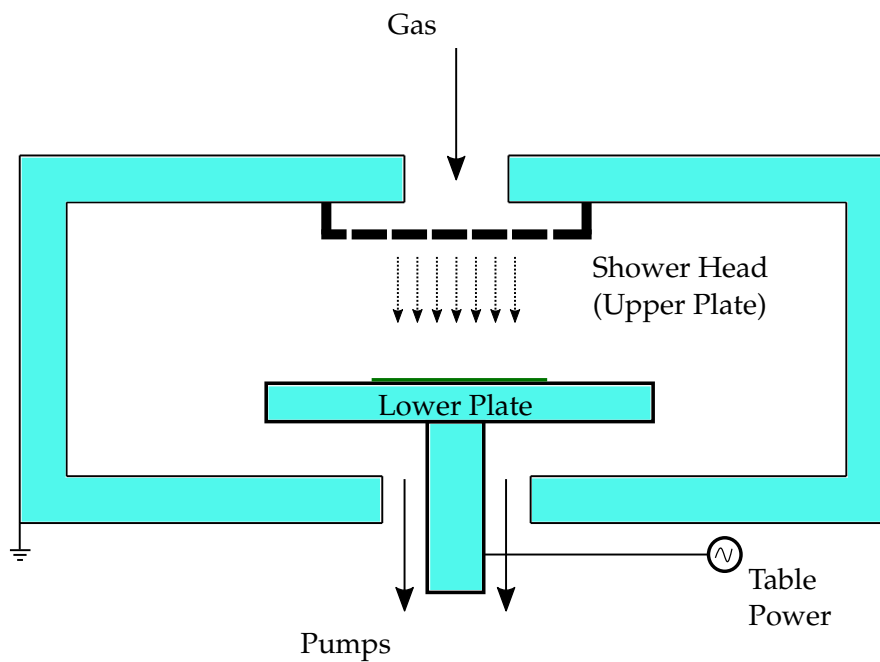


FIGURE 2.20: *Diagram of a Parallel Plate RIE System*

2.4.3 Deposition

With an understanding of how to remove material, the opposite of adding material was equally required to be reviewed. There are a host of deposition techniques which can be broadly categorised as such with the following description [124]:

- **Physical Vapour Deposition (PVD):**

Utilising a physical process (e.g. sputtering) to transform a solid or liquid source material into a gaseous state that solidifies on the sample.

- **Chemical Vapour Deposition (CVD):**

Reaction of multiple chemicals in a gaseous state to produce a vapour that solidifies on the sample surface.

- **Electrochemical or Chemical Deposition:**

Submersion of the sample in electrolyte, whereby the conductive deposited material forms on the sample through the exchange of electrons, e.g. electroplating.

- **Spray and Spin Coating:**

Materials (typically organic) in a liquid phase are sprayed or spun onto the sample to form a thin film, e.g. photoresist.

- **Solgel Technology:**

Dip based technique that employs small solid particles dispersed in liquid that are transformed in a gel for deposition.

Alongside the above, there are hybrids such as combining physical and chemical mechanisms to deposit thin-films. However Spin Coating, PVD and CVD are very common in the fabrication of micro-sized devices such as AFM cantilevers. The latter two shall be explored as these are key and require further understanding to properly appreciate their impact due to their more complex nature.

2.4.3.1 Physical Vapour Deposition (PVD)

PVD techniques can be separated into Thermal Evaporation or Plasma based techniques. The former evaporates the desired material which condenses on the samples surface while the latter typically employs ions in a plasma to eject particles from a target, whereby the particles then deposit on the samples surface (commonly called sputtering) [124]. Sputtering is the dominant technique for Plasma based, while Thermal Evaporation has multiple such as flash, resistive and electron-beam evaporation. The latter is commonly utilised and involves a beam of electrons that heats up the material desired to be deposited and vaporises it. This shall be further expanded below.

Electron-Beam Evaporation

This technique operates under vacuum and employs an electron beam focused onto an ingot of metal causing it to evaporate and solidify on the sample above. This set-up is very effective and utilised widely due to its low levels of contamination, good process control, directional deposition and efficient heat transfer [136]. Deposition thickness is controlled through the employment of Quartz crystals. The latter functions by measuring changes in the crystal's resonance frequency to infer the thickness deposited and are very accurate [124]. Furthermore, to enhance deposition uniformity, stages are typically rotated during deposition. A simplified diagram depicting such an e-beam system can be seen in Fig. 2.21.

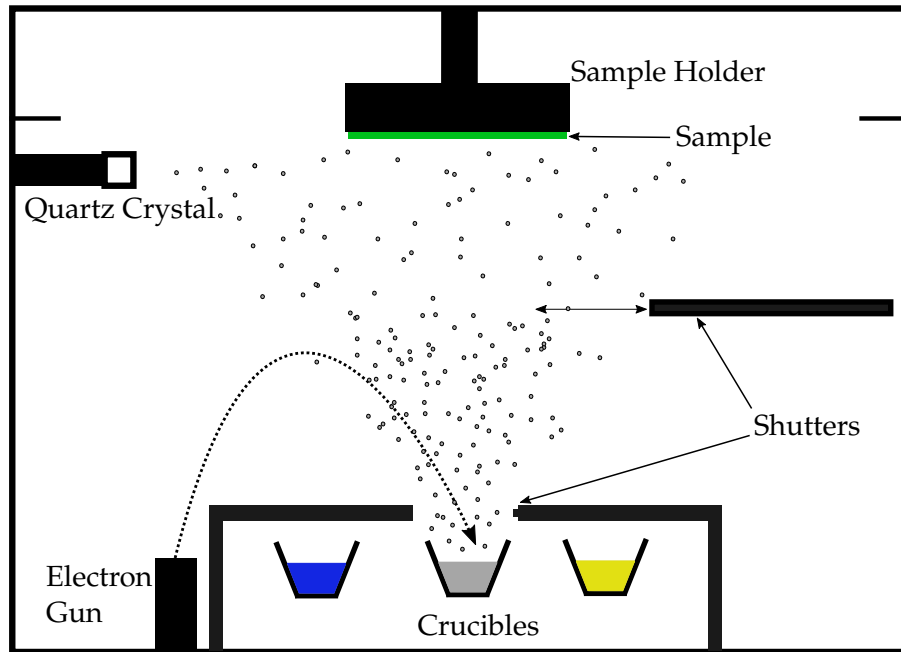
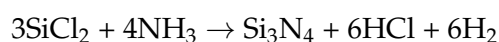


FIGURE 2.21: *Simplified Electron-Beam Evaporation Tool Diagram based on Plassys II & IV in JWNC*

2.4.3.2 Chemical Vapour Deposition (CVD)

As previously highlighted, this uses chemical reaction(s) to coat the desired substrate. As a result, there are a vast array of reactants, types of reactions and products involved in CVD. Moreover, there are sub-categories within CVD: Atmospheric and Reduced Pressure CVD; Low Pressure CVD; Plasma Enhanced CVD; Inductively Coupled Plasma CVD and Laser Induced CVD [124]. Low Pressure CVD (LPCVD) for example operates between 20 and 85 Pa. In this case, this low pressure is advantageous due to the resultant diffusion gradient generating minimal concentration gradient perpendicular to the gas flow direction. Therefore, this deposits very uniform films with good control. However, this set-up can render relatively low deposition rates such as 2.5-10 nm/s. A graphic depicting an example LPCVD set-up can be seen in Fig. 2.22. One pertinent example of a deposition material is SiN_x which is typically deposited through the reaction between dichlorosilane and ammonia [140]. The chemical reaction for which can be seen below which generally occurs between 700 °C and 800 °C:



Therefore, samples which undergo such a deposition need to consider both this above

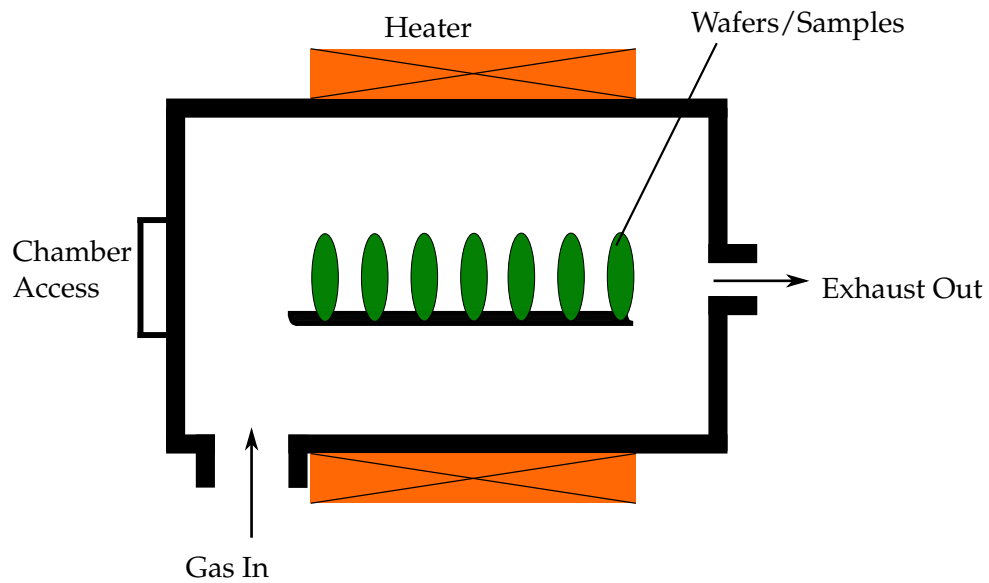


FIGURE 2.22: *Simplified Diagram of a LPCVD System*

reaction along with the temperatures. For example, samples with metals that reflow and/or melt up to this temperature will not be able to be processed using the above technique. This is a factor that is required to be borne in mind for the majority of CVD depositions and is a limiting factor relative to other techniques.

With all of the above, a general overview of Deposition, Etching and Lithography has been performed to provide a sound understanding of the processes and so factors involved in AFM and SThM probe manufacture. Furthermore, a good appreciation has been acquired for AFM, SThM and Thermal Drift from literature. All of this was useful for the project and will be employed in the coming chapters. Hence, the next stage was to outline the exact methods utilised to investigate thermal bend in AFM cantilevers.

3. Research Method

With a sound grasp of the relevant literature, the method applied in this project for the exploration of thermal bending in AFM cantilevers utilising SThM shall be expanded in this chapter. This has been broken down into three clear segments: AFM cantilever modelling; experimental quantification and attenuation of thermal bending through techniques and fabrication of new designs. However, before elaborating upon these, the exact type of SThM cantilever employed needs to be established. KNT-SThM-1an probes were chosen due to their well understood thermal attributes; sound conformity across probes due to batch fabrication and their susceptibility to thermal induced bending from their thick Au coating. In-conjunction with this, KNT-SThM-2an (the grooved cantilever) was investigated for its promise to attenuate thermal bending, but demonstrated lack of ability to completely do so. Therefore, these provided a good lens to quantify and examine thermal bending in AFM.

3.1 Modelling

The objective of modelling in this project was to obtain an enhanced understanding through its development along with its final utilisation as an easy, fast and flexible design tool to aid exploration of thermal bending and potential solutions to it. Once experimentally validated, the latter was possible along with the confidence that it was developed on good foundations. In addition, previous heat transfer models in the author's academic group [113], [141], [142] have been produced and an ability to advance these would be very powerful. This would open up the potential for these heat transfer models (e.g. thermal resistive networks) and their generated temperature distributions to have their thermal bend evaluated. These models utilised the Finite

Difference Method (FDM), where AFM cantilevers are simplified into a 1D model. Hence, an equivalent thermal bend model would permit integration.

FDM modelling was possible in determining mechanical displacement by using the method of superposition. This required development of the author's own modelling programme which provided an excellent vehicle for learning and understanding the fundamental factors and mechanisms involved in thermal bending alongside general AFM mechanics. In addition, complete control over the model's abilities was possible, providing a great degree of flexibility along with its low computational intensity making it much faster than Finite Element Analysis (FEA). Therefore, the FDM method was chosen and Python programming language utilised in the Spyder integrated development environment. However, other modelling techniques such as FEA were employed during the project to not only help initially validate the FDM model, but also when a more complex appreciation of AFM cantilevers was required. Hence, these two modelling techniques were employed using the following described method.

3.1.1 FDM Model

3.1.1.1 Thermal Bend Equations

As mentioned in Section ??, Equation 2.6 provides a sound relation between a multi-layered structure's curvature due to temperature change. However, this does not account for variable widths. This can be accounted for by including them in each material's expression in the equations as shown below:

$$c = \frac{(E_s w_s t_s \alpha_s + \sum_{i=1}^n E_i w_i t_i \alpha_i) \Delta T}{E_s w_s t_s + \sum_{i=1}^n E_i w_i t_i} \quad (3.1)$$

$$t_b = \frac{-E_s w_s t_s^2 + \sum_{i=1}^n E_i w_i t_i (2t_{i-1} + t_i)}{2(E_s w_s t_s + \sum_{i=1}^n E_i w_i t_i)} \quad (3.2)$$

$$K = \frac{3[E_s w_s t_s^2 (c - \alpha \Delta T) - \sum_{i=1}^n E_i w_i t_i (c - \alpha_i \Delta T) (2t_{i-1} + t_i)]}{E_s w_s t_s^2 (2t_s + 3t_b) + \sum_{i=1}^n E_i w_i t_i [6t_{i-1}^2 + 6t_{i-1} t_i + 2t_i^2 - 3t_b (2t_{i-1} + t_i)]} \quad (3.3)$$

Therefore, curvature due to temperature change of multi-material and layered

structures, as seen in AFM cantilevers, could be calculated for variable widths, thicknesses, locations and even temperature changes. The latter of which is typically assumed equal across micro structures like AFM cantilever's due to the micro or sub-micron thickness and its low thermal capacity.

In addition to the above, the literature review articulated how relatively thick coatings may be more accurately modelled by determining the effective modulus. The utilisation of which will depend on the particular AFM cantilever modelled. The SThM cantilevers predominantly utilised in this work have a coating-to-thickness ratio of 3:8. This exceeds the ratio of the bimorph where the effective modulus was employed by J. W. Yi et al. [86]. Therefore, it should be used for these and potentially other AFM cantilevers and was included as a capability in the FDM model. With this in mind and given Equation 2.7 does not include widths or more than two materials, a new equation needed to be derived. Based upon the original derivation by A. Li et al. [85], this was possible utilising the equations for determining the NA (Equation 2.12), Parallel Axis Theorem (Equation 2.13) and the Transformed Section Method (Equation 2.14). The latter two equations permit the second moment of area (I) to be determined and a graphic depicting this when appreciating an Au layer can be seen in Fig. 3.1. Application of these methods generated the following relations and the final effective

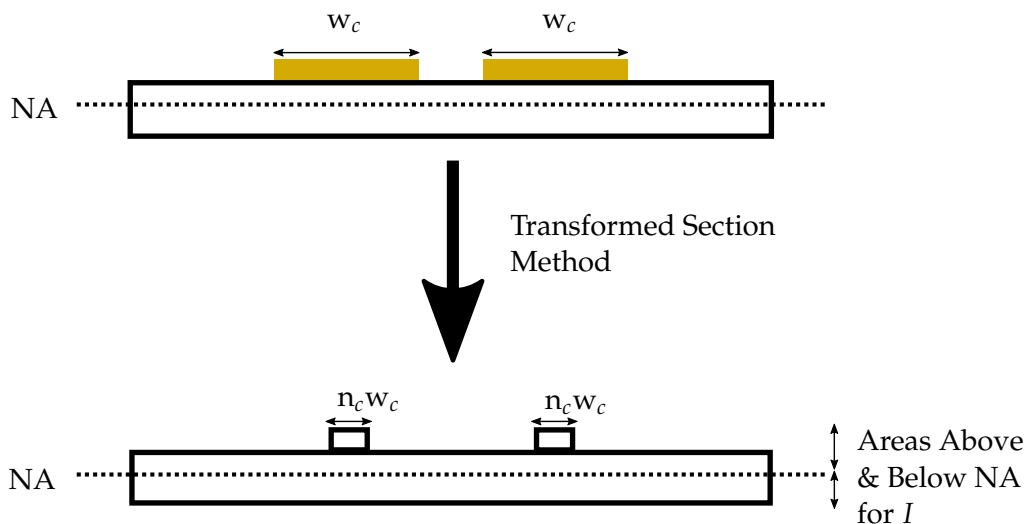


FIGURE 3.1: Diagram of the Transformed Section & Second Moment of Area Appreciation for Single Au Coating

modulus derivation for an n number of coatings:

$$x_{NA} = \frac{\frac{w_s t_s^2}{2} + \sum_{i=1}^n n_i w_i t_i \left(\frac{t_i}{2} + t_s + \sum_{i=1}^n t_{i-1} \right)}{w_s t_s + \sum_{i=1}^n n_i w_i t_i} \quad (3.4)$$

$$I = \frac{x_{NA}^3}{3} + \frac{(t_s - x_{NA})^3}{3} + \sum_{i=1}^n \left[\frac{n_i t_i^3}{12} + n_i t_i \left(\frac{t_i}{2} + t_s - x_{NA} + \sum_{i=1}^n t_{i-1} \right)^2 \right] \quad (3.5)$$

$$E_{eff,w} = \frac{12E_s I}{\left(t_s + \sum_{i=1}^n t_i \right)^3} \quad (3.6)$$

where $E_{eff,w}$ is the effective modulus with width appreciation. The equation pertaining to the second moment of area assumed that the NA lies along the substrate layer, which encompass the vast majority of AFM cantilevers due to the substrate providing the majority of the mechanical stiffness and cross-sectional-area. Although, if this was not the case, the same method can be employed to derive an equation assuming the NA lies along the coating if required. Regarding the manipulation to the effective modulus, like in all the literature explored, this assumes that the structure is rectangular as it aims to provide an adjustment for relatively thick coatings to the overall cantilever's stiffness. However, the structure is actually more accurately visualised as two stacked rectangles of varying widths. If this varied width structure was assumed in the effective modulus Equation 3.6, the same magnitude as the substrate is produced due to it essentially cancelling out the coating's contribution in the homogenising aspect that the calculation aims to achieve. Therefore, this was not utilised in the FDM Model and a simple rectangular structure assumed. With the above determined, interpretation into displacement and rotation of the thermal induced curvature (Eq. 3.3) and EF (Eq. 2.10 & 2.11) equations needed to be determined.

3.1.1.2 Solid Mechanics Theory

How to deduce the appropriate solid mechanics theory comes down to what type of structure the AFM cantilevers are best approximated to and how they respond to the application forces. Firstly, the AFM cantilever structure was required to be defined. The most appropriate structural member is a beam due to AFM cantilevers being long

and bearing loads that act across/perpendicular to their longitudinal axis. The main loads producing dominantly longitudinal bending (assuming the structure is symmetrical about the longitudinal plane and the tip is coincidental to this). For this project the loads are both tip forces and temperature changes that induce bending. It should be noted at this stage, that AFM cantilevers are typically raster scanned laterally and so are usually subject to some degree of twisting/lateral forces. However, deflection used to measure topography is along the longitudinal plane of symmetry and only pertains to the vertical axis. Twisting is due to lateral forces/friction and when just effecting the lateral axis at a relatively low magnitude to the main vertical load, the beam classification is still applicable. In addition to this definition, AFM cantilevers are generally considered slender beams. The exact definition of this term is ambiguous with different mathematical thresholds. However, the general definition is a beam with a small cross-section relative to its length, with J. M. Gere [88] stating it as a beam with a length-to-height ratio of more than 10. Taking either the subjective or objective definition, AFM cantilevers explicitly come under this description due to their relatively thin nature. For example, non-grooved or flat SThM cantilevers produce a ratio of 272.7, far exceeding the mathematical definition. The dimensions of which are typical of most AFMs and so it would be fair to assume all AFM cantilevers are slender beams. As a result, Euler-Bernoulli beam theory is the most applicable solid mechanical theory to AFM cantilevers as this accurately describes slender beams. An example depicting the appropriateness of this for SThM cantilevers can be seen in Fig. 3.2 from a proportional side-view. Moreover, there are many applications of this the-

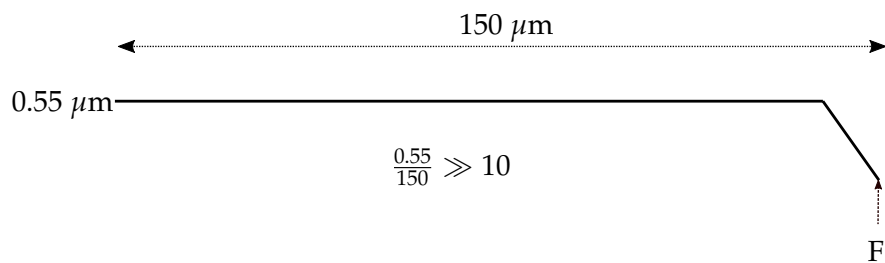


FIGURE 3.2: Scaled Side-View of a SThM Cantilever With Slender Beam Ratio

ory to AFM cantilevers [143]–[148], with the references stated to name but a few. One point, as articulated in Literature Review’s Section 2.2.2, is that the theory requires the

assumption of deflections not being significant. Hence, large tip forces or temperature changes that generate large deflections which change the cross-section's normal relation to the beam axis may not be best described by this theory. With the thin nature of AFM cantilevers alongside their relatively low force to cantilever spring constant, as well as the design of typical AFM systems, Euler-Bernoulli beam theory is applicable. Along with all of the above, it should be noted is that temperature change can be uneven and produce twisting (potentially contravening one of the theories assumption's). However, due to the thin and low thermal capacity of most AFM cantilevers, the vertical displacement is still the most significant and there is not a great temperature disparity across the widths. This would only not be the case if an abnormally wide and unique AFM cantilever was fabricated that would likely not follow many of the Euler-Bernoulli beam theory assumptions made for AFM cantilever's in general. Hence, twisting may occur in some AFM cantilevers, but it is relatively low in relation to the change in vertical displacement and this direction is the main concern in AFM for measuring force and outputting topography. Regarding tip-forces, the assumptions are completely applicable which is ideal for the resultant stresses, strains and displacements from a tip force. This is essential as modelling of this behaviour is required for theoretical comparison to AFM operation and interpretation of thermal bending. This is due to AFM's typical InvOLS calibration being based upon a vertical tip-force applied by a stiff surface. Alongside all of the above, it was possible to simplify the cantilevers into a 1D model. This is due to their beam classification and conditions rendering little or negligible change in cross-section dimensions. Hence, they can be assumed constant throughout temperature change and/or load application. What is more, with little deflection, the cantilevers do not plastically deform. This is the common operational case for AFM cantilevers as they demonstrate elastic behaviour which is essential for the application of Hookes Law (the whole theory behind AFM's force quantification). This 1D modelling also allows other heat transfer models within the academic group to be integrated. Overall, Euler-Bernoulli beam theory can be applied to describe the slender, elastic AFM cantilevers using 1D modelling of thermal bending and tip-forces.

With all of the above established, some AFM cantilevers are relatively wide in comparison to their length and thickness. For example, the flat SThM probes utilised

in this body of work are $120 \times 150 \times 0.55 \mu\text{m}$ (width \times length \times thickness). With AFM cantilevers shaped like this, they could be interpreted more as a plate and hence theory requiring 2D modelling. However, there would be problems with such an approach: orders of magnitudes greater computation time (reducing the benefit of a fast, flexible model in comparison to FEA); may not be compatible with 1D heat transfer models within the group; complex translation of thermal bend equations into the theory; over complication of how AFM typically measures deflection with vertical direction being the main focus that only requires 1D. The latter is in reference to the typical laser spot's large size relative to the cantilever width resulting in illumination across the majority of the cantilever's width. As a result, the deflection measurement is made from the change in reflected light intensity over a single spot size with a Gaussian type distribution. Hence, this will generate deflection measurements that represent an area of the cantilever that includes its complete width and a section of length, with greater representation towards the spot centre. Therefore, it would be necessary to simplify plate theory to accommodate this diffuse nature of the laser spot on the cantilever and allow measurement of its rotation. Moreover, as mentioned, the vertical axis is the direction deflection, force and topography are aligned to in standard AFM operation. Therefore, just an appreciation of the summed plate like behaviour in this direction would be required for each section. To that end, Euler-Bernoulli beam theory can be adjusted utilising the Biaxial Young's Modulus instead of the Young's Modulus. Therefore, this can be utilised to provide an appreciation for plate like deflection if appropriate to the AFM cantilever being analysed. Hence this was chosen as an option when applicable in the FDM model. This will maintain the goal and benefits of the model alongside providing accountability for plate type structures' behaviour when needed.

3.1.1.3 End-Force Equations

Utilising the EF equations articulated in Literature Review's Section 2.2.3.4, the applicable equations can be generated. As stated, the EF equations are not only required, but the bending moment that the EF generates with respect to the length from the end is too for the superposition principle. As a result, the following equations for vertical

deflection and rotation were generated:

$$\delta_{z,e} = \frac{FL_e^3}{3EI_e} + \frac{F(L-x)L_e^2}{2EI_e} \quad (3.7)$$

$$\theta_e = \frac{FL_e^2}{2EI_e} + \frac{F(L-x)L_e}{EI_e} \quad (3.8)$$

where L_e , I_e , x denote the element length, element second moment of area and point along the length of the cantilever respectively. The second moment of area can be determined utilising the Parallel Axis Theorem and Transformed Section Method. The result of which has already been determined for the effective modulus derivation seen in Equation 3.5 with the addition of the appropriate width terms. Thus, these equations were able to generate a theoretical method for generating the InvOLS as this is based upon the tip deflection and rotation along the cantilever due to an EF. Moreover, it allowed for a direct contrast between EF and thermally induced deflections and rotations to be theoretically performed.

3.1.1.4 FDM Model Generation

Using all of the above and the principle of superposition, a FDM model was able to be generated. As described within Literature Review's Section 2.2.3, this principle required Hookes law to hold true alongside only small deflections occurring. All of which are also the case for the Euler-Bernoulli beam theory and therefore the concepts are compatible. Subsequently, the AFM cantilever could be broken down into multiple elements and the thermal bend and EF equations (i.e. the load) applied to each, allowing the displacements and rotations to be computed. A visualisation of such a fracturing can be seen in Fig 3.3 for the example of an SThM cantilever, whereby each enclosed section is an element. In this diagram, as the cantilever is symmetrical along its length, only half the structure is needed to be drawn and fractured as the geometry can be simply doubled. Moreover, a variable mesh was generated: incorporating coarse (1 μm long) and a fine (0.025 μm) elements. This was to permit the finer features of the tip to be accounted for and align to the other thermal models that required such a meshing strategy.

As stated in the Section 2.2.3, for the superposition principle, the displacements



FIGURE 3.3: *Example of a Fractured, Half SThM Probe Drawing to Generate Elements*

and rotations then must be calculated. For the thermal bending Equations, this was possible through the Euler-Bernoulli beam theory that relates the curvature to the deflection and rotation of beams thusly:

$$\begin{aligned}
 K &= \frac{d^2z}{dx^2} = \frac{M}{EI} \\
 &\therefore \\
 \theta &= \int K dx = Kx + c_1 \\
 z &= \iint K dx^2 = \frac{Kx^2}{2} + c_1x + c_2 \\
 \theta &= 0 \text{ \& } z = 0 \text{ when } x = 0 \\
 &\therefore \\
 c_1 &= 0 \text{ \& } c_2 = 0 \\
 x &= L \text{ at maximum length} \\
 &\therefore \\
 \theta &= KL \\
 \delta_z &= \frac{KL^2}{2} \tag{3.9}
 \end{aligned}$$

Hence, substitution of Equation 3.3 into the derived Equations of 3.9 was possible to

ascertain the rotations and deflections. However, for the EF Equations, no conversion to rotation or vertical deflection was required as the governing equations were already set-up to determine these with the Euler-Bernoulli beam theory. With this, the subsequent equations were substituted into the mathematical relations set out by the principle of superposition in Equations 2.9 and combined to determine the vertical deflection from an AFM cantilever utilising the desired number of elements. These are shown below, where the small angle approximation was made regarding rotation:

$$\begin{aligned}\delta_{z,e,\theta_{e-1}} &= \sum_{e=1}^e L_e \theta_{e-1} \\ \delta_{z,e,total} &= \sum_{e=1}^e \delta_{z,e} + \delta_{z,e,\theta_{e-1}} \\ \delta_{z,TOTAL} &= \sum_{e=1}^{TOTAL} \delta_{z,e} + \delta_{z,e,\theta_{e-1}}\end{aligned}\tag{3.10}$$

where $\delta_{z,e}$ and θ_{e-1} can be determined from either the EF equations or thermal bending for each element. Each of these elements were included by the generation of arrays of numbers representing each property, e.g. substrate and coating widths. The main properties that experience a change along the cantilever are the aerial dimensions due to fabrication typically producing uniform thicknesses. These were produced by either manually defining each property for each element, or application of Computer Aided Design where 2D models can be read to produce these dimensions (as seen in Fig. 3.3). As the model was generated using Python in Sypder's integrated development environment, this was possible using L-Edit software that is commonly employed for lithography definition. Alongside complex and non-prismatic aerial geometries, more involved cross-sections were also deduced. Specifically, alongside the layered flat SThM's layered structure, grooved cantilevers could be considered using the Parallel Axis Theorem. Furthermore, additional features were implemented such as:

- **Gaps:** width reduction at a specified location(s) along the cantilever
- **Element Angling:** angling elements relative to the flat
- **Offset Force:** offsetting the end force further towards the base
- **Sensitivity Analysis:** ability to vary one or multiple parameters through the model and output results in 2D and 3D graphs

Hence, a FDM model based upon sound assumption and theory was generated that allowed for multi-material, layered AFM cantilevers to be theoretically appreciated with regards to their thermal bend and EF mechanical behaviour. Moreover, due to its flexibility, complex cross-sections could also be accommodated.

3.1.2 FEA Model

The method above describes the approach employed in the FDM model, but FEA is an additional powerful method. A lot of background theory has already been presented regarding the valid assumptions and simplifications that can be made for AFM cantilevers in the FDM Model. These can all be made in FEA, but as the FDM model already utilises these, the FEA would only mirror the FDM output and not provide additional insight. As a result, FEA was used to provide a more detailed, structurally flexible and all encompassing analysis when required. However, this does come at the expense of ease and speed. This would make no simplifications to the physical nature of the cantilever such as assuming it is 1D or 2D. Therefore, a 3D, deformable solid model was produced that utilised hexagonal, structured elements with quadratic geometric order, hybrid formulation and reduced integration. The exact element type was based upon previous work within the academic group by L. Avilovas alongside literature by E. Sun [149]. These articulate that this should provide an accurate depiction of bending in a beam and prevent the shear locking phenomenon. Moreover, both of these conclude that at least four elements across the thickness should be utilised to prevent hour-glassing. Alongside this minimum, a mesh convergence analysis of the final SThM model was performed to determine the number of elements across the material thicknesses. The result of which highlighted that a greater number of elements across the SiNx thickness rendered the greatest impact with 12 being an optimal number between result convergence, computation intensity/time and mesh generation. The impact for Au was far less and four elements across its thickness was optimal. Beyond these model conditions, the same mechanical and thermal properties utilised in the FDM models were used in FEA's. Abaqus Unified FEA by Simulia was employed to perform the FEA analysis and an example model can be seen in Figure 3.4 with a full mesh generation. It should be noted, that in this image, the tip requires a different method for generating its mesh. This is due to its more variable and complex

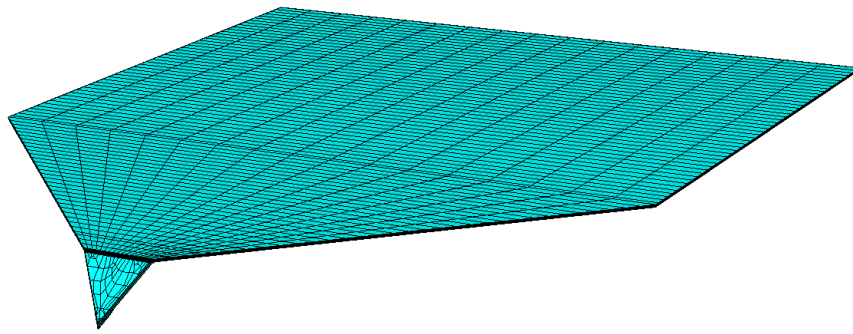


FIGURE 3.4: FEA - SThM Cantilever Constructed with Hexagonal Elemental Mesh

geometry with the Pd sensor requiring more flexible mesh generation and so a sweep construction instead of a structured one was employed. However, the same element type was used to maintain consistency across the model.

Regarding some of the further conditions of the modelling method, the cantilever models utilised fixed mechanical boundary conditions at its base and, in order to permit the desired element type, partitioning was only possible through simplification of some geometry features. For most AFM cantilevers, simplification was not required due to their uniform material layers. However, for cantilevers with patterned layers (e.g. SThM cantilevers) this was required. Specifically, for the SThM cantilevers utilised in this work, simplification of the Au and Pd pattern near the tip was required. This was in regards to the region of overlap between the Au and Pd where it was simplified so only one of these was present (as assumed in all FDM models within the academic group) alongside the Au coating terminating at the base of the tip. Not doing so was very challenging to generate a sensible mesh and majorly enhanced its computational time and intensity alongside limited different designs to be modelled. These simplifications are highlighted in Fig. 3.5, whereby an image of a fabricated SThM tip and its FEA representation are shown together. Furthermore, as can be seen in the figure, the tip base is assumed straight in the FEA model as opposed to the slight triangular nature in reality. The latter of which will have a near negligible impact. In addition to these, the NiCr adhesion layer (approximately 5 nm thick) was substituted with Au as its inclusion would produce severe problems for partitioning and so mesh generation due to it being very thin in the overall model. However, all

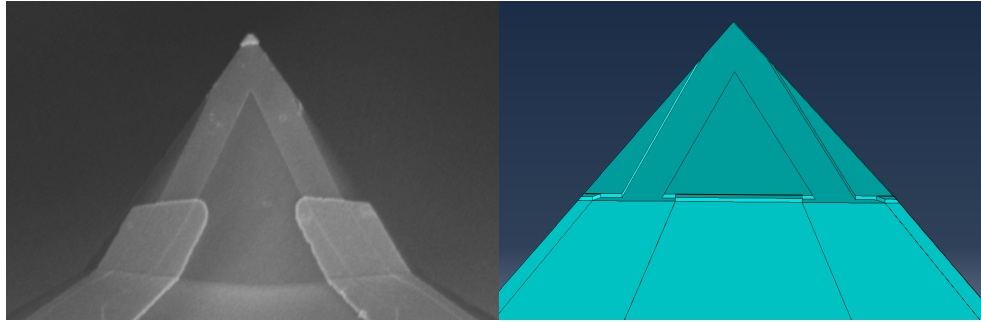


FIGURE 3.5: *Fabricated SThM Tip Compared to FEA's Tip Simplifications*

these differences cause little impact on the final deflection magnitude and behaviour outputted due to the vast majority of the Au coating being appreciated and being dimensionally accurate along greater than 92 % of the cantilever length. Moreover, the fabrication of the SThM cantilevers have some steps that have inherently uncertainty with respect to the blue-print dimension. For example, wet-etching is utilised for the pyramid definition (Step 12 in Appendix D) that dictates the location of the tip's base along the cantilever length. Therefore, due to a lack of etch-depth monitoring, it is a lot more prone than other processes to over or under-etching. Hence, even a nominally 100 % accurate FEA model will not exactly represent all SThM cantilevers fabricated. Moving towards how the model is thermally disturbed to appreciate thermal bending, a temperature change was imparted using the predefined fields functionality in Abaqus. This meant temperature changes were stated as step changes in the model. Therefore, with all of this modelling method and structure created, FEA models of AFM and SThM cantilevers were developed, allowing their mechanical and thermal bend behaviour to be theorised.

3.2 Experimental Quantification

With the theoretical work in place, real-world measurements were required to validate the modelling outputs and provide a comparison to temperature induced bending, deflection, force and topography change. Performing such work required an analysis of the approach and tools that are best suited alongside the desired experiments and practice.

3.2.1 Measurement Approach & Tools

The approach used for the quantification and experimental work needed to be simple and accurate. The former offering a reduction in problems, time-lost and enhanced clarity of the resultant measurement, while the latter allowed a good representation of the measurand. Overall, this helped provide quick and sound measurement for optimal project progression.

3.2.1.1 Deflection Measurement

Regarding tools for deflection quantification, there were three potential options for AFM cantilevers: AFM, Interferometry and SEM. The benefits and drawbacks of each are articulated in Table 3.1. As can be seen, with the desire for both simplicity and accuracy, SEM was not an ideal option due to its manual measurement method using each image's scale bar and its confined form factor for experimental set-ups. Hence, it was quickly disregarded for this type of quantification. Focusing on AFM and Interferometry, the former provides an immediate interpretation of thermal bending in an AFM, while Interferometry a direct and accurate measurement of cantilever vertical deflection. Hence, as this body of work was focused on analysing both of these functions, they were both chosen. However, Interferometry was first employed to provide an initial contrast to theoretical models and raw vertical deflection quantification. This was then followed by the respective interpretation in an AFM system undergoing the same thermal bending. Specifically, a Bruker Contour GT-X 3D Optical Microscope (white light Interferometer producing 3D images) and Digital Instruments Dimension 3100 AFM were employed. Pictures of these tools are shown in Fig. 3.6 & 3.7.

3.2.1.2 Temperature Measurement

Alongside the above tools for deflection quantification, the other key component was the temperature measurement. As mentioned, SThM was chosen for this very purpose: measuring the resistance change from its Pd tip inferring temperature change. The resolution of this is sub-Kelvin, where a Wheatstone Bridge was employed to output this degree of resolution. A simple circuit diagram depicting this can be seen in Fig. 3.8. The left and right side resistances were then balanced through use of fixed

TABLE 3.1: Cantilever Deflection Measurement Tools: Benefits & Drawbacks

Tool	Benefits	Drawbacks
AFM	<ul style="list-style-type: none"> + Direct Interpretation of Thermal Bend Induced Measurements in an AFM + High Resolution, Sensitive Measurement + Simple Set-up 	<ul style="list-style-type: none"> – Indirect Vertical Deflection Measurements – Only Single Point Measurements – Challenging Laser/Point Measurement Location – Calibration to EF Tip Deflection
Interferometry	<ul style="list-style-type: none"> + Direct Vertical Deflection Measurement + High Resolution, Sensitive Measurement + Multiple Point Deflection Measurement + Simple Set-up 	<ul style="list-style-type: none"> – Susceptible to Some Imaging Artefacts (Easily Mitigated Though) – Material Optical Properties Influences Deflection Measurement
SEM	<ul style="list-style-type: none"> + High Resolution 	<ul style="list-style-type: none"> – More Complex Set-up – More Difficult Direct Deflection Measurement – Greater Experimental Restrictions – Limited to Vacuum Conditions – Time-Consuming Measurement Process

resistors. As a result, the V_{out} would be highly sensitive to any temperature induced resistance changes from the SThM Pd tip. Resistors R_{L1} and R_{L2} limited the maximum current while R_M was used to match the parallel combination of the SThM probe and its parallel resistor, R_P . Moreover, this signal was amplified through an in-house designed low-noise amplifier that produced a gain of -101. This permitted conventional laboratory oscilloscopes and multi-meters to measure the low voltage and hence low resistance changes for high temperature resolution. This Wheatstone Bridge was then powered by an isolated variable battery power supply. This provided a low-noise power supply that enhanced measurement accuracy alongside protected the Pd tip from current spikes. Hence, the Wheatstone Bridge enabled sound ability to measure

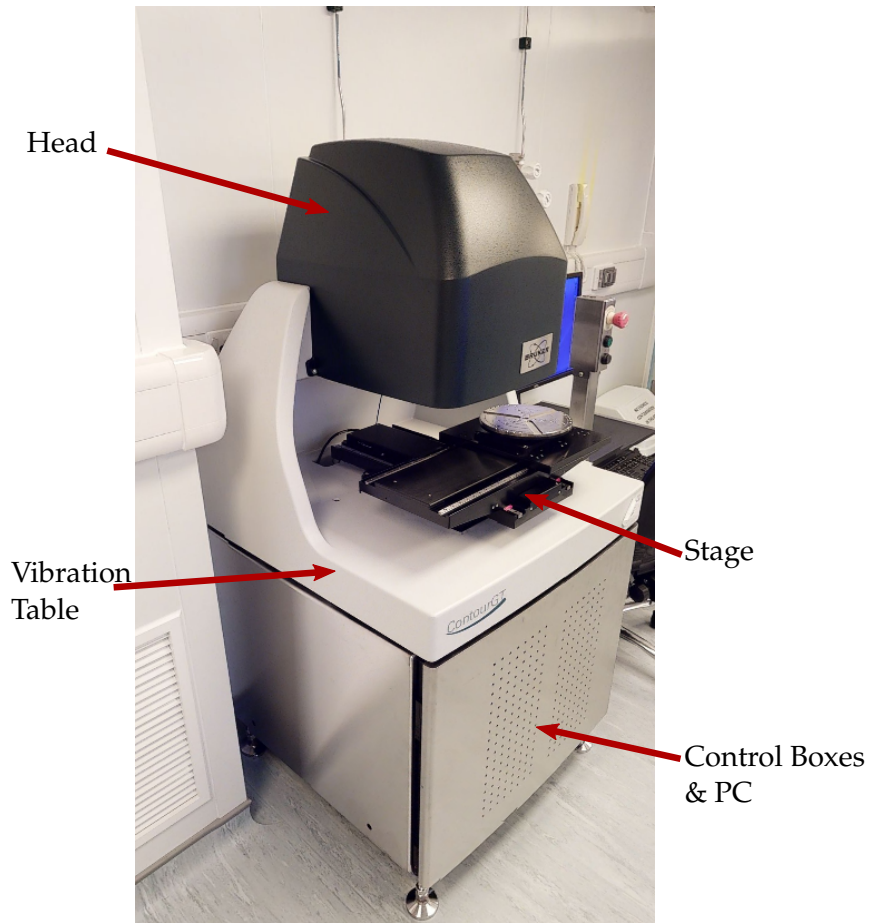


FIGURE 3.6: *Bruker Contour GT-X 3D Optical Microscope Utilised in Project [139]*

resistance at the SThM tip. However, the next step was to relate this to the temperature change undergone. To do this, the temperature coefficient of resistance (TCR) was required to be determined. This provides the calibration of the Pd resistor's linear relationship to temperature in the typical ambient regime with it abiding to the following equation (a relation that has been established in the scientific community from 1910) [150]:

$$\alpha = \frac{\frac{R}{R_0} - 1}{T - T_0} \quad (3.11)$$

From this, a reference resistance for a certain temperature needed to be established alongside simultaneous measurement of the tip's resistance and the surrounding temperature. To perform this, an in-house set-up was produced. This involved a highly conductive and low thermal resistance container that was well isolated from the ambient environment and was heated through a low noise Peltier Heater. The former permitted a quick and uniform a temperature change as well as being thermodynamically

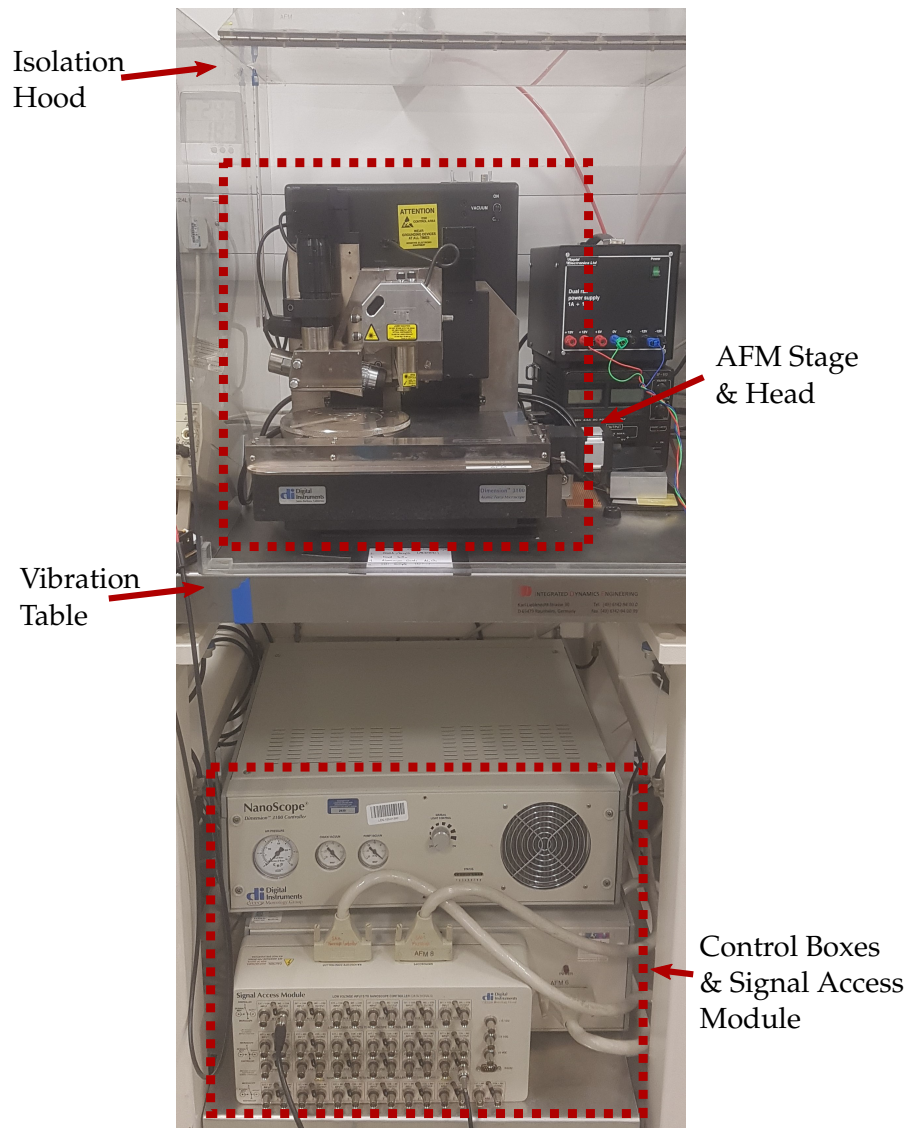


FIGURE 3.7: *Digital Instruments Dimension 3100 AFM Employed in Project*

well isolated (i.e. approaching being isothermal) from ambient temperature changes once the Peltier Heater's imparted temperature change reached a steady-state. The SThM probe was then placed inside this with fluorocarbon liquid (flutec pp3) to produce a heat bath. The latter ensured better temperature uniformity, greater thermal capacity than air, low surface tension to minimise chances of cantilever damage and a low thermal resistance between the SThM probe and a PT-100. The latter was additionally placed in as close a position as possible to the probe in the heat bath to provide the most accurate temperature change to the cantilever. PT-100 devices are also well understood, reliable and accurate resistance temperature detectors (RTD) that employ the same phenomenon as SThM for measuring temperature change. Therefore,

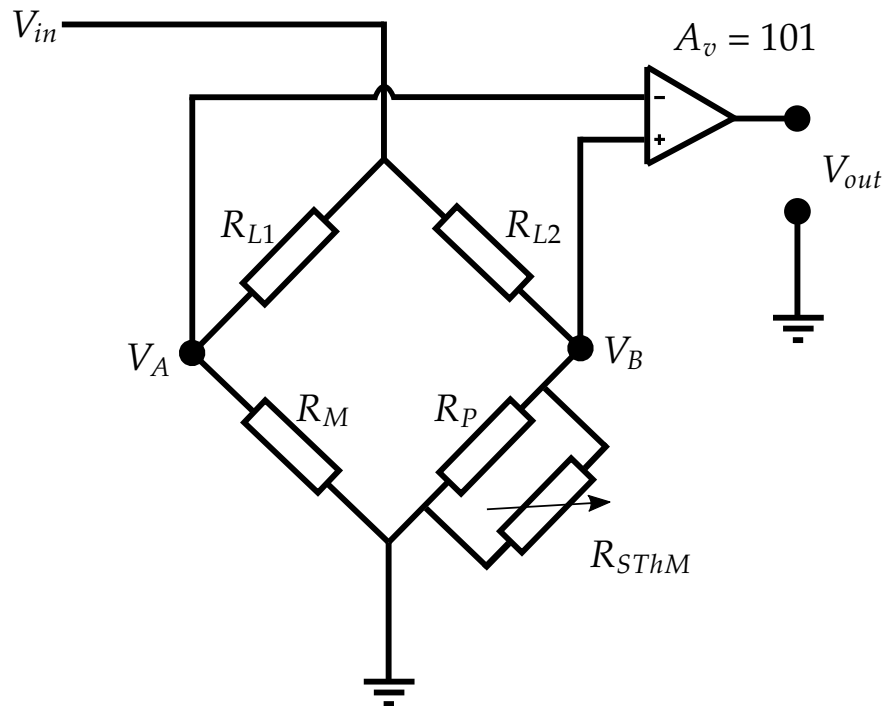


FIGURE 3.8: *Wheatstone Bridge Employed in SThM - Simplified Circuit Diagram*

through resistance measurement and the PT-100 equation shown in Appendix B.1, its temperature could be measured. A photograph of the experimental set-up can be seen in Fig. 3.9. The method of utilising this set-up and determining the TCR involved

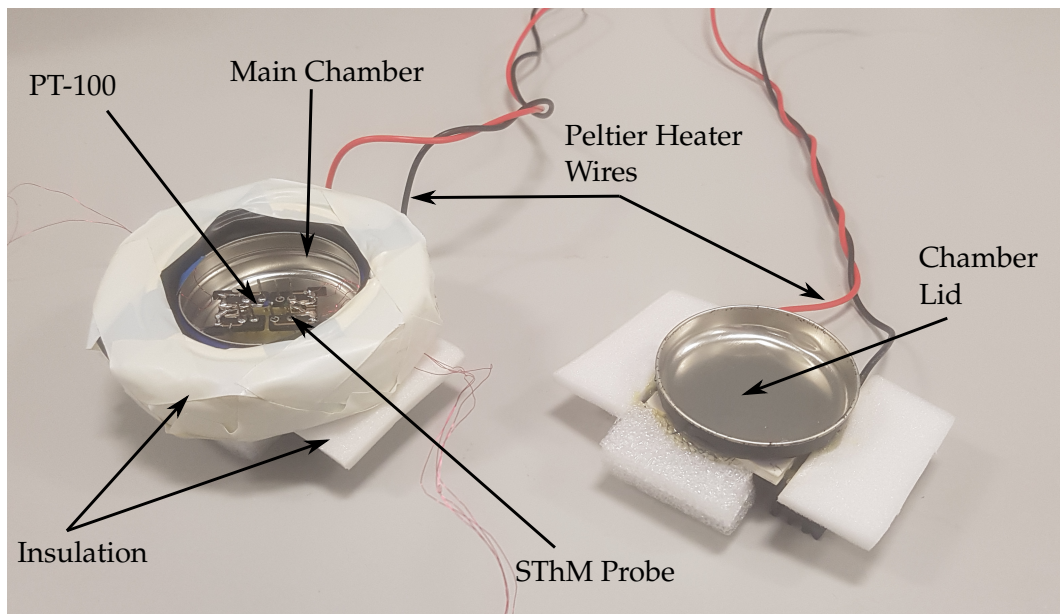


FIGURE 3.9: *Equipment Employed for Determining SThM Probe's TCR*

changing the Peltier heaters' input voltages and obtaining periodic measurements of

the SThM voltage and PT-100 resistances until a steady-state temperature was reached and maintained for greater than five sets of measurements. Once achieved, the Peltier heaters had their voltages changed and the same method replicated over multiple temperatures for a range sensible to the experiments the SThM had undergone. Extraction of the steady-state temperature measurements were then taken to determine the TCR according to Equation 3.11.

As a result, the tools to measure deflection and temperature were possible and established. However, the final piece was the application of these. Bespoke experimental set-ups needed to be constructed for the different aspects of thermal bending to be explored. This will be elaborated upon in the respective Out-of-Contact (OC) and In-Contact (IC) sections, as different methods were required due to their dissimilar conditions and caveats of each scenario. With all this borne in mind, the mechanically simpler OC situation was first explored.

3.2.2 Out-of-Contact

The OC situation for AFM cantilevers is relatable to the approach, retraction and non-contact scanning phases of AFM operation. As a result, the probe's cantilever does not require immediate proximity to a surface for quantification in this scenario. Hence, the cantilever can be orientated in any position as long as the deflection perpendicular to its flat (i.e. vertical deflection during AFM operation) can be measured. Regarding imparting temperature change, many options are viable but one that is inexpensive, has no-moving parts (limiting vibration), reliable, highly controllable, flexible and currently utilised in SThM calibration procedure was Peltier heating. Therefore, this method of imparting temperature change to AFM cantilevers was an obvious one to utilise. However, as it will be highlighted in the IC Section 3.2.3, this has a drawback of the Peltier surface displacing by a significant magnitude with temperature change, but this only becomes a problem when direct mechanical contact is made between it and the cantilever. Regarding controlling the temperature, Peltier heater's have a relatively simple method of controlling heat flow: increasing the current results in increased heat flow and so temperature change. The operating principle is based upon the Peltier effect, whereby an electrical current flows across a junction constructed from two dissimilar conductors [151]. The difference in the conductors

electrical conductivity results in a heating and cooling effect at the two respective sides of the junction that both materials are connected to. The efficiency of this is called the coefficient of performance and temperature range can be increased by improving this. One method of achieving this is through connecting a heatsink to one side of the heater. In this body of work, temperature increase of the SThM cantilever's was arbitrarily chosen, and hence a heatsink on the cold side would render increased performance and temperature range increase.

With the method of heating established, the subsequent set-ups using it in the desired experiments shall be elaborated. First, experimental quantification that was translatable to the FDM & FEA models was required for validation of the models. This was then followed by a more comprehensive AFM Interpretation Experiment that aimed to link deflection of AFM cantilevers' and what AFM system's outputs from the common thermal bend deflection detection system.

3.2.2.1 Direct Deflection Quantification

The first decision was on the method of deflection measurement. As the desire was to provide a direct vertical deflection quantification alongside an experimental comparison to the FDM and FEA models, Interferometry was utilised through the Bruker Contour GT-X 3D Optical Microscope in the JWNC. This produces 3D topographic images of surfaces, where an example of this can be seen in Fig. 3.10 for a flat SThM cantilever showing an example plane used for extracting the longitudinal deflection profile. Within this figure, two common artefacts that are ubiquitous in Interferometry are clear: the batwing effect [152] (i.e. sudden increase in the deflection near a step change) and the vertical drop off at edges. The latter suggests a thicker feature than in reality and although these are notable artefacts, they can be easily avoided by using topographic measurements taken away from sudden step changes or edges. For comparison of these cantilever deflection measurements to the respective model, they need to be under the same mechanical and thermal conditions. The former is simple to align by keeping the cantilever free-standing and away from a surface, while the latter requires more thought. The simplest scenario is uniform temperature change of the AFM cantilever, such as an ambient temperature change. Considering the low thermal capacity of AFM cantilevers and whole probe body (approximately 2×10^{-8} &

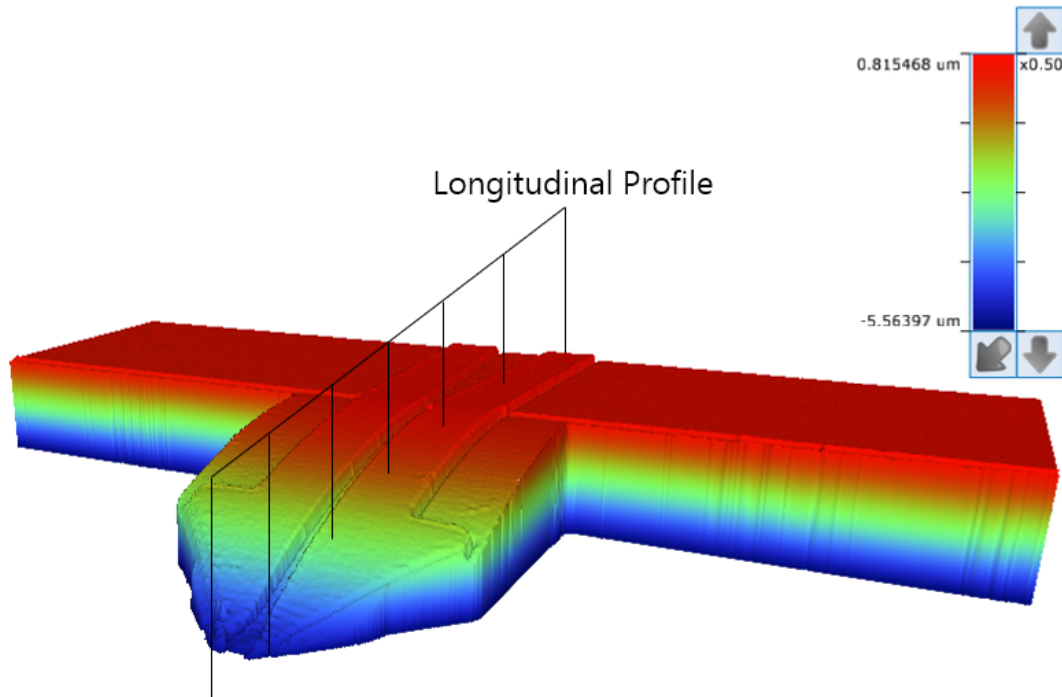


FIGURE 3.10: 3D Topographic Image Produced by the Bruker Contour Interferometer

3×10^{-3} J/K for SThM respectively) relative to the Peltier heaters' used that can generate up-to 60 W over a 40 x 40 mm area this should not be challenging. For example, assuming that half of the power (30 W) is outputted, based upon bulk material values of the Si, SiNx and Au utilised alongside assuming an even spread of this power across the Peltier surface area with zero thermal resistance, the cantilevers and probe body would change by 324 & 1.5×10^5 K/s respectively. As a result, both will change temperature quickly and by a significant magnitude that will cause little temperature difference aerially. Moreover, due to AFM and SThM's very thin nature (easily assumed a sheet theoretically), there will be negligible variation vertically through its thickness. Hence, with a low thermal resistance between the cantilever and Peltier surface, a near uniform temperature will be generated that can be easily compared to models. One further component added to this was a PT-100 used to measure the temperature change of the Peltier surface. This reliable, accurate RTD was easy to install and measure to provide a sound temperature quantification alongside the SThM output. Moreover, the PT-100 in the set-up allowed for future non-thermal AFM cantilevers to have their thermal bend profiles quantified. However, SThM cantilever's were first explored due to their unique capability for direct cantilever temperature

measurement for the most accurate depiction of thermal bending in AFM cantilevers. The subsequent set-up is visualised in Fig. 3.11. With all of this, a standard procedure of greater than five different temperatures that were allowed to reach a steady-state with simultaneous image acquisition was implemented.

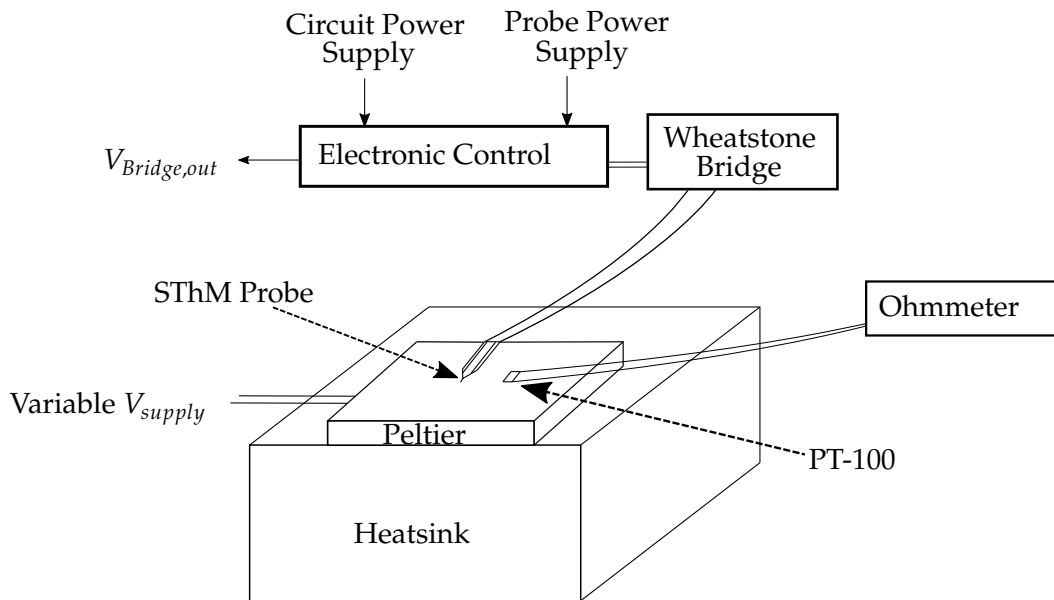


FIGURE 3.11: *Direct Deflection Quantification Experimental Set-up*

3.2.2.2 AFM Interpretation Experiments

Following the above, the next logical step was to connect cantilever vertical deflection from models and the Interferometer to that interpreted by an AFM. As a result, a set-up was required to align the thermal environment of the models to the Interferometer and AFM set-ups. Again, for its ease of conformity, uniform temperature change from a Peltier heater was chosen initially. For a sound appreciation of this, two different experiments were prepared and executed. The first aimed to demonstrate the link between the three separate methods, while the following one articulated the general trends between them that would be expected after the proof of connection. Both of these methods could be utilised for non-thermal AFM cantilevers once experimentation with SThM had validated the method by employing the PT-100 for temperature measurement (however this would not be as accurate as the SThM's measurements).

1st Experiment: Each techniques' exact implementation in this experiment is described below, where they all aimed to produce the same heat transfer conditions for a uniform temperature change, similar temperature ranges, employment of the same AFM cantilever and electronic equipment (applicable to SThM) and the heater:

- **Models** - Both FEA and FDM models were generated for uniform temperature change of the AFM cantilever model. The InvOLS would then be determined to enable comparison between Interferometry and AFM deflection outputs. The exact deduction of the theoretical InvOLS is further elaborated in Chapter 5, Section 5.1.1.2.
- **Interferometry** - Utilising the previously employed Bruker Contour GT-X 3D Optical Microscope, whereby the cantilever had its deflection measured with the tip facing towards and away from the Peltier surface. The latter provided the cantilever orientation utilised in AFM systems for it to be under as-similar a conditions as possible. Additionally, it enabled verification that both orientations are capturing the same deflection. Moreover, a spacer was utilised between the probe holder flat and Peltier surface to keep the AFM probe and surface a consistent distance apart for tip-down measurements.
- **AFM** - Measurement in the Digital Instruments Dimensions 3100 AFM was performed with the probe mounted in the typical fashion (tip downward to the Peltier surface) and the same spacer employed in the Interferometer to enable consistent heat transfer conditions and enhance comparability. The laser was then focused on the cantilever and an image of this location taken for determination of its longitudinal position. The photodetector's vertical voltage was then noted alongside the temperatures with the InvOLS determined to convert the voltage to tip deflection. The InvOLS was measured using conventional Voltage-distance curves as articulated in Literature Review's Section 2.1.4 where at least five curves were extracted for an average and uncertainty to be ascertained.

With the above conditions, a schematic showing the set-up for both the Interferometer and AFM can be seen in Fig. 3.12 for the cantilever tip facing towards the heated surface.

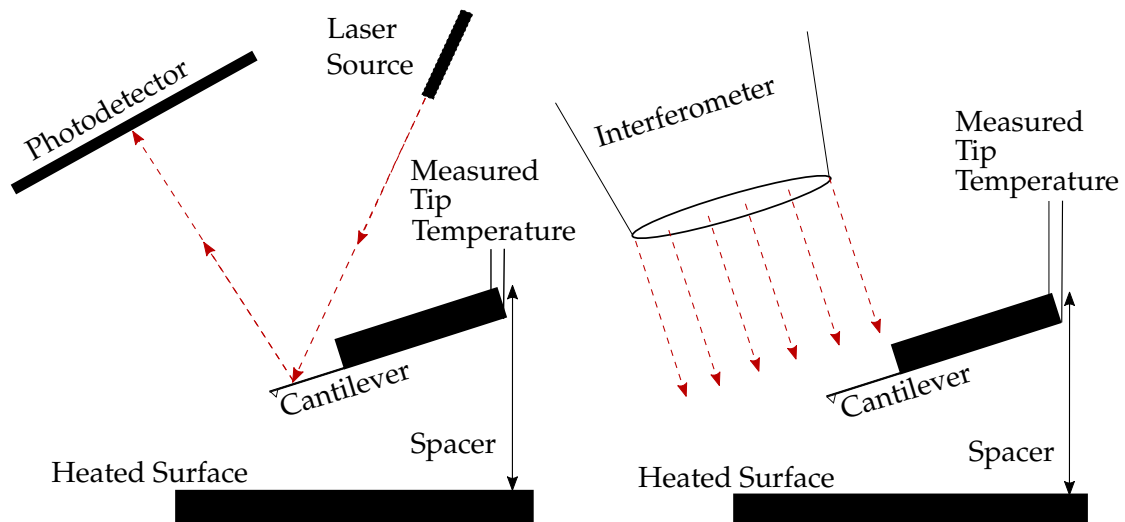


FIGURE 3.12: *AFM Interpretation Experiments - 1st Experiment: AFM & Interferometer Set-up (left-to-right)*

2nd Experiment: Building upon the previous experiment's demonstration and validation of each technique's link, it was required to explicitly display the general trend between them for OC thermal bending. Again, SThM was employed initially due to its ability to measure cantilever temperature change imparted by the Peltier heater. To enable demonstration of the longitudinal deflection profile in the AFM system, multiple laser spots were taken along the length. At each location, multiple temperatures (at least five) induced by the Peltier heater were utilised and the photodetectors vertical voltage measured. From this, the thermal bend induced deflection-temperature gradients for each location was generated. Alongside this, multiple Voltage-distance curves were taken to obtain the InvOLS along with an image of the optical view of the cantilever when stationary and in-contact with a surface to measure the longitudinal location of the laser. For the latter, the cantilever was brought IC with a surface as the point of reflection is very similar between the surface and cantilever so a clearer and more accurate image of the whole laser spot was possible. As a result, the longitudinal position of the thermal bend gradient could be combined to produce a profile. A visual of the overall experiment in the AFM can be seen in Fig. 3.13 with five separate laser locations shown.

With the above quantification method, an ability to understand the nature of thermal bending occurring in AFM cantilevers when OC was possible. This was in terms

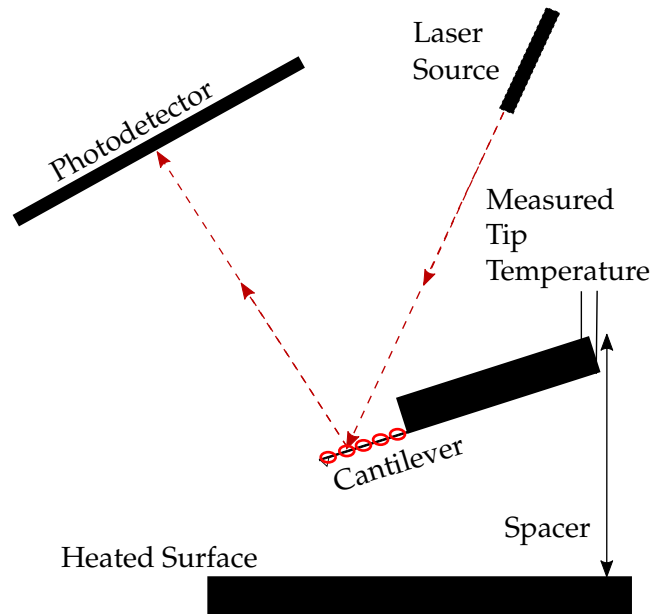


FIGURE 3.13: *AFM Interpretation Experiments - 2nd Experiment: AFM Set-up*

of both the direct vertical deflection and how it was interpreted by the AFM's thermal bend system.

3.2.3 In-Contact

The above provided a template for sound OC thermal bending quantification, but not all scans are OC with contact mode scanning a popular technique that involves bringing the AFM cantilever tip into contact with the sample to infer its topography. When IC, as elaborated in Literature Review's Section 2.1.5, the tip interacts with many forces of an attractive and repulsive nature. Moreover, once contact occurs, adhesion (attractive) forces additionally keep the tip strongly linked to the sample alongside repulsive forces that resist it from indenting into the sample. As a result, the tip has a complex array of forces keeping a strong mechanical link to the sample surface, providing sound and consistent topographic measurement from the cantilever's deflection. Therefore, it is reasonable to assume that this different mechanical link at the tip will result in a different mechanical boundary condition (BC). With this, the way that thermal bending manifests itself may be different and so it was desirable to quantify this common scenario. In addition, this is the most common situation for SThM cantilever scanning as it minimises thermal resistivity to the sample.

With the above justification, a similar process of measurement utilising both an Interferometer and AFM was executed to provide two separate, independent measurements. With this approach, IC thermal bending provides a different challenge to OC. This is because the cantilever tip is mechanically connected to a sample, meaning any displacement of the sample or AFM instrument (e.g. through thermal expansion) will produce cantilever deflection and a different EF resulting in a multi-loaded cantilever deflection profile. This is not ideal when the cantilever's thermal bending is the sole property being quantified. Hence, to determine this isolated profile, a heat source that produced concentrated heating of the cantilever and negligible heating of the sample and surrounding environment was required so that thermal expansion and displacement of these would be minimal. As a result, the previously utilised Peltier heater could not be employed due to significant vertical displacement occurring (+ 0.3 $\mu\text{m}/\text{K}$ was determined through experimentation). However, two different heat sources were able to provide isolated heating of the cantilever: SThM self-heating and external heating from a microheater sample. The former involves increasing the current flow through SThM's Pd tip resistor and so from Joule heating, heat can be generated that is transferred down the cantilever. Hence, it can produce a concentrated cantilever temperature change with low thermal energy that has very limited spreading into the sample and surrounding structure. This permitted trivial IC thermal bend quantification of SThM cantilevers using both an Interferometer and AFM with very similar thermal conditions. However, while this would provide a sound and accessible method for initial demonstration of IC thermal bending, it would not permit experimental quantification due to external heating that other non-thermal AFM cantilevers are subject to. Therefore, a microheater on a sample was utilised that was thermally isolated. This would provide verification whether or not external heating can produce the same thermal bend behaviour alongside the added capability to measure it in non-thermal AFM cantilevers. A diagram depicting such a microheater can be seen in Fig. 3.14

No matter what heat source, both involved the cantilever's temperature change with the vertical deflection measured once a steady temperature was established. The temperature was then brought back down to ambient and the experiment zero-ed

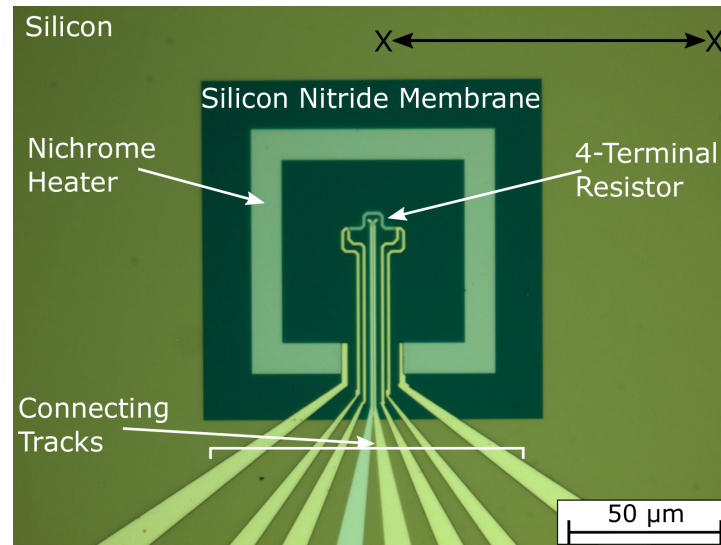


FIGURE 3.14: Image of Microheater Fabricated by P. S. Dobson et al. [153], Whereby Line Scans Were Performed Along the X-X Line

again for the required number of times (greater than five). This aimed to reduce systematic and spurious drift from offsetting and convoluting the results. In addition, alongside the cantilever tip being brought IC and its temperature and deflection measured, this was performed OC to provide a clear contrast. With this common theme of experimental approach for each heat source, each one is hence further elaborated upon in greater detail.

3.2.3.1 Self-Heating Experiment

This experiment method required an ability to bring the SThM cantilever tip in and out of contact with the sample, imaging this in both the Interferometer and AFM. The latter was logistically trivial as AFM is designed to perform this task, but the laser was required to be translated across the cantilever length to obtain the deflection profile. This was performed by obtaining the InvOLS at each longitudinal laser position (the location determined from the optical image of the cantilever when IC with the surface) and the deflection and temperature measurements taken for OC and IC. These produced thermal induced deflection gradients at each longitudinal position and permitted a profile to be pieced together. This was similar to the set-up to previously employed in the 2nd AFM Interpretation Experiment. However, as touched on, a zero-ing method (zero voltage and current application for heat generation) before each temperature change was performed followed by applying the maximum safe

current to generate self-heating. This not only rendered the benefits noted previously, but additionally maximised the SNR in the experiment. This was especially important due to self-heating's low imparted thermal energy and so lower deflection. This method had not been utilised in previous experiments due to the Peltier heaters producing a large magnitude of thermal energy. However, for self-heating the thermal energy magnitude is very low which had a benefit: very low heat-up and cool-down times meant thermalisation within less than a second. Overall, a representation of the subsequent AFM experiment can be seen in the top image in Fig. 3.15.

Regarding the Interferometry set-up, greater preparation and set-up was required due to its lack of ability to control the AFM probe and cantilever's exact vertical positioning. As a result, a set-up was required that allowed the SThM in a standard AFM holder to be actuated in and out of contact while permitting access of the objective lenses of the Interferometer to the cantilever. Hence, the probe was attached to a linear, vertical translation stage (analogue micrometer with 10 μm vernier scale) through a short and stiff mechanical structure. The latter was especially important due to the Interferometer's lack of an isolation hood leaving it susceptible to mechanical drift and vibration from the surrounding environment and strong laminar air flow. A diagram depicting this and the AFM set-up can be seen in the bottom image in Fig. 3.15. Replicating the zero-ing method articulated with a statistically significant number of simultaneous temperature and image acquisitions allowed for the OC and IC thermal bend profiles to be generated.

3.2.3.2 Microheater Experiment

With a sound method demonstrating the impact from bringing an AFM cantilever IC with a sample from both the Interferometer and AFM, it was required to show this from external heat sources and provide a method for non-thermal AFM cantilevers. Hence, a thermally isolated microheater on a sample was chosen. An image of the exact one chosen can be seen in Fig. 3.14. This had been previously fabricated by P. S. Dobson et al. [153], consisting of a NiCr film resistive heater on a thin SiN_x membrane with a Si substrate. Hence, thermal isolation of the heater from the main Si chip and its relatively low thermal energy result in negligible temperature change and thermal expansion of the Si chip (verified through experimentation). Therefore, AFM

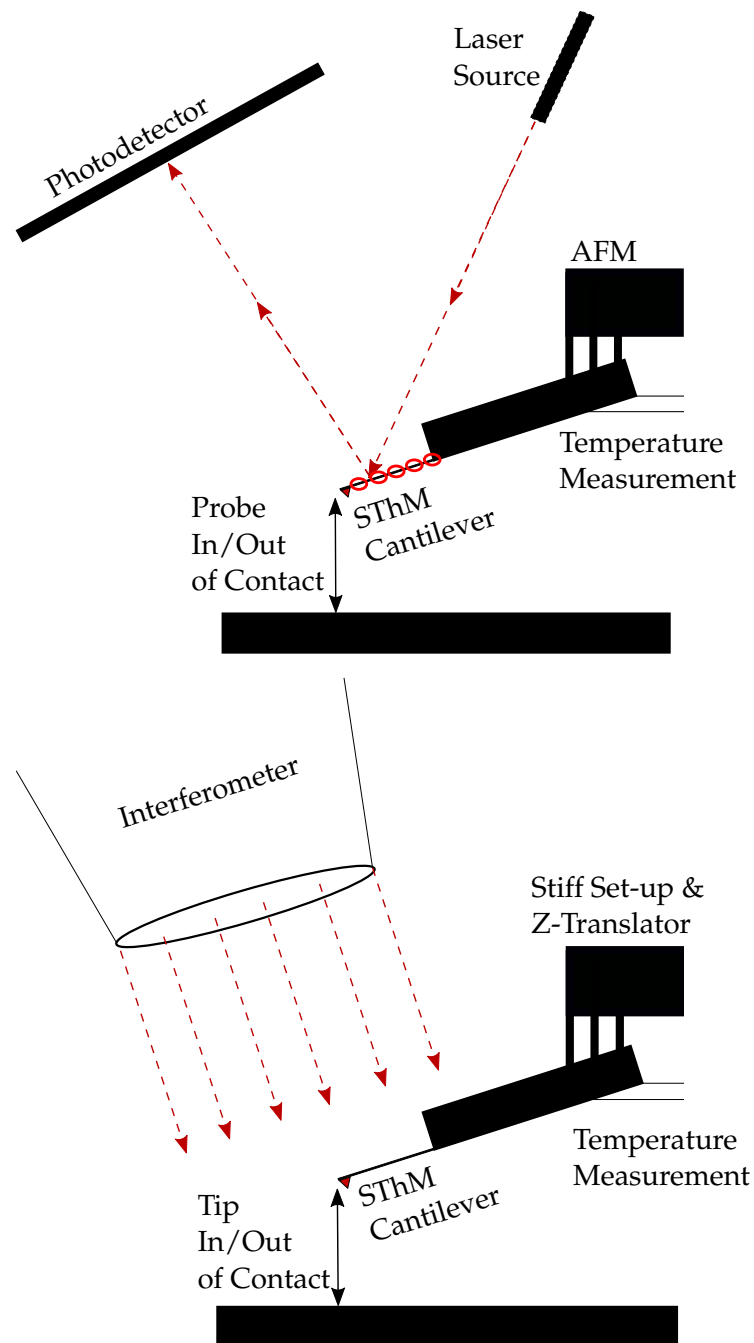


FIGURE 3.15: Self-Heating Experiment: AFM & Interferometer Set-ups (top-to-bottom)

cantilevers could then be brought IC with the Si sample without the substrate displacing and changing the tip force and affecting the deflection results. With positioning of the cantilever body over the heater, it would then change temperature without sample/surface expansion. Both the temperature change and deflection measurements

were taken while IC and OC for multiple laser locations to produce the respective profiles (as described for the previous two AFM experiments). The microheater's temperature was altered by changing the input voltage and applying a similar method described for self-heating of zero-ing prior to application of the maximum safe current for a statistically significant number of data points. This was similarly possible due to the microheater's low thermal energy producing short heat-up and cool-down times. This helped mitigate any systematic drift effects and maximise the SNR. With SThM probes, the cantilever's tip temperature could be measured, however, as the microheater provided a small heat source, the tip may not provide the most accurate temperature measurement of the rest of the cantilever. Therefore, the temperature relation with the microheater power in the centre of the membrane was obtained and averaged with the tip temperature change during the experiment to provide an average cantilever temperature change.

Alongside the above static experiment, line scans and full scans were performed. These were used to demonstrate the translation of the static results on actual operation and scanning in an AFM along with that of non-thermal AFM cantilevers. More specifically, they aimed to show how the AFM's feedback system responds and the magnitude of this on topographic images for all types of AFM cantilevers. The first experiment was a line scan. This involved a simple 100 μm lateral scan without any movement longitudinally, whereby the cantilever was brought over the microheater and the tip making contact with the Si chip. The exact region is shown in Fig. 3.14 by the X-X line. Performing these scans with zero microheater current and then with a current inducing sample temperature change (possible to be measured by an SThM tip) permitted these to be subtracted from each other to show the impact of the IC thermal bending. In addition, with a contrast between the colder and hotter region across the line scan, it should demonstrate the difference in the scan itself (disregarding other forms of drift) alongside the subtraction of the unheated and heated scans. With this explicit impact of IC thermal bending on AFM's feedback system, many scans are actuated over a 2D area with movement laterally and longitudinally to produce a full topographic scan. This was also performed through a large 100 x 100 μm scan with this executed across the same lateral line scan region as before, with the tip moving down across the right-side of the microheater. This was achieved with

zero microheater current and two different currents/powers to provide a clear contrast. However, the exact temperature over this full scan would not be quantified due to the microheater and SThM tip resistor potentially electrically connecting over the NiCr heater. Therefore, only point temperature measurements by an SThM probe were linked to the images.

With all the above methods, a sound ability to understand and quantify thermal bending in both the OC and IC for all types of AFM cantilevers was possible. These were taken forward in theorising and fabricating new AFM cantilever designs, especially in ones that require metallisation of the cantilever, like in SThM.

3.3 Thermal Bend Attenuation

With a clear method for modelling and quantifying thermal bending, the final piece of the puzzle was to do the same for a solution to minimise thermal bending. The simplest method for attenuating thermal bending is removing the source of the problem and constructing the AFM cantilever from one material so there is no mismatch of material CTEs. As a result, this solves the problem at the core and negates the phenomenon itself for AFM cantilevers. However, as previously mentioned, this is not always possible due to some probes requiring metallisation for functionality (such as in SThM) or for a sound laser reflection and topographic output. In such conditions, a solution is less straight forward and simple. Therefore, exploration of these design constraints, utilising SThM as a case study, was performed. Moreover, SThM provided the benefit of accurate temperature measurement for a sound quantification of thermal bend and hence permitted an excellent vehicle for study. Beyond the broad general theme to reduce thermal bend, it was aimed to minimise this not only in the absolute sense for the tip, but for the interpretation in an AFM system for both the OC and IC scenarios. The techniques and design changes implemented were aimed to align with the general theme throughout this body of work of simplicity. The objective of which was to minimise complexity, project time, process time, accelerate concept proof and enable wider applicability. As a result, modelling resources (relatively easy and less time consuming to experimental work) were utilised followed by

the established quantification methods. However, beyond this general approach, the method employed for fabrication of new SThM designs are required to be expanded.

3.3.1 Fabrication

Each of the three main processes within micro and nano-fabrication were used to fabricate SThM probes and so their specific roles are elucidated here.

3.3.1.1 Lithography

Both Photolithography and EBL were employed to fabricate SThM cantilevers within this project. The former enabled a single step to define the large array of patterns onto the 3" Si wafers that the SThM cantilever were constructed on. Therefore, it provided an ability to define patterns at various stages for multiple SThM devices (224 per wafer) in a batch fashion. Specifically, the definition of features that did not require sub-micron resolution and/or alignment were defined in this manner. This included the pattern for the pyramids (an angled surface to form a tip that protrudes away to the main probe body); probe chip backside (i.e. its rectangular form) and bulk topside SiNx. These were all exposed with the mask and wafer in contact due to its simplicity and ability to enabled high resolution which proximity exposure would limit. As this was performed on a 3" Si wafer, a Photolithography tool able to align and expose masks appropriate to this was required. The SUSS Mask Aligner MA6 tool (Fig. 3.16) in the JWNC was utilised to perform this.

However, for SThM, there are a number of high resolution and alignment sensitive sub-micron features. This is well within EBL's sub-10 nm range and so it was employed to define them. Specifically this was used to define the SThM cantilever outline and tip; Pd resistive wire at the cantilever tip and Au wire pad pattern leading up to the tip. As it can be realised, the common feature in all of this work is the precise alignment and resolution for consistent and sound definition of patterns relative to the cantilever's tip. Nominally SThM tip's have a radius of curvature of 50 nm and so EBL provides a sound technique to generate and place patterns precisely to this. Furthermore, this enabled masks to be formed in software rather than physically, providing greater flexibility and speed to implement different patterns. Hence,

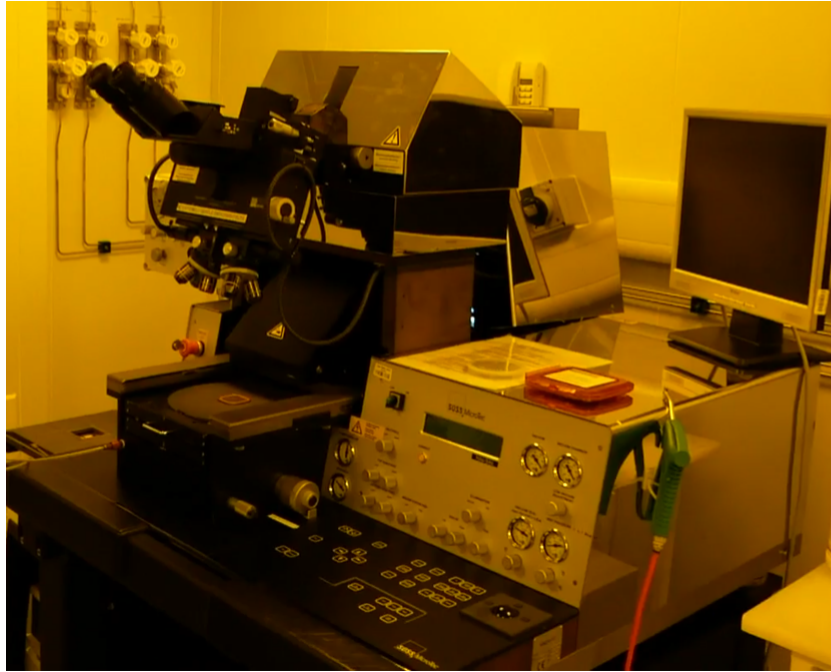


FIGURE 3.16: *SUSS Mask Aligner MA6 in the JWNC [139]*

it was a great method for exploring multiple and different SThM designs for thermal bend attenuation. Regarding alignment, square etched markers were utilised that were defined at the pyramid (probe tip) etch stage from Photolithography. These were defined at the corner of each SThM device in a 2×4 array. These were used for both global and local alignment, whereby the large number provided contingency if any were damaged along with alternative markers for multiple EBL defined patterns for each SThM probe to be performed. The latter is due to the markers being exposed during the alignment procedure making them susceptible to subsequent steps. To execute all of this, the Raith EBPG 5200 (100 kV E-beam) was employed in the JWNC as shown in Fig. 3.17. One final aspect should be highlighted at this stage that is highly unique to SThM fabrication that was not mentioned in the literature review due to its novelty. This pertains to the resist coating of the PMMA resist used to define the EBL patterns. Conventional procedure involves spinning the resist on for an uniform and controllable resist thickness. However, due to the highly topographic nature of the pyramids that generate the SThM tips, a new technique was developed at the University of Glasgow enabling resist coverage on the pyramid [154]. This involved float coating the resist alongside spinning. The former included the wafer being submerged in reverse osmosis water, resist dropped onto the water surface which evenly

disperses and once the solvent in the resist has evaporated the water abstracted. This then left a relatively uniform resist coverage over the pyramid and enabled pattern definition through EBL of tip features.

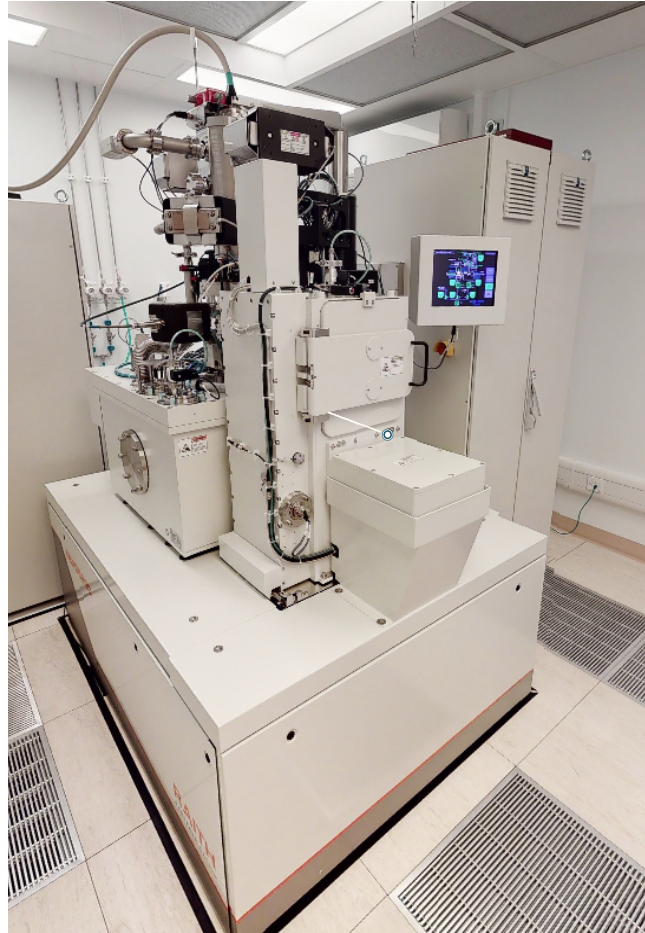


FIGURE 3.17: Raith's EBPG 5200 in the JWNC [139]

3.3.1.2 Etching

With the specific methods articulated for the pattern definition, the same was required for the steps involving the removal of material. For SThM fabrication both wet and dry etching were utilised. The former enabled relatively large volumes of material to be removed and specific angled features to be generated that were based upon the chemical selectivity of Si's diamond cubic structure. This provided the pyramid's to be constructed to generate their 54.7° angled side for SThM cantilever's tip alongside the probe chips backside. This process employed a hydroxide-based reaction whereby TMAH (25 %) or KOH (29 %) were employed. As highlighted in the Literature Review, the hydroxide reacts with the Si to remove it in such a way that the $\{111\}$ plane etches

far more slowly than the others to manifest the 54.7° etch angle. An image can be seen depicting one of the wet etch kit's utilised to perform these in Fig. 3.18. Furthermore, additional wet etches were employed such as Hydrofluoric Acid etches to remove native Silicon Oxides, although these employed conventional procedures.

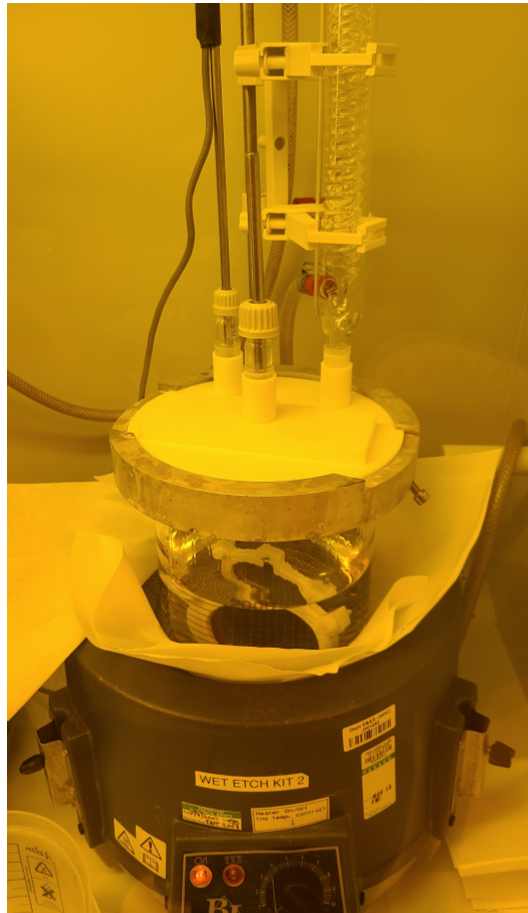


FIGURE 3.18: *Wet Etch Kit in the JWNC [139]*

In addition, dry etch RIE was also used during probe fabrication. This was employed due to its ability to control the etch very well and generate more anisotropic etches. Specifically, it provided etching of SiO_x , SiN_x , Si and photoresist. The two RIE etch examples shown in the Literature Review (Hexafluoroethane and Trifluoromethane based) were performed to etch all the Si-based materials. Moreover, O_2 plasma was additionally utilised frequently throughout the probe fabrication process to strip or de-scum carbon-based photoresist. Within the JWNC the Oxford Instruments RIE 80+ tool (seen in Fig. 3.19) and Asher RF PlasmaFab Barrel was used to perform all of these [139]. The exact recipes being based upon historically verified recipes within the facility.



FIGURE 3.19: *Oxford Instruments RIE 80+ in the JWNC [139]*

3.3.1.3 Deposition

Two main types of deposition techniques were employed for the fabrication of SThM cantilevers: E-beam Evaporation and LPCVD. Regarding the former, two tools were utilised in the JWNC: Plassys II and IV which are different generations of the MEB 550 S model [139]. With a 10 kW electron gun that is focused onto an ingot of metal, these tools rapidly evaporate metal that rise and condense onto samples up-to 150 mm in diameter, with a cryo-pump being used to achieve vacuum. As a result, the sample is mounted directly above the ingot being evaporated and facing downward, with the rate of deposition and the total thickness being controlled through a control loop that monitors the resonance frequency of a quartz crystal (the more metal deposited, the lower its frequency). An image of one of these Plassys tools in the JWNC can be seen in Fig. 3.20. Using these tools Nickel Chromium (NiCr), Au, Pd and Al were deposited at various stages of probe fabrication (full process seen in Appendix D). It should be noted that there are two shutters in the system: one to permit the metal to

evaporate into the chamber and another to enable coverage over the stage and sample. This is useful in providing a "dummy" run of metals. In addition, these tools can rotate the sample during deposition to enhance uniformity with Plassys IV additionally providing stage tilting during deposition. Fig. 2.21 previously shown in the Literature Review for an e-beam evaporator provides a reasonable depiction of Plassys II and IV. The only other material deposited on the probe was LPCVD SiN_x that formed the cantilever and tip structure. This was deposited commercially at the University of Chalmers in its Centrotherm LPCVD horizontal furnace. The most significant aspect of this process was its ability to deposit very low stress SiN_x films that is required for minimal bend in the SThM cantilevers once free-standing and limit delamination.

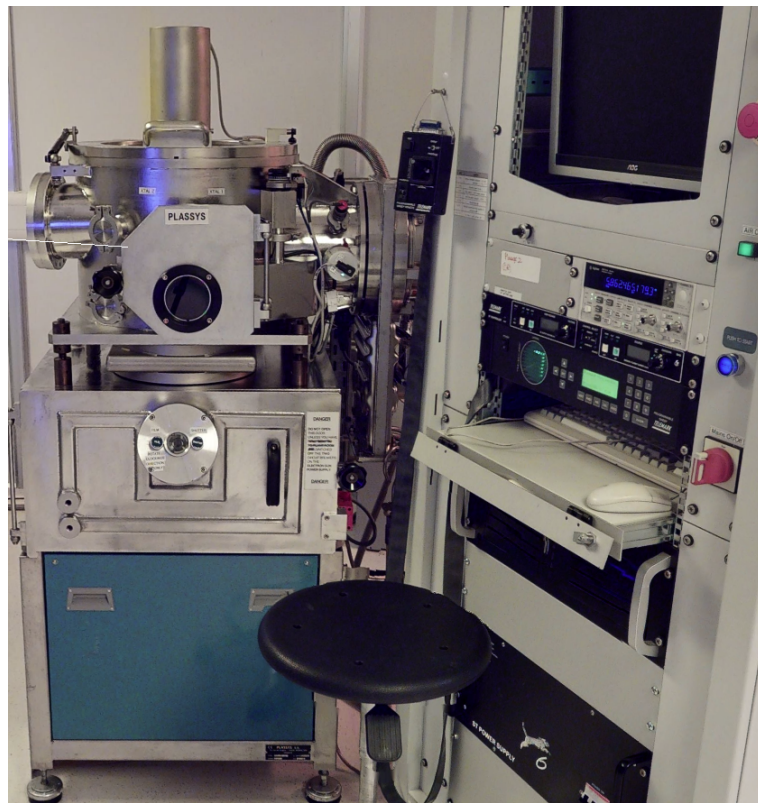


FIGURE 3.20: Plassys Tools in the JWNC [139]

With all the above mentioned, a method of investigation was possible for thermal bending along with the ability to fabricate new SThM probes to explore solutions to it. Modelling of thermal bending was first looked into prior to any experimentation or fabrication to provide a sound theoretical baseline.

4. Mechanical & Thermal Bend Modelling of AFM Cantilevers

Applying the methods described in previous chapters, SThM cantilevers were predominantly employed in this body of work thanks to their direct cantilever temperature measurement. Hence, their mechanical and thermal bend behaviour needed to be comprehensively theoretically modelled. This aimed to provide a sound basis of understanding to inform and contrast to experiments. Moreover, once validated, it enabled a quick method to explore various SThM cantilever designs. Additionally, this theory was translated to more common, non-thermal AFM cantilevers to provide insight into them and contrast their behaviours to SThM.

4.1 SThM Cantilevers

SThM cantilevers were modelled when Out-of-Contact (OC) and In-Contact (IC) for both their mechanical and thermal bend behaviour. OC is the simplest scenario and was first explored before expanding to consider IC. However, before any modelling was possible, the type of SThM probe employed needed identifying. This was the flat, SThM cantilever previously shown in Fig. 2.16 that is commercially known as KNT-SThM-1an [2] or VITA-XX-GLA-1 [155]. With all the stated strengths listed in Section 2.3.2, it was the best SThM probe for this project's objective. These probes shall be referred to as flat SThM probes henceforth due to an alternative SThM design (KNT-SThM-2an) having a groove in the cross-section. This flat nature was chosen over the grooved one due to their lack of cross-section variation that would have added complexity to the mechanical behaviour, making them less comparable to most non-thermal AFM cantilevers with flat cross-sections. As a result, the conclusions and

understanding acquired will have a wider applicability to general AFM cantilevers. With this stated, before modelling the flat SThM cantilevers, their material properties needed to be defined. This was essential in providing a sound representation of each material and so sensible theoretical quantification of the SThM cantilever's subsequent behaviour.

4.1.1 Material Properties

The nominal values for SThM probes' material properties were not well known due to their unique thicknesses, deposition conditions, tools employed and post-processing techniques involved in their fabrication. Moreover, limited work has been performed on accurately ascertaining this through experimentation in the past. Therefore, the material properties needed to be comprehensively explored using the most relevant literature.

4.1.1.1 Mechanical

The most significant mechanical properties can be seen from the governing FDM Equations established in the Literature Review (Eq. 2.10 & 2.8): Young's Modulus and Poisson's Ratio. The former is by far the most influential, while the latter is applicable when the Biaxial Modulus is desired to be determined. However, the latter can very important as some literature directly measures/determines the Biaxial Modulus from their experimental method, hence requiring the Poisson's ratio to calculate the Young's Modulus. Moreover, its influence may be more pronounced when employing FEA as this can model the cantilever in a full 3D model where it can ascertain which structures it most affects. Therefore, both Young's Modulus and Poisson's Ratio needed to be well defined.

Before each properties value was individually deduced, a general approach was desired to aid consistency in identifying appropriate values. A combination of utilising the most relevant literature magnitudes with averaging was applied. The former aimed to provide values for materials that had as similar as possible deposition conditions, post-processes and film thicknesses to those used in the SThM probes. Furthermore, if applicable, the crystal orientation of the material and measurement technique were attempted to be appreciated. This is due to some materials are notably

anisotropic such as Au. Therefore, some literature clearly defines this and measures properties in exclusive directions and needs to be appreciated to not warp the extracted value. For example, as Au is significantly anisotropic there are many pieces of literature exploring this, but an evaporated Au film is typically poly-crystalline so a predominant direction is not generated. Hence, property measurements in exclusive directions will not appreciate this well. As this was the case for all the materials reviewed, it was borne in mind when analysing literature. Alongside choosing the most relevant literature values, as mentioned averaging was performed. This was to mitigate the effects of any form of bias from selecting one paper if possible. With this said, averaging across a range of papers results in a value that has not been determined directly. However, as the materials in the SThM probes could not be determined due to time and scope constraints within this project, a general magnitude of each respective property was only required. Thus, averaging provided this with mitigation of spurious data from a single paper where possible. Overall, the above method should ensure a reasonable representation of each material and its property for sound theoretical modelling of SThM cantilevers. This was applied to the first property of the Poisson's Ratio as shown in Table 4.1. From the list of references for each material, the following set of values were generated with the associated explanation:

- $\nu_{SiNx} = 0.263$

Average from the LPCVD SiNx references [156]–[158]. Property values for PECVD SiNx were not included due to literature demonstrating different density to LPCVD which potentially would translate into their mechanical properties.

- $\nu_{Au} = 0.445$

As a result of the lack of literature on thermally evaporated thin Au films, values from the non-textured sputtered films [162], [163] were utilised.

- $\nu_{NiCr} = 0.31$

Due to general limited literature on thin NiCr films for SThM cantilever's specific composition, the median for the range from CES EduPack Software [165] was chosen. In addition, due to the NiCr's film's very thin nature in SThM (typically 5 nm), its mechanical influence is minimal meaning a value notably adrift from reality will have very little effect on models.

TABLE 4.1: SThM Materials - Poisson's Ratio Literature Values

Material	Reference	Material Thickness (nm)	Details	Poisson's Ratio
SiNx	[156]	100 & 500	LPCVD SiNx 2x2 mm 3.5x1.5 mm Membranes	0.27 & 0.24
	[157]	104	LPCVD (at 835 °C) SiNx Monolayer	0.22-0.29
	[158]	290	LPCVD; Bulge Test	0.28 ± 0.05
	[159]	305 & 680	Low Temperature PECVD SiNx at 125 °C & 205 °C	0.23±0.02 & 0.25±0.01
	[160]	Unknown	βSiNx	0.23-0.27
	[161]	Unknown	Pressureless sintered	0.22-0.27
Au	[162]	500 ± 10	Sequenced Ion Beam Sputtered; Non-Textured Gold; Theoretical & Experimental (Tensile Testing)	0.420 & 0.45 ± 0.026
	[162]	700 ± 10	Continuous Ion Beam Sputtered; {1 1 1} Fibre-Textured Gold; Theoretical & Experimental (Tensile Testing)	0.529 & 0.566 ± 0.310
	[163]	1000	Sputtered; Indenter and Micro-Switch	0.44
	[164]	NA	Theoretical Modelling; {1 1 1}, {1 1 0} & {1 0 0}	0.25, 0.49 & 0.57
NiCr	[165]	Bulk	Nickel-Chromium (90-70:10-30) Alloys	0.305 - 0.315
Pd	[166]	Bulk	Handbook Value	0.39

- $\nu_{Pd} = 0.39$

There are few, if any references for thin Pd films. Therefore, a handbook, bulk value was extracted. Moreover, as this material is only present at the tip of the cantilever, its Poisson's Ratio has a near negligible impact and does not require in-depth investigation.

With the above established, the other and most influential property is the Young's

Modulus. Similar to Poisson's Ratio, Table 4.2 was constructed from the relevant literature.

TABLE 4.2: SThM Materials - Young's Modulus Literature Values

Material	Reference	Material Thickness (nm)	Details	Young's Modulus (GPa)
SiNx	[167]	80	LPCVD; Nano-Indentation	212.3
	[148]	389	LPCVD; Nano-Indentation of Cantilevers with SEM (5 kV & 20 kV)	178 & 273.5
	[168]	200 & 500	LPCVD; Resonance Frequency From Thermal Noise (1st Mode); E_{eff} Determined to Account for Size Effects	228 & 266
	[168]	200 & 500	LPCVD; Resonance Frequency From Thermal Noise (2nd Mode); E_{eff} Determined to Account for Size Effects	274 & 272
	[169]	160, 162 & 165	LPCVD; Bulge Test	257.5, 266.1 & 241.8
	[170]	236, 264, 387, 392, 409 & 423	LPCVD; Ultra-Fast Pump Probe	217 ± 4, 271 ± 4, 273 ± 6, 259 ± 5, 255 ± 5 & 280 ± 5
	[158]	290	LPCVD; Bulge Test & Nanoindentation	222 ± 3 & 216 ± 10
	[171]	520	LPCVD; Laser Based Ultrasound Technique	260
Au	[172]	300, 500 & 1000	E-beam Evaporation; Membrane Deflection Experiment	53-55
	[173]	Cr-Au: 10-100, 30-300 & 50-500	E-beam Evaporation; Nanoindentation Test	56, 64, 89
	[174]	855	Sputtered (111); Magnetostriction	75.9
	[175]	1500-90	Sputtered; Magnetostriction	81-131

	[176]	19-62	Metal Plasma Immersion Ion Implantation and Deposition; Microcantilever Beam Test	69.1±2.6
	[177]	1000	E-beam Evaporation; Microbeam Testing & Nanoindentation Test	57 & 74
	[178]	500	Multi-user Microelectromechanical Systems Processes; Microcantilever Beam Test	78
	[179]	180, 310, 500, 680, 950 & 1000	Sputtered; Microtensile Test	61.0, 49.5, 53.9, 51.2 & 57.5
	[180]	200, 500 & 1000	Evaporated; Strip Bend Test	Average: 32.4, 33.0 & 30.8
	[180]	200, 500 & 1000	Evaporated; Nanoindentation Test	68.0, 69.2 & 82.5
	[181]	Thin (Un- known), Bulk	Ion-beam Sputtered; Tensile Test	91.8±6.0 & 89.7
	[182]	200	Evaporated; Nanoindentation Test (+Substrate Correction)	75
	[183]	Cr-Au: 10-100, 30-300 & 50-500	E-beam Evaporated; Nanoindentation Test	55.5, 64.1 & 88.8
NiCr	[165]	Bulk	Nickel-Chromium (90-70:10-30) Alloys	200 - 220
Pd	[166]	Bulk	Handbook Value	121
	[184]	40	Evaporation (at 360 °C)	125

From the extensive list of references for each materials' Young's Modulus, the following set of values were determined with the accompanying reasoning:

- $E_{SiNx} = 241.62$ GPa

When analysing the literature, the magnitude is highly variable; ranging from

178-280 GPa. However, extracting the values from all the identified LPCVD SiNx references, an average of 241.62 GPa was deduced [148], [158], [167]–[171].

- $E_{Au} = 64.39$ GPa

A significant variation in literature values of 30.8-131 GPa can be seen due to the multiple deposition techniques, measurement methods, thicknesses and structures. The impact of these factors on and/or by Au's crystallographic orientation is a prominent factor [172], [180] due to Au's notable degree of anisotropy (zener anisotropy factor = 2.87 [164]). As a result, very different Young's Moduli could be perceived with B. Merle [164] determining a variation of 59-82 GPa. In addition, as it can be seen, some papers demonstrate variation with thickness, while others do not. Bearing all this in mind, the most appropriate value appears ambiguous. Therefore, only values for thermally evaporated films without a specific crystallographic orientation analysed were used in the average determined [172], [173], [177], [180], [182], [183].

- $E_{NiCr} = 210$ GPa

With limited literature for thin NiCr films, the median bulk value from the only reference acquired was employed [165].

- $E_{Pd} = 121$ GPa

Similar to Poisson's Ratio, the handbook bulk value was acceptable and utilised. Moreover, this is very similar to the Poisson's Ratio value in S.U. Jen et al. [184] for a 40 nm thick Pd of 125 GPa. Hence, the general handbook value was consistent with the Poisson's Ratio while appearing reasonably accurate.

With the above nominal values established, there may be a notable degree of uncertainty. However, in the absence of a more thorough review and experimentation of each material in SThM probes, it was accepted that reasonable variance for each magnitude will exist. This was due to the crucial aim of the models being to capture the general behaviour and relationships seen in real-world cantilevers. Hence, pinning the above values down with very low uncertainty was not fully required and their magnitudes should provide a good enough representation.

4.1.1.2 Thermal

With the mechanical properties set-out, the appropriate thermal properties in relation to thermal bending was required. As seen in Equation 3.3, the main property is the linear CTE. Therefore, Table 4.3 was constructed and states the relevant literature for each of the key materials in SThM probes.

TABLE 4.3: SThM Materials - Linear Coefficient of Thermal Expansion Literature Values

Material	Reference	Material Thickness (nm)	Details	Linear Coefficient of Thermal Expansion (ppm K^{-1})
SiNx	[185]	230	LPCVD; Stoichiometric SiNx at Room Temp.	2.15
	[185]	Bulk	LPCVD; α -SiNx at Room Temp. along a & c axis	1.26 & 2.61
	[186]	478	LPCVD; Brillouin Light Scattering + Finite Element	3.0
	[187]	Thin Film	PECVD; Fast Fourier Transform Method	3.27
	[188]	Bulk	Hot Isostatically Pressed SiNx; 10% Theoretically Dense	2.9
Au	[189]	870	Evaporation; Bending Beam Experiment; Multiple Anneals (1;2;3)	13.9; 14.6; 14.8
	[190]	10 & 100	Evaporation; Thermo-Resistive and Piezo-Resistive Based Method; 10 nm with variable deposition rates (0.015-0.21 nm/s)	67.3-87.1 & 17.3 \pm 0.3
	[191]	115, 224, 543 & 1200	Sputtered; Thermal Bulge Method	9.6 \pm 1.4, 10.6 \pm 1.2, 12.9 \pm 0.3 & 13.6 \pm 0.2
	[192]	880	Evaporation; Joule Heating Experiment	22.6 \pm 0.3
	[193]	785	Sputtered; Wafer Curvature Technique	14.66

NiCr	[165]	Bulk	Nickel-Chromium (90-70:10-30) Alloys	12 - 14
Pd	[166]	Bulk	Handbook Value	11.2

The same methodology applied for the mechanical properties was used and hence the following values determined:

- $\alpha_{SiNx} = 2.575 \text{ ppm } K^{-1}$

This average was deduced from the LPCVD, thin film, non-textured SiNx references [185], [186]. As for the mechanical properties, only LPCVD was used to avoid the potential for other techniques, that may have notable variation due to their nature and the resultant film density, having a pronounced influence on the CTE.

- $\alpha_{Au} = 15.6 \text{ ppm } K^{-1}$

Thermally evaporated, thin film, non-post processed Au literature [189], [190], [192] were extracted and averaged. Notable variation was observed (likely due to varying crystal orientation) across literature and so a reasonable uncertainty should be noted.

- $\alpha_{NiCr} = 13 \text{ ppm } K^{-1}$

Due to a limited number of references and its actual low level of significance in the models, the handbook bulk value was utilised.

- $\alpha_{Pd} = 11.2 \text{ ppm } K^{-1}$

The bulk handbook value was extracted to stay consistent with the mechanical properties in tandem with more investigation not being required due to Pd's low impact on the models output relative to the SiNx and Au materials.

With the above stated, as mentioned regarding the mechanical properties, there is reasonable variation in the literature values. As a result, notable uncertainty in the determined nominal values above should be borne in mind for model application of thermal bending.

4.1.2 Construction

With the material properties explored, the main cantilever utilised in this work needed to be dimensionally defined for a clear definition in models. Therefore, a 3D Computer Aided Design drawing was produced. An engineering drawing of this can be seen in Fig. 4.1, where it was constructed from the four main materials already explored that are hence listed with their nominal thickness alongside reasoning to why they are used in the cantilever's construction:

- SiNx ($t = 400$ nm) - This provides the majority of the cantilever's mechanical stiffness due to its relatively large thickness and Young's Modulus. In addition, with its low thermal conductivity, it conducts and abstract very little heat from the Pd resistor at the tip or the sample permitting more accurate temperature measurement.
- Au ($t = 145$ nm) - Provides a low electrical resistance connection to the Pd resistor and a reflective surface for force measurement in the Optical Lever system.
- NiCr ($t = 5$ nm) - Acts as the adhesion layer for the Au and Pd onto the SiNx.
- Pd ($t = 40$ nm) - Forms the RTD at the probe tip and is used for its good linear response of electrical resistance to temperature change.

With these nominal geometry values, a degree of uncertainty in their absolute magnitude is present to real-world SThM cantilevers. Focusing on SiNx which provides the majority of its stiffness, its aerial geometry is less prone to variation. This is due to its definition from a combination of EBL and Photolithography that employs a consistent mask, alignment and exposure conditions that has been demonstrated in the academic group to produce a consistent definition to the designed nominal values. However, the thickness of SiNx deposited through LPCVD at Chalmers University of Technology is known to have a greater degree of uncertainty. For example, one wafer exhibited a range of 35.4 nm in SiNx thickness. This is significant enough to show an appreciable difference in cantilever stiffness/spring constant alongside thermal bending induced deflection (as seen in the second moment of area Equation 3.5). A magnitude to this effect can be ascertained from a sensitivity analysis of the FDM model

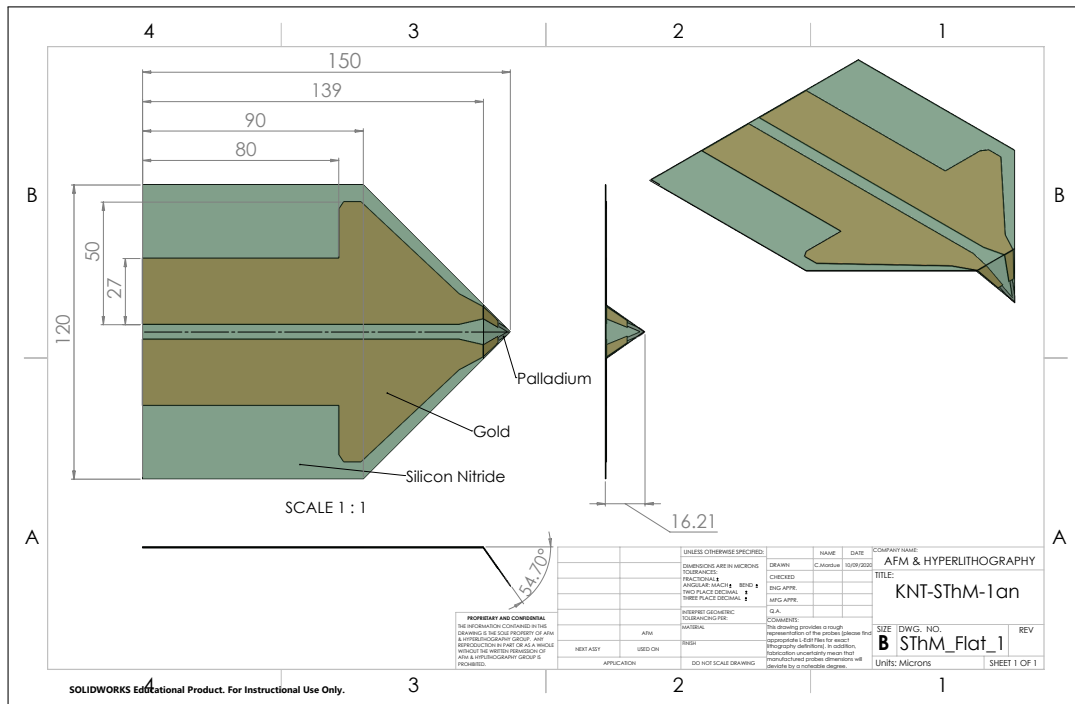


FIGURE 4.1: Engineering Drawing of Flat SThM Cantilever Design

that will be performed later in Section 4.1.3.3. Regarding the other materials, these are defined utilising EBL and deposited by thermal evaporation. As a result, they similarly have consistent definition of their aerial geometries with thickness likely having notable uncertainty. However, from the author and the academic group that have developed and researched these SThM probes, the experience is that this varies far less than the SiN_x and is of less concern. Therefore, the SiN_x thickness is likely the source of greatest uncertainty of all the dimensions defined. With this established and all the required material properties for SThM cantilevers, they can be entered into the models for sound theoretical quantification. The first port of call was the OC condition as this was the simplest scenario to explore initially.

4.1.3 Out-of-Contact

Before going straight into the modelling results, the BCs for SThM should be explicitly established. This was required for both the mechanical and Thermal BCs, whereby these should additionally be applicable to non-thermal AFM cantilevers.

4.1.3.1 Boundary Conditions

Mechanical

Mechanically, SThM and AFM cantilevers have a fixed or encastré BC at their base by their definition as cantilevers. This can be simply understood from a free-body diagram (FBD) as shown in Figure 4.2 where the addition of an EF and Temperature change can be seen. As a result, the base does not displace or rotate while the rest of

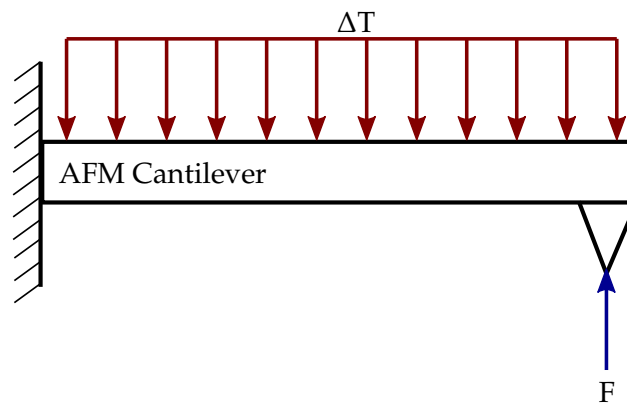


FIGURE 4.2: FBD of an AFM Cantilever OC

the cantilever can. However, this assumes no displacement or rotation in the probe chip, holder and AFM head. This may not be the case as previous research has shown the whole AFM system can contribute to Thermal Drift [37]. Although, this project was aimed at investigating the contribution of AFM cantilevers to the phenomenon of Thermal Drift. Therefore, this BC was still considered appropriate. In addition, it is worth noting that this BC is idealised in this way due to the cantilevers low stiffness relative to the other components in the AFM and sample. This coupled with its low thermal inertia make it highly desirable to fully understand and minimise its sensitivity to thermal induced artefacts. To this effect, the next BC needed to be defined related to its thermal/heat transfer.

Thermal

For SThM and most AFM cantilevers, there is a strong thermal connection to the probe chip through solid conduction [141], [194]. In parallel to this, the cantilever also experiences convection loss to the ambient fluid (unless scanning under vacuum). Moreover, if the cantilever is OC and near a surface, fluid conduction may occur with the nearby surface adding to the heat loss to the immediate environment. These paths are demonstrated visually in Fig. 4.3.

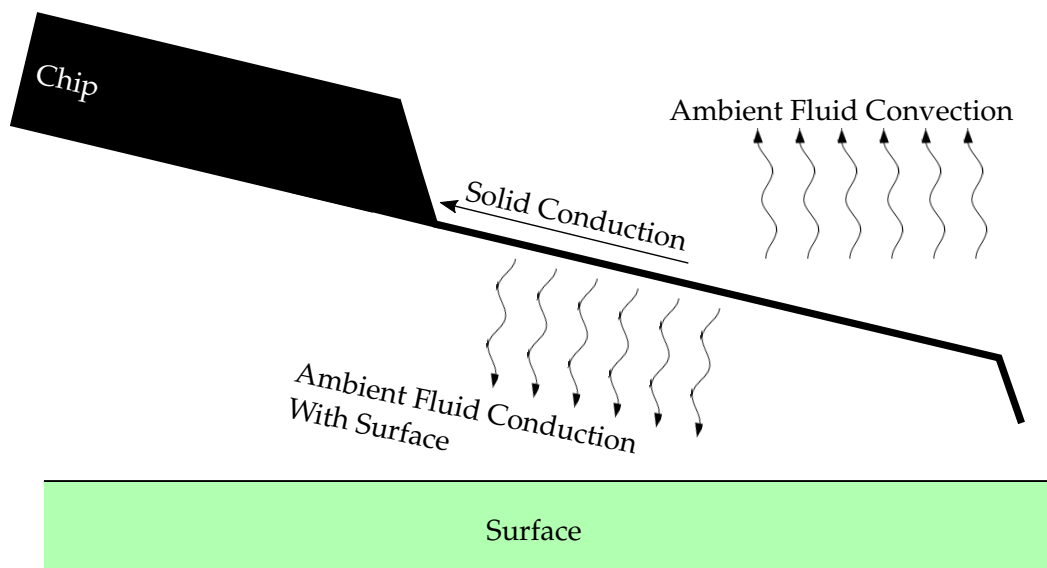


FIGURE 4.3: SThM Cantilever OC Heat Transfer Diagram

The above heat transfer paths in cantilevers are can be modelled using thermal-resistance models. Therefore, for designing OC experiments, if the nearby chip, sample surface and immediate ambient fluid are at an equal temperature to the cantilever, it could be regarded as a steady and uniform temperature across the whole cantilever. Regarding the scale of a SThM probe chip ($3.45 \times 1.5 \times 0.38$ mm) and the immediate environment to the cantilever, a relatively small heat source should be able to replicate uniform temperature change. This uniform temperature change is the simplest and easiest one to reproduce in theoretical models and so with the relatively trivial ability to heat most of the chip and immediate cantilever fluid, it is possible to replicate in experiments. Therefore, it was employed in the project for quantifying OC thermal bending. However, before its use in modelling thermal bending, the mechanical EF was first explored due to it defining the InvOLS which AFMs' use to interpret

induced rotation and deflection such as from temperature change.

4.1.3.2 Mechanical Modelling

The static mechanical behaviour for all AFM cantilevers is induced from an EF imparted due to the mechanical interaction with a surface. For this, the stiffness or normal spring constant dictates how much the tip deflects for a given force. Moreover, how the deflection manifests itself along the cantilever length and so how it bends is key. This is due to the optical lever essentially measuring rotation at the laser spot's location and applying the InvOLS that relates this to the cantilever's tip deflection. Therefore, this EF induced behaviour completely influences the interpretation of all vertical deflection readings. As a result, any temperature induced rotation and deflection will be outputted according to this and hence needed to be fully understood to deduce thermal bend's impact on AFM measurements. This was initially explored using flat SThM cantilevers due to their closer relation to other non-thermal AFM cantilevers. However, grooved SThM cantilevers were explored later in the project due to the theory behind their function relying on their cross-sectional and mechanical form which has been shown to not fully operate as theorised.

Flat Cantilevers

With a sound idea of the general make-up of SThM cantilevers, they could be modelled in the FDM and FEA programmes. Regarding the former, a simple analysis of the basic governing mechanical equation for vertical deflection of cantilevers from an EF (Equation 2.10) needed to be performed. It should be stated that this behaviour, although dependent on contact, was explored in this OC section. This was due to contact generating the EF itself which, from a FBD perspective, has no restriction in the tips degrees of freedom (as seen in Fig. 4.2). Therefore, it is best regarded as OC for this scenario. With this assumption explicit, the main contributing factors are listed below with their relationship to vertical deflection:

Force - Directly Proportional: $\delta = mF$

Young's Modulus - Inversely Proportional: $\delta = E^{-x}$

Cantilever Length - 3rd Order Polynomial Increase: $\delta = aL^3 + bL^2 + cL + d$

Width - Inversely Proportional: $\delta = w^{-x}$

Thickness - 3rd Order Polynomial Decrease: $\delta = at^3 + bt^2 + ct + d$

From the above, it can be seen that cantilever length and thickness have the greatest impact on deflection and so similarly its stiffness/spring constant. This applies to all AFM cantilevers alongside SThM ones. As previously mentioned, the cantilever's aerial dimensions are consistently defined through EBL and Photolithography meaning its length is very controllable with a relatively low magnitude of uncertainty. Therefore, it is the most effective property to control the cantilever spring constant and mechanical behaviour. However, of a similar significance, the cantilever thickness is harder to control due to the nature of the LPCVD SiNx deposition rendering appreciable thickness variation (e.g. 35.4 nm) as highlighted earlier. Hence, only nominal values can be targeted, but with a relatively high magnitude of uncertainty. In addition, there has been frequent observations of wide ranging spring constants for individual designs of commercially manufactured SThM cantilevers. This known variation in thickness and its cubic polynomial relation strongly suggests it is a likely contributing factor. Furthermore, the Young's Modulus is not well characterised for the LPCVD SiNx in SThM probes which additionally could be a significant influence on cantilever stiffness. With this established, the influences of these properties on rotation is also important due to its direct measurement by the AFM's optical lever system. This is seen in Equation 2.10, whereby only length's relation changes with its impact reduced to a squared relation, e.g. half length = quarter deflection. Therefore, it should change less with length than the corresponding vertical deflection.

With this basic appreciation, the next step was to employ the equations derived for EFs in the FDM model of the SThM cantilever's heterogeneous and non-prismatic construction to provide a more exact understanding. The relationships employed are shown in Equation 3.7 with the more elaborate derived second moment of area previously determined in Equation 3.5 (with the inclusion of each material's respective width in each term). Utilisation of these alongside the bending moment expressions shown in Equation 2.11 in each element's calculation, enabled the structure to be fully modelled. This provides the exact coefficients to their respective relations. Applying

these with the BCs, geometry (based upon the L-Edit image seen in Fig. 3.3) and mechanical materials properties, the vertical deflection for a 100 nN EF and the respective spring constant was produced by the FDM Model. This used no adjustment through the Biaxial Modulus and so assumed the SThM cantilever as a beam. The subsequent values and profiles for the vertical deflection and rotation due to an EF can be seen in in Fig. 4.4 and 4.5.

FDM - SThM Mechanical Results

Vertical Deflection of Tip (EF 100 nN) = 0.589 μm

Spring Constant = 0.170 N/m

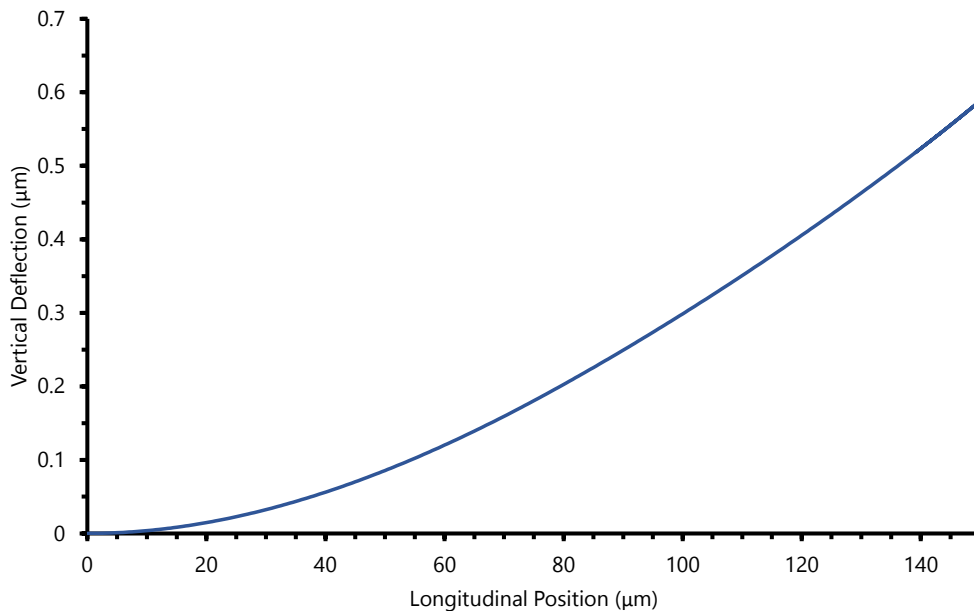


FIGURE 4.4: *FDM - Flat SThM 100 nN End-Force Displacement Profile*

Analysing these results, sensible tip deflection and spring constant values of 0.589 μm and 0.170 N/m were produced respectively. Regarding the latter, distributors quote a range of stiffness of 0.25 [195], 0.3 [196] and 0.5 N/m [197]. This is a significant range with the model's value being lower than this range would suggest. However, as demonstrated by L. Avilovas [148], the thermal tune method typically utilised for spring constant determination can be highly inaccurate for SThM cantilever's due to their unique construction and non-uniform internal stresses. Moreover, there can be significant variation in any of the spring constant measurements with the theoretically

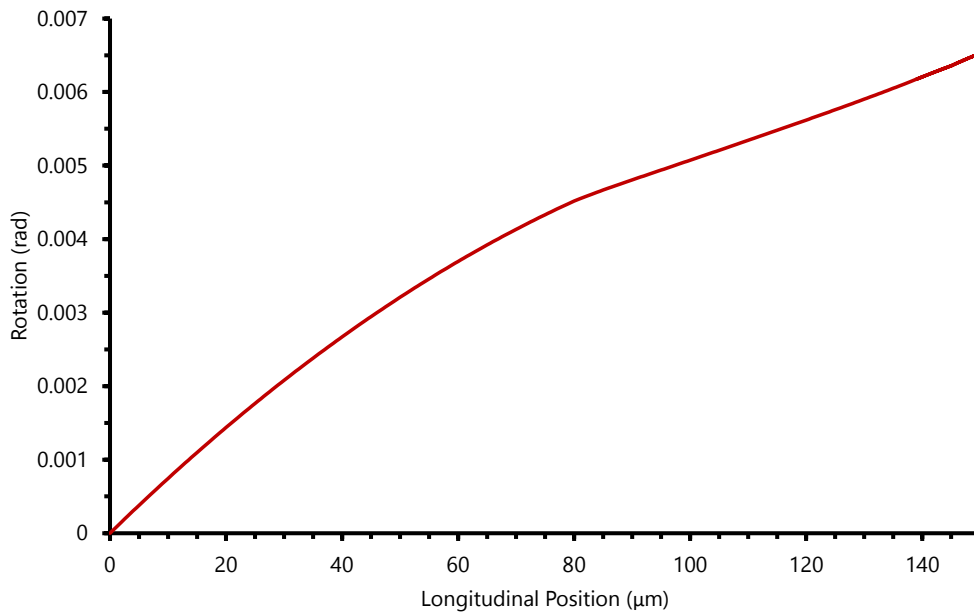


FIGURE 4.5: FDM - Flat SThM 100 nN End-Force Rotation Profile

more accurate spring-on-spring methods generating a range of 0.173 to 0.389 N/m for a particular set of SThM cantilevers [148]. As a result, a significant error should be attributed to any value. For example, a flat SThM cantilever demonstrated a spring constant of 0.22 N/m according to work performed by L. Avilovas with his more accurate quantification technique. Bearing in mind the known variation and this value being lower than stated by distributors, the spring constant outputted by the FDM Model is perhaps on the lower side, but still reasonable.

Moving towards the profile graphs, a sound deflection profile was produced in Fig. 4.4 with it increasing towards the tip with a near cubic polynomial order. However, this is not completely cubic due to the unique Au pattern and taper from 90 μm along the SThM cantilever generating a reduction in the gradient towards the tip. Therefore, as the rate of rotation change is reduced, there is a similarly reduced rate of increase in vertical deflection with it becoming more linear in profile. In addition, the rotation graph shown in Fig. 4.5 theoretically mirrors the vertical voltage change measured by the AFM photodetector. Thus, this general profile should be generated if the laser spot was translated longitudinally for the same applied tip force. With this said, the above values and profiles employed each materials Young's Modulus as opposed to their Biaxial Modulus. Applying the latter, vertical deflection and spring constant values of 0.407 μm and 0.246 N/m respectively were outputted. To indicate whether

this is more accurate and validate the FDM Model, FEA was employed. Although, a direct comparison to the above structure modelled was not ideal due to difficulty with partitioning to create a sensible mesh when including the 5 nm thick NiCr layer in the FEA models. As a result, it was not included with just a 150 nm thick Au coating. Due to FDM's flexibility, it was trivial to match this and compare completely like-for-like. The results from both the FEA & FDM models (with and without the Biaxial Modulus) are contrasted for the flat SThM cantilevers with no NiCr in Table 4.4.

TABLE 4.4: Flat SThM Model Comparison for an End-Force

Model	Modulus	Vertical Deflection of Tip ($\mu\text{m}/100 \text{ nN}$)	Spring Constant (N/m)
FDM	Young's Modulus	0.593	0.169
	Biaxial Modulus	0.410	0.244
FEA	NA	0.572	0.175
Percentage Difference	Young's Modulus	-3.72 %	+3.58 %
	Biaxial Modulus	+28.4 %	-39.6 %

It can be seen from Table 4.4 that the Biaxial Modulus produced a pronounced reduction in deflection and increase in the spring constant in the FDM Model. The magnitude of this change is far greater than that outputted by the FEA model with it far more aligning with the Young' Modulus for EFs. This subsequently suggests that the mechanical behaviour seen in SThM cantilevers is closer to a conventional beam or strip as opposed to a plate. One explanation for this is the cantilever's tapered tip. As the EF is applied at the tip (positioned along the cantilever centreline), it causes the force to spread evenly across the width as it translates along the tapered sectioned. As a result, this even distribution of force results in less synclastic deflection behaviour and so very equal deflections and behaviour across the width. This can actually be seen in the FEA output for vertical deflection in Fig. 4.6.

In addition to this conventional beam behaviour, the impact of the NiCr is minimal when comparing the FDM models with ($0.589 \mu\text{m}$) and without ($0.593 \mu\text{m}$) it. This is

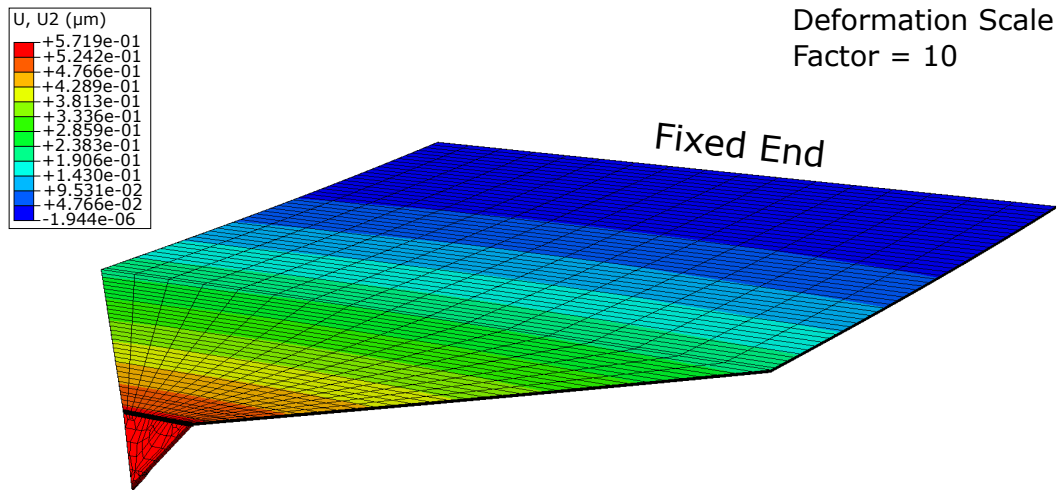


FIGURE 4.6: FEA - Vertical Deflection of a SThM Cantilever with 100 nN Tip Force Applied Vertically

logical due to its very thin nature and Au substituting it. Hence, other factors such as SiNx's thickness that has been demonstrated to vary by 35.4 nm on a 3" wafer, will likely cause a greater variation than the substitution of NiCr in models. Alongside this, other notable factors such as the SiNx's Young's Modulus could easily have a greater impact. To quantify these, a Sensitivity Analysis was performed in the FDM model thanks to its flexibility and ease of modification. Moreover, Au's thickness and Young's Modulus was also explored to mirror the SiNx analysis as it is the second most mechanically significant material. These can be seen in Fig. 4.7 and 4.8 whereby realistic variation for each property has been applied.

Taking a first look at the impact of Young's Modulus for both SiNx and Au, a fairly linear relation can be seen with an increase for both resulting in a greater spring constant (in agreement with the basic analysis conclusions). Hence a gradient between 0.5-0.6 mN/m/GPa was determined for both materials which is significant considering the low spring constant of SThM cantilevers. Analysing the influence of thickness in both, a polynomial relation was produced with SiNx showing a greater rate of change than Au. This is due to SiNx's greater nominal Young's Modulus and so changes to its mass has a greater influence. Hence for the previously quoted 35.4 nm of SiNx thickness variation, the FDM model would suggest around 0.04 N/m (24 % change relative to the base 0.170 N/m spring constant) potential variation in SThM cantilever stiffness. This is significant and provides quantified evidence to its potential contribution to the observed spring constant variation.

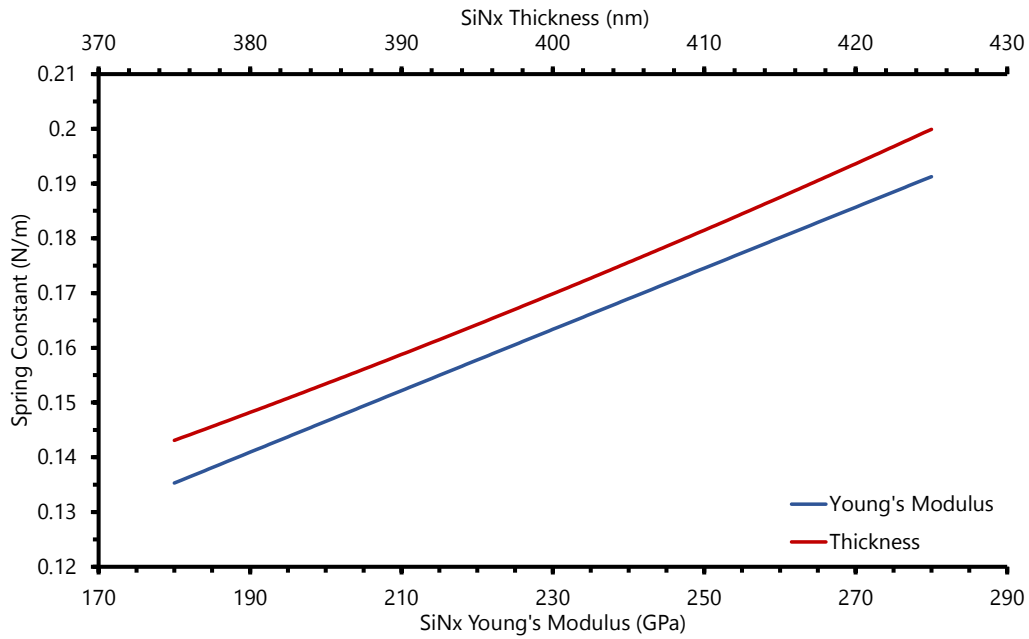


FIGURE 4.7: FDM - Sensitivity Analysis of SiNx Young's Modulus (180-280 GPa) and Thickness (375-425 nm) vs Spring Constant

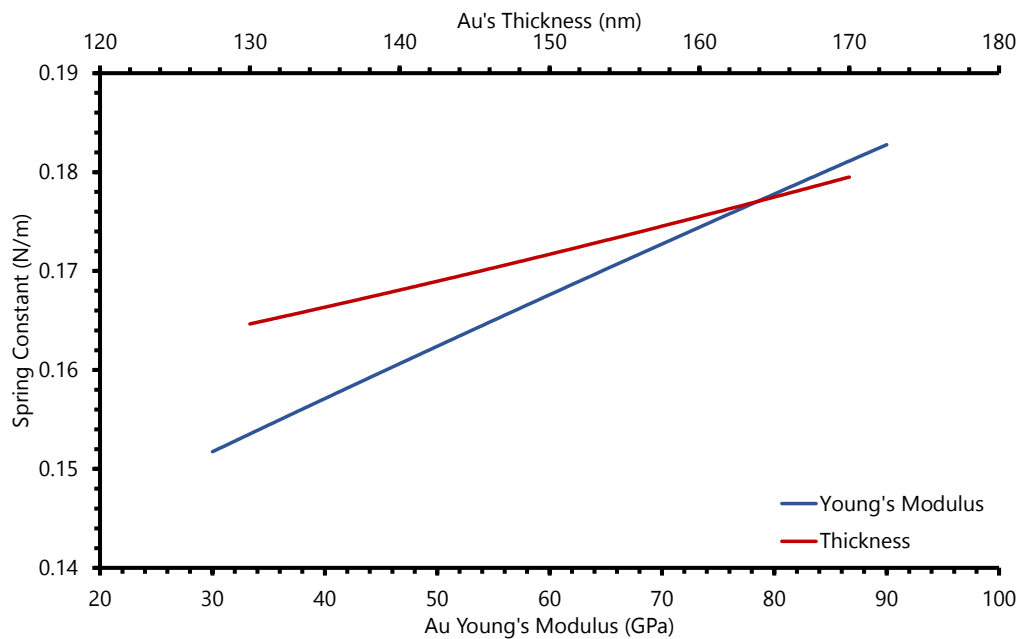


FIGURE 4.8: FDM - Sensitivity Analysis of Au Young's Modulus (30-90 GPa) and Thickness (130-170 nm) vs Spring Constant

With sound modelling of flat SThM cantilevers and both models demonstrating reasonable alignment, the next step was to theoretically determine how this translated within an actual AFM. Firstly, the theoretical InvOLS was deduced. This is the tip deflection divided by the rotation at each position along the cantilever length. This is due to the vertical voltage change on the AFM's photodetector being equivalent to

rotation at the laser spot's position along the cantilever. The subsequent relation is shown in Fig. 4.9, whereby a \log_{10} scale has been employed for the x and y axes for clarity due to the decaying relation of InvOLS with length.

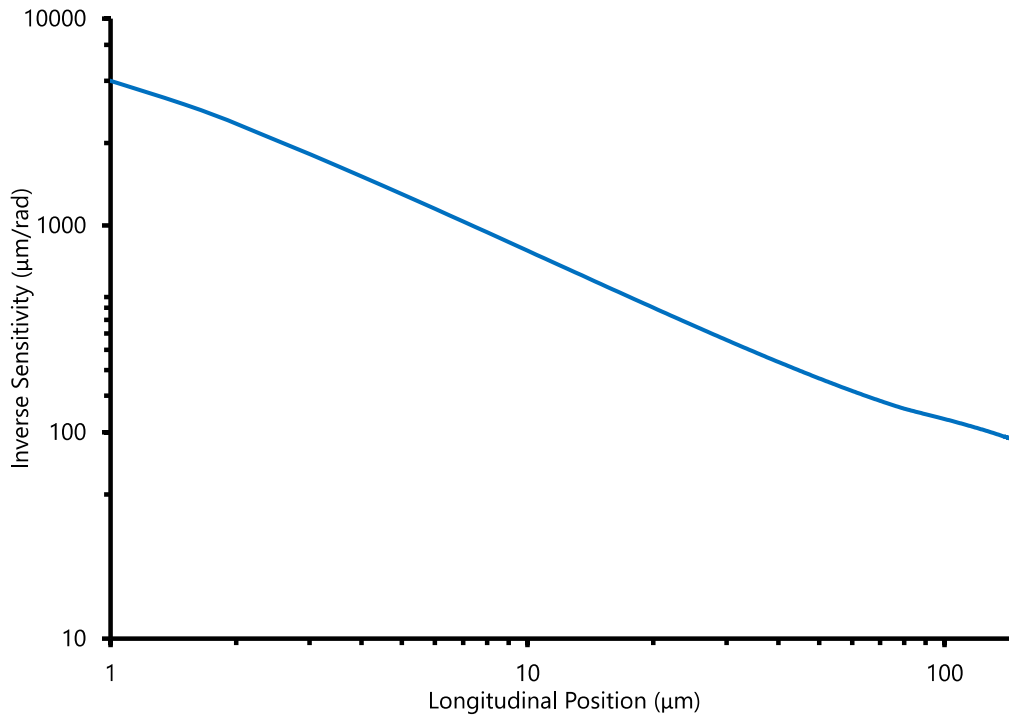


FIGURE 4.9: *FDM - Flat SThM Theoretical InvOLS vs Longitudinal Position*

This graph effectively demonstrates the inverse of the rotation shown in Fig. 4.5, but multiplied by the constant coefficient of the tip deflection. Therefore, applying the above in whatever longitudinal position will produce the same tip deflection from an EF applied to the cantilever. Analysing the form of this relation, what is very clear is how rapidly the inverse sensitivity degrades near the base with it theoretically approaching infinity. This concurs with the understanding in the AFM community that you should position the laser spot nearest the end/tip of the cantilever as this is the region of greatest sensitivity (i.e. experiences the most rotation for the given tip deflection). If we look at a realistic position of 60-130 μm for the laser spot's longitudinal position, a relative change of around 37.7 % occurs in the InvOLS. Therefore, through simple inversion of the InvOLS to obtain the sensitivity, a change of 60.5 % will occur across this length. As the SNR is always of importance for AFM, this case emphasises how much the laser spot's longitudinal position can alter this. Furthermore, due to SThM cantilevers taper and so greater reduction in rotation, it would be expected

the relative change in sensitivity for other, prismatic cantilevers to be even more pronounced. With these key mechanical aspects explored for flat SThM cantilevers, modelling and analysis was required for the more complex grooved cantilevers that had not achieved their theoretical complete attenuation of thermal bending in fabricated cantilevers.

Grooved Cantilevers

Grooved SThM cantilevers are flat SThM cantilevers, but with a central groove/ingress along the majority of their length resulting in a variable height of the SiN_x cross-section. The previously shown image in Fig. 2.15 from literature demonstrates this alongside an aerial SEM image in Fig. 4.10. In the latter, the groove can be seen from its outline located along the centre of the cantilever. From the original paper by Y.

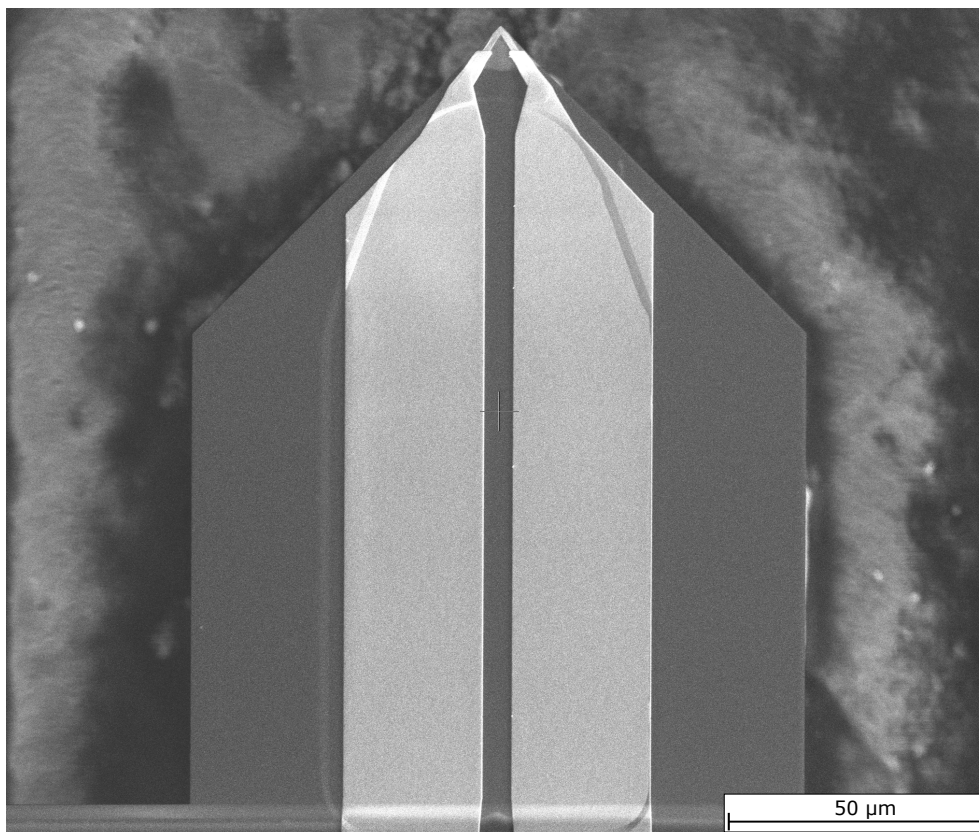


FIGURE 4.10: *Aerial SEM Image of a Grooved SThM Cantilever*

Zhang et al. [114] that introduced grooved SThM cantilevers, temperature induced deflection still occurred with a maximum and minimum reduction of 79.5 % and 45.5 % respectively. This was initially attributed to the Au not being completely deposited

within the groove. However, once corrected, thermal bend induced deflection still occurred. The concept behind the design was to mimic the conditions of a sandwich structure; equal mass of SiNx above and below the Au. This would produce a NA location half-way through the Au's thickness and result in equal and opposite magnitudes of stress and strain for any thermal bending on the structure, like in a sandwich cross-section. It should be noted that an actual sandwich structure was not attempted due to the inability to deposit SiNx on top of Au. This was because of SiNx's high deposition temperature for LPCVD and Au's low melting point. Therefore, for this grooved cross-section, it metaphorically hinges on the mechanical characteristics of the groove mimicking a sandwich one. As a result, this was re-examined to determine whether or not it was erroneous in application or the concept itself is flawed.

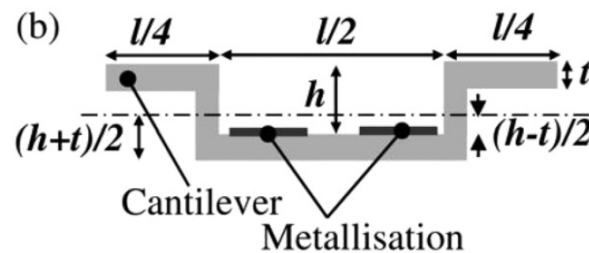


FIGURE 4.11: Grooved SThM Cross-Section Diagram [114]

In the paper [114], a SThM cantilever with a groove length, width and depth of $120 \times 60 \times 0.5 \mu\text{m}$ respectively for a 350 nm thick SiNx was fabricated. This subsequently had its thermal bending characterised experimentally for verification of the concept. The fabricated cantilever aligns with the equation stated of $\frac{h-t}{2}$ in Fig. 4.11 as this will generate a NA location 75 nm above the top surface inside the groove half-way through the Au. Before verifying if this is the case, it should be noted that it is incorrectly stated within the paper that when $t = h$ (i.e. thickness of the SiNx is equal to the groove depth) there should be zero bending moment from temperature change. This contradicts the $\frac{h-t}{2}$ equation and what cantilever was derived. The latter is correct with the groove depth requiring to be equal to the SiNx thickness plus the Au thickness ($t_{\text{SiNx}} + t_{\text{Au}} = h$) when there is equal widths of SiNx above and below the Au. With this clear, the structure fabricated based on the concept was verified through the application of NA Equation 2.12 to the idealised structured shown in Fig. 4.11. This

produced the following simplified expression:

$$x_{NA} = \frac{\frac{w_s t_s^2}{2} + h t_s \left(\frac{2w_s}{c_{rat}} + h \right) + n w_c t_c \left(t_s + \frac{t_c}{2} \right)}{w_s t_s + 2h t_s + n w_c t_c} \quad (4.1)$$

where $c_{rat} = \frac{2w_s}{w_w}$ and h are the total-to-wing width ratio and groove depth respectively. The nominal values from the paper were inputted ($l = w_s = 120\mu\text{m}$; $t = t_s = 350\text{nm}$; $w_c = 54\mu\text{m}$; $t_c = 150\text{nm}$; $h = 500\text{nm}$) and the NA location from the underside of the substrate in the groove calculated. This produced a value of 423.6 nm, 1.4 nm below the desired location half-way through the Au thickness (425 nm). The reason for this was due the groove and wing sections not actually being equal in width. From visual inspection of Fig. 4.11, the total width of the bottom section of the SiNx is the groove width plus the width of the groove side-walls. Hence, there is greater SiNx below the Au, resulting in a NA location below the ideal location. A more explicit visual of this can be seen in Fig. 4.12 for a proportional cross-section. As a result, a groove depth of

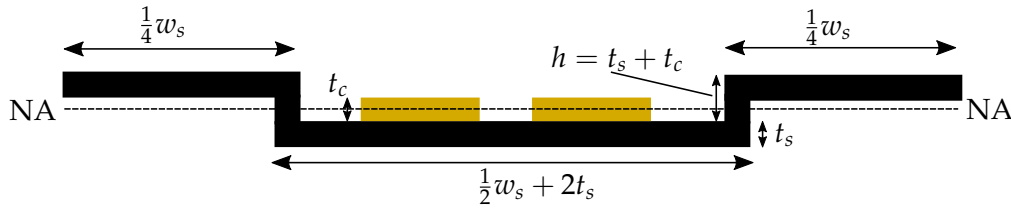


FIGURE 4.12: Grooved SThM Cross-Section Diagram With Proportional Key Dimensions For Ideal NA Position

503 nm would produce a NA location half-way through the Au thickness. This should theoretically render the structure to completely attenuate thermal bending. Moreover, Equation 4.1, can be rearranged to form equations so that other factors can be changed to produce the desired NA location. For example, inputting the desired NA location and a known groove depth and width to determine the required overall cantilever width. These permit the widths to be changed to shift the position of the NA. All of these equations are shown in Appendix A alongside the respective second moment of area equation for this grooved cross-section. The latter was possible using the Parallel Axis Theorem and Transformed Section Method which enabled comparison of the grooved cross-section with that of a flat cantilever. As a result, the second moment of area was calculated for key cross-sections and shown below. These included the cross-sections in Y. Zhang et al.'s paper [114] of a flat cantilever with 350 nm thick SiNx and

a grooved one with a depth of 500 nm. Furthermore, the standard SiNx thickness of 400 nm for a flat SThM cantilever was determined with the newly proposed groove depth of 503 nm. Hence, the following second moment of areas are shown below:

$$I_{flat,400nmSiNx} = 8.003 \times 10^{-25} \text{ m}^4$$

$$I_{flat,350nmSiNx} = 5.611 \times 10^{-25} \text{ m}^4$$

$$I_{500nmgroove,350nmSiNx} = 3.076 \times 10^{-24} \text{ m}^4$$

$$I_{503nmgroove,350nmSiNx} = 3.107 \times 10^{-24} \text{ m}^4$$

From the above, it can be seen that a flat cantilever using 400 nm of SiNx experienced an increase of 284.4 % to a 500 nm groove depth with a SiNx thickness of 350 nm. However, using the same SiNx thickness of 350 nm for the flat cross-section, an increase of 448.2 % was calculated. As the second moment of area is directly proportional to stiffness/spring constant, a reduction of 74.0 % and 81.8 % in deflection would be seen relative to the flat SThM cantilevers with 400 nm and 350 nm SiNx thicknesses respectively. Interestingly, the 74.0 % is within the 79.5-45.5 % reduction in deflection noted by Y. Zhang et al. [114] when comparing the grooved cantilever to the 400 nm SiNx flat SThM one. Therefore, this indicates that potentially the simple increase in the second moment of area and so stiffness of the cantilever could be providing the majority of the reduction observed in the paper. However, this relation is only true up to the Au width increasing 80 μm along the cantilever where some of the Au is patterned outside the groove (shown in Fig. 4.11) causing a different cross-section. As a result, this may generate lower than expected reduction in the fabricated cantilevers. This could then explain the lower portion of the range in the reduction of thermal bend induced deflection. With this said, the spring constant determined in the paper for the grooved and flat cantilever only showed a 14.3 % increase using a spring-on-spring method [198] which translates to a 12.5 % expected reduction in thermal bending from simple stiffening. Therefore, the full explanation for the results is not completely clear, but does shed a light on the grooved stiffening effect being a significant factor.

However, all of the above assumed an ideal perpendicular and vertically edged groove with only a single coating as seen in the both Fig. 4.11 & 4.12. This is not the case as, during fabrication, Si is etched using RIE employing a two part Oxygen and

Carbon Tetrafluoride recipe with deliberate resist reflow that produces an angled side-wall for the cross-section. The angle of which is dependent on the flow-rate, RF Power and Pressure [139], but for SThM cantilevers these are controlled to generate a side-wall angle (θ_{sw}) of 50° . This is designed to permit a continuous Au deposition over the side-wall. A visual of this cross-section with a side-wall can be seen in Fig. 4.13. As a result, a re-derivation of the previous x_{NA} equation was required:

$$x_{NA} = \frac{\frac{w_s t_s^2}{2} - h^2 t_s \tan \theta_{sw} + \frac{2w_s t_s h}{c_{rat}} + n_{c1} w_{c1} t_{c1} (t_s + \frac{t_{c1}}{2}) + n_{c2} w_{c2} t_{c2} (t_s + t_{c1} + \frac{t_{c2}}{2})}{w_s t_s + n_{c1} w_{c1} t_{c1} + n_{c2} w_{c2} t_{c2}} \quad (4.2)$$

where θ_{sw} denotes the angle of the side-walls with the additional equations related to this seen in Appendix A. Using an angled side-wall of 50° and the dimensions in [114], a NA location was calculated. This produced a NA location of 423 nm which is a slight shift downward from the ideal position resulting in a greater required groove depth for an ideal cross-section (around 505.1 nm). Moreover, within Equation 4.2 there is the capability to include the NiCr undercoating and determine whether this additionally has a significant influence over the NA location. Utilising the nominal thickness's of 5 nm and 145 nm for NiCr and Au respectively, the same angled side-wall cross-section produced a NA location of 422 nm which is again lower. Therefore, this suggests an even greater groove depth being required which may explain why the previously fabricated grooved cantilevers were so deficient in reducing thermal bend induced deflection.

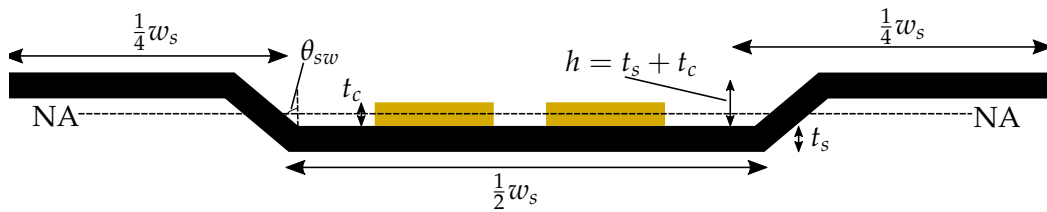


FIGURE 4.13: Grooved SThM Cross-Section Diagram with Angled Side-Wall

Overall, a good theoretical appreciation of the influences to the NA location in grooved cross-sections was obtained. This varied from the simplified straight side-walled with a single coating, to the more accurate and complex angled wide-wall with multi-coatings. These propose an increase in groove depth to the current grooved SThM cantilevers and demonstrate that the widths of the SiNx were not equal. In

addition, unequal widths can actually be utilised to shift the NA position which can be mathematically determined. Furthermore, the theoretical calculation of the second moment's of area suggest that the stiffening effect from the grooved cross-section could be a significant contributor to the change in thermal bending seen in the original paper. However, this needs further modelling and experimentation of thermal bending beyond this mechanical analysis to verify this hypothesis. Exploration of this is described below.

4.1.3.3 Thermal Bend Modelling

With the mechanical behaviour well understood, the next step was to determine how temperature change induced bending, rotation and deflection in SThM cantilevers when OC. Again, flat SThM cantilevers were first examined.

Flat Cantilevers

To analyse flat SThM cantilevers, the first port of call was to explore the mathematical relation pertaining to thermal bending for a simple, prismatic cantilever. Analysing Equation 3.3 shown in the Research Method, it can be seen that not only each material's CTE determines the extent of curvature (single order relation), but the Young's Modulus has a significant second order impact. These both are directly related to vertical deflection based upon the Euler-Bernoulli relation developed in Equation 3.9. Regarding the Young's Modulus, it represents each material's stiffness and so the stiffer the material, the greater the ability to impart its behaviour. Therefore, a material with high CTE, but low Young's Modulus may result in a lower bending moment and deflection than a material with a lower CTE, but greater Young's Modulus. The exact extent of this for flat SThM cantilevers shall be elucidated later. However, before exploring this, the next major material property is the Poisson's Ratio (inversely proportional) which plays a significant role if the Biaxial Modulus is employed. It has been determined to not be applicable for an EF, however, for thermal bending it may be significant due to the cantilever's tapered shape. The effect of the Biaxial Modulus depends on the geometry of each material alongside their respective Poisson's Ratio values. In addition, the impact of the geometry can be rudimentarily determined from Equations 3.1, 3.2, 3.3, 3.9 for vertical deflection. These are listed thusly:

Temperature Change - Directly Proportional: $\delta = mT$

Cantilever Length - 2nd Order Polynomial Increase: $\delta = aL^2 + bL + c$

Width - 2nd Order Polynomial Increase: $\delta = aw^2 + bw + c$

Thickness - 3rd Order Polynomial Decrease: $\delta = at^3 + bt^2 + ct + d$

The notable differences between the above and that for an EF are that length has a single lower order relation while width has a greater one. However, thickness has a similarly pronounced 3rd order polynomial relation. Hence, thickness of each material appears to have the most impact on thermal bending followed by width and length. However, to better analyse thermal bending for SThM cantilevers, a more advanced analysis utilising the developed models was required. Initially, the FDM model was utilised to provide a theoretical appreciation of thermal bending. However, as stipulated in the Research Method, there are multiple assumptions and/or options before settling on a final model. The first of these was the use of the Effective Modulus for the substrate when covered in a relatively thick coating(s). As the ratio of Au-to-SiNx in SThM cantilevers exceed that in the paper's cantilever the work was originally based upon [86], it should be utilised. However, to ensure this is sound, it should be compared to FEA as this will highlight whether the assumptions made for the Effective Modulus are sensible. Alongside this, the use of the Biaxial Modulus instead of the materials Young's Modulus needs to be determined. This should be employed if thermal bending manifests in a manner similar to a plate structure. Again, this was best verified through comparison to FEA with its full 3D modelling. In addition, both the FDM and FEA outputs are compared to experimental results for a comprehensive validation in the subsequent chapter. Before this, a table for the various model results was collated for flat SThM cantilevers. This can be seen in Table 4.5, whereby no NiCr was included in the models due to its 5 nm thickness causing mesh generation issues in FEA's 3D model (as previously highlighted).

In Table 4.5, it is clear that both the Effective Modulus and Biaxial Modulus increase thermally induced deflection. The modulus that is in closest alignment to FEA is the Effective Modulus (based on Equation 3.6) and the Young's Modulus. The theoretical structure for this being one with a thick coating and beam like behaviour. As the

TABLE 4.5: SThM Model Comparison for Uniform Temperature Thermal Bending

Model	Substrate Effective Modulus	All Materials Modulus	Theoretical Structure	Vertical Deflection of Tip ($\mu\text{m}/\text{K}$)
FDM	None	E	Thin-Beam	0.114
	None	$E_{Biaxial}$	Thin-Plate	0.141
	Eq. 3.6	E	Thick-Beam	0.163
	Eq. 3.6	$E_{Biaxial}$	Thick-Plate	0.183
FEA	NA	NA	NA	0.155
Percentage Difference	None	E		-26.5 %
	None	$E_{Biaxial}$		-9.0 %
	Yes	E		+5.2 %
	Yes	$E_{Biaxial}$		+18.1 %

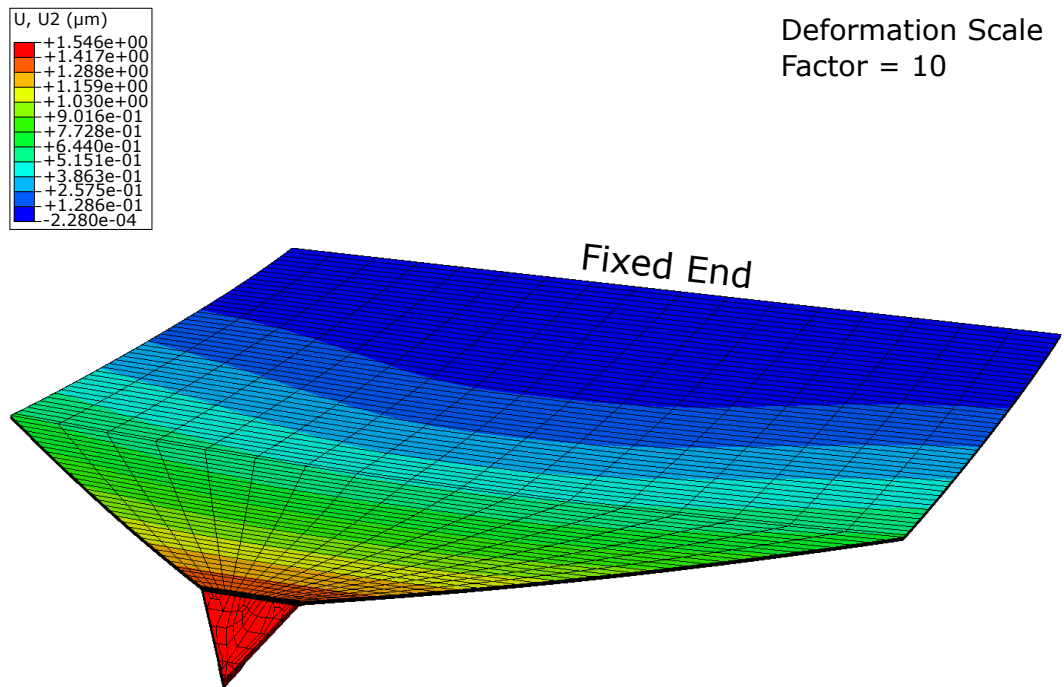


FIGURE 4.14: FEA - Flat SThM Cantilever 10 K Uniform Thermal Bending OC

SThM's SiNx-to-Au ratio exceeds that for its application L. Yi et al.'s paper [86], then the former seems logical. However, the results are not in exact alignment. This could

be due to the Effective Modulus's simplifications potentially not being completely accurate, possibly due to the hybrid nature of thermal bending in SThM cantilevers. This is because, as seen in Fig. 4.14, up to the tapered section the deflection is notably greater towards the edges than the centre (i.e. synclastic curvature like a plate). However, for the tapered section, the difference reduces with width causing the cantilever to be more beam like and the final tip deflection like a beam's. We can analyse the extent of the plate-like behaviour up-to the taper by comparing the centre and edge deflection outputs in the FEA model to the FDM's Young's Modulus and Biaxial Modulus deflections 90 μm along the cantilever. The values for which can be seen in Table 4.6 where the centre and edge positions in FEA show similar magnitudes to the Young's and Biaxial Modulus respectively. Therefore, it is clear that up until the taper

TABLE 4.6: Flat SThM Models Lateral Position Comparison for Uniform Temperature Thermal Bending 90 μm Along Cantilever

Model	Position/Modulus	Vertical Deflection at 90 μm Along ($\mu\text{m}/\text{K}$)
FDM	E	0.055
	$E_{Biaxial}$	0.062
FEA	Centre	0.050
	Edge	0.067

occurs, thermal bending for SThM cantilevers manifests like that of a plate structure to some degree. However, with the tapered section, this funnels the deflection across the whole width towards the centre up to the tip and acts more like a conventional beam. As a result, the cantilever is perhaps best described as a beam-plate hybrid structure. Although, in regards to tip deflection, assuming the whole cantilever is a beam produces a more accurate tip quantification than a plate. Therefore, without producing a theoretically convoluted structure where plate and beam assumptions are applied at different sections, the Thick-Beam one was decided as the prevailing approach in the FDM model. Furthermore, clearly stating this assumption and its uniform application provides a simpler understanding and interpretation of its results. The respective FDM tip deflection due to temperature change was henceforth deduced alongside the respective deflection and rotation profiles in Fig. 4.15 & 4.16, where NiCr (5 nm) was

included for the most accurate possible quantification.

FDM - SThM Uniform Temperature Thermal Bend Results

Vertical Deflection of Tip = $0.166 \mu\text{m}/\text{K}$

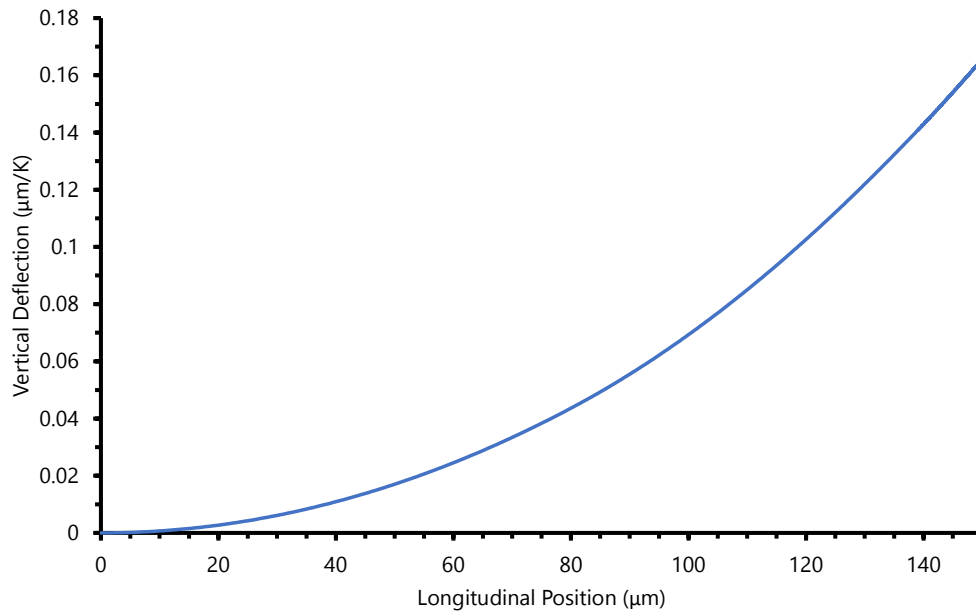


FIGURE 4.15: FDM - Flat SThM Uniform Temperature Thermal Bend Vertical Deflection Profile

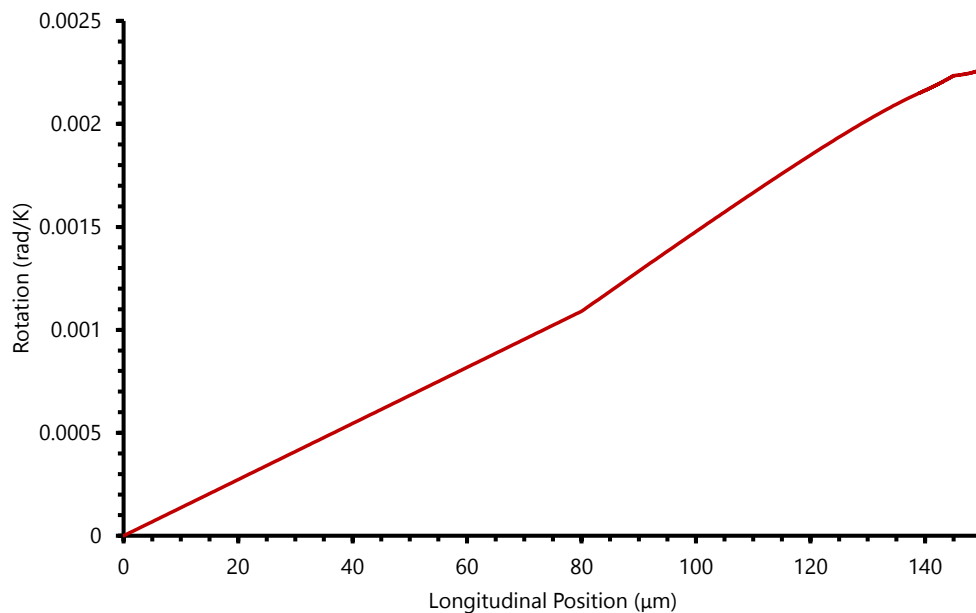


FIGURE 4.16: FDM - Flat SThM Uniform Temperature Thermal Bend Rotation Profile

Analysing Fig. 4.15 & 4.16, a similar general shape to that from an EF was produced. However, the vertical displacement and rotation increase by a greater degree further along the cantilever relative to an EF. Moreover, with even one Kelvin of temperature change, a significant tip deflection of $0.166 \mu\text{m}/\text{K}$ at the tip was produced. This highlights the pronounced influence temperature change has on SThM cantilevers. Therefore, with these profiles and magnitudes established, the final theoretical component that was desired to be explored was the interpretation of thermal bending in an AFM. This was possible by utilising the theoretical InvOLS deduced for an EF. The InvOLS values were extracted and multiplied by the thermal bend induced rotations along the cantilever length with the subsequent profile shown in Fig. 4.17. From this, it is very apparent that the previously noted difference in rotation between

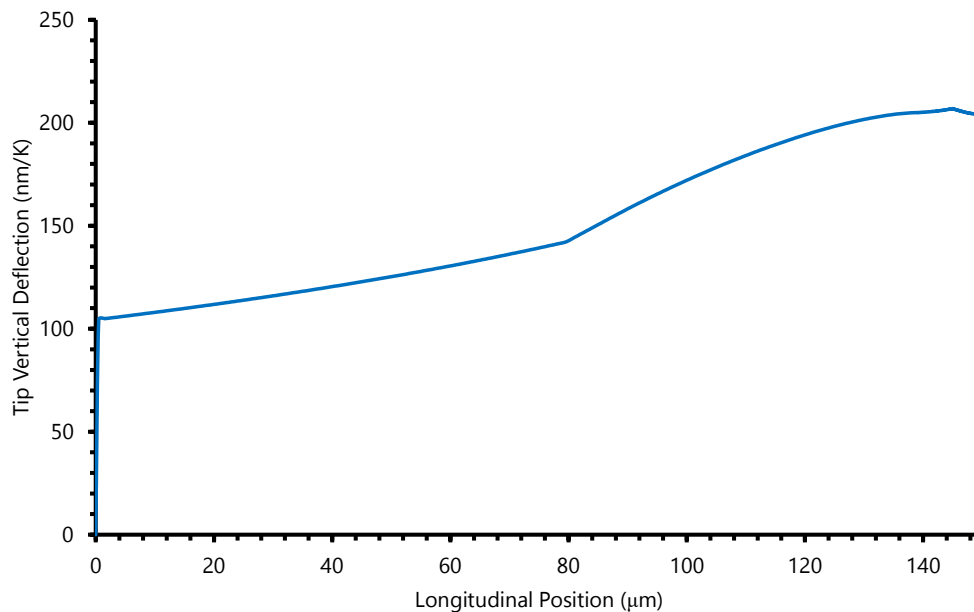


FIGURE 4.17: *FDM - Flat SThM Theoretical AFM Interpretation of Uniform Temperature Thermal Bend*

an EF and thermal bending does produce a different interpretation by the AFM's optical lever system. For an EF, this profile would be constant and a flat line that corresponds to its tip deflection is outputted (e.g. $0.598 \mu\text{m}/100 \text{ nN}$ EF). However, as the rotation due to thermal bending varies significantly along the cantilever length when compared to that from an EF, a variable interpretation is produced. Therefore, the laser position will not only dictate the InvOLS, but the resultant tip deflection measurement for thermal bending in an AFM. Moreover, AFM's interpretation is mostly incorrect. In the above case the actual tip deflection due to thermal bending is $0.166 \mu\text{m}/\text{K}$ which

is only measured when the laser is positioned $95.5 \mu\text{m}$ along the cantilever. Hence, the AFM's optical lever system produces a variable and erroneous measurement of thermal bending for flat SThM cantilevers which heightens the complexity of the problem. If the above is the case experimentally alongside for other bi-material AFM cantilevers, then it could have profound influence in the understanding of thermal bending, drift and designing solutions.

Before acting on the above conclusion experimentally, one final OC thermal bending situation was studied theoretically. This was SThM's unique ability for self-heating. A theoretical appreciation of this was desirable to help understand SThM's active application in scanning alongside its use as an initial heat source for investigating IC thermal bending later discussed in Chapter 5. To achieve this, a thermal-resistance model previously developed within the academic group by R. Lambert [141] was employed. This simulates various electrical and thermal characteristics of SThM cantilevers, allowing it to determine spatial-temperature change due to electrical current through its wires and sensor. The subsequent spatial-temperature array could then be utilised in the FDM model to determine the resultant thermal bend induced deflection (as long as the meshes of the two aligned). This was performed with the temperature profiles due to 0-1.5 mA of current graphed in Fig. 4.18 alongside each one's respective average Pd sensor temperature change. The subsequent thermal bend induced deflection profiles according to the FDM model was generated and outputted in Fig. 4.19 with a tip deflection up-to $1.239 \mu\text{m}$. These tip deflections translate to a consistent $0.017 \mu\text{m}/\text{K}$ when temperature change is based upon that of the Pd sensor's average. This is around a tenth of the $0.166 \mu\text{m}/\text{K}$ generated from a uniform temperature change. This is understandable as the cantilever length not covered by the Pd (i.e. up to $145 \mu\text{m}$ along the cantilever) experiences a lower temperature change and so a lower magnitude of vertical deflection that is related to this pronounced decaying towards the base. Before moving on, it can be seen that both the temperature and tip deflection has a non-linear relation with current. This is due to current's squared relation to the fixed electrical resistance according to the combination of Joule's and Ohm's Law ($P = I^2R$) with power being linear with temperature change (due to power being linear with heat energy and so temperature change). This means that power at any given point along the cantilever is linear with vertical deflection. Therefore, through

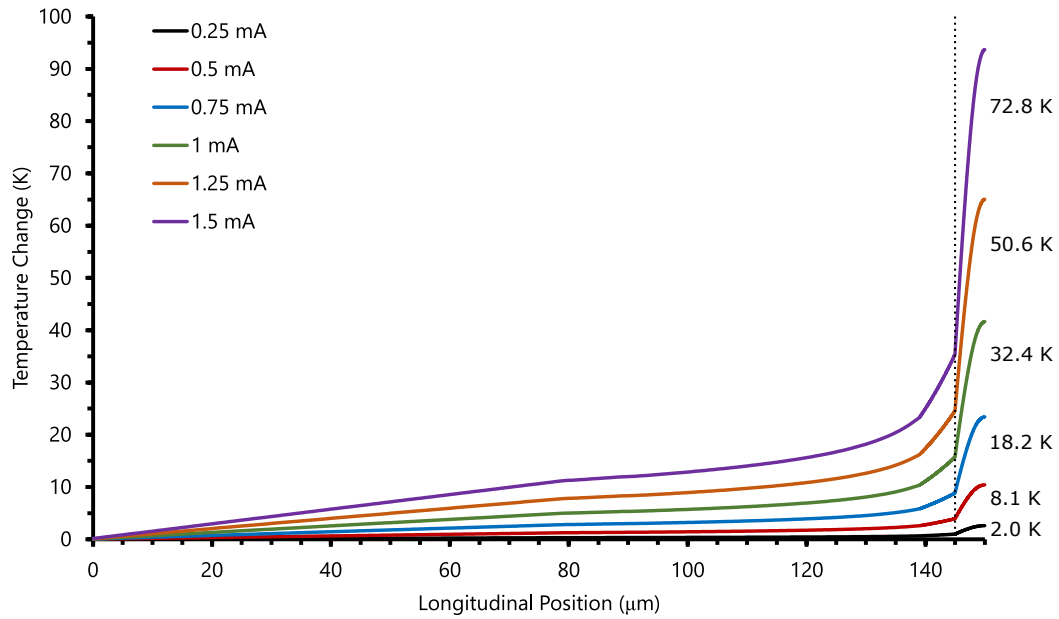


FIGURE 4.18: Flat SThM Cantilever's Self-Heating Temperature Distributions With Average Tip Sensor Temperature Change

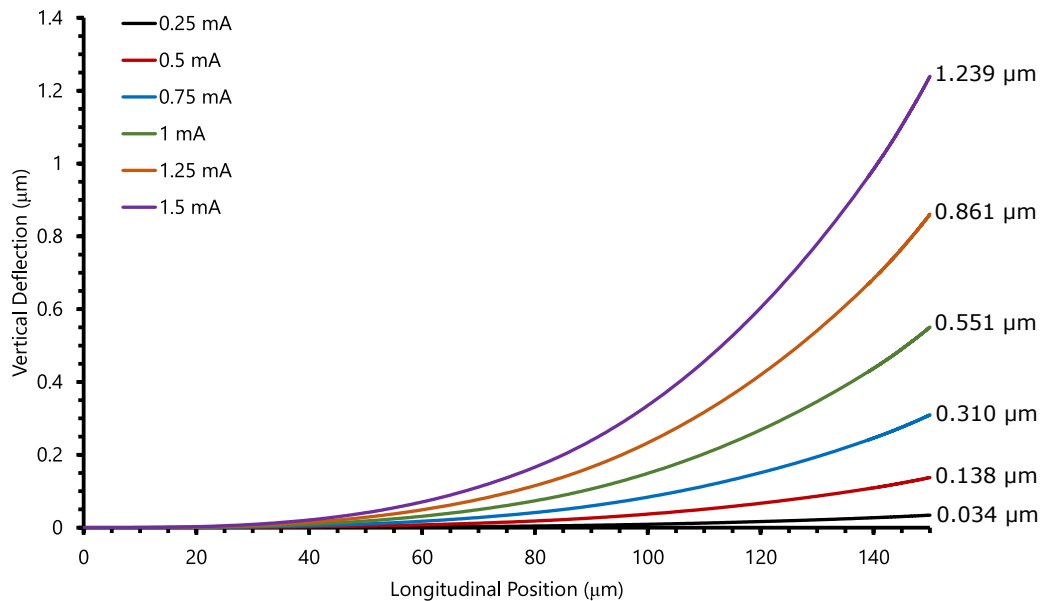


FIGURE 4.19: Flat SThM Cantilever's Self-Heating Vertical Deflection Profiles With Tip Deflection

simple determination of SThM cantilever's total electrical resistance, power can be calculated and a constant gradient linking it with temperature and deflection. According to R. Lambert's model, a flat SThM probe is nominally 86.52Ω . As a result, averaging across the Pd tip sensor a $0.374 \text{ K}/\mu\text{W}$ self-heating relation was generated. This translates to a tip deflection of $6.4 \text{ nm}/\mu\text{W}$. However, these relations do not account for heat loss to the ambient environment or to the sample. These can be appreciated within the

thermal-resistance model, but if it is assumed that this heat loss is uniform with area then contrasting deflection per tip temperature change should theoretically not be influenced by this and comparable to experimental results. This is due to the tip temperature measurement effectively providing an accurate adjustment to any mis-match in the resistance and power to it between the model and a real-world probe. Contrasting any electrical property (current, power, voltage) with the subsequent temperature or deflection may not be comparable between models and experiments unless in a vacuum. Now with a sound theoretical appreciation of the OC thermal bending situations relevant to flat SThM cantilever's, the next step was to explore this in grooved SThM cantilevers.

Grooved Cantilevers

Following on from the mechanical analysis and modelling of grooved cantilevers in Section 4.1.3.2, the first step was to produce the relevant thermal bend equations in the FDM model. As this model is 1D and assumes no impact from lateral position of the materials, it can be imagined that the model realises each material in a stacked fashion directly on top of each other. Hence, theoretically, the FDM model will regard it like a sandwich structure and should simply output results for this structure as opposed to the open nature of the grooved design. However, to verify this, the previously derived thermal bend Equations of 3.1, 3.2 and 3.3 were employed by segmenting the cross-section and regarding them as separate layers. How this was sectioned up can be seen visually in Fig. 4.20, whereby L is short for layer.

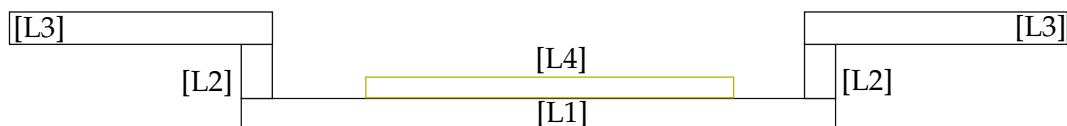


FIGURE 4.20: Grooved Cantilever Cross-Section Layer Separation Diagram

With this sectioning, the question of whether the groove's structural compensation theory aligns with the 1D approach can be answered alongside whether the newly deduced groove depth is correct or not. This was analysed by inspecting the initial $75\ \mu\text{m}$ long section in grooved cantilevers as the grooved cross-section is constant (prismatic) during this length of the cantilever and so no other changes in geometry can influence

the analysis. The previously determined groove depth of 503 nm in the mechanical analysis was chosen along with the typical width and thickness as this theoretically should output zero thermal bend induced deflection. For this, a value of -3.3×10^{-9} nm/K was determined which is effectively zero. When this is contrasted with a normal, flat SThM cantilever, a deflection of 37.7 nm/K $75 \mu\text{m}$ along the cantilever was produced. This clearly demonstrates that the 1D model validates the structural compensation theory. Moreover, it agrees with the conclusion that the groove depth derived by Y. Zhang et al [114] was incorrect with it requiring to be deeper. However, whether or not the FDM Model's 1D simplification for such a complex cross-section is applicable need to be verified through FEA. Similar to that used for flat cantilever, a deformable 3D solid model with hexagonal, structured elements of a quadratic geometric order, hybrid formulation and reduced integration with 12 and 4 elements across the SiNx and Au thicknesses respectively was employed. This means that the results will be comparable to that of the flat cantilever models alongside bringing confidence that no simplification will generate inaccuracies in the results. The same dimensions as the FDM model were utilised and the overall FEA output seen in Fig. 4.21 for a 10 K uniform temperature change. This generated central and edge deflections of 10.8 nm/K and 23.0 nm/K respectively.

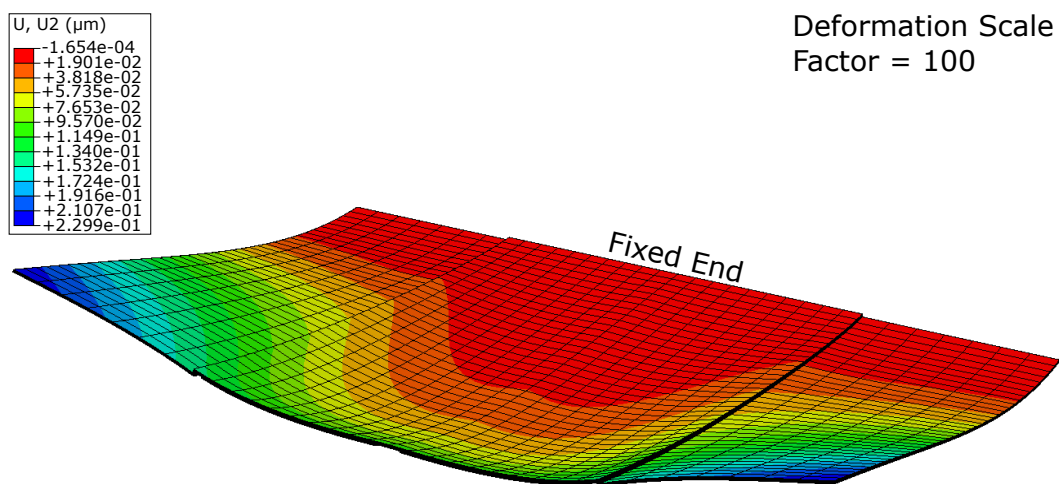


FIGURE 4.21: FEA: Theoretically Ideal $75 \mu\text{m}$ Long Groove Cantilever Undergoing 10 K Uniform Thermal Bending

As it can be seen from Fig. 4.21, significant thermal induced deflection still was produced, especially near the edges of the cross-section. This contradicts the result from the FDM model and the concept the design was motivated by. This suggests that

the lateral positioning of the SiNx does affect the ability for it to balance and produce a NA position half-way through the thickness of the Au. Therefore, the question is why is this not the case. One hypothesis could be that because of the variable height and positioning of the SiNx in the cross-section, the structure is not as laterally stiff and even. Hence, the SiNx in the groove and raised on the sides are not equal in their influence mechanically in the cross-section. One method to test whether this was the case was to vary the cantilever length. The longer the cantilever, the more 'beam' and 'strip' like it would become, resulting in less relative lateral variation across the width to the longitudinal deflection behaviour. A preliminary study was executed that explored this by modelling 75 μm and 600 μm long grooved cantilevers. Initially, the previously determined 503 nm groove depth was employed with the results shown in Table 4.7. With

TABLE 4.7: *Groove Depth vs. Cantilever Length Preliminary Study*

Groove Depth (nm)	Cantilever Length (μm)	Deflection (nm/K)	
		Central	Edge
503	75	10.8	23.0
	600	24.4	57.0
525	75	10.4	22.9
	600	4.3	37.0
550	75	9.7	21.7
	600	-15.3	17.6

the octuple increase in length, both the central and edge deflections doubled. This initially highlights that the theoretically derived groove depth did not produce the desired complete attenuation effect for both lengths. However, with length's squared relationship to thermally induced deflection, this is $\frac{1}{32}$ to what would be expected. This implies that perhaps the groove is having an effect with either it having a limited impact or its depth not being great enough. The latter was explored, whereby 525 nm and 550 nm groove depths were chosen with the deflection outputted for 75 μm and 600 μm long cantilever's shown in Table 4.7. From this, it is clear that the groove depth eventually has an effect as a change in direction of the central deflection occurred for the 550 nm deep groove. Therefore, length does seem to have a clear influence on the ability for the groove to take effect. Moreover, a greater groove depth to that theoretically determined produces the same effect. The most probable influence being the

materials Poisson's Ratios. This was deduced when each material's Poisson's Ratio was removed and the theoretically derived groove depth (503 nm) generated central deflections that plateaued at $6.2 \mu\text{m}$ from $300 \mu\text{m}$ and longer cantilevers. Therefore, contrasting this with that shown for the same groove depth in Table 4.7, it is clear that Poisson Ratio's impact increases the required groove depth and perhaps the length for it to take full effect.

As a result of the above preliminary work, a study incrementally determining the impact of a single groove depth with length was required to deduce the point at which it does start to have a significant effect with fully defined materials. As a groove depth of 525 nm produced the closest convergence to zero central deflection with its $600 \mu\text{m}$ long cantilever, it was chosen for this study as this would be ideally aimed to attenuate thermal bending. The results of which can be seen in Table 4.8 below alongside Fig. 4.22 depicting the vertical deflection outputs for the shortest ($75 \mu\text{m}$) and longest ($600 \mu\text{m}$) sections along with their respective spring constants.

TABLE 4.8: Grooved Cantilever Length Study

Cantilever Length (μm)	k (N/m)	End Deflection (nm/K)		
		Central	Edge	Δ
75	3.27	10.4	22.9	12.5
150	0.64	8.8	40.0	31.2
225	0.20	9.0	42.1	33.1
300	0.09	9.2	42.1	32.9
375	0.05	8.9	41.7	32.8
450	0.03	7.9	40.7	32.8
525	0.02	6.4	39.1	32.7
600	0.01	4.3	37.0	32.7

Analysing the results seen in the table, both the central and edge deflections begin to reduce in magnitude from $300 \mu\text{m}$ (5:2 length to width ratio) and longer. Therefore, this appears to be the length at which the grooved cross-section generates a pronounced effect. Moreover, the difference between the central and edge deflections plateaus from $300 \mu\text{m}$ and longer. This suggests that the grooved design has reached its maximum ability to impart itself by remaining relatively constant, whereby greater

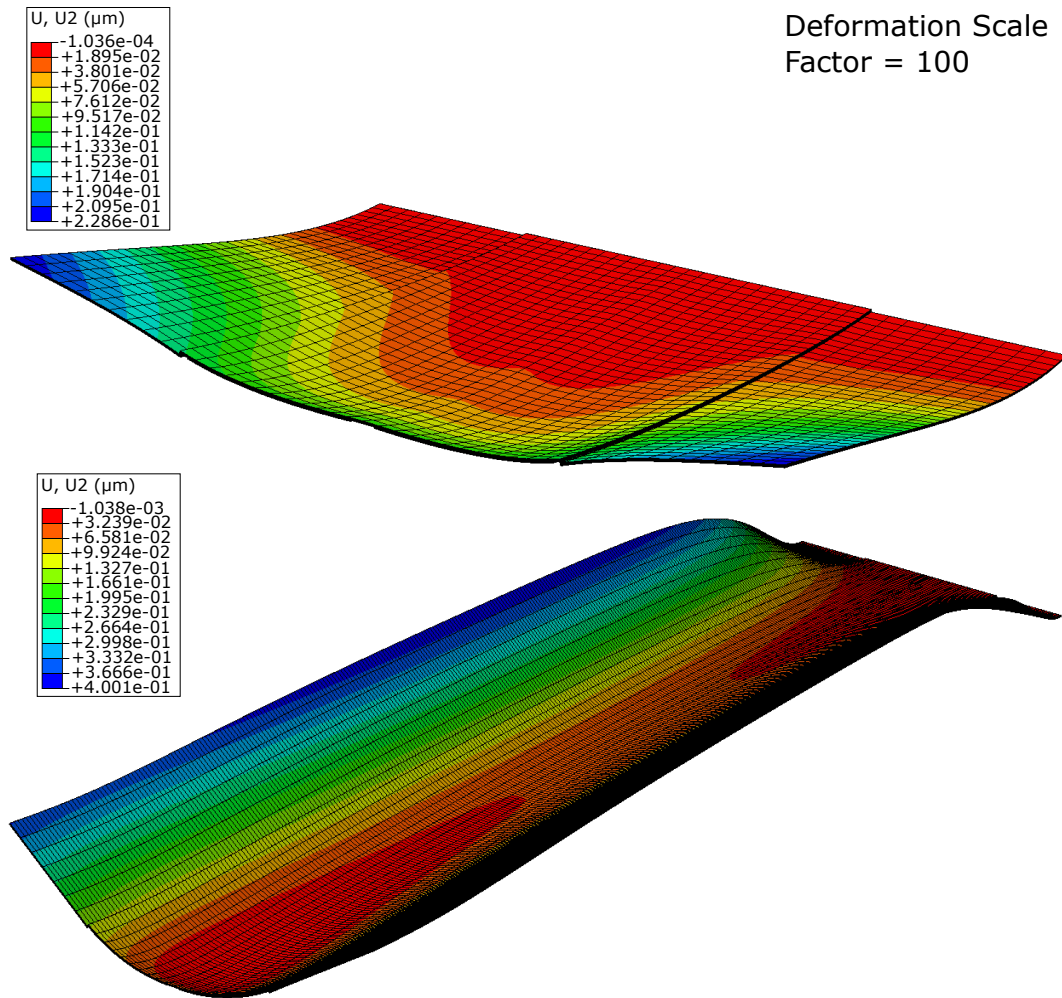


FIGURE 4.22: Grooved Cantilever FEA Model Length Study: 75 μm & 600 μm Long 10 K Temperature Change

length enables a greater opportunity to change the end deflection magnitude. Alongside the end deflections, a change in the deflection profiles occurred with increased cantilever length. This can be seen from the centre-line profiles for each cantilever as seen in Fig. 4.23. These all follow a common profile with the longer cantilevers able to have greater opportunity for the groove cross-section to take effect. If profiles like that seen in Fig. 4.23 are taken along the edge, a different but similarly consistent set of deflection profiles is seen with it being more positive (up to the magnitude shown in Table 4.8). However, this general lateral variation with length will not be uniform for all groove depths as significantly shallow or deep grooves will have far reduced or greater impact. Alongside all of the above, current grooved SThM cantilevers have a taper from 90 μm along to produce a fine tip. As highlighted previously, it was hypothesised that this can act as a funnel for deflections across the widths. Therefore,

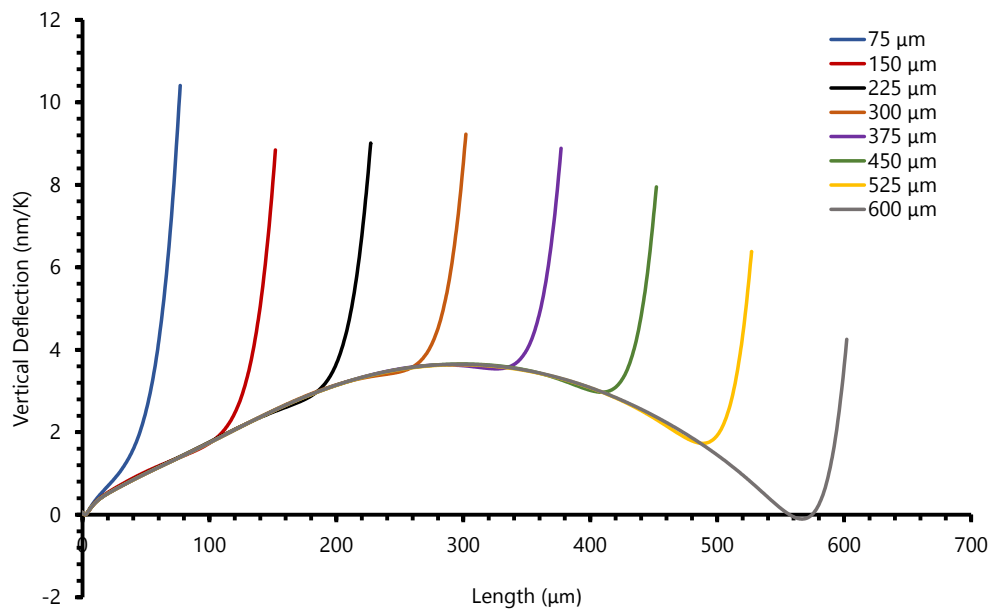


FIGURE 4.23: *Grooved Cantilever Length Study - Centreline Deflection Profiles*

the deflections measured at the edges would contribute to the final tip deflection and as they are greater in magnitude, would generate greater deflection of the tip.

With the above conclusions, currently fabricated grooved SThM cantilevers are 150 μm long with a grooved cross-section only spanning 120 μm along it. Therefore, the current design is too short with a length-to-width ratio of 1:1 that is too low for the effect to come to fruition coupled with the groove also being too shallow. If the latter was increased, the groove would likely need to span as much of the cantilever length as possible with the maximum possible of 139 μm for the current length due to the tip beginning from this position onward. With a groove depth around 525 nm, the above modelling suggests that SThM cantilever would be required to be at least double the length for even the effect to start to reduce vertical deflection. However, as seen with the spring constant determination, this would render significantly reduced stiffness (due to lengths cubic polynomial impact) that could make them unusable for users and applications in contact mode. Conversely, this would result in greater deflection per tip force and so less interpreted tip force per thermal bend induced deflection. Although, an increased length would result in longer Au wires and hence increasing its contribution to the probes overall electrical resistance and impede its thermal measurement (through reduced resistance ratio of tip sensor-to-wire). Alongside these

negatives, the fabrication of longer cantilevers would be a notable challenge and require many changes to the current process sheet. It would involve significant changes to the many lithography steps employed (EBL and Photolithography) and tweaking of other steps such as wet-etching of the pyramid's for the tips.

However, an alternative to increasing the cantilever length could be through simply increasing the groove depth as FEA suggests this may reduce the required length until a change in deflection will occur and the groove to take effect. Although, the free-end of the cantilever notably deflects upward regardless along with it varying significantly across its width for all groove depths modelled (up-to $1\ \mu\text{m}$ explored in this project). Therefore, increasing the groove depth does not prevent the need for a significant length for the groove's effect to span over most of the cantilever or the variation seen across its width. The latter could potentially be worse with the stiffening causing greater interpreted force to rotation in an AFM optical lever system coupled with the groove depth causing even greater difference between the groove and edge sections. With all this said, changing the groove depth would be relatively trivial from a fabrication perspective as it would only require an increase in etch depth.

An additional alternative to increasing the cantilever length or groove depth could be to reduce the cantilever width. This would impact the stiffness less as width has a single order impact on stiffness, but this would present other problems. These would require both the groove and the edge sections of the cross-section to be reduced significantly resulting in limits on the Au wire width. For example, to produce the equivalent 5:2 ratio stated in the above study for a $150\ \mu\text{m}$ long groove, the total width would need to be reduced to $60\ \mu\text{m}$ resulting in a groove less than $30\ \mu\text{m}$ wide and wires less than $15\ \mu\text{m}$ wide (almost half what they are currently). This would increase the effects of Joule heating (and so the effects from thermal bending during active SThM operation) and effect thermal measurement. Moreover, it would require a significant change in a number of EBL and Photolithography and subsequent processes. However, even with all the above challenges and drawbacks it would be possible to produce grooved SThM cantilever with either increased length, groove depth or reduced width. Although, the final design would still be unideal with notable thermal bending occurring even at $300\ \mu\text{m}$ long cantilevers and significant lateral variation in

deflection that would generate notable horizontal voltage change on the AFM photodetector with temperature change.

One final point regarding grooved cantilevers is the robustness of the structural compensation concept it is based upon. The effect is dependent on the aerial definition of the etch that produces the groove, SiNx and Au thickness and the etched groove depth itself. The former is dependent on Photolithography which is reliable at the resolution for the SThM aerial dimensions (10s of microns). However, the latter components of thickness and depth have significant uncertainty. The SiNx is known to vary between wafers and even on the same wafer, with one example exhibiting a 35.4 nm range in thickness. The metal thickness is typically more consistent, whereby the Plassys II tool utilised for the Au deposition in the JWNC employs an accurate quartz crystal for thickness monitoring and is regularly checked and monitored for consistency. Therefore, it is less prone to variation. The groove depth on the other hand has the potential for reasonable variation due to the lack of real-time depth measurement during dry etch and only previous experimental time vs etch depths being employed. Alongside this, any degree of variation in the etch rate across the wafer could produce a notable change in groove depth. Hence, it appears highly unlikely that the exact groove depth for a precise material thickness will be possible. If this is coupled with some alternative requiring a gross amount of change of the SThM design required for the structural compensation effect to even occur alongside it still demonstrating notable vertical deflection, it appears an unideal solution overall. With the above comprehensive theoretical analysis of SThM cantilevers when OC for both the mechanical and thermal components, the next natural step was to explore the more complex scenario when the cantilevers are IC.

4.1.4 In-Contact

A similar process to OC was performed for IC, whereby the BCs for mechanical and thermal aspects first needed to be established.

4.1.4.1 Boundary Conditions

Mechanical

The mechanical situation is far more complex for SThM and AFM cantilevers in general when IC regarding their degrees of freedom (DOF). Similar to OC, the base is fixed, but the tip that interacts with the surface will experience an array of forces. The extent of this is dependent on the shape and material of the tip and surface alongside their relative position to one another to produce the resultant forces. In this analysis, the feedback of the AFM will be mostly ignored to establish the mechanical situation prior to it responding. This enables a firm understanding of the initial mechanical situation and deflection prior to it intervening.

Regarding SThM cantilevers, the tip has a radius of curvature nominally 50 nm with the Pd tip resistor making the immediate contact with the surface. The type of surface potentially ranging from polished Si to sticky biological samples. Hence, these can produce almost entirely different DOFs at the tip from their topography and adhesion properties. However, there is some common ground and the best method of elucidating this was to separately explore each of the six DOFs that dictate the mechanical BC. These were broken down into the two types: translation (vertical, lateral and longitudinal) and rotation (pitching, rolling and yawing). These are visualised in Fig. 4.24 for a flat SThM cantilever tip.

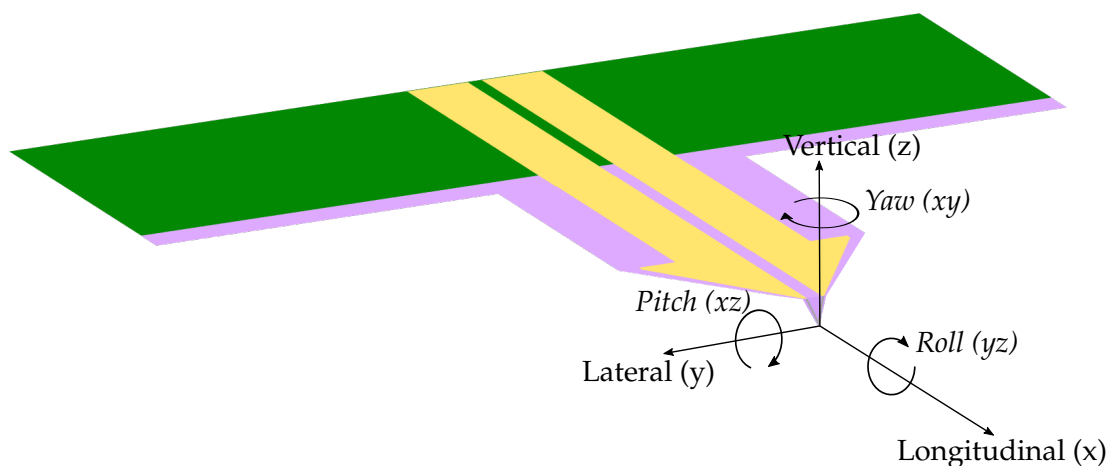


FIGURE 4.24: SThM Cantilever Tip DOF Diagram

Translation

Vertical (δ_z): The best method to understand the vertical direction is to look at how AFM's displacement through its piezoactuator influences the force and interaction of the tip with the sample surface. If it is assumed the sample is significantly stiffer than the cantilever, then when a piezoactuator drives the cantilever into the surface, an equal and opposite force will be applied to the tip. This equal and opposite surface force is shown in the linear contact region of a F-d curve, like that shown in Figure 4.25 for a flat SThM cantilever making contact with polished Si. Therefore, under this assumption of a relatively stiff sample, when a cantilever tip is driving into a surface no vertical displacement occurs in the sample or tip until the forces exceeds the elastic limits of either. When the piezoactuator moves the cantilever away from the surface while IC, the tip is fixed (as the linear portion remains consistent in the F-d graphs) until the drive-in and adhesion force is overcome. Hence, the tip is essentially fixed vertically with either downward forces exceeding the elastic limits of the tip/sample (typically beyond the photodetector force range) or upward forces overcoming the drive-in and adhesion forces. For example, multiple Voltage-distance curves (including the one in Fig. 4.25) were generated for a flat SThM against a polished Si surface that displayed an adhesion force that translated to 1.578 ± 0.015 V vertically on the photodetector. Based upon the cantilever's determined InvOLS, this equals to a tip displacement of 149 ± 3 nm. What tip-force this represents depends on its spring constant. Applying the nominal magnitude stated by some SThM distributors of 0.3 N/m [196], this suggests an adhesion force of 44.8 ± 0.8 nN. However, if the cantilever is driven beyond the initial contact point, the required force will be greater with 5 V being the equivalent of 141.8 nN in this case. In the opposite direction, if the elastic limits are exceeded for either the cantilever tip or sample surface then tip displacement will occur. For polished Si this was beyond the photodetector limits (i.e. greater than 10 V or 283.6 nN as most SThM cantilever's are engaged near the zero vertical voltage photodetector position). As a result, these forces have to be overcome for notable vertical displacement of the tip, with an excess of adhesion forces resulting in loss of contact.

With these tip force magnitudes for vertical tip displacement, it was desired to relate this to temperature induced thermal bending due to these mechanical BC's being investigated for their impact on it. For this, the temperature-to-tip-force relation was

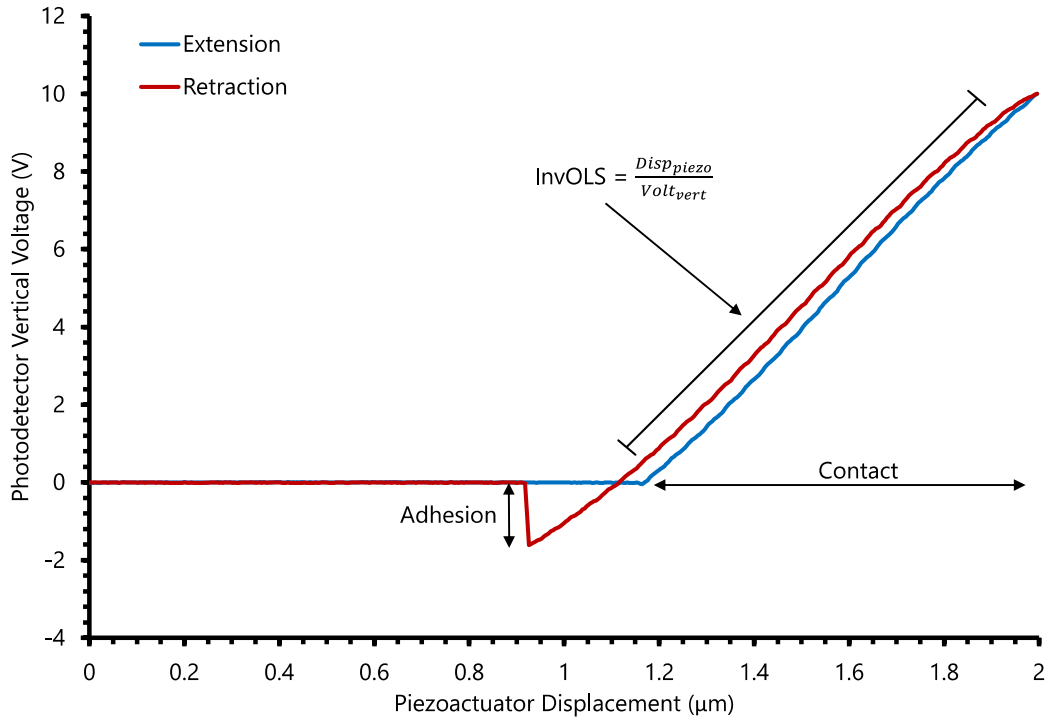


FIGURE 4.25: Flat SThM Voltage-distance Curve on Polished Silicon

required as this would be crucial in establishing their relative influences. For example, if a very low temperature change overcomes the adhesion tip forces stated above, then thermal bending for a cantilever when IC and bending away from contact may be best modelled without any vertical tip constraint. As a result to obtain a gauge, the tip vertical deflection for OC thermal bending from the FDM model can be employed with the following calculation:

$$k_{nominal} = 0.3 \text{ N/m}$$

$$\delta_{z,tip,Th.B.} = 0.166 \text{ } \mu\text{m/K}$$

$$\therefore \quad (4.3)$$

$$\text{Equivalent Tip Force} = k_{nominal} \times \delta_{z,tip,Th.B.}$$

$$= 49.8 \text{ nN/K}$$

Hence, dividing the above 49.8 nN/K for any determined tip force produces the equivalent temperature change. For the previously determined 1.578 V (44.8 nN) and 5 V (141.8 nN) adhesive force, a temperature change of 0.9 K and 2.85 K would overcome them respectively. This is not insignificant and indicates that the vertical BC should

not be ignored for temperature induced deflection. What should additionally be mentioned is that algebraically this value is unaffected by the cantilever spring constant applied if the same stiffness is applied to both the EF and thermal bend deflections: $\frac{k\delta_{EF}}{k\delta_{Th.B.}} = \frac{\delta_{EF}}{\delta_{Th.B.}}$. Therefore, only the tip's vertical displacements for either impact the final magnitude. Whether or not the model employed here is sound will be experimentally verified later in the thesis, but at this stage it gives some indication of temperature's impact. In addition, it should be noted that most AFM cantilevers have their metal coating on-top, instead of the underside like in SThM. This means that temperature would have to decrease for the cantilever to overcome adhesion forces.

Going back to one of the initial assumptions that will not be the case for all samples, is it being relatively a lot stiffer than the AFM cantilever. This may not be plausible for biological sample. Hence, vertical displacement of the tip toward the sample may occur with lower tip forces resulting in displacement with resistance. Under this condition, the InvOLS and the resultant topographic measurement will be compromised to potentially produce a consistently erroneous measurement. Furthermore, in this scenario the vertical BC is complex where the author would model this as a viscoelastic type behaviour and best represented with a combination of springs and dashpots. Moreover in the opposite direction, adhesion forces may be greater when based upon biological samples greater tendency to be rougher, contaminate the tip and have more humid local atmospheric conditions increasing the water meniscus's effect. Therefore, greater force may be required to pull the cantilever tip away from the surface while less to indent it. As a result, the magnitudes for the polished Si surface should be taken specific to one of a relatively smooth, clean surface. This also still required significant force and temperature change to exceed the various fixations and so the vertical BC demonstrated should be applicable to most thermal bending models, but notable variations to the limits of this will occur across samples.

Before proceeding onto the next section, as has been stated earlier, this analysis is ignoring the feedback loop. However, when engaged the latter will keep the tip in contact with the surface. Although, as has already been theoretically explored, the AFM will not accurately respond to thermal bending due to the EF based InvOLS. As a result, adhesive and elastic limits will only be overcome if the difference in the interpreted tip deflection and force to the actual value is greater than these. For example,

using the above experimentally determined values, this difference would need to be the equivalent to 0.9 K and 2.85 K. In addition, the feedback loop does not have an instantaneous response and rapid thermalisation could cause temporary loss of contact.

Lateral (δ_y): The lateral DOF can be examined through exploration and analysis of lateral force microscopy in AFM. Within this, surface topography and the coefficient of friction are the main drivers of the forces and hence the DOF laterally. The coefficient of friction is dependent on the key factors of the normal tip force, lateral radius of curvature and local humidity (with many other factors relating to the sample and environmental conditions) [199]. Regarding topography, as these BCs are explored statically, if the tip is adjacent to a surface asperity then the forces experienced in the normal F-d curves will apply in providing attraction and repulsion. This will likely provide lateral fixation similar to that seen in the vertical axis. Hence, the lateral regime is potentially subject to the same behaviour seen in the vertical direction. However, if the sample is topographically flat, then an offsetting resistance from the tip-sample friction will occur. An example of this can be seen in the friction loop of a SThM cantilever as depicted in Fig. 4.26 with sketches of the respective cantilever movement. What can be seen, is that when static friction is exceeded (around 0.01° appears to induce this here), lateral displacement of the cantilever can occur with a resistance to motion continued from the kinetic friction. To obtain this rotation, the lateral voltage was converted into rotation using the 'Tilting a Reflective Surface Method' detailed by M. Munz [200]. This involved a mirror that was underneath the AFM head in a position similar to that of a cantilever. This aimed to mimic the reflection that an AFM cantilever would have for the laser in the optical lever system. Hence, when this mirror was rotated and the horizontal voltage change noted, the torsional sensitivity (s_θ) could be determined. Specifically, a chrome mirror was tilted using the actuation from the AFM's stage. This functioned by the mirror being the hypotenuse in a triangle and the stage's y-displacement changing the triangle's flat edge. A diagram depicting this can be seen embedded in Fig. 4.27. Vernier callipers were then used to measure the triangle's initial dimensions and the change in stage position permitted trigonometry to determine the change in tilt angle of the mirror. With all of this, a torsional sensitivity and standard deviation of $0.0178 \pm 0.00038^\circ/V$ respectively was

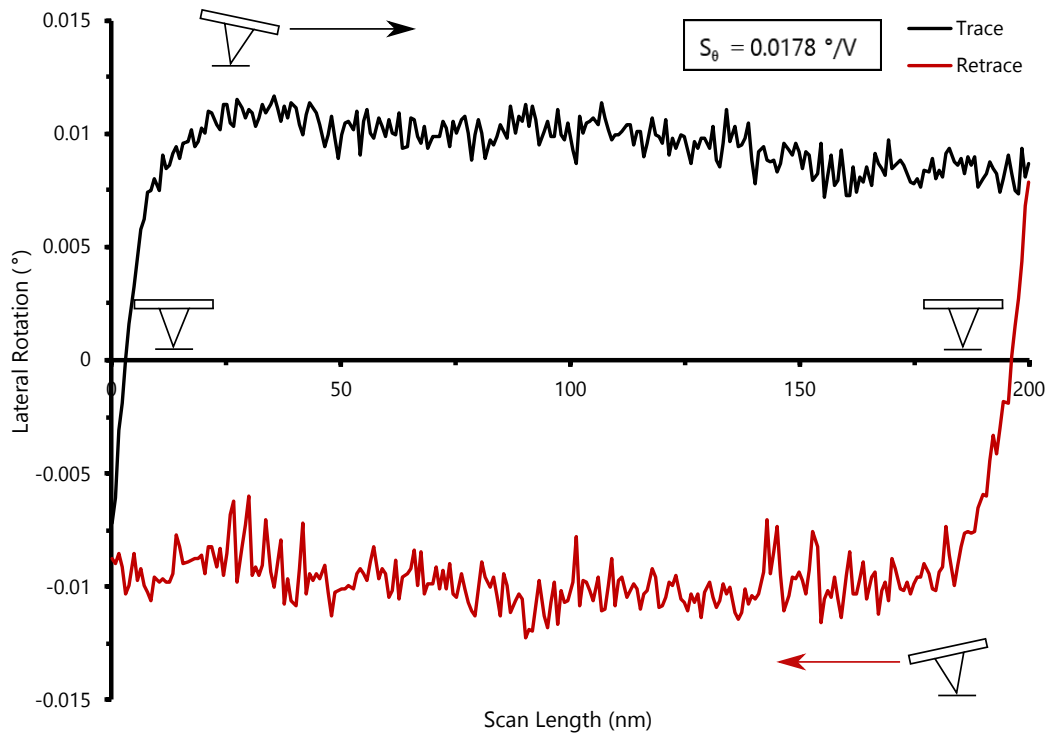


FIGURE 4.26: SThM Friction Loop on Polished Silicon Surface

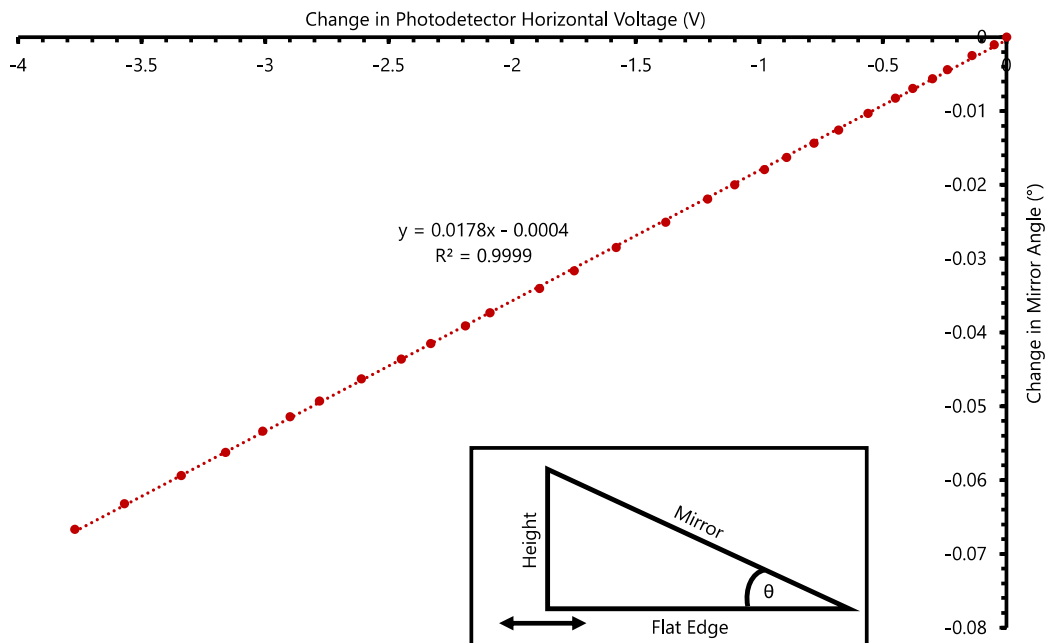


FIGURE 4.27: Tilting a Reflective Surface Method Experiment - Change in Horizontal Voltage vs Mirror's Angle

deduced as seen from the gradient in Fig. 4.27. This value is highly certain with very

low standard deviation and an R^2 value of 0.9999. However, for insight into the coefficient of friction and so its impact on lateral DOF, it was necessary to translate this into force. This could not be achieved experimentally, but the FEA cantilever model described previously was able to provide a theoretical value. Therefore, assuming the cantilever's torsional behaviour and its torsional spring constant (k_θ) were reasonably appreciated in this, a ratio between lateral rotation and lateral tip force could be deduced. This outputted a torsional spring constant of $5.356 \mu\text{N}/^\circ$ for the longitudinal laser spot location in the experiment of $112 \mu\text{m}$. With this established, multiple lateral scans, such as that seen in Fig. 4.26, were performed with exactly five different normal tip forces. This produced a coefficient of friction and standard deviation of 0.21 ± 0.13 for a polished Si surface, whereby the normal spring constant was employed from the same FEA model of the SThM cantilever for normal force determination. This meant that the absolute magnitudes of the torsional and normal springs constants are irrelevant. This is because both were applied in the calculation and so the main assumption is that the model's ratio between the two is representative of real-world SThM cantilevers. It should be noted that the standard deviation is significant; highlighting notable uncertainty in the accuracy of this value. However, as this exercise was to determine an estimation of a typical SThM lateral BC, it was still sound for the application. Therefore, for an applied normal force range of 0-100 nN, an expected 0-21 nN (± 1.3 -13 nN) of static friction will occur. If exceeded, then lateral displacement will be induced based upon the applied lateral tip force minus static friction with kinetic friction during motion.

Longitudinal (δ_x): Along this direction, the same forces and so influences as the lateral direction apply due to it being on the horizontal plane. As a result, it will experience the same DOF, except with potentially different coefficients of friction due to different tip curvature. If the curvature is greater, then the coefficient of friction experienced shall be greater and vice-versa. However, if assumed equal to the lateral, then the same magnitude of friction effecting the BC should be applied. Under this assumption, based upon the data previously describe and acquired, a similar range of normal tip force of 0-100 nN should equal 0-21 nN (± 1.3 -13 nN) of static friction. This will counteract any applied longitudinal force and once exceeded, longitudinal

displacement will occur. However, the stiffness longitudinally for the cantilever will be different to that laterally and so the force-displacement relation is dissimilar. In addition, it is worth noting that the cantilever does expand longitudinally by a notable degree when undergoing temperature change. This can be seen in FEA models, whereby a longitudinal displacement of 21 nm/K occurs at the tip. As a result, temperature change will induce a longitudinal force. Employing the 0-21 nN of static friction for a 0-100 nN normal force range and a similar calculation method previously demonstrated for vertical translation, this was determined. The longitudinal spring constant from the established SThM FEA model was used due to the lack of quantification in literature and the challenging nature for its accurate measurement. Therefore, the required temperature change to overcome the static friction can be deduced and is shown below:

$$k_{long.} = 7.84 \text{ N/m}$$

$$\delta_{x,tip,Th.B.} = 21 \text{ nm/K}$$

∴

$$\text{Equivalent Tip Force} = k_{long.} \times \delta_{x,tip,Th.B.}$$

$$= 164.7 \text{ nN/K}$$

∴

For 0-21 nN Static Friction Range:

$$0 - 0.13 \text{ K}$$

As a result of the above, it can be seen that very little global temperature change will exceed the static friction. Even in the scenario of a large 100 nN normal force, only 0.13 K worth of temperature change will induce displacement. This is approaching the assumption that longitudinal displacement will occur in all scenarios for temperature change exceeding a tenth of a Kelvin. Therefore, it is plausible to assume that the cantilever tip will displace longitudinally with temperature change unless there is a clear asperity limiting it. However, as previously highlighted, the friction experienced and so the temperature to overcome it will vary based on a number of factors and conditions and so variability to the values determined are probable.

Rotation

Rolling (θ_{yz}): The ability for rotation around the longitudinal axis can be fairly simply surmised from the documented and observed phenomenon of stick-slip in lateral force microscopy. As the name suggests, this behaviour exhibits two components of stick and slip. The former pertains to the tip not translating while the AFM actuates at 90° causing the cantilever to rotate that translates into a change in the horizontal laser position on the photodetector [200]. However, once the local static friction has been overcome, the tip slips into the adjacent area in the scan direction. An example lateral scan can be seen in Fig. 4.28 where the saw-tooth like form depicts this. Therefore,

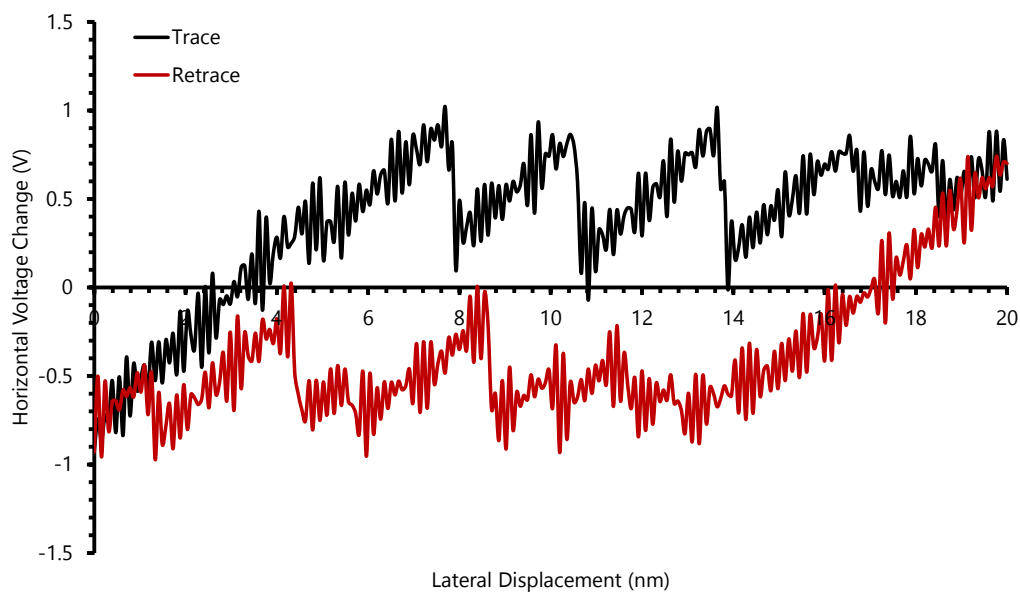


FIGURE 4.28: Friction Loop Demonstrating Stick and Slip of a SThM Cantilever

rolling can occur from contact, with the extent of it depending on the actuation (i.e. if the cantilever is directly rolled from motion or temperature induced deflection) and tip-sample coefficient of friction. The latter essentially sets the threshold for rolling occurring and as an example, the previous data for a polished Si surface should generate rolling up to 0.01° when around 21 % of the normal force is exceeded laterally. Moreover, it should be noted that beyond the simple linear expansion of material laterally in the cantilever, unless there is an imbalance/asymmetry in the coating and/or substrate laterally, then no temperature induced rolling should occur.

Pitching (θ_{xz}): Rotation around the lateral axis is equally understood through the

observed stick-slip motion that can occur during longitudinal scanning. The difference between this as opposed to rolling is that the scan direction is longitudinal and hence a different cantilever stiffness is experienced along this direction (i.e. longitudinal spring constant). This results in a different magnitude of rotation and photodetector voltage change. Therefore, pitching can occur with a similar dependence on the cantilever actuation and coefficient of friction. Furthermore, as established for longitudinal translation, little temperature change will result in longitudinal displacement. Hence, the tip will likely not provide adequate resistance to prevent pitching and so even though there may be the same resistance from friction to that experienced laterally, it will likely have minimal impact.

Yawing (θ_{xy}): Rotation along the vertical axis is far less intuitive than the aforementioned rotations based upon typical AFM operation and actuation. As the horizontal plane is determined to be only restricted by topographic features and coefficient of friction, yawing is possible. It then follows a similar resistance to that determines for lateral and longitudinal translation. However, due to AFM's typical operation directions and planes, this will very unlikely occur unless a very bespoke AFM system and scan direction is applied. In addition, an asymmetry in the cantilever substrate and/or coating may generate some yawing, but this is likely very low. Hence, it is a DOF that will likely have minimal impact if restricted or free and is one that further investigation was not required for the scope of this project.

Overall, from exploring each DOF, the clear mathematical expression for SThM and general AFM cantilever tips when IC and static could be established and are as follows:

$$\begin{aligned}
 \delta_x &= 0 \quad \text{for Force} \leq \mu_s \text{ (Thermal Bending Easily Exceeding)} \\
 \delta_y &= 0 \quad \text{for Force} \leq \mu_s \\
 \delta_z &= 0 \quad \text{for Force} \leq \text{Adhesion/Elastic Limits} \\
 \theta_{xy} &= 0 \\
 \theta_{xz} &= 0 \quad \text{for Force} \leq \mu_s \text{ (Thermal Bending Easily Exceeding)} \\
 \theta_{yz} &= 0 \quad \text{for Force} \leq \mu_s \text{ (Easily Exceeded in Lateral Scanning)}
 \end{aligned} \tag{4.4}$$

where μ_s is the static friction. What should be noted regarding the horizontal translations (x & y), it that the coefficient of static friction is completely dependent on the factors previously mentioned, including tip curvature; tip and sample material; humidity and surface roughness. However, as it was seen in the case study on a polished Si surface for y-translation from lateral scanning, this frictional force is relatively low. Hence, for the adhesion force determined of 44.8 nN, 9.2 nN of static friction would oppose displacement. Longitudinally, this translates to only 0.06 K of temperature change required to overcome it. Therefore, only under very small magnitudes of change (smaller than would be expected when thermal bending and drift is a problem) will zero displacement be observed longitudinally. In addition, if there is any lateral a-symmetry in the cantilever, then it would likely exceed that as well. Furthermore, if the feedback system is brought into play, it provides control of the normal force and so vertical position. This then results in control (although likely inaccurate) in this DOF. As a result, the author would propose that essentially the lateral and longitudinal displacements are non-zero while the vertical approaching closer to zero. This would result in the tip's BC being closest to that of a Roller support with an offset dependent on the known/speculated coefficient of friction. Therefore, a Roller BC was chosen to be employed and utilised in models. This is depicted visually and mathematically in Fig. 4.29.

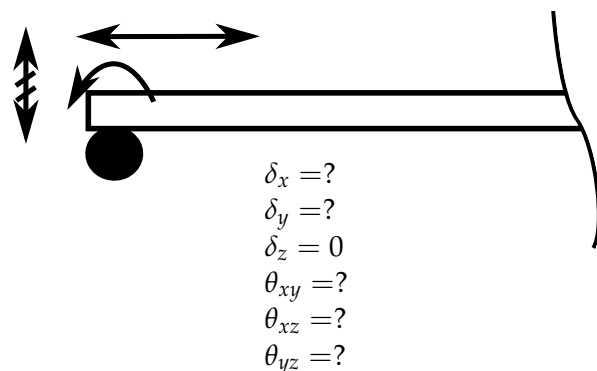


FIGURE 4.29: Roller Tip Boundary Condition on a Cantilever

Thermal

Regarding IC, as the SThM is designed, the Pd tip resistor is highly thermally conductive making direct contact with the sample when contact scanning. Therefore, when

the tip is IC, heat transfer occurs through solid-solid conduction, gas conduction (if not in a vacuum), water meniscus conduction and radiation. As a result, the Pd resistor is sensitive to heat flow with the surface, allowing for sound thermal measurement. This means that when temperature is being measured while IC, the tip resistor will be highly influenced by the sample temperature with a determined contact thermal resistance of $8.33 \times 10^5 \text{ K/W}$ by Ge et. al [194]. This translates to a metal-metal interfacial thermal resistance of $6.53 \times 10^{-9} \text{ m}^2 \text{K/W}$. With the Pd tip resistor's sound thermal connection and low thermal resistance to the Au wires, this will be appreciably affected likewise. The degree of this can be acknowledged through a thermal-resistance model such as the one developed by R. Lambert [141] for SThM cantilevers if desired.

Alongside the above, fluid conduction of the cantilever with the surface will be more pronounced due to it being more immediate to it. Hence, surface temperature will have a greater influence on the cantilever temperature. Therefore, if a similar approach of uniform temperature change was imparted in models, the experiment would need to have the contact surface, immediate fluid and the probe chip all at the same temperature. This may be achievable, however, the mechanical connection to the contact surface is likely a problem. This is due to surface temperature change causing expansion/contraction and so displacement that will produce a change in applied tip force. As a result, any measured temperature induced displacement will be coupled with a change in EF from the surface and so convolute the results. Hence, a method to get around this would be required for sound connection between thermal and mechanical changes.

With these BCs stated, the next step was to model this IC behaviour. Mechanical modelling of EF's for the IC is not elaborated in this section due to the surface generating the EF itself and the AFM's feedback system maintaining control over this. Therefore, the mechanical modelling of EF's in this work maintains the AFM cantilever as a theoretical cantilever and no other type of structure. However, this is not the case for thermal bending as its effect is not isolated to tip-sample interaction. Therefore, IC should dictate the thermally bent cantilever form and is hence explored in-depth below.

4.1.4.2 Thermal Bend Modelling

As stated, thermal bending should be affected when the cantilever is IC, whereby its complex array of attractive and repulsive forces should change the experienced BC alongside the AFM's feedback system maintaining contact. As a result, it is clear that the most appropriate tip BC is a Roller with potential limits based upon the known adhesion force and coefficient of friction when attempting to simulate the surface. However, scanned surfaces varying significantly in their roughness and material(s) alongside the ambient conditions and even inconsistency in the SThM tip radius will have an effect. Therefore, with such ambiguity, a theoretically ideal Roller would suffice for modelling purposes to provide a reference scenario with no horizontal resistance (i.e. frictionless). The next task was to determine which model to utilise. The FDM model would require extensive manipulation and alteration to make it appreciate this new "bridge" like mechanical scenario. Furthermore, the thermal bending equations may not be completely applicable. Hence, it was decided for ease and accuracy to utilise FEA to theoretically appreciate the subsequent thermal bending behaviour and contrast this with experiments. Employing the same FEA model utilised for OC, but with a Roller BC at the tip, the overall FEA output is shown for a uniform 10 K temperature change in Fig. 4.30. The centreline vertical deflection and rotation profiles (normalised to per Kelvin for comparison to previous graphs) in Fig. 4.31 & 4.32 respectively is additionally shown. The latter was deduced through polynomial regression analysis of the vertical deflection trendline (6th order polynomial utilised due to the significant number of data points) and the equation differentiated to produce the rate of change or rotation.

As can be seen immediately from the FEA result, the thermal bending behaviour is completely different to that for OC thermal bending. Instead of the deflection increasing towards the tip, it is fixed vertically resulting in a humped profile along the length. This is reminiscent of the deflection one would expect from a bridge with a uniformly distributed load. As a result, a maximum deflection magnitude of -14.4 nm/K occurred around 89 μm along its cantilever (59.3 % along), whereby a point-of-inflexion (POI) occurs and so a change in rotation direction. This is apparent from the

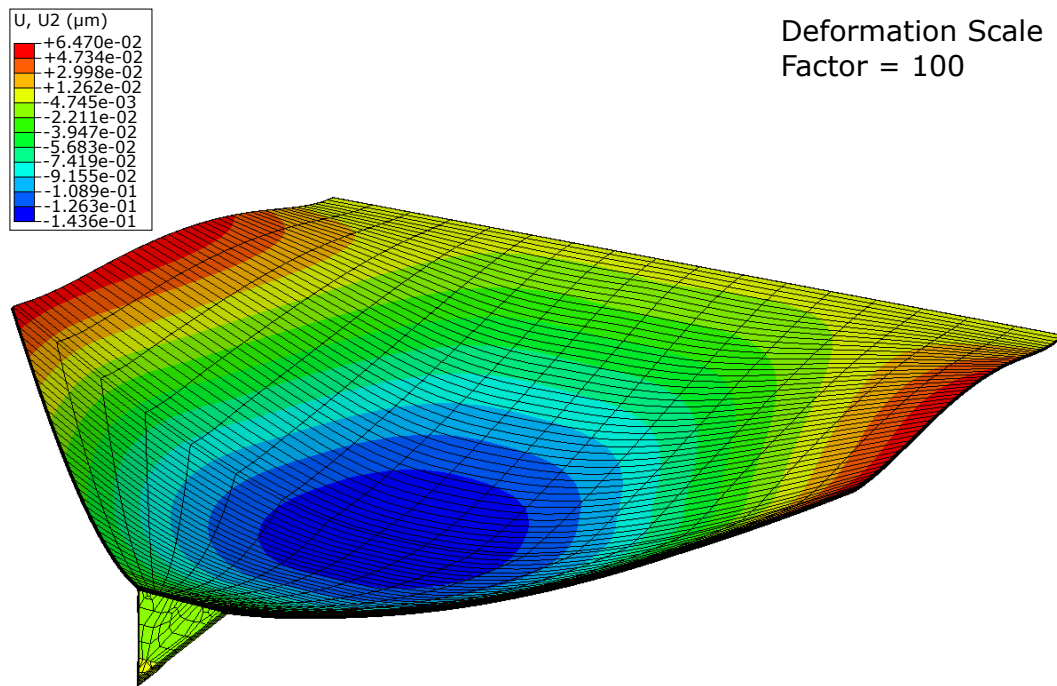


FIGURE 4.30: FEA: Flat SThM Cantilever Thermal Bending (10 K) with Roller Tip BC

blue area in the FEA output in Fig. 4.30. This deflection is around a tenth of the maximum deflection magnitude for OC (155 nm/K) and so less thermal bending should be expected to be measured in an actual AFM. However, as it has been mentioned, the optical lever directly measures the rotation at the location the laser is focused at. Therefore, the rotation is key and at the POI no rotation occurs which would theoretically result in zero vertical voltage change on an AFM's photodetector and so no interpreted vertical deflection from thermal bending. Hence, if the laser is focused at this position, thermal bending should have a negligible effect on topographic scans. This presents a surprisingly simple solution to minimising or eliminating the impact of thermal bending for contact, bi-material cantilevers. This is further explored experimentally in Chapter 5. From a modelling perspective, the next step was to determine the exact theoretical deflection interpretation by an AFM across the whole cantilever length. This was performed utilising the same theoretical InvOLS used previously in the FDM to enable them to be comparable. The determined rotation (Fig. 4.32) was then multiplied by this to produce the profile seen in Fig. 4.33.

This demonstrates that the AFM's optical lever system will interpret this deflection completely differently to the actual cantilever displacement. Therefore, if the optical

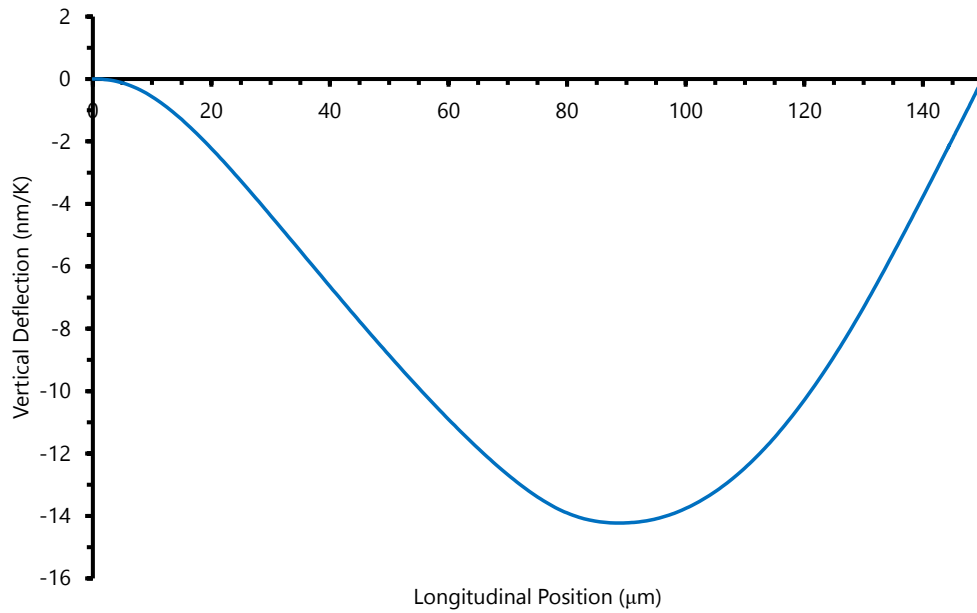


FIGURE 4.31: FEA - Flat SThM Cantilever Thermal Bending with Roller Tip BC Deflection Profile

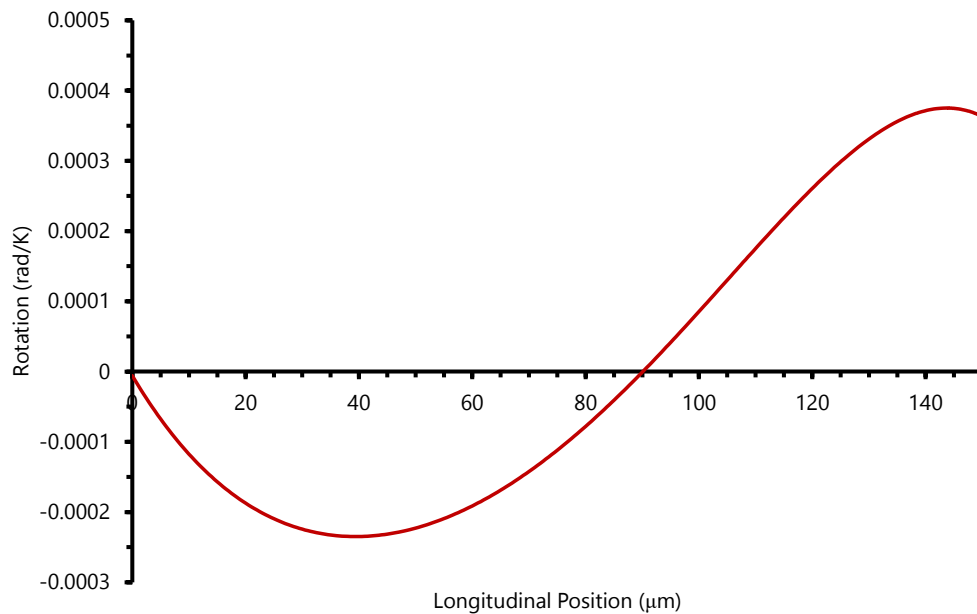


FIGURE 4.32: FEA - Flat SThM Cantilever Thermal Bending with Roller Tip BC Rotation Profile

lever laser is focused between the base and $89 \mu\text{m}$ (or less than 59.3 %) along the cantilever, the deflection will be negative. However, if it is focused $89 \mu\text{m}$ or 59.3 % along the cantilever, it will output zero interpreted deflection. Positioned further along, a positive deflection will be measured that again will be of a lower magnitude to that seen for OC thermal bending with a peak of 35.5 nm/K . This strongly indicates that contact mode scanning generally will be less prone to thermal bending deflection

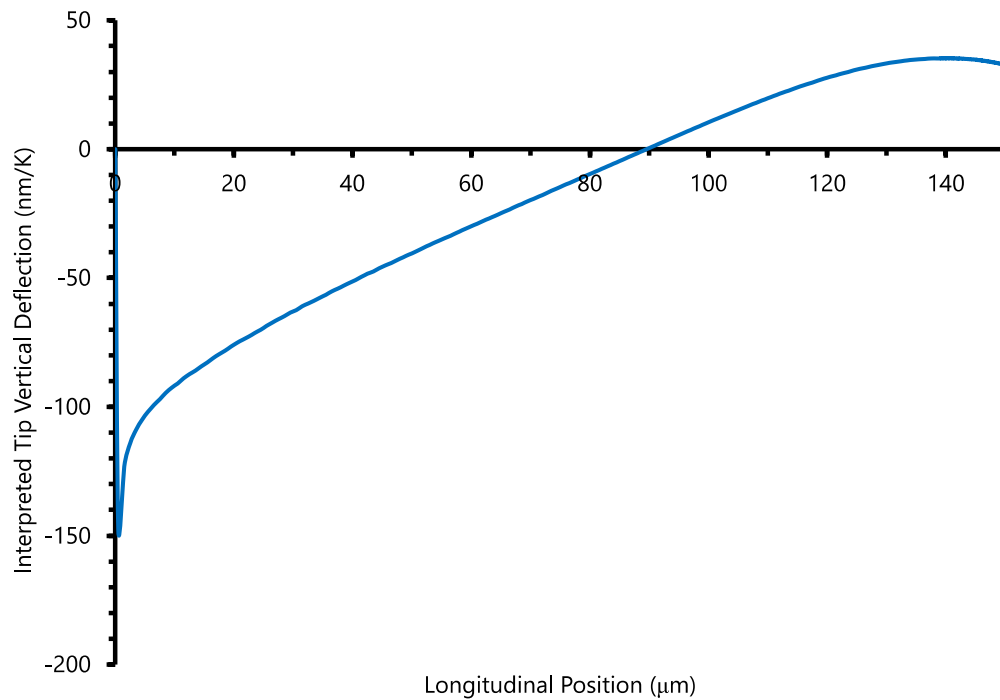


FIGURE 4.33: FEA - Theoretical AFM Interpretation According to FDM Theoretical InvOLS

from the cantilever and so associated topographic artefacts and drift. However, this deflection can be positive, negative or zero in magnitude making it far more variable in direction. If this model is correct, then this provides a whole new perspective of thermal bending for contact mode scanning (i.e. the most common scanning mode for SThM). With this said, even though less or even negligible deflection may be measured when IC, thermal bending will still generate a resultant force at the tip due to temperature change. For SThM, when temperature increases it will deflect away from the sample while for most other AFM cantilever's with metallisation on the opposite side, this will be towards it. This could then exceed the adhesion forces if the difference between interpreted and actual tip force is greater during scanning that could result in loss of contact with the sample. Oppositely, indentation of the sample surface could also occur which could damage surfaces and cantilever tips.

With a good theoretical understanding of uniform temperature induced thermal bending, the same should be explored for the specific case of self-heating in SThM cantilevers as was performed for OC. However, the specific temperature distribution from self-heating was more challenging to be imparted in FEA. To achieve this, instead of 3D stress elements, coupled temperature-displacement elements were required to

enable a complex distribution to be generated along and across the cantilever structure. Therefore, a temperature distribution could be imparted through temperature BC's applied to the model. However, to enable this, the addition of three more properties were required: density, thermal conductivity and specific heat. These provided the essential thermal properties for the temperature BC's to produce the subsequent diffusion of heat through the cantilever structure and so temperature distribution. Regarding the values for these properties, bulk values were utilised. The reason for this as opposed to a comprehensive review of literature values was the desire to conform it to R. Lambert's already established FDM thermal models [141]. The latter has been demonstrated to be a sound representation of SThM cantilevers and so to conform the FEA's temperature distribution to this and permit comparison to the self-heating modelling performed already for OC was logical. Therefore, the FEA model was modified to include additional BC's along the cantilever length. These can be seen graphically in Fig. 4.34 for a 0.5 mA current through the tip resistor that generated a peak tip temperature of 10.41 K (an average tip sensor temperature of 8.09 K). A subsequent temperature profile with these BC's can be seen in Fig. 4.35 that contrasts it to R. Lambert's thermal-resistive model.

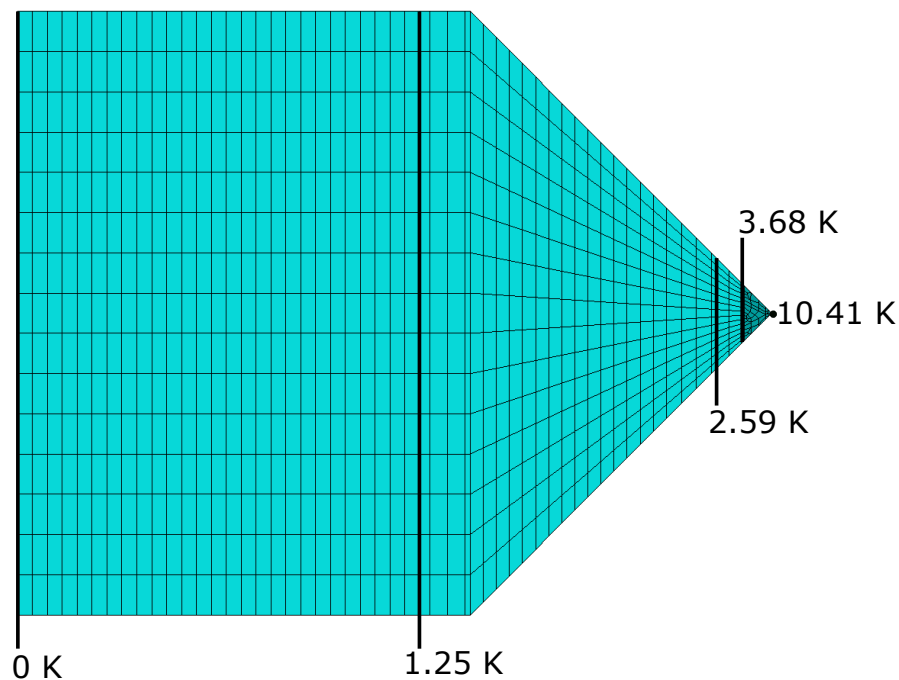


FIGURE 4.34: FEA - Diagram of the Temperature BCs Imposed Along the SThM Cantilever

TABLE 4.9: FEA: Additional Self-Heating Material Properties

Material Properties	SiNx [201]	Au [202]	Pd [203]
Density (kg/m ³)	3250	19,300	12,000
Thermal Conductivity (W/m°C)	26	312	71.8
Specific Heat (J/kg°C)	735	130	240

With such a good alignment of FEA's temperature profile using BCs and bulk magnitudes for the additional properties, it is clear the approach was sound. The bulk properties that were employed are stated in Table 4.9 for clarity. Hence, taking this temperature profile, a comparable IC thermal bend deflection profile could be generated in FEA. This can be seen in Fig. 4.36. As expected, a far lower deflection magnitude to that produced from uniform, global temperature change was observed with a peak -3.9 nm/K at 96.5 μm (64.3 %) along the cantilever. This can be contrasted to the respective experiment along with the knowledge to inform the experimental methodology.

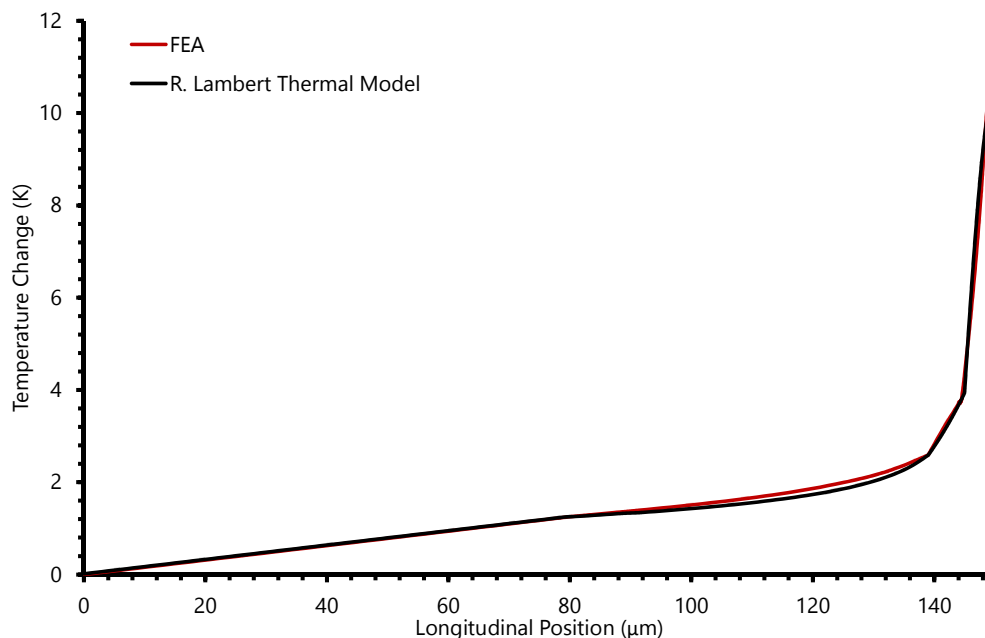


FIGURE 4.35: Longitudinal Temperature Distributions for SThM Cantilever's for Self-Heating

To briefly sum up the above work on SThM cantilevers, a good theoretical appreciation has been obtained for both OC and IC thermal bending. Specifically, FDM

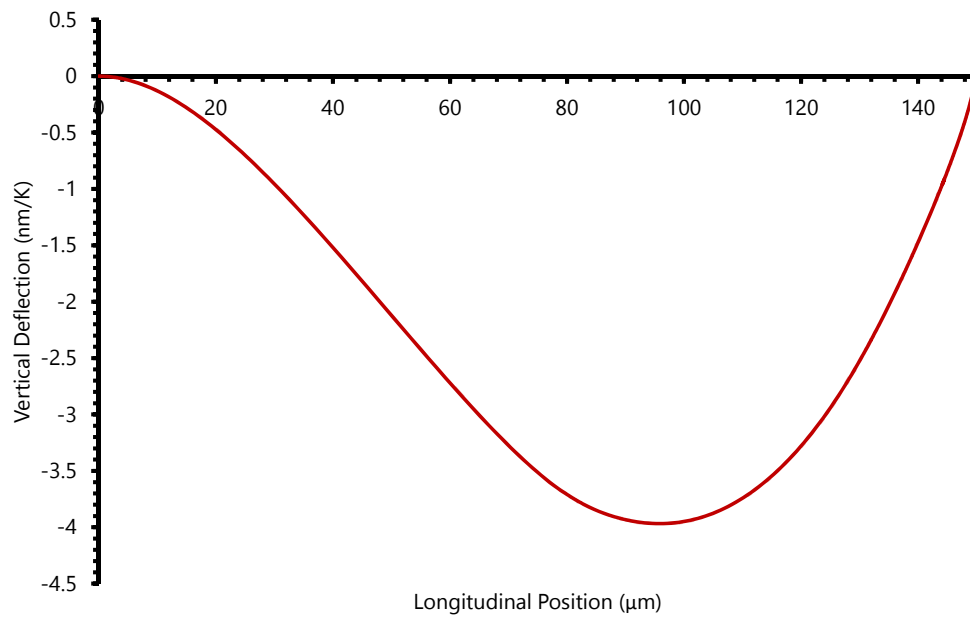


FIGURE 4.36: FEA - Self-Heating Induced IC Thermal Bending Vertical Deflection

and FEA models have established clear profiles for EF and thermal bend induced deflection. These have been combined to provide a theoretical interpretation within an AFM that highlights variable and erroneous measurement of thermal bending due to the InvOLS. For example, a range of 105 nm/K to 200 nm/K occurred for flat SThM cantilevers. In addition, analysis of grooved cantilevers highlights their ineffectiveness at replicating the sandwich structure. This has been hypothesised as being due to lateral stiffness and/or their lack of slender nature where improvements to current fabricated cantilevers likely from simple stiffening. However, for non-grooved cantilevers that are brought IC, these models predict a bridge like behaviour when exposed to temperature change. As a result, a humped form occurs that causes a massive shift in AFM's theoretical interpretation. This suggests that the deflection direction interpreted by the AFM will change along the cantilever with a point of inflexion near mid-way along. With all of this performed for SThM cantilevers, the next step involved exploring whether similar findings can be found in non-thermal, bi-material AFM cantilevers.

4.2 Non-Thermal AFM Cantilever Modelling

Non-grooved SThM cantilevers are relatively similar to other AFM cantilevers due to their flat cross-section and multi-material make-up. However, there are some differences with the main one being the patterning of the reflective coating. For SThM, this pattern produces a variable width across the cantilevers (as seen in Fig. 4.1), while for most non-thermal AFM cantilevers it is uniformly coated over the whole structure. Moreover, the coating for SThM cantilevers is deposited on the underside as opposed to the topside for typical non-thermal AFM cantilevers. This will manifest as the opposite direction in the vertical deflection for the same temperature change, i.e. negative deflection for temperature increase when on the topside. Therefore, these differences will have an effect, notably the change in direction, but the general behaviour is completely translatable. In the theme of the project, this was initially investigated through modelling. Both FDM and FEA methods were employed for a comprehensive theoretical appreciation. The probes chosen were other contact AFM cantilevers to additionally explore their IC thermal bend behaviour that has been unexplored within the academic community thus far. Hence, the probes and their manufacture details are listed in Table 4.10, whereby a non-metallised (blank) SThM cantilever was additionally analysed to provide a zero thermal bend reference. Images of these cantilevers as fabricated can also be seen in Fig. 4.37 for a clear depiction of their structure. It should be noted that the Blank SThM cantilever had a chrome etch to remove the metal. However, in the region where there is designed overlap of the Au and Pd tip, some of the latter remained as it is underneath the Au. This was not reflected in the theoretical models where there was no metal in the model.

4.2.1 Out-of-Contact

With the nominal cantilever geometry established, the FDM Model was employed to produce their respective vertical deflections, rotations and theoretical AFM interpretations when the tip was OC. The same property values determined for SThM materials were utilised in these models in the absence of knowledge regarding the exact fabrication techniques employed to manufacture the cantilevers. Therefore, these model

results may not produce accurate absolute magnitudes, but should provide a reasonable relative depiction. Furthermore, the structures were assumed Thin-Beams (i.e.

TABLE 4.10: Non-Thermal AFM Probe Details

Probe	Spring Constant (N/m)	Shape	Material(s)	Geometry [L x w x t] (μm)	Manufacturer
MLCT-B [204]	0.02	Rectangular	SiN _x + Au	210x20x0.55 ($t_{Au} = 0.045$)	Bruker
MLCT-C [204]	0.01	Triangular/A-Shaped	SiN _x + Au	310x20x0.55 ($t_{Au} = 0.045$)	Bruker
PNP-DB-100 μm [205]	0.48	Rectangular	SiN _x + Au	100x40x0.5 ($t_{Au} = 0.07$)	Nanoworld
Blank SThM	<0.5/0.3 /0.25	Rectangular + Taper	SiN _x	150x120x0.55	AFM & Hyperlithography Group

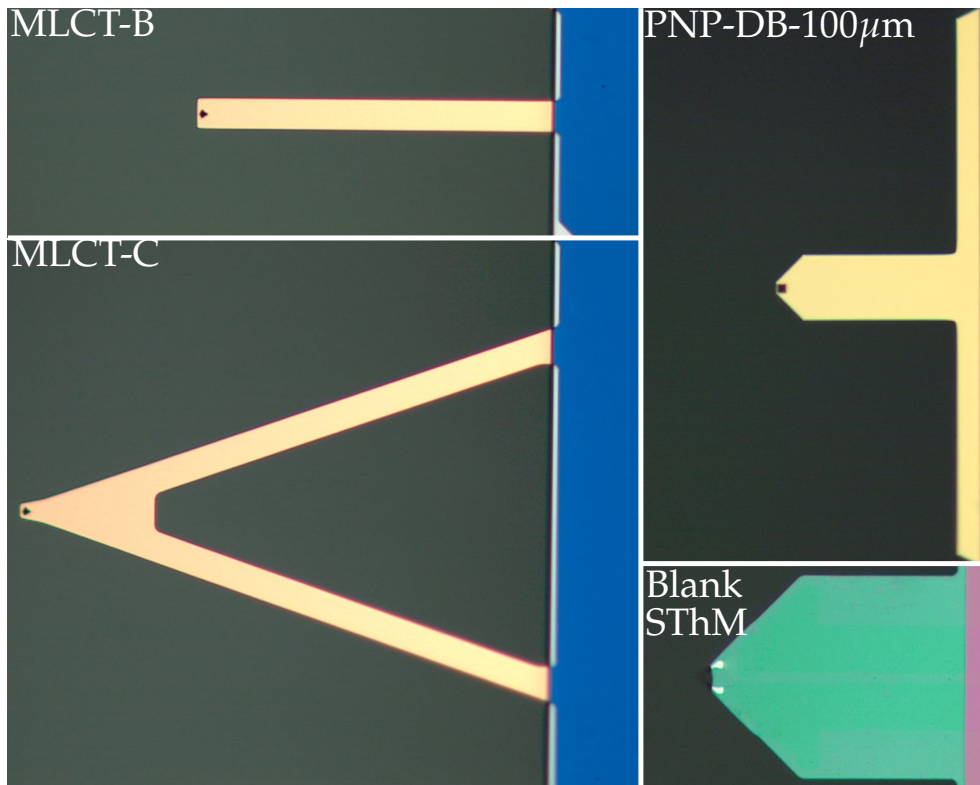


FIGURE 4.37: Optical Images of Non-Thermal AFM Cantilevers

no Effective Modulus employed) due to the relatively thin coating to the substrates for each cantilever. With the above in mind, each of the vertical deflection, rotation and interpreted tip profiles are shown and described under their respective title. The profiles are shown in Figures 4.38, 4.39 and 4.40 for 1 nN and 1 K worth of EF and temperature change for thermal bending respectively. The latter is not shown for Blank-SThM probes as this is zero for both the vertical deflection and rotation resulting in zero interpreted deflection as well. Each set of profiles are hence shown and described under their respective title.

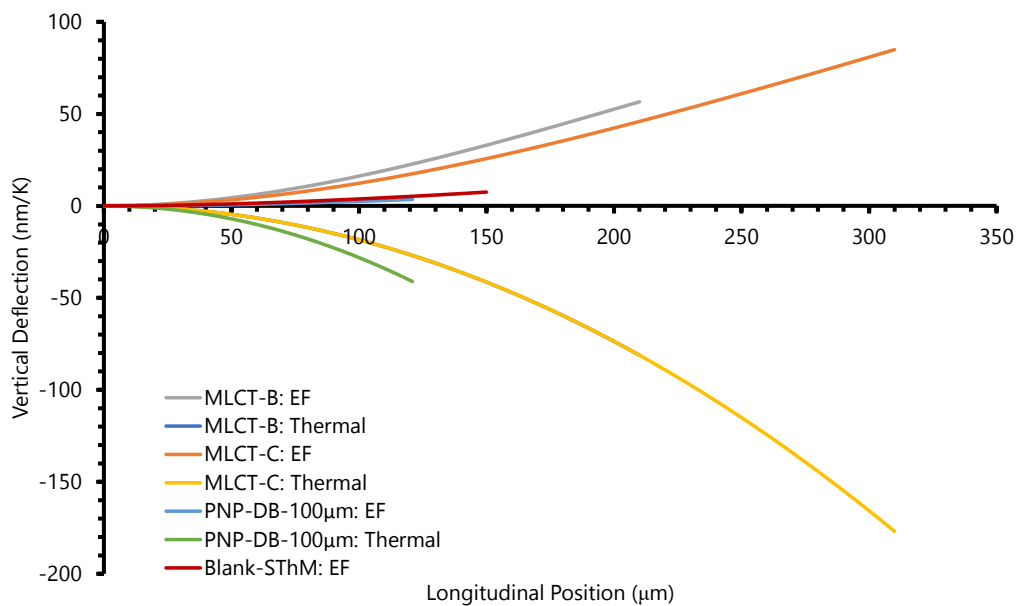


FIGURE 4.38: FDM OC - Non-Thermal Cantilevers Vertical Deflection Profiles

Vertical Deflection

The vertical deflection profiles in Fig. 4.38 immediately shows the side of metallisation through the negative thermal bend directions shown (i.e. topside metal location). The MLCT cantilevers overlap in their deflection behaviour due to them possessing the same materials and respective thicknesses (as noted in Table 4.10). The PNP-DB-100μm cantilever produces greater deflection magnitude over the same length due to its greater coating thickness, but as it is shorter, its final tip deflection magnitude of -41.1 nm/K is less than that of -81.2 nm/K and -176.9 nm/K for MLCT-B and C respectively. Moving towards the EF deflections, the MLCT cantilevers are far more compliant than the PNP-DB-100μm cantilever due to them being longer, narrower and

having a thinner Au coating. As a result the FDM models predict spring constants of 0.0177 N/m, 0.0118 N/m and 0.285 N/m for the MLCT-B, MLCT-C and PNP-DB-100 μm respectively. These are of a similar magnitude as those demonstrated in Table 4.10 apart from the PNP-DB-100 μm 's being lower than expected from the manufacturer's nominal value. However, it was observed that the PNP-DB-100 μm cantilever has a wide section at its base that should contribute to its EF and thermal bend behaviour. As a result, this is considered in the models causing it to be approximately 21 μm longer (measured through the previously employed Bruker Contour GT-X 3D Optical Microscope) than that stated for the nominal value in Table 4.10 from NanoWorld [205]. Hence, this could explain the discrepancy if their spring constant measurement did not appreciate this section.

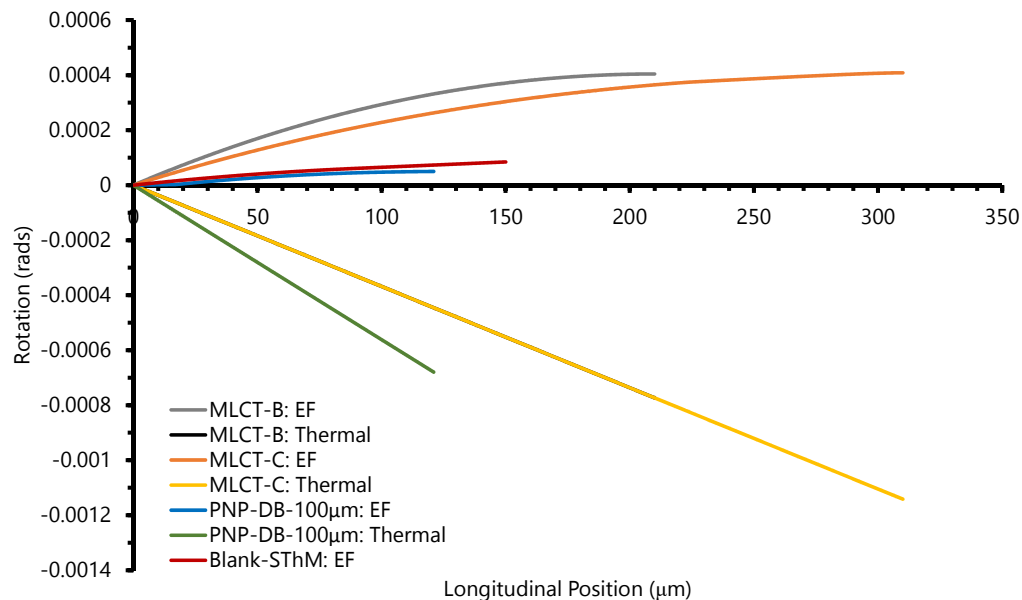


FIGURE 4.39: FDM OC - Non-Thermal Cantilevers Rotation Profiles

Rotation

Focusing initially on the thermal bend induced rotation profiles in Fig. 4.39 for each cantilever, a constant gradient was produced. This is due to the substrate and coating having equal widths and therefore the generated Bending Moment across the lengths are equal and constant. The difference in gradients between the MLCT and PNP-DB-100 μm probes is due to the difference in the substrate and coating thicknesses. For the EF rotation profiles, these demonstrate the expected reduction in rotation towards

the tip where the force is applied. This is due to the moment arm from the tip force reducing the closer the point along the cantilever is to it.

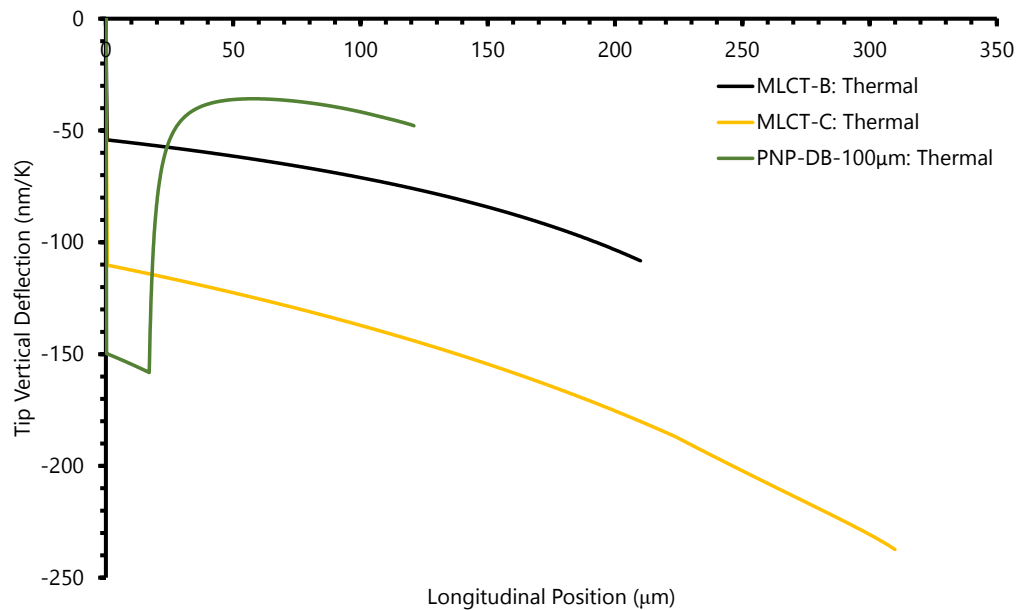


FIGURE 4.40: FDM OC - Non-Thermal Cantilevers Theoretical AFM Interpretation Profiles

Theoretical AFM Interpretation

Only the thermal bend interpretation is shown in Fig. 4.40 due to the EF producing a constant deflection across the length that abides to the tip deflection shown in the vertical deflection graph (Fig. 4.38). Hence, analysing the thermal bend profiles, they show that MLCT cantilevers produce the same general trend with MLCT-C producing a greater expected deflection due to its longer and so less stiff nature resulting in a larger tip deflection which is translated in the interpreted deflection. The PNP-DB-100 μm cantilever shows a more complex form due to its wide base section. However, as the section is so wide, it may not conform to the Thin-Beam analysis method and so the interpretation in this location should be taken with notable degree of uncertainty alongside its immediacy to the probe chip. With this said, the main body of the cantilever should be more predictable, whereby this demonstrates a similar trend to that of the MLCT cantilevers of increased negative deflection further along the cantilever. This deflection is lower than the MLCT cantilevers due to its shorter, wider, thicker and hence stiffer construction resulting in lower interpreted tip deflection. One key aspect to extract for all of these cantilevers is that the interpreted deflection is variable

across them all. This explicitly demonstrates that theoretically AFM's interpretation of thermal bending is inaccurate, whereby in the absence of strict laser location control, it will vary between each set of scans where a laser re-alignment is performed. This is similar to the flat SThM cantilever analysed in previous sections.

4.2.2 In-Contact

With the OC behaviour established, the IC behaviour needed to be theoretically appreciated. This utilised FEA with the same elements and mesh strategy as that employed for SThM cantilevers in Section 4.1. Furthermore, the properties previous employed in the OC modelling was used for consistency. The thermal bend induced deflection profiles are shown in Fig. 4.41 followed by the rotation and theoretical AFM interpretation in Fig. 4.42 and Fig. 4.43 respectively. These are analysed under their respective titles below.

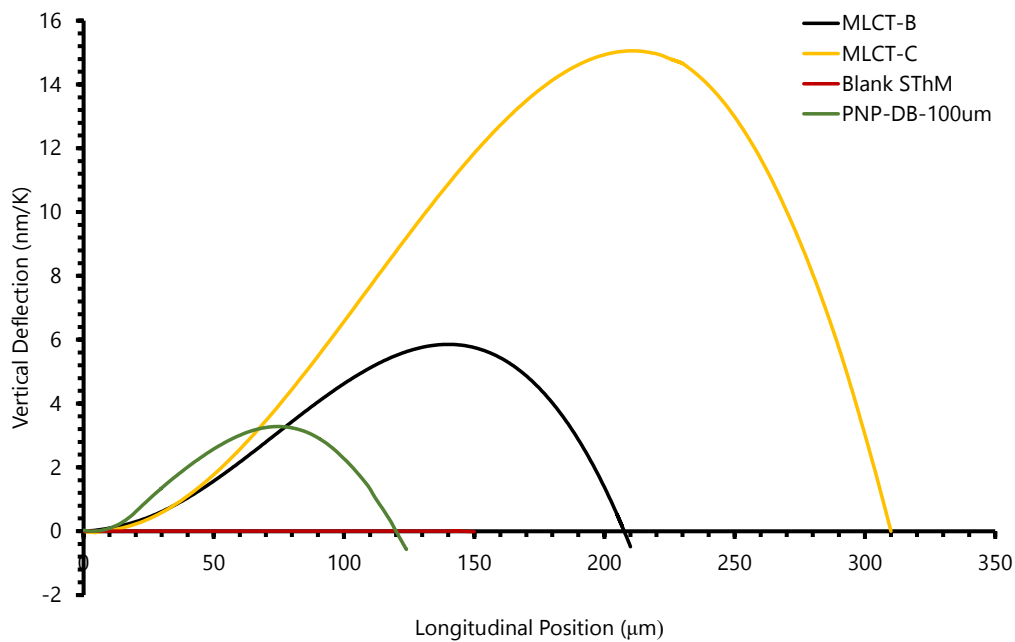


FIGURE 4.41: FEA IC - Non-Thermal Cantilevers Vertical Deflection

Vertical Deflection

The three metallised cantilevers all show in Fig. 4.41 a similar humped profile when a Roller contact was imparted at their tip. This is very similar to that seen in Fig. 4.32 for flat SThM cantilevers, but in the opposite direction due to the metal location on the top-side. From these, a similar trend to the IC vertical deflection profiles was seen with

the MLCT-C cantilever demonstrating the largest deflection (15 nm/K) followed by MLCT-B (5.9 nm/K) and PNP-DB-100 μm (3.3 nm/K). Furthermore, although not clear due to the varying cantilever length, each has their peak or POI at very similar relative positions. The MLCT-B and C have their 67 % along while the PNP-DB-100 μm 60 %. This disparity is likely due to the latter having a very wide base relative to the rest of the cantilever causing it to shift further towards it. The Blank SThM demonstrated negligible deflection with it being slightly positive until the tip's base 144 μm along where it then decreases towards zero.

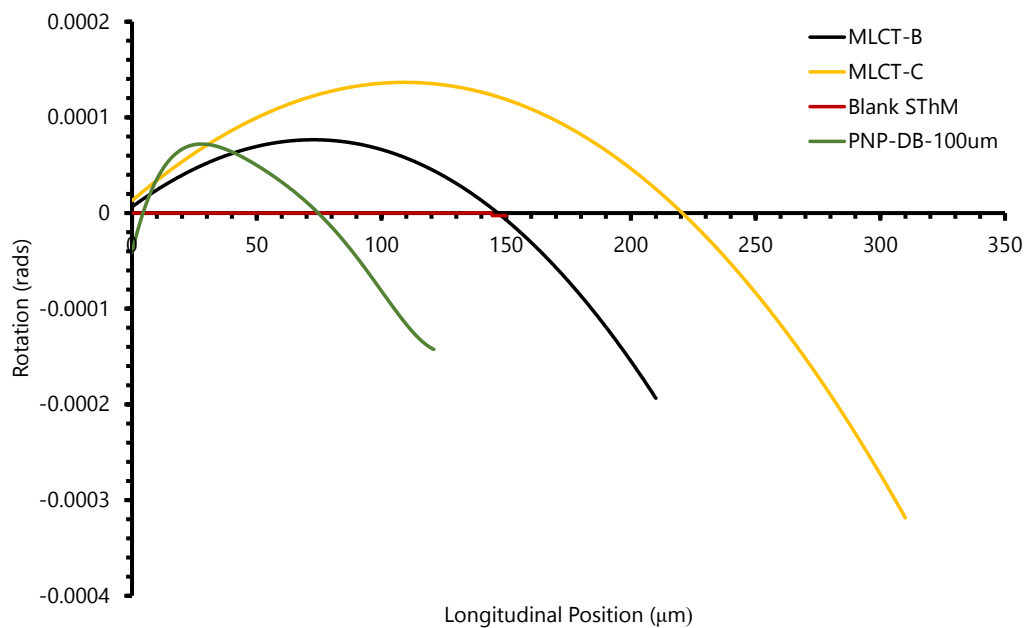


FIGURE 4.42: FEA IC - Non-Thermal Cantilevers Rotation

Rotation

Initially, the effect of the wide-base on PNP-DB-100 μm 's cantilever is quite apparent in Fig. 4.42, with it causing it to arc upward in a position closer to the base. This is less consistent than the other profiles due to this sudden change in width which the MLCT-B and MLCT-C do not exhibit. Therefore, this highlights the shifting of the behaviour further towards the base which aligns to what was previously articulated in the vertical deflection's POI. Analysing the MLCT-B and MLCT-C profiles, they are far more consistent in their trend with a clear second order relation shown. This is interesting as without tip fixation, thermal bending generates a linear relation for rotation along the cantilever and so a single order increase in the governing relation

has occurred. For the Blank SThM cantilever it is very flat which reflects the vertical deflection graph.

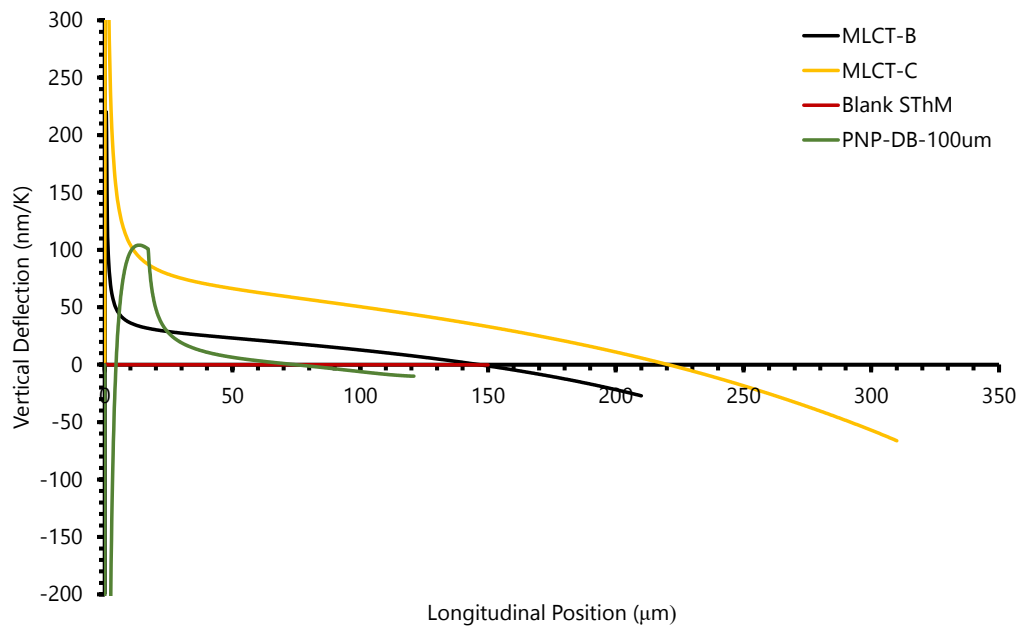


FIGURE 4.43: FEA IC - Non-Thermal Cantilevers Theoretical AFM Interpretation

Theoretical AFM Interpretation

Analysing the interpreted profiles in Fig. 4.43, the MLCT-B and MLCT-C show similar shaped profiles with the latter having a greater deflection magnitude for each position along its length. This starts positive and then goes negative in accordance to the POI. At the base, a spurious interpretation occurs while a couple of microns beyond this more sensible values are obtained due to the InvOLS. For the MLCT-C this ranges from 300 nm/K to -66 nm/K while for the MLCT-B 100 nm/K to -27 nm/K. It should be noted that the FDM's theoretical InvOLS was utilised to be consistent and more comparable with the OC graphs as was performed for the flat SThM cantilever. Moving towards the PNP-DB-100 μ m cantilever, this demonstrated a short hump upward peaking at around 104 nm/K due to the base section. It subsequently drops down suddenly along the main body of the cantilever which then outputs a similar relation to the MLCT cantilevers and a tip value of -10 nm/K. This highlights that the base section should manifest quite differently in experiments, but still show a logical behaviour along the main cantilever body. The Blank SThM cantilever is logically low,

however, it is above zero until the base of the tip with a value around 0.004 nm/K for the vast majority of its length.

Overall, a good theoretical appreciation has been obtained for non-thermal AFM cantilevers. OC and IC thermal bend profiles show sensible quantification which demonstrate a similar trend to flat SThM cantilevers. Moreover, AFM's theoretical interpretation of them has similarly been predicted to be variable and erroneous. This reinforces that all these bi-material cantilevers have very similar thermal bending with IC in particularly showing a humped deflection profile. With this theoretical base, experimentation was carried out to verify and contrast to these findings.

5. Experimental Quantification of Thermal Bending in AFM Cantilevers

With comprehensive theoretical work performed, the next step was to obtain real-world figures for comparison to these models. This aimed to provide verification of the model's results and conclusions along with measuring the impact of thermal bending in AFM's measured deflection and topography. This involved direct vertical deflection measurement of thermal bending alongside AFM's interpretation of SThM and non-thermal AFM cantilevers. From this, conclusions could be drawn for OC and IC thermal bending with a simple solution proposed to mitigate the latter. Initial measurements employed SThM cantilevers to make use of their tip temperature measurement and establish a sound experimental quantification of thermal bending. Once performed, non-thermal AFM cantilevers were investigated by using the same approaches.

5.1 SThM Cantilevers

This section is structured similarly to Chapter 4, with SThM cantilevers analysed for their OC and IC thermal bend behaviour separately. Within each, an initial set of experiment(s) to directly measure vertical deflection induced by thermal bending is detailed followed by the AFM's interpretation.

5.1.1 Out-of-Contact

The first port of call was to measure the vertical deflection from thermal bending, for both flat and grooved cantilevers. The former was investigated in accordance to the

Research Method for the first experiment described in Section 3.2.2.1 and is expanded below.

5.1.1.1 Direct Deflection Quantification

In this experiment, an Interferometer (Bruker Contour GT-X 3D Optical Microscope) was employed with a Peltier heater on the stage to generate a uniform temperature change to the cantilever. This involved increasing the Peltier voltage in 0.5 V increments that produced a temperature change due to the thermoelectric effect. For each increment, the probe was allowed to reach a steady-state temperature (typically taking 2-3 minutes) and 3D topographic images of the cantilever were taken using the Interferometer. This was performed over 15 different temperature's that enabled a statically sound temperature-deflection relation to be drawn. A position as far along the cantilever length that was not prone to imaging artefacts was chosen. This was to provide the highest SNR for the deflection measurements and appreciate the longest possible length of the cantilever. The latter of which would allow the maximum modelled length to be contrasted to real-world cantilevers and so test its simulation as much as possible. As a result, the deflection was taken 133 μm along the cantilever, as highlighted in Fig. 5.1. When measured in-conjunction with the tip temperature,

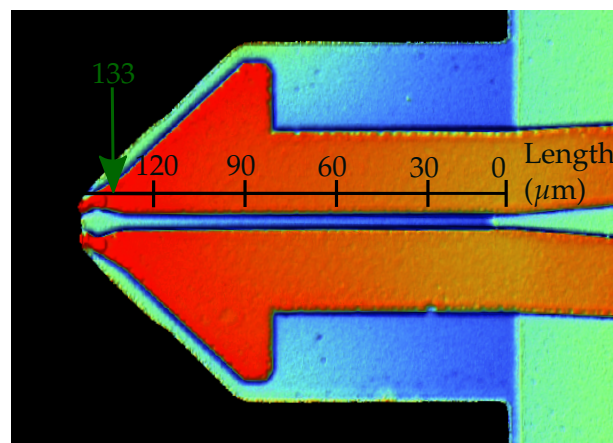


FIGURE 5.1: Interferometer Image of a Flat SThM Cantilever with Annotated Scale Bar

the trend seen in Figure 5.2 was generated and plotted alongside the FDM and FEA models deflection outputs for an uniform temperature change. The experimental data

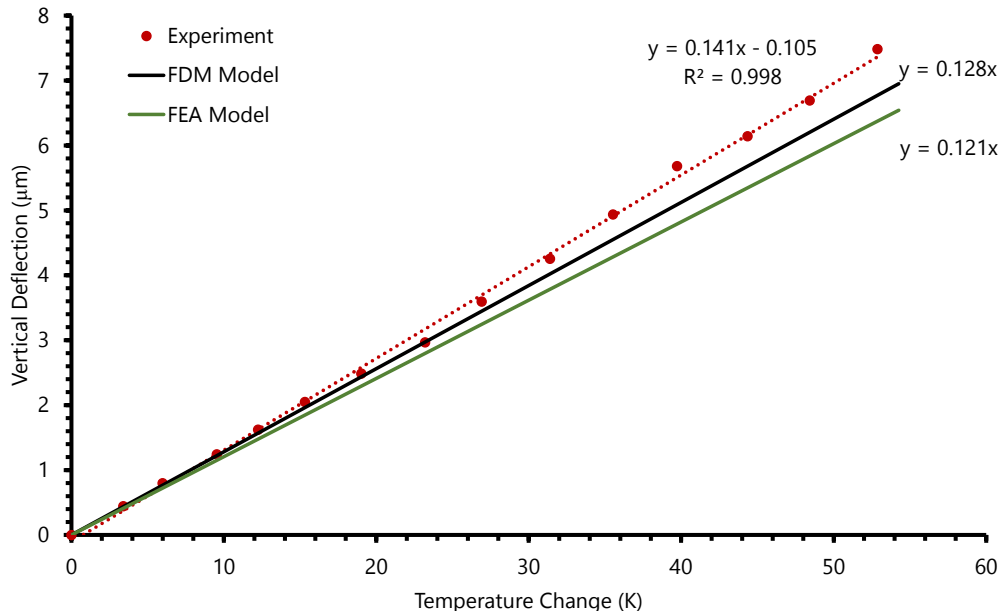


FIGURE 5.2: Flat SThM Cantilever's Uniform Temperature Induced Thermal Deflection 133 μm Along

demonstrates a significant deflection gradient of $0.141 \mu\text{m}/\text{K}$ at $133 \mu\text{m}$ along the cantilever. This is an appreciable deflection gradient and so reiterates the general observation of thermal bending's pronounced effect on SThM cantilevers. Contrasting this to the models output, a sound correlation is seen with the FDM and FEA outputting gradients of $0.128 \mu\text{m}/\text{K}$ and $0.121 \mu\text{m}/\text{K}$ respectively. This is notably less than measured, but considering the probable variation in SiN_x thickness and literature defined material properties utilised in the models, it is a reasonable agreement. Alongside this, the experiment verifies the strong linear relationship temperature has with vertical deflection, even for a significant temperature range of 53°C from ambient. As a result, it can be concluded any complex thermo-mechanical effects such as temperature changing the materials Young's Moduli do not need to be appreciated for this or any temperature range equal or less in future experiments. However, the above only compared one point along the cantilever length and not the whole thermal bend induced deflection profile (i.e. along the full cantilever length as demonstrated by the scale bar seen in Fig. 5.1). Due to the Interferometer producing 3D images, this was possible and a comparison is shown in Fig. 5.3 for another SThM cantilever.

In this case, the experimental data shows a very similar relative change in deflection along the cantilever when compared to models, demonstrating a clear second order relationship that was expected theoretically from Equation 3.9. Proof of this was

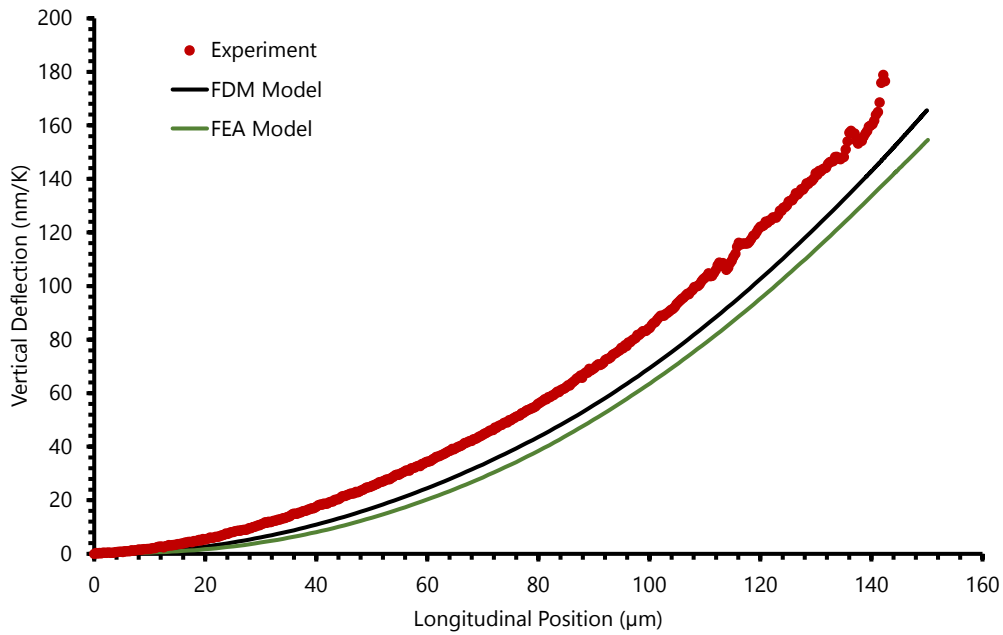


FIGURE 5.3: Flat SThM Cantilever's Uniform Temperature Thermal Bend Deflection Profile

key for the model to provide a good theoretical representation and subsequently be utilised further in this work. However, there is a notable difference in magnitude with experimental data demonstrating greater deflection than the models. This could be initially interpreted as the models under-representing the cantilever deflection. However, from extensive experiments performed in this body of work on SThM cantilevers, variation in the magnitude thermal bending was seen. For example 90 μm along flat SThM cantilevers deflection produced gradients from 52-77 nm/K (FDM producing 55 nm/K) for a uniform temperature change and the same experimental set-up. Therefore, with this range of 25 nm/K and the model's output sitting within this range, it is fair to say the prediction is accurate with such variation. Furthermore, this data emphasises that no matter how perfect the model, real-world SThM cantilevers can be notably inconsistent and so the desire for an exact match between models and experiment is not probable or required. Hence, with this sound agreement in deflection gradients and most importantly profiles, conclusions based upon the models should be translatable to real-world flat SThM cantilevers regarding thermal bending when OC. In addition, the models (especially the FDM with its flexibility) can be used as design tools and to model other types of cantilevers such as non-thermal cantilevers (experimental results of which are contrasted to models later in Section 5.2).

With the above determined for flat SThM cantilevers, it was additionally desired to replicate the result for grooved SThM cantilevers to similarly provide verification and contrast to the models generated. The same method was employed, but with measurements taken at a longitudinal position of $75\ \mu\text{m}$ so that the prismatic grooved structure was isolated (dimensions changing beyond $80\ \mu\text{m}$ along the cantilever) in the analysis to allow easy comparison to models. These results can be seen in Fig. 5.4 where the models are based upon the nominal grooved cantilever dimensions of commercial cantilevers (groove depth equalling $350\ \text{nm}$).

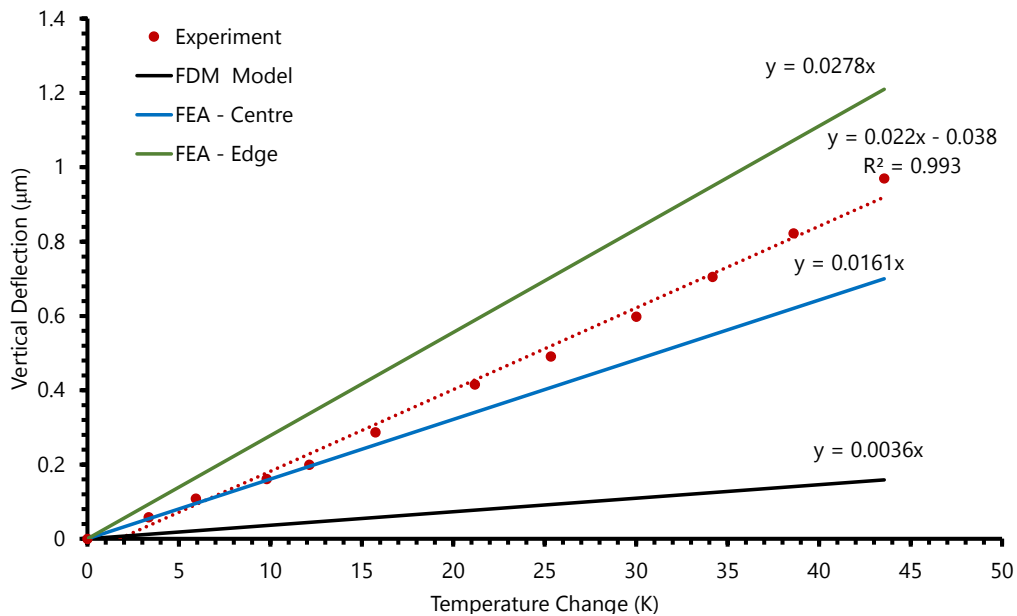


FIGURE 5.4: Grooved SThM Cantilever's Thermal Deflection Gradient's at $75\ \mu\text{m}$ Along

As it can be seen, the deflection gradients exhibited in the experiment far exceed what the structural compensation concept and FDM model would suggest. The latter of which still predicted some degree of deflection due to the $350\ \text{nm}$ nominal groove depth not being deep enough for the ideal near zero deflection to occur. However, the real-world cantilever showed far better agreement with FEA's results with the experiment gradient coming in-between its central and edge deflections. This is logical as the lateral position the deflection measurements were taken from in the experiment were off-centre and along the Au for sound reflection as required by measurement using the Interferometer. These FEA results were taken from a cantilever $75\ \mu\text{m}$ long and as highlighted in the groove length study, this may output greater deflections than would be expected if the cantilever were longer. However, the groove needs to much

longer for this effect to be pronounced as opposed to the 120 μm in this case. With this noted, the FEA outputted range still encompasses the experimentally determined gradient. Therefore, the above supports the conclusion that the current grooved cantilever's do not produce the desired effect from the original design implementation of the structural compensation concept. This is likely a combination of the groove being too shallow and the groove portion of the cantilever being too short for the effect to even come into prominence. Hence, the increase in stiffness with the groove is likely providing the most significant impact between the grooved and flat SThM cantilevers. This is demonstrated in the mechanical analysis for the second moment of area of flat and grooved cantilevers in Section 4.1.3.2. Contrasting the second moment of area of a flat cantilever to a grooved one with a thickness and depth of 350 nm, a very similar change in the inverse of the second moment of area with deflection occurs. A reduction of 54 % in the former is determined, where $I_{350\text{nmgroove}, 350\text{nmSiNx}} = 1.740 \times 10^{-24} \text{ m}^4$, which is similar to the 56 % reduction seen 75 μm along the flat to the grooved cantilevers seen in Fig. 5.3 & 5.4. With all of this in mind, the experimental data aligns with the representation and conclusions of the modelling work and explains why current grooved cantilevers do not provide the desired thermal bend attenuation.

Overall, a direct measurement of real-world SThM cantilevers was performed that showed good agreement in magnitude and trend to models. However, the interaction between the Mechanical and thermal bend components of the models was required to be contrasted with experiments to determine AFM's interpretation of thermal bending. This is explored in the proceeding section, whereby only flat SThM cantilevers were explored due to their ubiquitous use, grooved cantilever's lack of efficacy and their greater applicability to other non-thermal AFM cantilevers due to their similar cross-section.

5.1.1.2 AFM Interpretation Experiments

To determine the interpretation of the above uniform temperature change induced Bending in an AFM, again a Peltier heater was employed to change the cantilever temperature with the SThM providing its measurement. Based upon Section 3.2.2.2's defined method, the same vertical position of the cantilever over the Peltier heater's hot surface was possible with a consistent 4 mm spacer between the probe holder and

heater surface (resulting in less than 3 mm gap between tip and Peltier surface). This enabled a near uniform temperature distribution across the cantilever and so a comparable heat transfer condition to the direct deflection measurement employing the Interferometer to that measured by an AFM system (Digital Instruments Dimensions 3100). Figures depicting these set-ups are shown in Fig. 3.12. This was broken down into two different experiments to link the Interferometer and AFM results alongside the model's. The first experiment aimed to show alignment of the AFM, Interferometry and model results at a single point along a flat SThM cantilever. With proof that all three are measuring the same thermal bending, the second aimed to demonstrate AFM's interpreted profile of the bend.

1st Experiment:

Both the Interferometer and AFM were utilised as the connection between their measurements needed to be established alongside the FDM model. For each technique, the cantilever was under the same mechanical conditions and the same relative position to the Peltier heater. Therefore, they had very similar heat transfer conditions allowing for comparison. Alongside this, as mentioned in the Section 3.2.2.2, tip-up and tip-down orientations of the cantilever were additionally measured in the Interferometer to prove there was no difference in the deflection interpretation between the two. If correct, this means they can be definitively contrasted to the AFM's measurements, where the method of linking the two was only required. This was needed due to the AFM outputting tip deflection while in the Interferometer deflection is taken from a position on the cantilever with the tip unable to be directly imaged. The latter is due to the tip's 54.7° angle being too large from the imaging plane (as seen in Fig. 3.10). As a result, either the AFM needed to be converted to vertical deflection at the same position, or the Interferometer would be converted to the respective tip deflection from an EF that the AFM measures. The latter was chosen as the Interferometer has been shown to align well to theoretical models from the previous experiments. Therefore, as the models were able to link rotation and vertical deflections from both EF and thermal bending they could convert the Interferometry results to be compared to the AFM's. If these produced similar results, it would not only prove they are measuring the same behaviour, but also bring confidence to the understanding of AFM's optical

lever system and model's appreciation of this. To perform the conversion, the previously derived theoretical InvOLS from the FDM Model (seen in Chapter 4, Section 4.1.3.2) was employed. This allowed theoretical conversion of rotation to tip deflection according to an EF. Extracting the same longitudinal position in the model and Interferometer image, the latter's measurements could be converted. However, the Interferometer outputs vertical deflection as opposed to rotation that the theoretical InvOLS relates to. Therefore, either the whole longitudinal deflection profile is required to be taken and regression analysis employed to produce a trendline (at least third order to account for the geometry changes with length for thermal bending) that could then be differentiated for rotation, or a simple conversion using the FDM Model for vertical deflection to rotation based upon their ratio at that position. The latter was chosen as it was simpler and less prone to any profile artefacts that would effect the regression analysis. Moreover, it would maintain just the FDM and Interferometry having an influence on the result, as opposed to any other processing or mathematical methods. Hence, the following equations would provide a conversion coefficient ($c_{\delta:\theta}$) of vertical deflection to rotation at the specific longitudinal position (x) alongside the InvOLS and resultant interpreted tip deflection:

$$c_{\delta:\theta} = \frac{\theta_{x,Th}}{\delta_{x,Th}}$$

$$InvOLS = \frac{\delta_{ip,EF}}{\theta_{x,EF}} \quad (5.1)$$

$$\delta_{ip,Int} = \delta_{x,Int} \times c_{\delta:\theta} \times InvOLS$$

With the above, comparison was possible for both the tip-up and tip-down orientations of the SThM cantilever in the Interferometer. Moreover, a 15 ° angle in the FDM model for the InvOLS was applied to additionally account for the angling of the cantilever when it was mounted in the AFM for a more accurate depiction of the final tip deflection. A low range of temperature changes (6 K) was utilised due to the AFM's photodetector limits, whereby the Peltier voltage was changed in 0.4 V increments up to 1.6 V. For each voltage change, up to 5 minutes was given for the steady-state temperature to be reached before image/data acquisition. With the data acquired, error bars were constructed for each experiment data point. The X-errors

represent the min-max temperature during measurement, while the Y-errors were different for each measurement technique. For the AFM readings, the min-max InvOLS acquired through the respective F-d curves was utilised while the Interferometer was based upon the standard deviation for each image as six different extracted deflections could be acquired making it statistically significant and providing a better representation of each point's data spread. A TCR of $8.00 \times 10^{-4} \text{ K}^{-1}$ was determined for the SThM cantilever employed (as per Section 3.2.1.2), permitting temperature measurement. The results can be seen in Fig. 5.5.

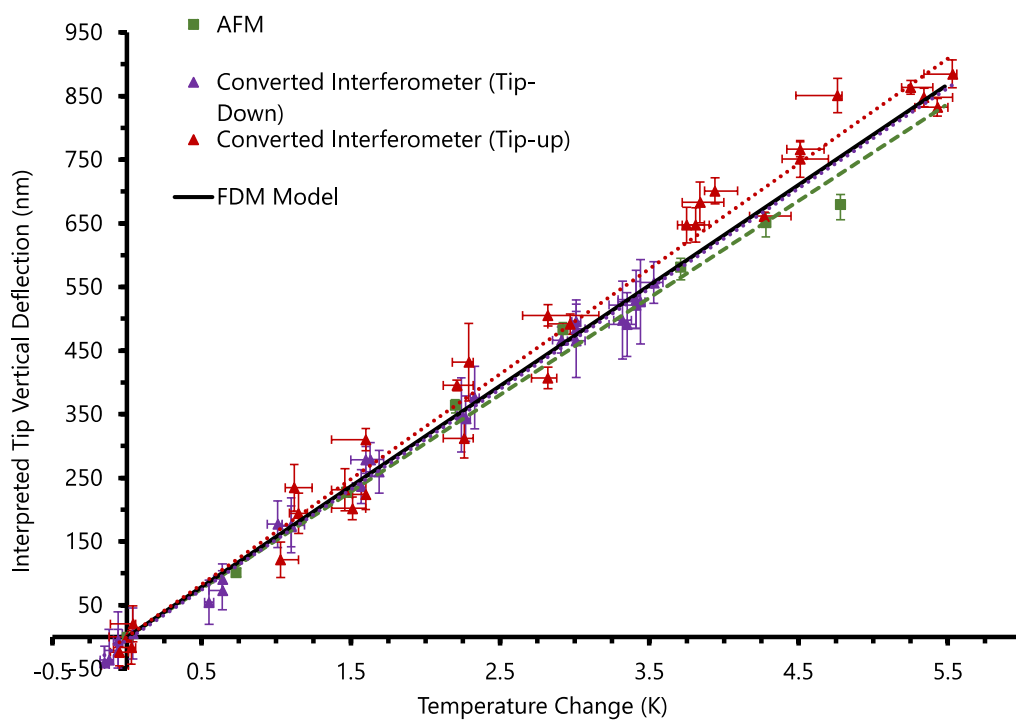


FIGURE 5.5: *AFM's Interpretation of OC Thermal Bending - 1st Experiment*

The first aspect to look at is the converted Interferometer results. Both the tip-down and tip-up results show a good match. This provides confidence that both orientations are measuring the same deflection and it is not being notably influenced by factors such as the light's path of either reflecting directly off the Au or refracting and/or reflecting off the more transparent SiN_x. The Interferometer's trendline also agrees well with the FDM Model which indicates the vertical deflection data extracted and converted is of a similar magnitude to the model's. Comparing these to the AFM data, a very similar gradient to both the FDM and Interferometer was produced. This strongly supports the assertion that all three are quantifying the same phenomenon at

a very similar magnitude and that the theoretical conversion is valid to AFM's optical lever system. Moreover, it indicates that the optical lever's laser location technique employed (measuring it through the AFM's optical feed of the cantilever near a surface) provides a good determination of its location. It should be noted that greater variation was observed as is reflected in the error bars. This is a combination of greater environmental perturbation (such as the strong laminar air flow in the facility and greater user movement causing vibration) and DC oscillation in the SThM probe's temperature output (not typical of most SThM probes). The latter was exacerbated by the environmental factors mentioned alongside electrical interference in the set-up and potential sensor contamination. However, even with this in mind, the results overall are still sound with statistically significant errors defined, providing greater confidence on the final gradients and the quantification techniques.

2nd Experiment:

With the 1st experiment validating the link between the Interferometer and AFM readings, the next step was to demonstrate the general link along flat SThM cantilevers by obtaining their thermal bend deflection profile in an AFM system, as seen in Fig. 4.17. As set-out in the Section 3.2.2.2, the above method for the AFM set-up was repeated but with multiple optical lever laser positions along the cantilever length with the thermal induced deflection gradients determined (as seen in the graphical insert in Fig. 5.6). These were then combined together to produce a profile. Specifically, only five different longitudinal positions were taken to produce the profile due to limitations in the spot centre measurement translation and accuracy from the cantilever optical view. These were positioned evenly along the length within the limits of the AFM laser positioning system. The thermal bend deflection gradients were obtained from five separate temperature changes induced by 0.1 V increments from the Peltier heater with the photodetector's vertical voltage noted after a steady-state time of around 5 minutes. With this data, linear regression analysis was employed to produce the subsequent gradients. The results of which can be seen in Fig. 5.6, whereby the relation predicted by the FDM model is contrasted to this. The experimental data had X-errors equal to $\pm 5 \mu\text{m}$ that represent the radius of the laser spot and so provide the degree of uncertainty of its measurement. The Y-errors were constructed from addition of the

relative error from the standard deviation of the InvOLS (determined from five F-d curves) and the linear regression analysis that deduced the gradients.

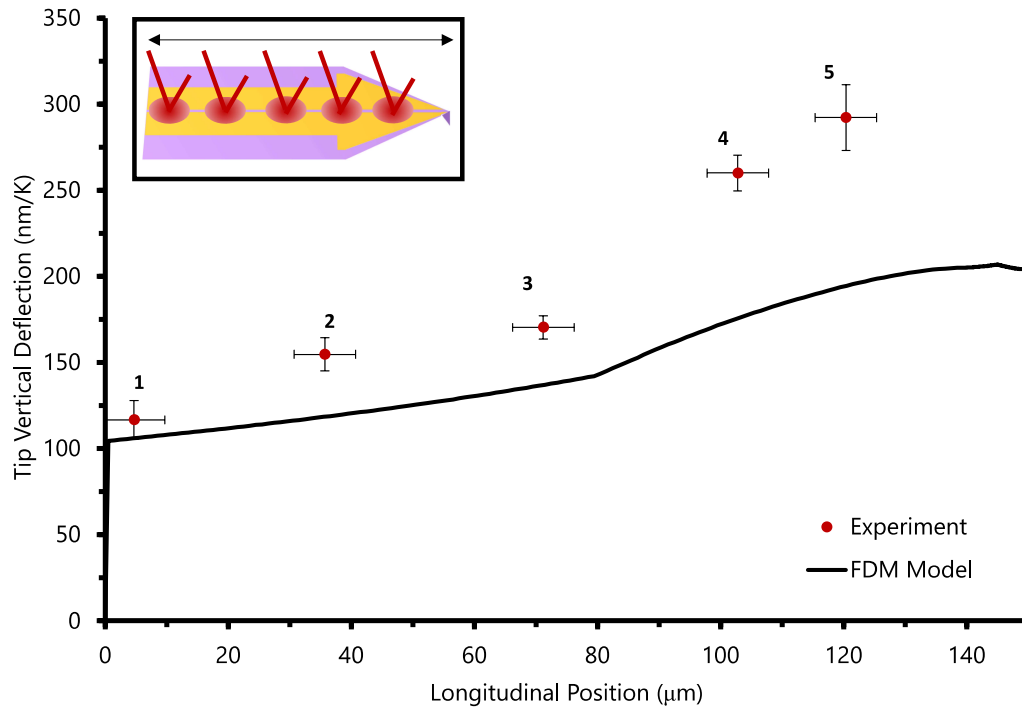


FIGURE 5.6: AFM's Interpretation Profile of OC Thermal Bending - 2nd Experiment with Graphic Depiction of Optical Lever Laser

Analysing this, a comparable relation to that determined theoretically was produced. A flatter and more linear behaviour up-to $80 \mu\text{m}$ along the cantilever was observed with it then non-linearly increasing towards the tip. The exact magnitude shown in the experiment is greater than that determined theoretically. However, this is not drastically larger and well within the same order of magnitude. The difference for which can be explained through differences in material property values such as Young's Modulus and/or CTE. With the tangential nature of thermal bend's rotation being interpreted through the expected rotation and tip deflection from an EF, the general similarity in their shape and magnitude is impressive. In addition, regardless of the absolute comparison to the FDM model, it is consistent with the basic conclusion of AFM's interpretation being erroneous and variable (up to 250 % according to the experiment) for OC thermal bending. As a result, during any measurement of thermal bend's induced deflection in an AFM system, the laser location should be specified. This is clearly the case for SThM, with non-thermal AFM cantilevers being explored later on, but their previous modelling results strongly suggest a similar conclusion.

5.1.2 In-Contact

With OC thermal bending experimentally explored and contrasted theoretically, the same was performed for IC. As mentioned, when a tip is brought IC, a change in the mechanical BC appears to occur. Therefore, thermal bending should manifest differently with this additional mechanical constraint. However, this has not been experimentally verified within the academic community. This may be partly explained by the challenging nature of measuring this as any surface displacements induced from temperature change will contribute to cantilever deflection. Hence, isolated heat sources on or immediate to the cantilever are required. For this, SThM's self-heating capability provided the ideal experimental stimulus as it would provide a low energy, cantilever specific temperature change. The vertical deflection could then be directly measured through the Interferometer and/or an AFM system to elaborate its interpretation. However, this is a SThM specific temperature change and is not possible for non-thermal AFM cantilevers. As a result, a thermally isolated microheater was utilised in a subsequent experiment. Both of these experiments are described in the following sections.

5.1.2.1 Self-Heating Experiment

The experiment was performed according to Section 3.2.3.1, whereby a self-heating induced thermal bend profile was generated. Similar to the previous experiment, this was produced by obtaining the thermal bend gradients at various longitudinal locations and plotting them on a single graph. Both the Interferometer and AFM were employed, with the OC profiles extracted alongside that of the IC to provide a reference as this type of temperature change and induced deflection had not been characterised before. Moreover, the previously described cycling from zero to the maximum safe current for self-heating in Section 3.2.3.1 was employed to minimise drift and SNR issues. This was performed more than five times to obtain gradients of statistical significance and allow for the determination of standard deviation for their Y-errors. The latter was the lone contributor for the Interferometry results while the InvOLS standard deviation was additionally determined for the AFM results with them combined through addition of their relative error (as utilised in Fig. 5.5). Furthermore, the same

$\pm 5 \mu\text{m}$ X-error in the AFM data was employed for the laser's longitudinal location uncertainty. As a result, the following profiles seen in Fig. 5.7 & 5.8 for the Interferometer and AFM respectively is shown for a SThM cantilever with a TCR of $7.33 \times 10^{-4} \text{ K}^{-1}$. Third and second order polynomial trendlines were additionally employed in the Interferometer and AFM profiles respectively. The former was due to the limited number of laser positions that could be obtained in the AFM and so for a like-for-like comparison the same positions were taken in the Interferometer. For the AFM, due to its complex tip-interpreted deflection, a simple second order polynomial was appropriate to simply guide the eye and provide a general form across the cantilever length.

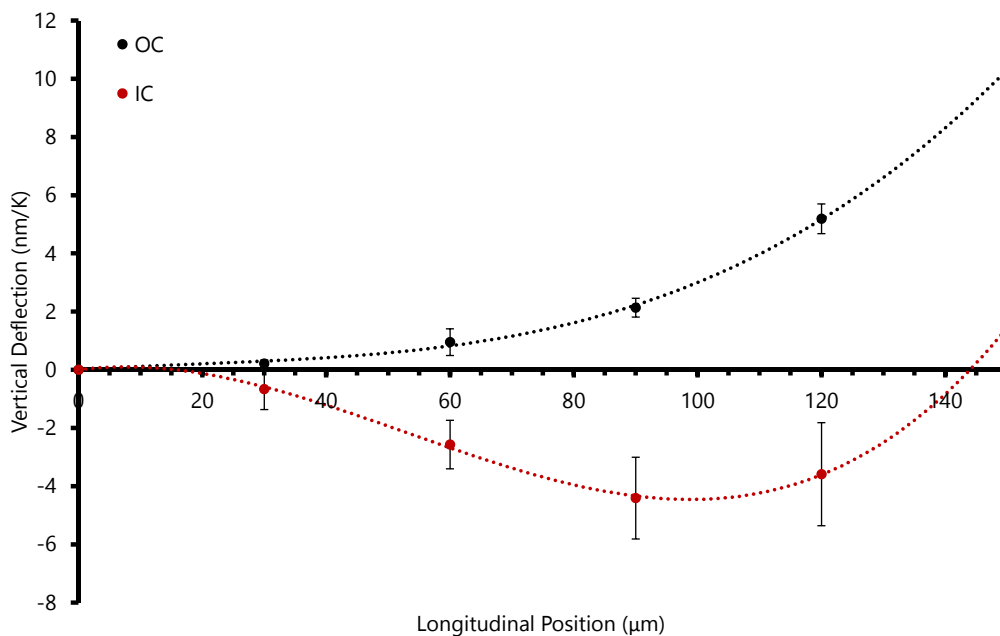


FIGURE 5.7: SThM Self-Heating Experiment - Interferometer OC & IC Deflection Profiles

Focusing initially on Fig. 5.7 for the Interferometry results, the errors seen in the IC results in contrast to those from OC should be first examined. This was due to any instability in the linear translation stage and contact surface causing a change in the tip force and so greater uncertainty. However, with 24 data points contributing to each point's gradient, there is statistical confidence in the results. With this accounted for, the OC deflection is one that partially mirrors what has been seen before for uniform temperature change with it increasing towards the tip. However, the absolute magnitude is far less with a peak result of 5.2 nm/K $120 \mu\text{m}$ along the cantilever (uniform

temperature change producing around 100 nm/K). Moreover, far less deflection occurs at the base. This is due to the tip increasing in temperature more than the rest of the cantilever and as the temperature is measured at this location, a lower subsequent deflection-temperature gradient will be produced, especially nearer the base. A theoretical appreciation of this is possible from the thermal resistive model previously employed as seen in Fig. 4.35. With this reference, the IC behaviour shows a vastly different profile that strongly indicates that the tip's contact is imparting a change in its mechanical BC and so the cantilever's thermal bending behaviour. A humped type profile is shown with an initial negative direction and deflection magnitude at a position around 100 μm where its rotation changes (POI) resulting in an increase towards zero at the tip. Comparing this to the self-heating models for IC thermal bending seen in Fig. 4.36, it agrees well with the general shape with a similar POI position alongside a comparable magnitude with the experiment showing a peak of -4.5 nm/K and the model -4 nm/K. Overall, it provides compelling experimental evidence of what was demonstrated theoretically; that tip contact changes the manifestation of thermal bending.

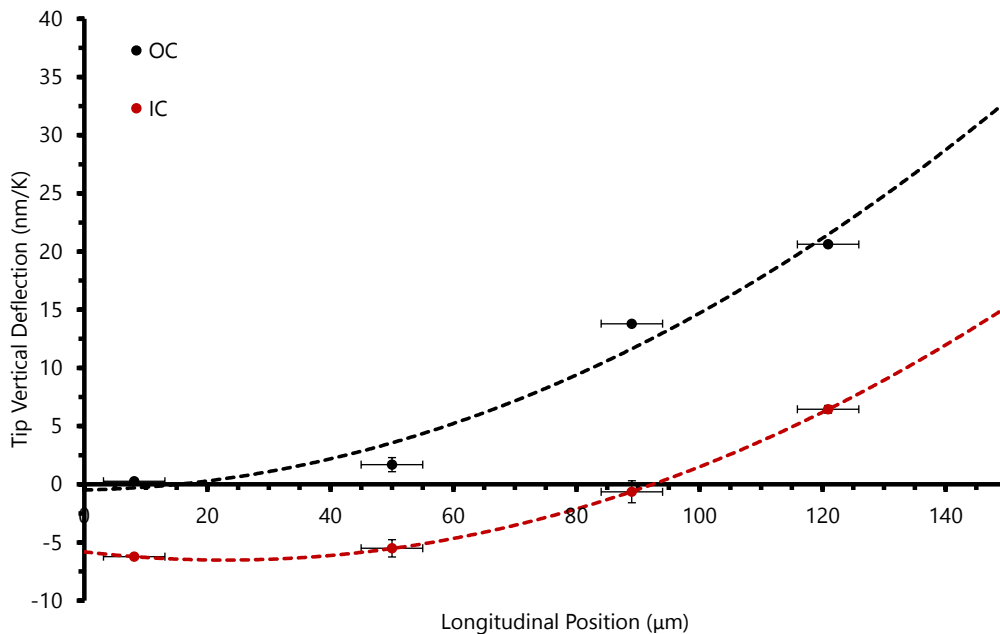


FIGURE 5.8: *Self-Heating Experiment - AFM OC & IC Deflection Profiles*

Moving towards the AFM results in Fig. 5.8, it further backs-up the Interferometer's profiles. From the same cantilever, OC demonstrates a reasonable deflection

profile and magnitude that is greater than the respective positions in the Interferometer profile. However, this is significantly less than would be expected from a uniform temperature change (seen in Fig. 5.6) which fits in to the previous explanation. Moving towards the IC profile, initially it appears to have a very different profile to that depicted in the models and from the Interferometer for vertical deflection. However, understanding that the AFM's optical lever system directly measures the cantilever's rotation, it makes sense. At around $95 \mu\text{m}$ along, there is a change in direction of the vertical deflection interpreted. Towards the base the rotation is negative, while beyond $95 \mu\text{m}$ along it is positive. If this is rotation, the respective vertical deflection graph should show a decreasing deflection up to $95 \mu\text{m}$ along, whereby beyond it should then begin to increase and become less negative. This is exactly what was depicted by the Interferometer and models. Therefore, it is displaying the same phenomenon and supports the modelled IC thermal bending. Furthermore, it also conforms to the understanding of how an optical lever functions in an AFM. Even though this is a unique heat transfer condition confined to SThM probes, the isolated and direct temperature change of the cantilever means that the cantilever's thermal bending was the only contributor to the deflection measured beyond background vibration and noise. Hence, this provides ideal experimental conditions allowing the conclusion that contact of the tip changed its mechanical BC and so changed manifestation of thermal bending.

Before exploring the microheater experiment, the above also demonstrated what was speculated in Section 4.1.3.3 for In-Contact thermal bending, that there is a laser location where zero thermal deflection is measured. In the AFM experiment, not only does the trendline cross the x-axis, but one of the data points very nearly hit this "sweet spot" producing a value of -0.64 nm/K . This is around a tenth of the minimum and maximum deflection magnitudes (-6.2 and 6.4 nm/K respectively) in the overall profile. Moreover, if this is contrasted with the OC condition that is applicable to tapping or non-contact AFM scanning modes, the maximum deflection of 20.6 nm/K is around 33 times larger. Therefore, contact mode scanning presents an innate situation that renders measured thermal bending from AFM cantilever's lower, offering the possibility to negate it if the optical lever's laser is placed in this ideal location. For SThM cantilevers undergoing self-heating, this appears to be around $95\text{-}100 \mu\text{m}$ or

63-66.7 % along according to the experimental data. Whether the same position is observed from external heating more akin to global/uniform heating was subsequently explored through employment of a microheater.

5.1.2.2 Microheater Experiment

A thermally isolated microheater was utilised as seen from the optical image in Fig. 3.14 and underneath the SThM cantilever in Fig. 5.9. This was employed with the Dimension 3100 AFM, enabling two experiments to be performed: one static, as in the previous experiments, and the other scanning in contact mode over the heater. Regarding the initial static experiment, the SThM cantilever was positioned over the microheater while making contact with the thermally isolated Si chip to prevent surface displacement effecting the cantilever deflection. An optical image of the cantilever in this position can be seen in Fig. 5.9 alongside annotations of the five different longitudinal laser locations used to generate the profile.

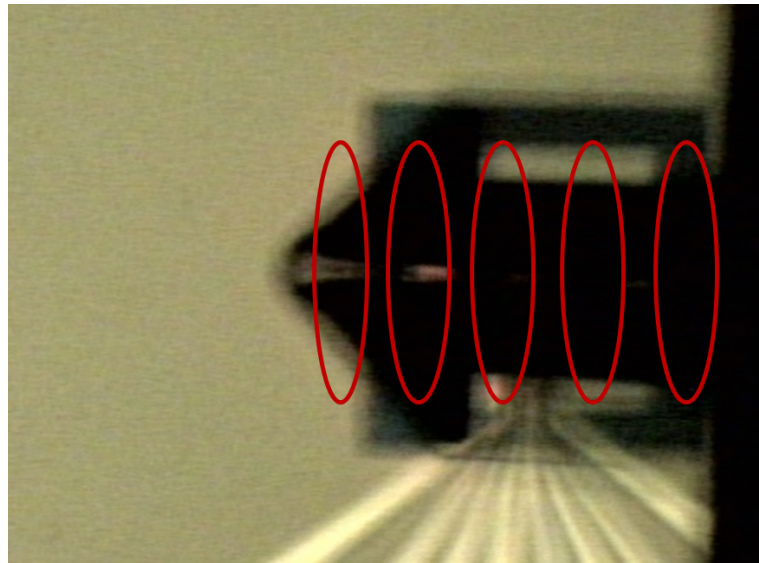


FIGURE 5.9: *Microheater Experiment - Flat SThM Cantilever With Annotated Laser Locations*

Following Section 3.2.3's described zero-ing technique between temperature changes that reduced the effects of systematic drift and maximised the experiment's SNR, the temperature-deflection gradients at each laser location were measured and a profile produced. Specifically, around 1.5 mW power was input into the microheater to

induce temperature increase with 16 measurements taken for each gradient determination (using linear regression analysis). As was the case for the self-heating experiment, both the OC and IC profiles were taken due to the microheater's unique imparted temperature distribution on the SThM cantilever requiring an OC reference for the IC profile. The result of which can be seen in Fig. 5.10, whereby the same SThM probe employed in the self-heating experiment was utilised. This approach aimed to provide greater confidence when contrasting the two. The X-errors were constructed from the previously defined error for the longitudinal laser location of $5 \mu\text{m}$, while the Y-errors were determined from the combined standard deviations from the InvOLS and linear regression determined thermal bend gradients through relative addition. A second order polynomial trendline was imparted to guide the eye, as performed in Fig. 5.8, due to AFM's complex overlaid interpretation.

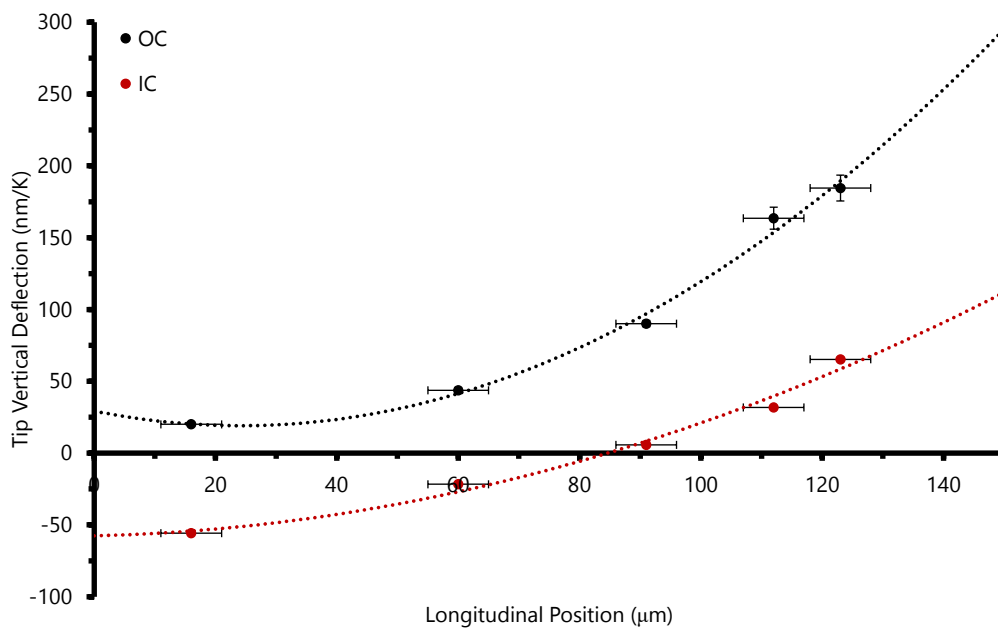


FIGURE 5.10: *Microheater Experiment - Flat SThM OC & IC Deflection Profiles*

Focusing on the OC profile initially, a deflection increasing towards the tip occurred with a measured range of 20-185 nm/K from base to tip positions. The general deflection of which is less than that imparted uniformly from the Peltier heater due to the microheater only heating the portion of the cantilever directly over the heater. In this case it was over the centre of the cantilever as seen in Fig. 5.9. Moreover, the probe's main chip and its tip's contact to the microheater's Si chip acted as heatsinks

resulting in the base and tip changing by a lower temperature than the rest of the cantilever. Therefore, less thermal bend induced deflection will have occurred in these regions. Moving towards the IC profile, a negative (-56 nm/K) to positive (65 nm/K) deflection measurement was seen as the laser was translated along the cantilever. This was of a greater magnitude than seen from self-heating and less than the FEA model undergoing an uniform temperature change. This aligns with the known heat transfer and boundary conditions that the OC deflection profile additionally supports. The cross-over or the point there is a change in interpreted deflection direction was slightly different to that from the self-heating with it occurring around 90 μm (60 %) along the cantilever. Although not a large change, this is closer to that of the FEA Model's POI location for uniform heating. This suggests that the concentrated heat increase at the tip in the self-heating experiment shifted the POI towards the tip, while for more uniform heating it will be more central along the cantilever. As a result, it clearly demonstrates that external heating can induce this humped thermal bend profile when IC and so providing further evidence that the tip BC changes with contact and is restricted to some degree. Moreover, it again shows there is a longitudinal laser position that exhibits insensitivity to thermal bending. Overall, this further cements the previous conclusions of a simple solution to dramatically mitigate thermal bend's influence on contact scanning with SThM and possible all bi-material AFM cantilevers.

With the above static experiment performed, a measurement of the actual impact of thermal bending on topography and AFM's feedback system in a scan was performed. This was accomplished through a lateral 100 μm line scan in the region that can be seen from the X-X line annotated on Fig. 3.14 that is repeated in Fig. 5.11 for convenience and clarity. With tip contact on the Si immediately above the microheater, translation would bring the cantilever body (not tip) over the microheater and the unheated Si chip. Therefore, along the scan it would experience a temperature change due to air conduction with the microheater. Moreover, as the tip is making contact over the Si chip that will experience negligible temperature change and surface expansion, there will be minimal interference and so isolated cantilever thermal bending will occur. The line scan was performed at a rate of 0.2 Hz to ensure enough time for the cantilever to change temperature as it translated across the microheater. With these conditions, three different optical lever laser locations at the base, middle/60 % and

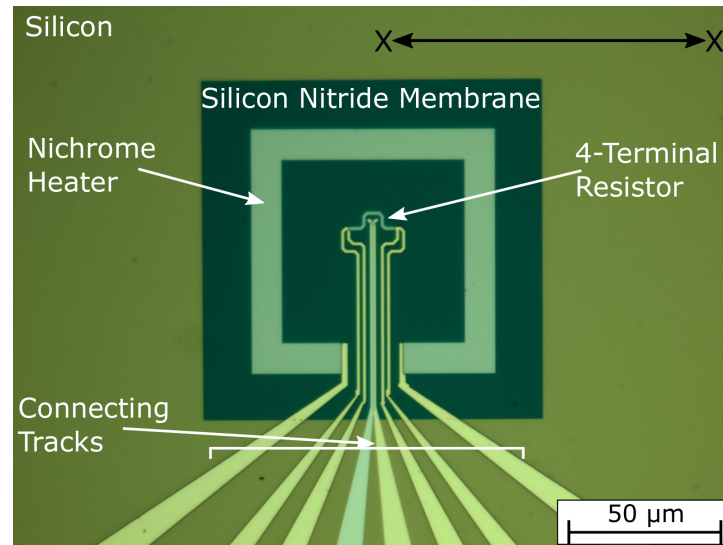


FIGURE 5.11: Image of Microheater Fabricated by P. S. Dobson *et al* [153], whereby line scans were performed along the X-X line

tip were utilised. Each one provided a depiction of the key regions of IC thermal bending seen in the static experiments. The powered (1.44 mW) and un-powered scans for each of these were then subtracted. This subsequently produced the line scans seen in Fig. 5.13 along with the measured tip temperature change in Fig. 5.12.

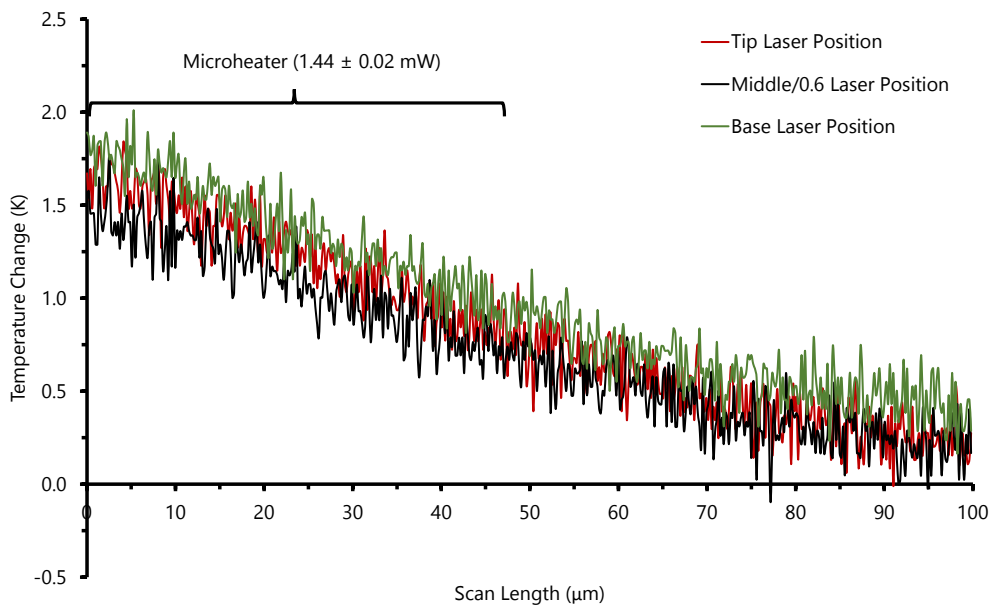


FIGURE 5.12: Microheater Experiment - Temperature Change Line Scans Measured by the SThM Probe

In the line scans, the left side shows the region where the microheater was positioned underneath the SThM cantilever. Therefore, in this region the greatest temperature increase occurred, as seen in Fig. 5.12, and therefore the influence of thermal

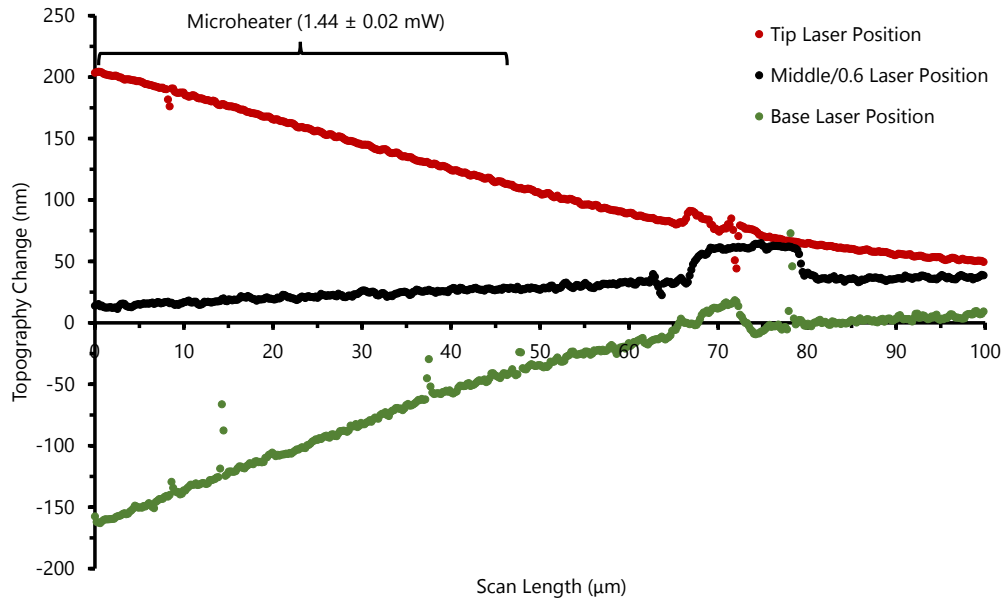


FIGURE 5.13: *Microheater Experiment - Topography Line Scans for a SThM Probe*

bending should be most pronounced. Each laser position undergoes very similar tip temperature changes (around 1.5 K across the scan) and so the cantilever will have experienced the same thermal bending. However, analysing the topography line scans (Fig. 5.13), the behaviour between each of the laser positions' was starkly different. The base laser position produced an increasingly negative output as it moved left to the hotter region with it outputting a total change on -172 nm from left-to-right. However, for the tip laser position, the opposite was seen. As it moved left and heated up, it produced an increasingly positive deflection for a maximum 154 nm increase. For a central laser region around 60 % along the cantilever, far less deflection change was measured of -25 nm. Each laser position's deflection change mirrors that seen in the preceding static IC experiments and provides clear evidence that during actual scanning, this behaviour similarly occurs and is translated into the topographic output. In addition, a marked reduction in the influence of thermal bending was seen with a maximum reduction of 85.5 % from a more central/60 % laser position. Furthermore, this may be able to be improved upon with this experiment indicating translation of the laser further towards the tip should additional reduced thermal bend interpretation.

Overall, the above experiments provide explicit evidence that thermal bending in SThM cantilevers produces erroneous and variable deflection in AFM's interpretation

of them. This occurs both when OC and IC, where the latter produces behaviour closer resembling that of a bridge than a cantilever. However, this produces a unique opportunity for significant reduction of thermal bending's interpretation with a laser spot region of insensitivity 60 % along the cantilever. Positioning the optical lever laser at this location rendered both reduced deflection and topographic output due to temperature change. SThM has provided the perfect vehicle for understanding and depicting this, but whether the results are similar to that seen in other non-thermal, bi-material AFM cantilevers was explored next.

5.2 Non-Thermal AFM Cantilevers

To investigate whether non-thermal, bi-material AFM cantilever exhibit the same or similar behaviour to that seen in flat SThM cantilevers, four different cantilevers were employed. These included MLCT-B, MLCT-C, PNP-DB-100 μ m and Blank-SThM. All of which are contact mode AFM cantilevers with the former three being fabricated commercially and constructed from a bi-material combination of SiNx and Au. The Blank-SThM probe was utilised to act as a zero thermal bend reference as it had no coating and was only constructed from SiNx. As a result, the OC and IC deflection behaviours were quantified through utilising some of the experimental methods explored and employed above for SThM. Specifically, the 2nd AFM Interpretation experiment for OC thermal bending in (Section 5.1.1.2) alongside the set of experiments employing the microheater for OC and IC thermal bend determination were utilised.

5.2.1 Out-of-Contact

Employing the 2nd Experiment in the AFM Interpretation in Section 5.1.1.2, the same method of quantifying the thermal bend induced deflection gradients along multiple longitudinal locations was performed using both the Interferometer and AFM. This produced profiles for each AFM cantilever using each technique, whereby the sample temperature was measured using a PT-100. As a result, this was not as accurate as SThM's cantilever tip temperature measurement previously utilised. However, it still provided a consistent temperature measurement to enable thermal bend gradients and profiles to be constructed. A 2 mm spacer between the probe holder flat and

Peltier surface (therefore cantilever tip and surface <2 mm) was utilised so each cantilever was in as similar a position as possible between their Interferometer and AFM readings to make them comparable. The results can be seen below for the Interferometer and AFM in Fig. 5.14 & 5.15 respectively. The Y-errors employed are similar to previous experiments of the standard deviation from the determined thermal bend gradients.

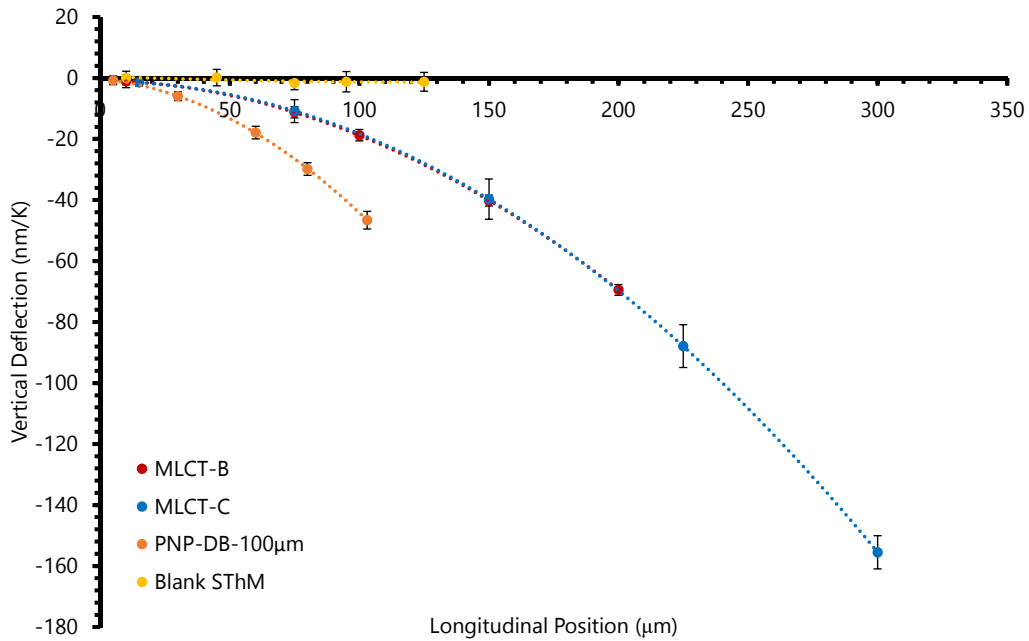


FIGURE 5.14: *Non-Thermal AFM Cantilevers - OC Thermal Bend Deflection Profiles Measured by an Interferometer*

Focusing on the Interferometer results in Fig. 5.14, second order polynomial trendlines were superimposed due to the second order relation of thermal bending with length. As a result, they produced accurate trends to the Interferometer's data points with the subsequent profiles aligning well with the shape and magnitude seen in the modelled thermal bend behaviour for these cantilevers in Fig. 4.38. For example, the MLCT-C cantilever 300 μm along produced a deflection of -156 nm/K from the experiment where the FDM Model predicted -166 nm/K. Although this is very similar, this slight difference will partly be due to the PT-100 measuring a higher temperature for the determined deflection than the cantilever experiences due to its direct contact with the Peltier surface. Alongside this, the models predicted an exact overlap of the MLCT cantilevers due to their matching materials and thicknesses which the experiment has captured exactly. For the PNP-DB-100 μm cantilever, a similar deflection was observed

to that seen in Fig. 4.38. However, this was slightly less (-47 nm/K at the tip) than the model (-41 nm/K) which was different to the MLCT cantilevers. This was potentially due to the thick pyrex block the cantilever was adhered to resulting in a closer proximity of the cantilever to the Peltier surface alongside potentially greater difference in material properties to those employed in the FDM model. Moreover, any variation in the actual material thicknesses from the nominal values utilised in the models can potentially account for this. Moving to the Blank-SThM, a near zero deflection profile was produced with slight variation due to simple measurement uncertainty from noise and residual strain in the cantilever that may have produced some longitudinal displacement manifesting as vertical deflection. Although, it still provides a clear demonstration of thermal bending being due to the bi-material structure of AFM cantilevers with a vastly lower magnitude of deflection than that from the other cantilevers.

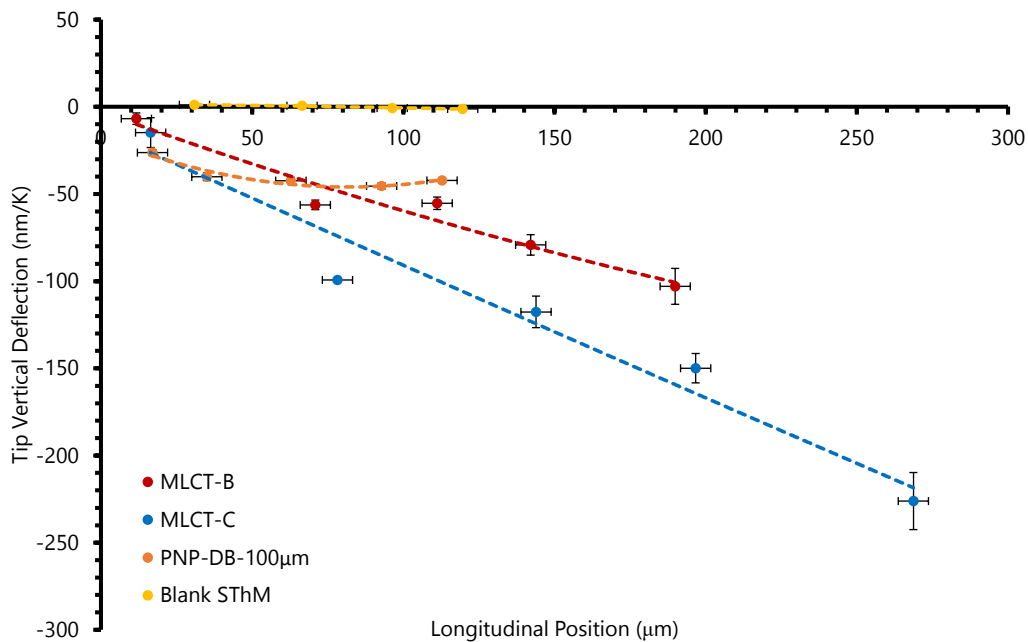


FIGURE 5.15: *Non-Thermal AFM Cantilevers - OC Thermal Bend Deflection Profiles Measured by an AFM*

Pertaining to the AFM results in Fig. 5.15, a similar second order polynomial was applied due to rotation's relation with length for an EF. The MLCT cantilevers exhibited very similar, linear profiles of increasingly negative deflection with laser translation along the cantilever to that as shown by the models in Fig. 4.40. The deflection

magnitude of which is very similar towards the tip to the FDM Models. However, towards the base, the experiment's results tend to zero as opposed a more negative value of -54 and -110 nm/K for B and C respectively in the models. This could be due to the model not considering the slightly curved connection to the probe chip with it assuming a planar connection. Analysing the overall profiles for these MLCT cantilevers, the optical lever (like for the SThM cantilevers) generated a variable and erroneous interpretation of thermal bending's actual tip deflection. This trend is similar to that predicted theoretically in Fig. 4.40. Regarding the PNP-DB-100 μ m cantilever, a more parabolic deflection occurred across its length with this decreasing and plateauing towards the tip, but slightly increasing at the laser position closest to the tip. The FDM model predicted a gradual tip decrease towards the tip (less than that expected from the MLCT cantilevers). This does not exactly match the experimental results, but it is of a similar magnitude and comes to the same conclusion that the interpreted vertical deflection is inconsistent and incorrect. Furthermore, with PNP-DB-100 μ m's parabolic profile and the theoretical model outputting a more gradual deflection change with length, it does indicate that there may be scope to change the geometry of AFM cantilevers to produce a more consistent interpretation. For PNP-DB-100 μ m this may be due to its wide base section. If a more consistent interpretation was possible, it would better align the EF and thermal bend rotations and so their interpreted tip deflection along the cantilever length. With this said, it will be challenging to produce an exact match and insurmountable differences will likely still occur, e.g. variable temperature distributions. For the Blank-SThM cantilever, only four laser positions were obtained. This was due to the laser position near the base being exactly on the base with the laser spot centred on it. As a result, the output had a gross-InvOLS of around 3201 nm/V (the other laser positions covering a range of 67-194 nm/V for their InvOLS) and so the SNR ratio was very low causing it to be highly prone to noise alongside artefacts associated with a laser position on the base. For example, the voltage sum on the photodetector changed more than is typical during the rest of the experiment, with this likely associated with the probe chip notably altering the reflection in a fashion not associated with cantilever rotation. With this noted, the other laser position gradients and subsequent profile produced near zero vertical deflection. This aligns with

the theoretical expectation and the Interferometer's output. Hence, this provides additional support that single material AFM cantilevers do not exhibit the same thermal bending phenomenon as bi-material cantilevers.

Overall, bi-material cantilevers appear to result in the AFM generating the same variable and erroneous interpretation of thermal bending as SThM cantilevers. Therefore, it is essential to state the laser position when reporting data to ensure correct interpretation of any results and for reproducibility. Moreover, whatever the laser position, it should be borne in mind that interpreted tip deflection and likely topographic output too will not provide an accurate representation of the actual tip deflection and simply the specific AFM cantilever, set-up and system's output due to this phenomenon. This will result in the AFM misinterpreting the real tip deflection and so the actual interaction of the tip with the surface.

5.2.2 In-Contact

With the above performed, the next step was to explore the IC thermal bend behaviour for these cantilevers and determine whether they produce a similar profile to that seen for the SThM cantilevers. As the cantilevers have no method of self-heating, the microheater experiment was employed. Similar to that performed with SThM cantilevers, both the OC and IC deflection profiles were extracted by determining the thermal induced deflection gradients at five separate longitudinal laser positions. These gradients were deduced using zero-ing between each temperature change, with the microheater power being driven up to around 1.5 mW for the latter. This was then converted to temperature utilising the average temperature vs. power relation determined by a SThM cantilever tip between the centre of the microheater and the immediate Si chip contact region for each cantilever. Therefore, this provided an estimate of the cantilever's average temperature change, although it should be noted that this is not as exact as for SThM probes, with additional notable variation in the temperature distributions between the cantilevers due to their varying length. The exact position of each cantilever can be seen in Fig. 5.16, whereby different locations relative to the heater were deliberately aimed for. The latter was to help elucidate whether these would generate notable variation in the OC and IC deflection profiles for enhanced insight. Errors were similarly determined to previous experiments with 5 μm X-errors and

standard deviation of both the linear regression and InvOLS for the Y-errors. The OC deflection profiles are shown in Fig. 5.17 to provide a reference and contrast the IC's with third order polynomial trendlines to help appreciate the variable temperature distributions.

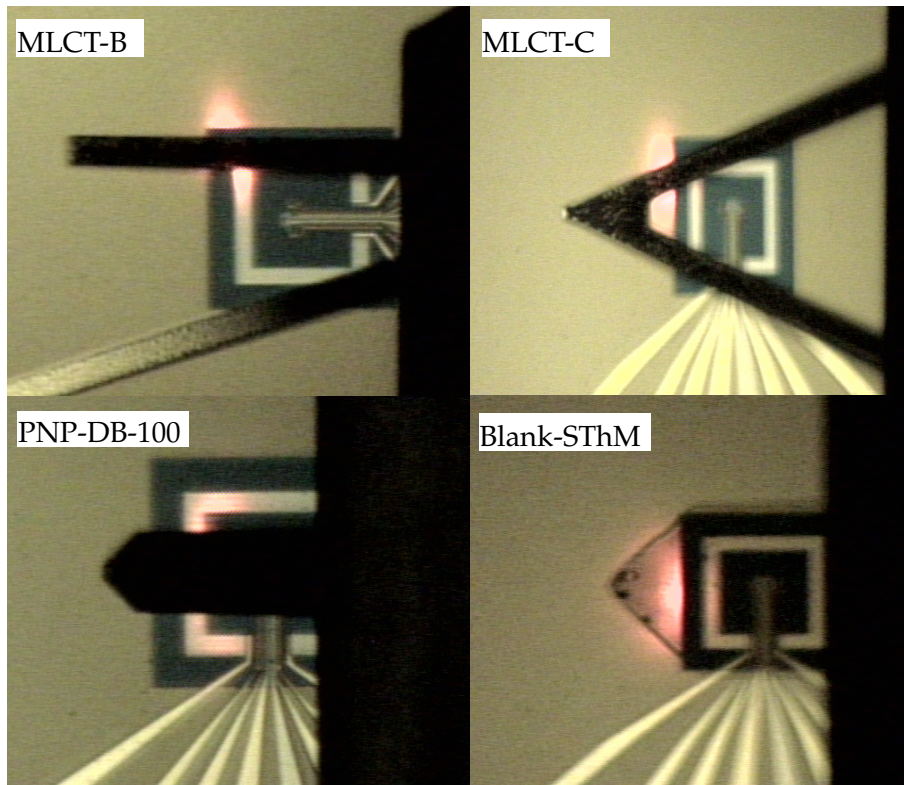


FIGURE 5.16: *Optical Images of Non-Thermal Cantilevers' Microheater Experiment Locations*

Before analysing each profile individually, it should be highlighted that the determined gradients in Fig. 5.17 are all greater than in the previous OC Peltier experiment seen in Fig. 5.15. This was due to a combination of different temperature distributions experienced by each cantilever when compared to the Peltier experiment alongside the cantilever temperature measurement. Regarding the former, the microheater will not generate a uniform temperature distribution like the Peltier with this being different for each cantilever. Moreover, with the Peltier experiment using a PT-100 for temperature measurement and the cantilever differing in distance to the heater, reasonable differences in deflection-temperature gradients magnitudes were expected. With this highlighted, their relative shapes will be accurate depictions as all the gradients along the cantilever lengths employed the same temperature measurement technique. Furthermore, the temperatures were consistently determined between the OC

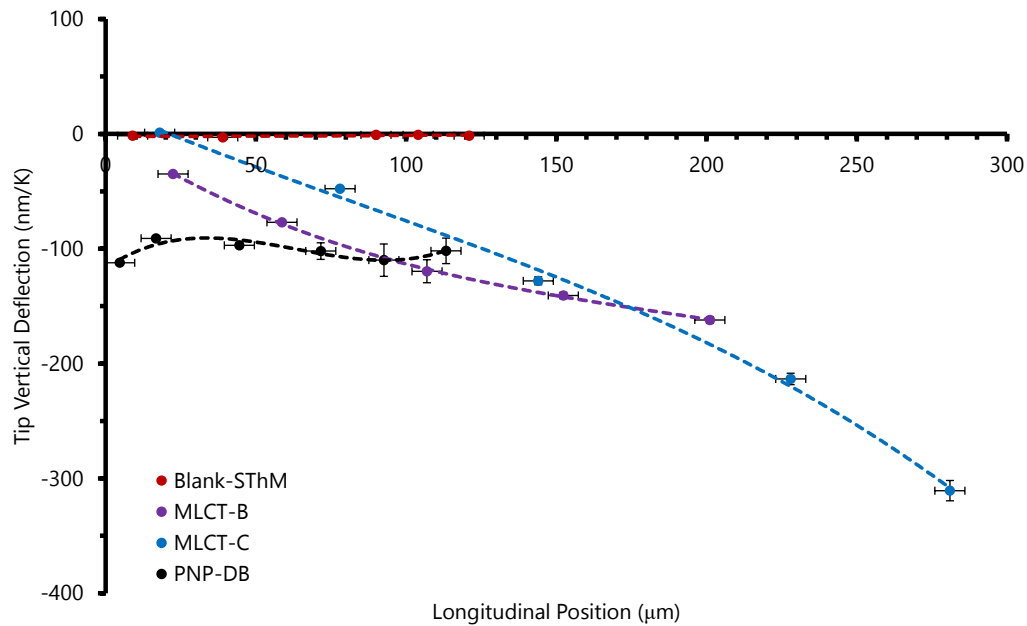


FIGURE 5.17: *Non-Thermal AFM Cantilevers - Microheater Experiment - OC Thermal Bend Deflection Profiles*

and IC profiles so they will be comparable. Analysing the MLCT-B profile, a similar general shape to that seen in the OC Peltier's uniform temperature change was seen with an increase in deflection with laser position closer to the tip. However, as expected with the tip region being above the Si chip as seen in Fig. 5.16, a less emphatic increase in deflection occurred at the tip due to a lower temperature increase. The MLCT-C experienced a different temperature distribution due its 100 μm greater length and the microheater's relative central position in relation to it. As a result, a greater relative temperature change will have occurred halfway along its length with the base demonstrating reduced change. This was reflected in the resultant tip deflection graph, whereby little deflection occurred near the base with it increasing further along than was seen in the Peltier experiment. The PNP-DB-100 μm 's heat transfer condition and temperature change should more closely resemble that seen in the SThM cantilever's due to them being of a similar length and so position above the microheater. Moreover, a more uniform temperature distribution than the other cantilevers will have occurred that may align better with the Peltier experiment's results. This was reflected in the experimental data with a similarly parabolic deflection profile from 10 μm towards the cantilever tip. However, another laser position along the wide base section was obtained which showed an increased negative magnitude in

deflection. This was predicted by the FDM Model's theoretical interpretation as seen in Fig. 4.40 which occurred due to the sudden width increase relative to the rest of the cantilever. Regarding the Blank-SThM cantilever, it re-illustrates what was expected and seen before of a near zero deflection. In addition, with a laser position adjacent and not focused at the base's connection to the main chip, a deflection gradient near the base was obtained that is consistent with the other data points. With these profiles providing references alongside evidence for the type of heat transfer conditions and temperature distributions each were under, the IC deflection profiles are shown below in Fig. 5.18.

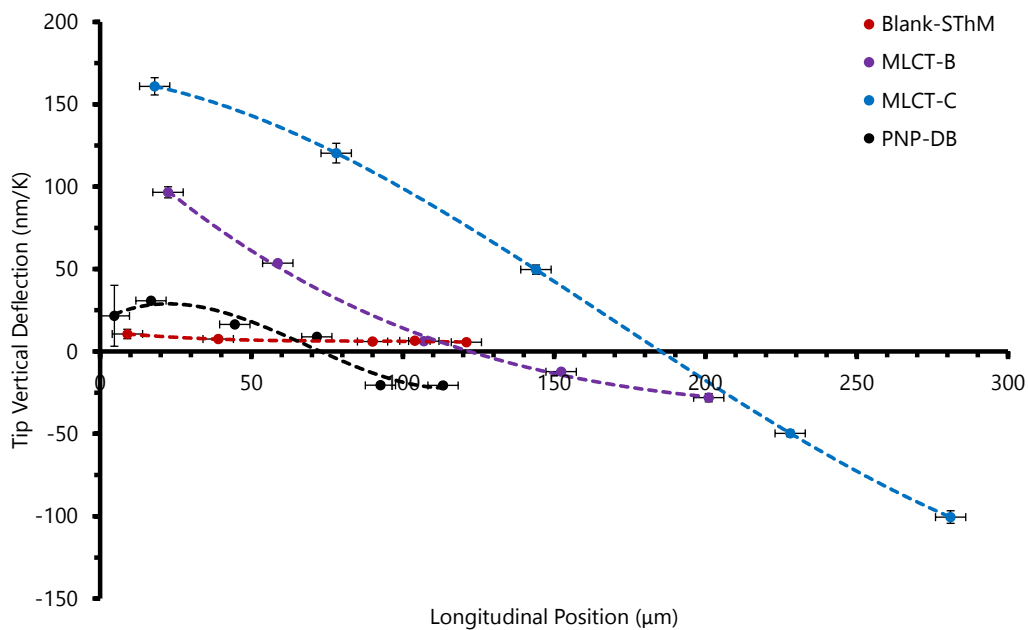


FIGURE 5.18: *Non-Thermal AFM Cantilevers - Microheater Experiment - IC Thermal Bend Deflection Profiles*

What is immediately apparent from the generated IC deflections is that all the metallised cantilevers exhibited a change in deflection direction as the laser was translated along their lengths. Towards the base, positive deflections occurred with opposite negative deflections closer to the tip. This is the reverse to that seen for SThM cantilevers due to metallisation on the opposite side causing a reversed deflection direction during thermal bending (as seen in the prior experiments). Before analysing each profile, the overall profiles immediately bolster the findings from the SThM cantilevers: contact changes the tip's BC causing changes in thermal bend's manifestation for all bi-material AFM cantilevers. Furthermore, the general behaviour aligns well

with that shown theoretically in Section 4.2.2 for IC thermal bending. Pertaining to each cantilever, the MLCT-B demonstrated a maximum and minimum deflection of 97 nm/K and -28 nm/K respectively with a change in direction around 120 μm . This compares really well to the theoretical interpretation in Fig. 4.43 with a similar magnitude range and approximate POI position. For MLCT-C a greater change was seen of 161 nm/K to -101 nm/K with a change in direction at 188 μm . This demonstrates a larger range than theory, but due to the disparity of their temperature distributions and the averaging of various positions for the temperature measurement, it aligns very well. The PNP-DB-100 μm then exhibited a 31 and -21 nm/K deflection with a cross-over point around 72 μm . Interesting, this reflects the FEA model's output of an upward arc near the base, validating that this wide-section does indeed play a significant role in the cantilevers mechanical and thermal bend behaviour. The Blank-SThM cantilever produced a greater deflection than measured in OC and was expected theoretically. Regarding the former, this was likely due to the tip having been restricted preventing longitudinal expansion of the SiNx. Therefore, some deflection and rotation will have occurred producing some deflection which was reflected in the FEA model. However, the latter was predicting sub-nano-metre per Kelvin measurements. Although, with some metal still present near the tip, potentially this manifested itself to generate a slight deflection output. With this said, this is still very low in comparison to the other cantilevers. In this experiment, all the cantilevers had different lengths at which point the deflection direction changed, but this begs the question of whether these are the same relative position along each cantilever. To answer this, the lengths were normalised by division of the longitudinal position by the total cantilever length. The results of which are seen in Fig. 5.19.

Normalising the length shows a consistent point around 60 % at which all the bi-material cantilevers' experience a change in the interpreted deflection direction. This was the case even though each had a different temperature distribution and geometry. This is most likely due to the mechanical BCs at each cantilever's tip being very similar, causing the same manifestation of thermal bending with only the magnitude at either side of the POI differing. As a result, this suggests that when in contact mode, a consistent laser position 60 % along all bi-material AFM cantilevers will exhibit insensitivity to thermal bending. This could provide a very powerful and immediate

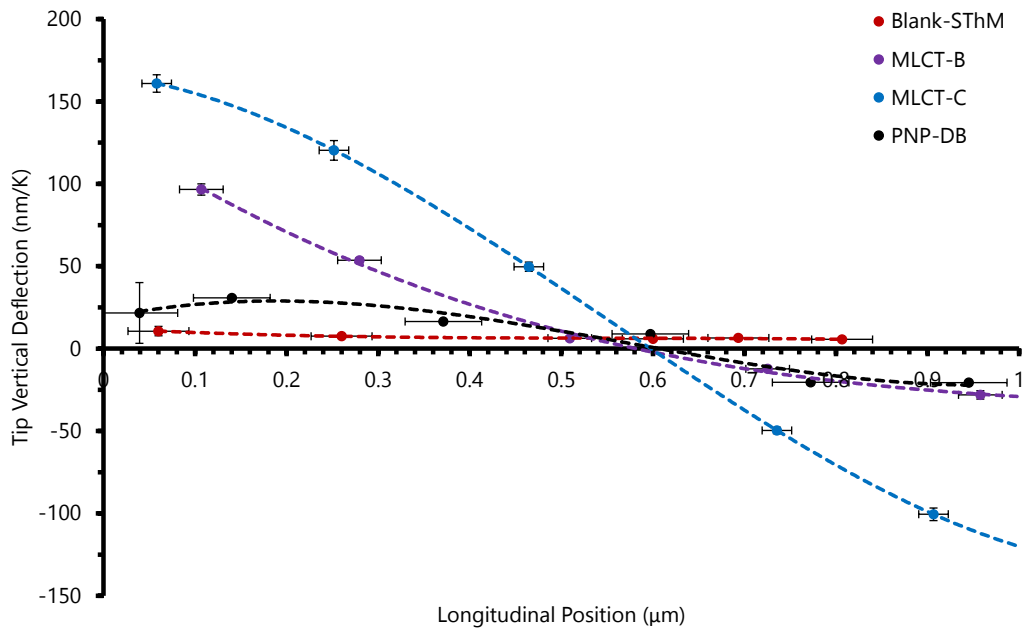


FIGURE 5.19: *Non-Thermal AFM Cantilevers - Microheater Experiment - IC Thermal Bend Deflection Profiles With Normalised Length*

solution that users can apply to mitigate or even eliminate their AFM cantilever's contribution to Thermal Drift. To further demonstrate this, one of the non-thermal AFM cantilevers was scanned along the same X-X line over the microheater, as was performed previously for the SThM cantilever. The MLCT-B probe was chosen due to its narrow $20 \mu\text{m}$ width which should provide a clear contrast between the unheated and heated regions of the scan. As this was performed under the same conditions as the SThM experiment, it will have experienced a similar or slight greater temperature change (1.5 K) due to the cantilevers narrower nature across the $100 \mu\text{m}$ scan length. The resultant change in topography can be seen in Fig. 5.20

A clear mirroring of the topography change was seen for each respective laser position to that of the deflection measurements in the static experiment for the MLCT-B cantilever. For a base laser position, a positive deflection was produced with a respective positive change in topography from the AFM's feedback system. In this case, an increase of 385 nm from right-to-left (i.e. from unheated to heated region) was interpreted by the AFM system. For a tip laser position, a negative deflection and so topography change of -248 nm was generated. Again, this aligns with the direction seen in the immediately preceding static experiment. For the middle/ 0.6 laser location, very little topography change occurred along the scan with a maximum change of round -9

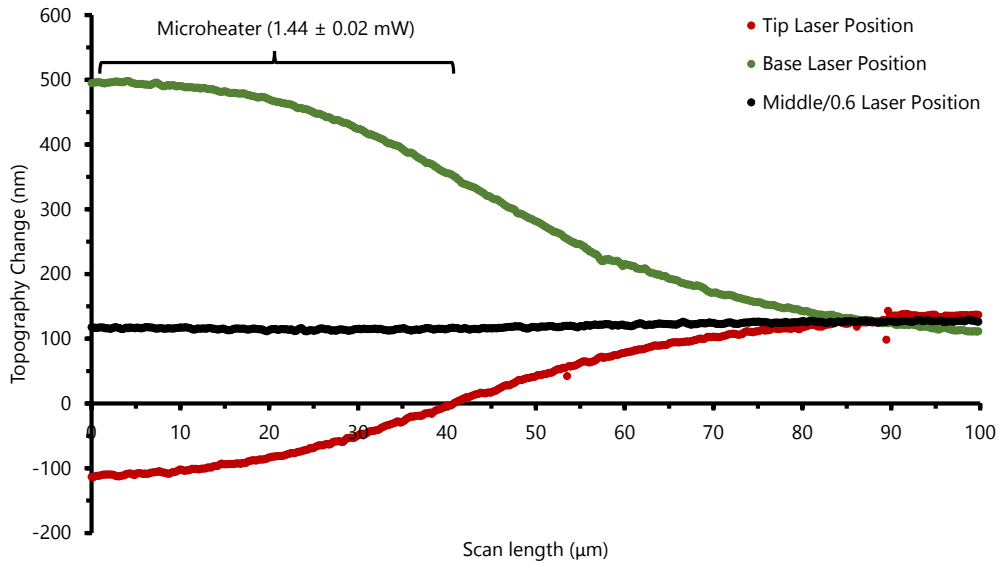


FIGURE 5.20: *MLCT-B AFM Line Scan Across X-X Line on Microheater*

nm. This position was very near the IC thermal bending POI as seen in the models and static experiment which directly fed-back to the topography. This is 97.7 % less than the topography change seen with the laser at the cantilever base, even though both experienced the exact same temperature change and scanned across the same section of Si. Overall, this provides emphatic evidence that simple translation of the laser to 60 % along the cantilever will mitigate thermal bending from contact scanning measurements. However, most AFM scans are produced through rastering across the whole horizontal plane. As a result, this was performed using the same MLCT-B cantilever, whereby scans of the microheater when unpowered/unheated were taken along with that when powered/heated. This scan was generated from the same lateral line pre-

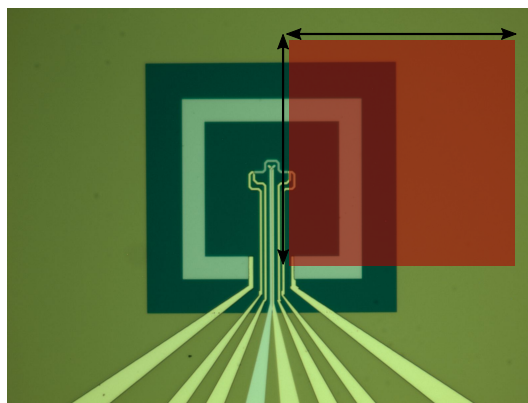


FIGURE 5.21: *Annotated Microheater Image of Scanned Area*

viously scanned with it rastering down across the right-side of the microheater by $100\ \mu\text{m}$ ($100 \times 100\ \mu\text{m}$ scan). This can be seen in Fig. 5.21. A similar power of $1.4\ \text{mW}$ was employed in the microheater with the maximum temperature from the microheater of $6.4\ \text{K}$ noted (determined through SThM tip temperature measurement). These were then contrasted for a similar mixture of tip, base and middle laser locations. Unlike in the line scans, subtraction was not performed of the unheated from the heated scan due to the large and long nature of the scan that would result in significant artefacts from the subtraction process. Moreover, it allows a clear and transparent images of

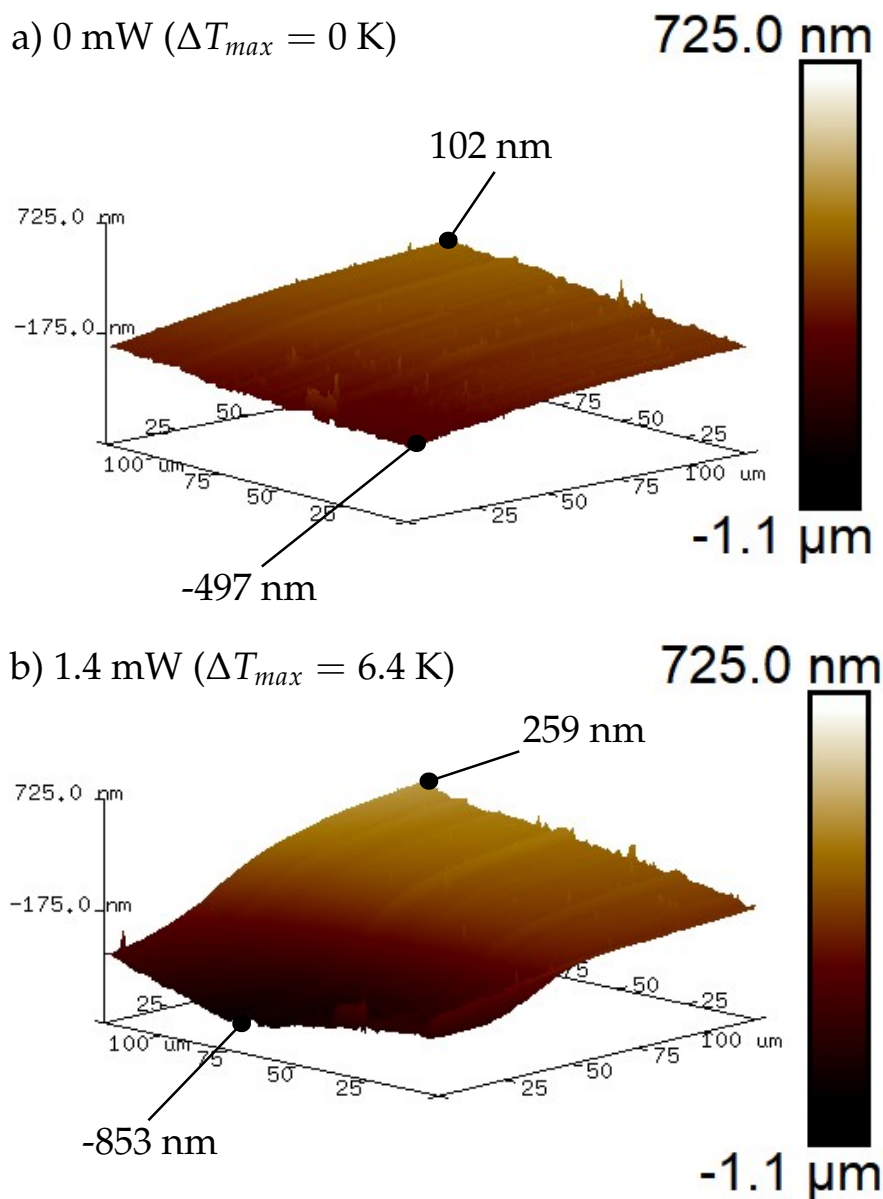


FIGURE 5.22: MLCT-B Full AFM Scan - Tip Laser Position

the surface image obtained in either case which is more translatable to what a user

would see if they compared scans which are influenced by contact thermal bending. The results are shown in Fig. 5.22, 5.23 and 5.24, whereby the same scale has been used for clear comparison between each image. Furthermore, only a low-pass filter was applied to remove extreme spikes, but not manipulate the general form of each scan.

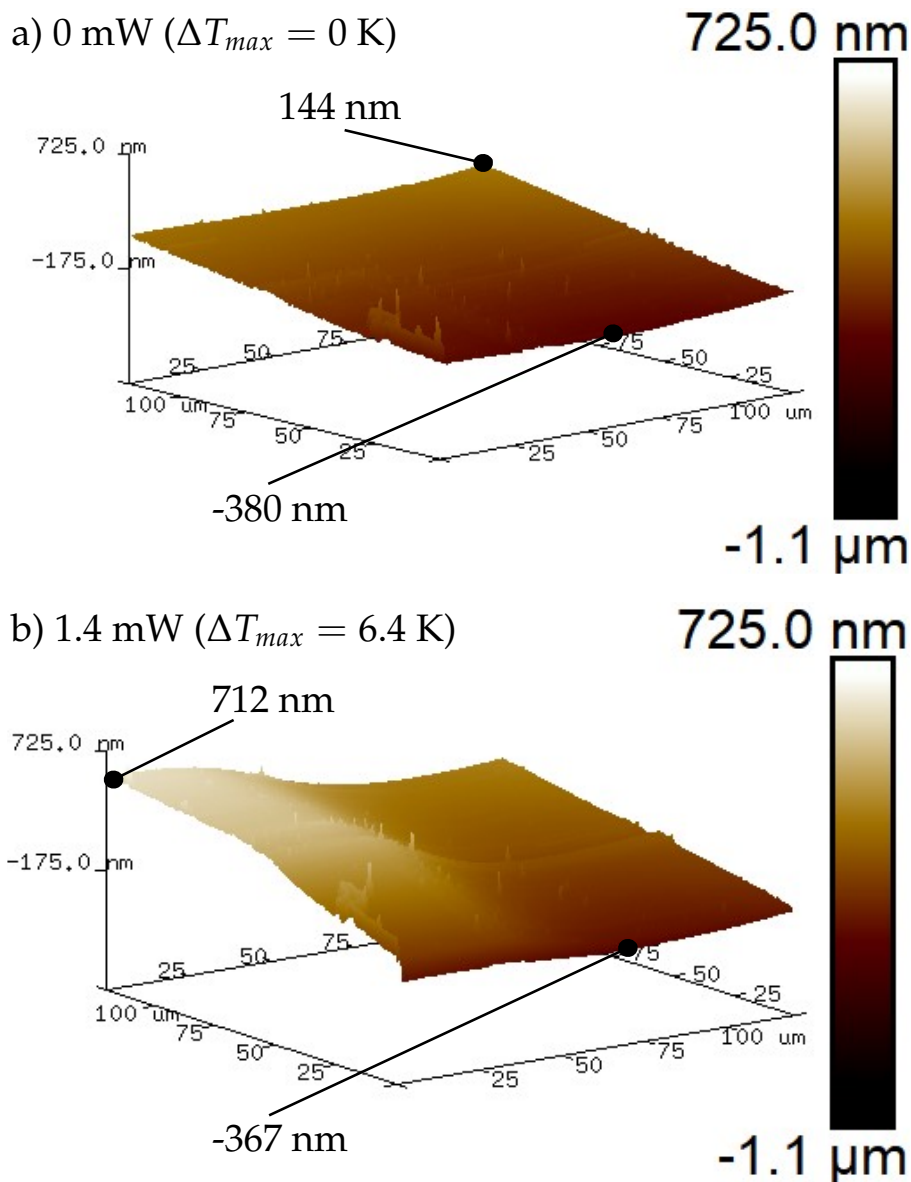


FIGURE 5.23: MLCT-B Full AFM Scan - Base Laser Position

Considering the tip laser readings in Fig. 5.22, the heated image shows a clear negative topographic change over the left-side of the scan where the microheater is situated. The change relative to the right-side is emphatic with a maximum change of $-1.11 \mu\text{m}$, which is around $-0.51 \mu\text{m}$ more than demonstrated in the unheated scan (0.6

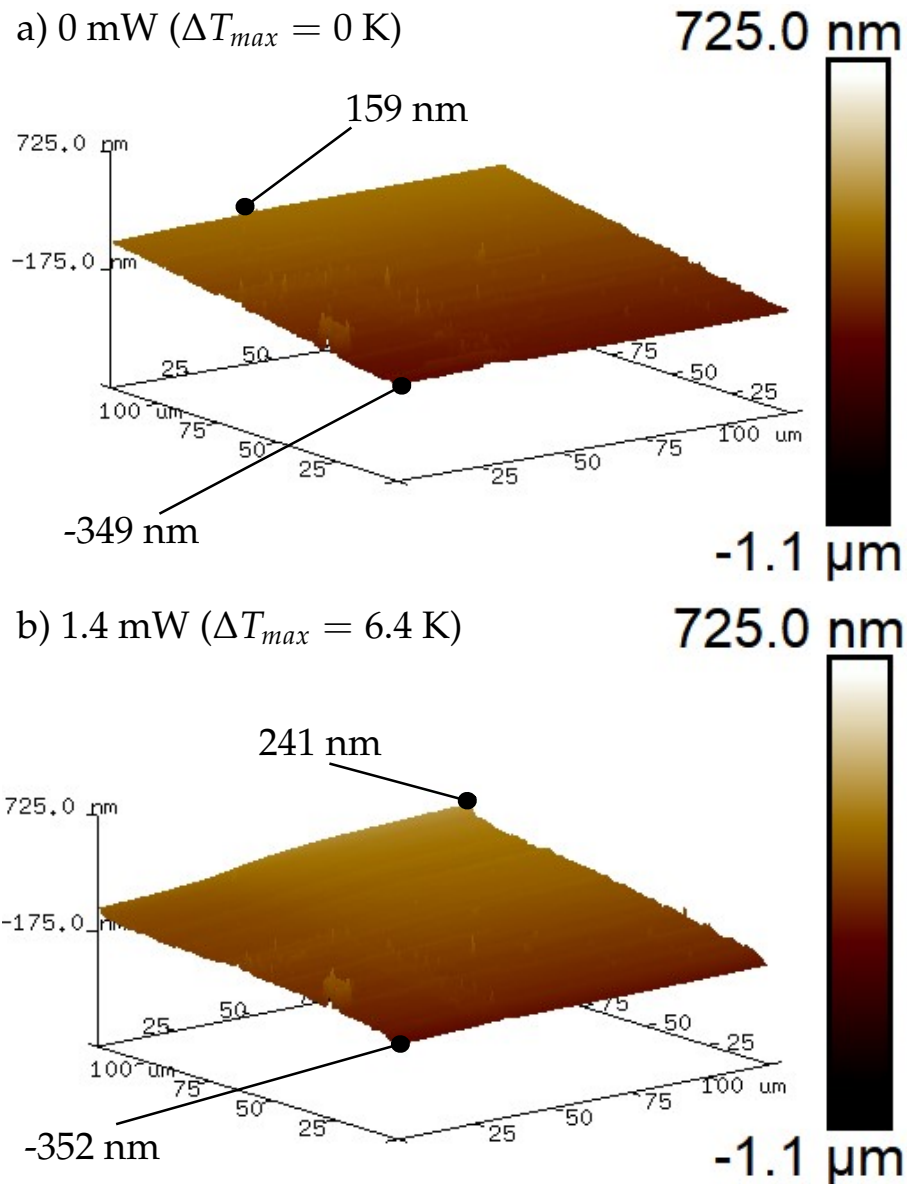


FIGURE 5.24: MLCT-B Full AFM Scan - Middle Laser Position

μm). It could be speculated that some of this topography change could be due to the microheater's membrane displacing. This will have occurred, however confirmation using the Interferometer indicated only 0-7 nm worth of displacement for the same power and temperature change. This clearly does not account for the 510 nm of change observed and all of the evidence appears to clearly indicate the majority of this was due to the cantilever's response to temperature change. This is further reinforced by comparison with the other scans. Regarding the base laser scans in Fig. 5.23, the opposite effect was produced to that from the tip's. A topography increase in the left region over the heated microheater with a change up to $1.08 \mu\text{m}$ while the unheated

scan only showed $0.52 \mu\text{m}$. This further backs-up that this topography change was not due to the microheater's SiNx membrane displacing and it was due to the cantilever and the laser's position. For a middle laser position in Fig. 5.24, there was a slight dip in the heated image towards the top left portion. However, this is far less than in the previous two graphs with a maximum topography change of $0.59 \mu\text{m}$ which is a relatively small increase of $0.08 \mu\text{m}$ from the unheated image of $0.51 \mu\text{m}$. Therefore, the middle laser position produced a significant reduction in the interpreted thermal bending relative to the other positions. This further verifies the benefits of this laser position as a way of mitigating the impact of thermal bending from AFM cantilever's and minimising its contribution to overall Thermal Drift.

To sum up the above for non-SThM bi-material AFM cantilevers, a consistent set of thermal bending profiles occurred. Their OC thermal bend behaviours' all differed from that generated by an EF and so produced a variable and erroneous interpretation of tip deflection. When the AFM cantilever was brought IC, the tip's new mechanical BC produced an almost bridge like structure that generated a pronounced and consistent change in the thermal bend profiles. This was emphatically different to that from OC, where it is evermore apparent the impact of optical lever's direct measurement of rotation in AFM systems. As a result of the latter, a POI in the deflection appeared consistently around 60 % along all the cantilevers when undergoing a temperature change induced by a microheater. Therefore, it can be concluded that, if the laser is positioned at this location, it will produce a consistently lower deflection and topography change due to thermal bending across a reasonable range of temperature distributions. This is backed-up from the experimental data, whereby the line and full scans of the microheater demonstrate a marked reduction of up to 97.7 %. All of these trends are mirrored in the SThM cantilevers as well; reinforcing the above conclusions. However, despite this remedy, the core problem of thermal bending still occurs and will cause a variable tip force from AFM's erroneous interpretation regardless of laser position. Hence, the work was expanded in an attempt to mitigate this problem at source through adjustments to cantilever design.

6. Attenuation of Thermal Bending in AFM Cantilevers

All the work described in the preceding chapters has been about understanding and quantifying thermal bending. The simplest solution identified to eliminate this phenomenon was to employ AFM cantilevers constructed from only one material (as shown by the Blank SThM data), although careful positioning of the AFM's optical lever laser could also help minimise its impact. However, it is not always possible to use single-material cantilevers, particularly as some AFM techniques require multiple-material cantilevers for additional functionality (such as SThM). In addition, repositioning the laser does not remove the impact thermal bending has on tip-sample interaction force. Addressing thermal bend in multi-material cantilevers was the motivation behind the grooved SThM cantilever and was proven to not be completely effective in the previous chapters. As a result, alternative solutions are needed for these multi-material probes, and this was explored by employing flat SThM cantilevers. For this, the aim was to attenuate both the OC and IC thermal bend behaviours, producing an all-in-one ideal solution. The concepts uncovered were then followed by work on non-thermal AFM cantilevers to explore the solution when applied to more widely used probes. However, before going straight into the potential solutions, the exact nature of what is desired and how to measure its success needs to be defined.

6.1 Objective & Approach

The main goal was to reduce and ideally render negligible thermal bending in AFM cantilevers. This was not only in terms of the absolute tip vertical deflection, but also

in the interpretation by AFM systems, ideally for both OC and IC. As the interpretation is based upon the rotation of the cantilever, this similarly needs to approach zero. However, the point on the cantilever that this rotation is measured from can be inconsistent due to the user's optical lever laser positioning being prone to variation. Therefore, zero rotation would ideally span a long and consistent section near the cantilever end/tip to account for this. Hence, the following statement neatly summarises the objective for attenuation of thermal bending in bi-material/metallised AFM cantilevers:

To consistently render zero vertical deflection of the cantilever tip and zero rotation spanning a relatively long section near the tip for both Out-of-Contact and In-Contact thermal bending of AFM cantilevers

The above provides a nice general summary and aim, but along with the above there is a caveat to the use of SThM cantilevers in this study. This is that these complex probes already have a large number of fabrication steps (up to 66 as seen in Appendix D). Therefore, the above objective should be a solution that adds little additional complexity onto the already challenging fabrication process. This consideration is not just true for SThM probes and many other AFM probes that require metallisation are also complex and so have lengthy fabrication procedures. Hence, a simple to fabricate solution would be desirable to AFM cantilevers overall. The exact approach to execute this was a methodical, tiered one which complied to the following procedure:

1. Design Brainstorming (based upon knowledge and understanding acquired)
2. Design Modelling - FDM & FEA
3. Measure Key Design Aspects from Models based upon the Objective Stated
4. Construct a General Fabrication Process for the new Design
5. Overall Design Effectiveness and Feasibility Analysis
6. Design Sensitivity Analysis
7. Simple & Quick Feasibility Study
8. Fabrication of Design(s)

9. Experimental Quantification of key thermal bending Measures and Objectives: Direct Vertical Measurement and Interpretation utilising Interferometer and AFM respectively for OC and IC

As a result of the above, a clear aim and pathway to achieve the goal was established, whereby flat SThM cantilevers were first explored and used as a metaphorical canary to investigate potential solutions. This would then be followed by work to ascertain how this solution would help other non-thermal AFM cantilevers.

6.2 SThM Cantilevers

Before a solution to thermal bending was explored, a reason why grooved cantilevers (as seen in Fig. 6.1) were not taken further should be elaborated. From the joint modelling and experimental efforts with grooved cantilevers, their poor efficacy at attenuating thermal bending was identified as being due to a combination of factors. The first one is that the current commercial design does not have a deep enough groove for the Au to be correctly positioned in line with the NA to benefit from the full effect. However even if this was corrected, as demonstrated in the modelling efforts, the effect only comes into play with a long enough cantilever for a large enough length-width ratio. For SThM's near the theoretically ideal groove depth, this appears to occur when it approaches 300 μm long for a reduction in vertical deflection to occur across the whole cantilever width. This is double the length of current SThM cantilevers. Although, the groove depth can be increased to minimise this, significant depths would be required that would similarly cause dramatic variation in spring constant; pronounced deflection change laterally (effecting the laser position on the photodetector); still be reliant on SiNx thickness that is known to vary across wafers and would need a large experimental study to ascertain the real-world required length-to-width ratio. Additionally, reducing the cantilever width to achieve the required length-to-width ratio is highly undesirable with the Au wires required to be narrower which will impede the thermal and topographic capabilities of the probes. Overall, whichever tactic was used to shift the design, it would not generate a great solution and with nominal dimensions likely produce a large variation in cantilever thermal bend attenuation performance across wafers and batches.

FIGURE 6.1: *Grooved SThM Cross-Section Diagram*

With this clear, an attempt was made to explore other potential solutions that would provide a theoretically more ideal, simpler and easier to fabricate solution with a greater degree of robustness. To achieve this, the defined objective and approach articulated was adhered to. The first exercise performed was a brainstorming of potential solutions theoretically possible and that fitted into the confines of the current probe fabrication process. Their efficacies were explored with the best and most practical solution taken forward. A greater depth into its effectiveness and fabrication process was investigated and elaborated, followed by a subsequent initial design study to properly analyse it experimentally. With the cantilevers fabricated, a main design study was executed with the results and its conclusion elucidated. The impact of which on the understanding of SThM and other bi-material cantilevers was then possible.

6.2.1 Potential Solutions

A list of potential solutions was informed from Chapter 4 and 5's work, with some having the potential to provide a complete solution, while others have a limit on their capability. All of them are listed below:

1. Lower CTE & Young's Modulus Wire Material

Instead of Au, another conductive and reflective material with a lower CTE and/or Young's Modulus could be employed to help reduce thermal bending. The candidate materials explored were Palladium, Platinum and Tungsten (this list was limited by the available evaporated metals within the JWNC). With these potential metals, this solution would only be able to reduce thermal bending and not completely remove it.

2. SiO_x on Coating-Side

SiO_x has a lower CTE than SiN_x with SiO₂ approaching 0.5 ppm K⁻¹ [206]. Therefore, if this were layered on-top of the SiN_x on the same side as the Au, then the SiN_x will generate a thermal bending moment towards the SiO_x that

could counteract the Au's to the SiNx. This could either mitigate the latter or even completely attenuate it.

3. Wider Coating Position

General thermal bending studies in FEA have indicated that when the Au wires are located further to the edges of the cantilever, the resultant thermal bending is reduced. Therefore, this could be exploited to minimise thermal bending from one simple lithographic step.

4. Backside Deposited Metal

If another material with a high CTE (i.e. a metal) is deposited on the back of the cantilever (i.e. the opposite side to the Au on the SiNx), then a thermal bending moment will be generated in the opposite direction to the one from the Au and so counteract it. This theoretically has the potential to provide a complete solution and be implemented from one single deposition.

With the above listed, each were explored theoretically and the findings articulated under the respective title.

6.2.1.1 Lower CTE & Young's Modulus Wire Material

One of the simplest solutions to reduce thermal bending would be to utilise a different wire material to the Au currently used, with a lower CTE and Young's Modulus. The lower CTE will result in a lower thermal expansion, longitudinal displacement and force disparity between the wire/coating and the SiNx, resulting in a lower thermal bending moment and vertical deflection. Moreover, if the material had a lower Young's Modulus, then the magnitude of force produced for any given temperature induced expansion and longitudinal displacement would be less, generating a lower thermal bending moment and subsequent vertical deflection. However, there are restrictions to what can be realistically utilised to substitute the Au for SThM probes. The material needs to exhibit low electrical resistance (minimal Joule Heating and resistance effecting the thermometry measurement), be highly reflective (to reflect the optical lever laser when it passes through the SiNx) and be unreactive with TMAH during the final release etch. A table depicting various potential alternative metals to Au that could be deposited at the JWNC facility are shown in Table 6.1 with their key

respective bulk properties. The latter are based upon the crucial criteria stated above, whereby only bulk property magnitudes are stated as an in-depth literature review of each metal's thin film properties was unmerited at such an early scope-out stage.

TABLE 6.1: *SThM Potential Wire Material Properties*

Coating Metal	CTE (ppm K ⁻¹)	Young's Modulus (GPa)	Electrical Resistivity (Ω m)	TMAH Reactivity
Au	15.6	64.39	2.05×10^{-8} [166]	NO
Pd	11.2	121	1.01×10^{-6} [166]	NO
Pt [166]	9	170	9.81×10^{-7}	NO
W [207]	4.98	340	1.165×10^{-7}	YES [208]

With the above values, these materials can be inputted into the models developed to analyse their relative ability based upon the current SThM cantilever dimensions. Due to its inherent flexibility and ease of use, the FDM Model was applied for this study as no exact quantification or IC thermal bend analysis was required at this stage. The results can be seen in Table 6.2 for their effect on SThM cantilever spring constant and tip vertical deflection from thermal bending. One aspect not appreciated in these results is any change in the geometry due to the use of any of the materials. For example, Au has a far lower electrical resistivity to each material explored and so if a similar resistance is desired, a far greater thickness of each metal would be required. Although, a similar argument could be made for reducing the thickness to produce a probe of similar stiffness, especially for Tungsten. However, this conjecture was not taken further in the modelling as it was deemed out-width the initial scope-out remit as well as making the comparison more convoluted. Therefore, it is something that should be borne in mind if this was further investigated in design studies.

Comparing the results in Table 6.2, the Pd produced little reduction in thermal bend induced deflection. When this is coupled with the x200 increase in electrical resistivity relative to Au, it would produce an order of magnitude increase in self-heating and a dramatic shift in resistance effecting SThM's thermal ability. For Pt, a reduction in thermal bending of 32 % occurred. This a notable decrease alongside

TABLE 6.2: SThM Potential Wire Material Mechanical & Thermal Bend Results

Coating Metal	Spring Constant (N/m)	Thermal Vertical Deflection ($\mu\text{m}/\text{K}$)
Au	0.170	0.166
Pd	0.198	0.138
Pt	0.220	0.113
W	0.289	0.051

an increase in the cantilever's spring constant. Moreover, out of all the alternative materials it has the closest matching electrical resistivity with it being around double Au's. However, this would still render an appreciable increase in self-heating of the cantilever and impede its temperature measurement. Regarding Tungsten, a significant reduction of 69 % in thermal bending would be produced, although this comes with a 5.7 fold increase in electrical resistivity when compared to Au. Its large Young's Modulus would also produce a large increase in cantilever spring constant that may effect SThM's ability for sound contact mode topographic imaging. Unfortunately it has another drawback relative to the other materials as it does react with TMAH. Although this reaction is relatively slow and typically used for etching a small amount of the surface in industry to lift-off contamination post chemical mechanical polishes. However, considering the 80 °C submersion for 90-180 minutes in the final release etch, a significant amount of material could be etched away that would alter the electrical, thermometry and mechanical properties of the probes. Overall, most of these materials are not ideal with Pt the most plausible alternative for SThM.

6.2.1.2 SiOx on Coating-Side

If SiOx were deposited on the same side as the Au, it could generate an opposing thermal bending moment to that from the Au to the SiNx. This is possible as SiOx has a lower CTE than SiNx [206]. Therefore, the SiNx would generate a thermal bending moment towards the SiOx. However, a reduction in thermal bending beyond stiffening would only occur if no Au was deposited on the SiOx. This is because the Au would generate a greater thermal bending moment to the lower CTE SiOx. Hence, any benefits from the SiNx-to-SiOx moment will be rendered moot. As a result, the SiOx

would need to be located on the areas the Au does not cover. A diagram showing this can be seen in Fig. 6.2.

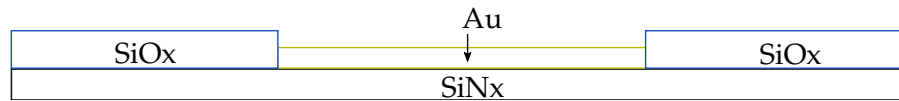


FIGURE 6.2: Cross-Section of a Flat SThM Cantilever with SiOx

To determine the potential efficacy of depositing SiOx, its relevant material properties were obtained. At this early stage of design exploration, the bulk SiO₂ properties were utilised and are listed below [206]:

- $\nu_{SiO_2} = 0.155$
- $E_{SiO_2} = 73 \text{ GPa}$
- $\alpha_{SiO_2} = 0.50 \text{ ppm K}^{-1}$

These properties can be employed in models to determine the potential efficacy of this design concept. A study of SiOx Thickness vs. Tip thermal bend induced deflection was performed with the SiOx covering all the areas not covered by the Au on the same side of a typically patterned, flat SThM cantilever. The FDM model was employed due to its in-built sensitivity analysis feature and speed with it able to output the results in seconds instead of days-weeks for the equivalent analysis through FEA. The result of this can be seen in Fig. 6.3 & 6.4 for a SiOx thickness range of 0 to 800 nm for the subsequent change in spring constant and tip deflection due to thermal bending respectively.

The graphs demonstrate that this design could potentially work as a complete solution with the tip deflection changing direction at around 500 nm of SiOx. This is good to be able to completely counteract the Au, but the required thickness indicated by the FDM model is substantial. As a result, it produced a pronounced increase in the spring constant from 0.17 to 0.51 N/m. This changes the cantilever's inherent mechanical behaviour for scanning by a significant degree and hence its potential usability. However, an effort can be made to minimise the required SiOx by reducing the magnitude of Au it needs to counteract, e.g. removal of the sudden width increase 80 μm along the cantilever. In addition, the Au pattern can be altered to produce a

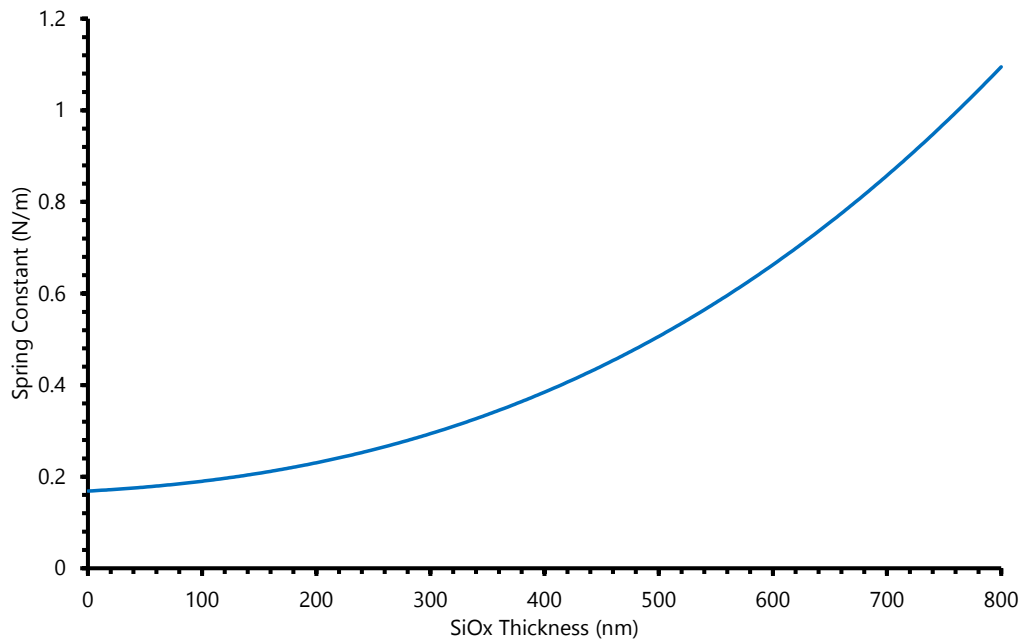


FIGURE 6.3: FDM Model - SiOx Thickness vs. Spring Constant

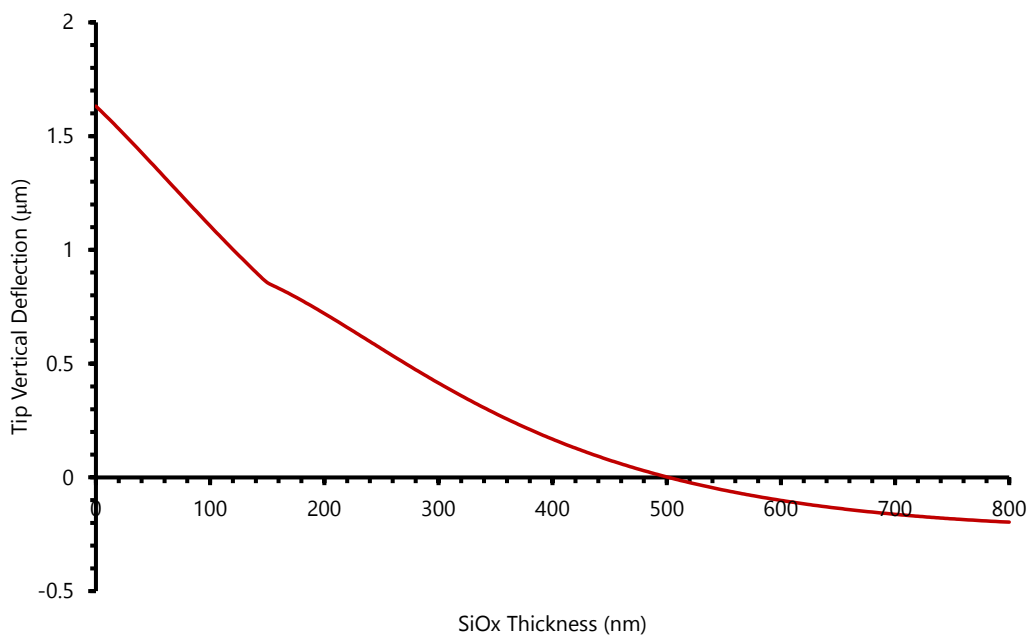


FIGURE 6.4: FDM Model - SiOx Thickness vs. Thermal Bend Induced Tip Deflection

more consistent balance of the SiOx and Au along the length to produce a more consistent longitudinal and lateral deflection mitigation and so magnitude. One thing to note is at 150 nm of SiOx, a kink and change in gradient occurred in the FDM Model's thermal bend output. This was due to the the SiOx exceeding the Au thickness and so affecting the Effective Modulus calculation. This is because the latter utilises the greatest coating thickness as seen in Equation 3.6. Therefore, a change in the rate of

change with thickness occurred.

With the above said, it may be possible to fabricate SThM cantilevers with SiO_x, but it would require a notable alteration and addition to the current fabrication process with potential issues of adding such a thick coating. Furthermore, the robustness of the design may be challenging with it relying on the Au and SiN_x thickness magnitudes to be consistent with the latter known to vary. In addition, it may be susceptible to the same issues the grooved cantilever has with varying deflection across its width. Overall, this solution is one that can provide a complete attenuation of thermal bending, but this comes at the cost of a significant change in the cantilever design, properties and fabrication process.

6.2.1.3 Wider Coating Position

This solution is not able to produce a complete attenuation of thermal bending, but it may provide a simple, single change to reduce it and its induced vertical deflection. The latter is based upon observations in various FEA models that a wider position of the Au wires seemed to reduce temperature change induced deflection. To determine the extent of this, a simple study was designed to explore the effects on both a standard rectangular cantilever and one with a taper, as is the case for SThM. A schematic showing these two cantilevers can be seen in Fig. 6.5. For each type of cantilever, a similar geometry to that found in SThM cantilever's was modelled. These were 150 μm long and 120 μm wide for the SiN_x with the Au running the whole length for two wires of 27 μm width. FEA was employed for this analysis due to its ability to appreciate the lateral location of materials. The same type of element type and mesh employed previously for SThM cantilevers was applied. The results based upon these are demonstrated in Table 6.3 with the end vertical tip deflection due to thermal bending calculated for the central and edge regions.

In Table 6.3, there is only central deflections for the tapered cantilever due to it funneling to the centre for the tip. Analysing the results, it is clear that placement of the coating further to the edge reduced thermal bend induced deflection. This is in the opposite direction than the spring constant change would suggest with it reducing with wider coating position. For the tapered cantilever that resembles a SThM cantilever, a reduction of 12.4 % was observed. This is surprisingly significant considering the

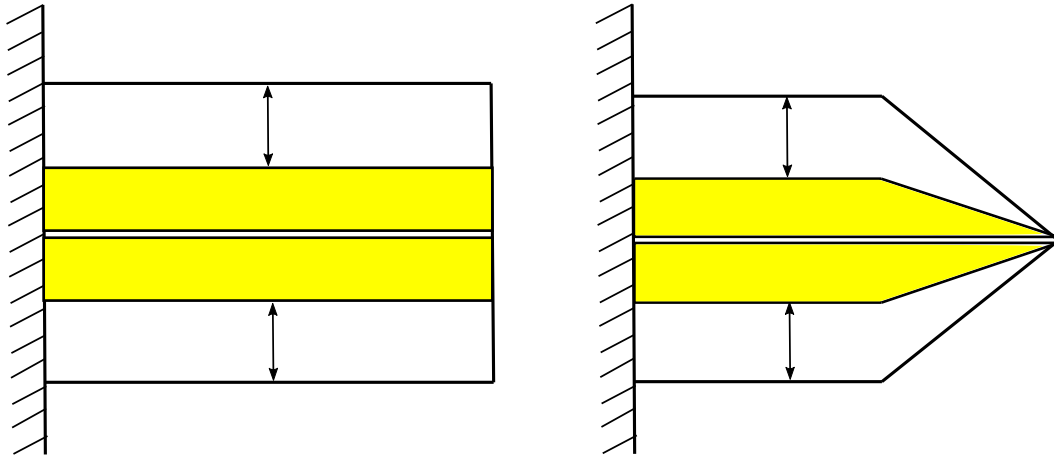


FIGURE 6.5: Coating Lateral Positioning Graphic

TABLE 6.3: Wider Coating Position Study Data

Cantilever	Coating Lateral Position	Spring Constant (N/m)	Thermal Vertical Deflection (nm/K)	
			Central	Edge
Rectangular	Centre	0.33	91.1	103.8
	Wide	0.32 (-3 %)	85.6 (-6%)	91.2 (-12.1%)
Tapered	Centre	0.31	94.3	NA
	Wide	0.30 (-3.2 %)	82.6 (-12.4%)	NA

same quantity of Au is present in-conjunction with the spring constant reducing as well. Therefore, based upon this simple study, it would be recommended to validate the results experimentally and if correct, implement them not only in flat SThM cantilevers, but in AFM cantilevers with a patterned coating where thermal bending and drift should be minimised.

6.2.1.4 Backside Deposited Metal

The last solution explored was one involving deposition of a metal on the opposite side of the cantilever to the Au wires, counteracting its thermal bending moment. Hence, sandwiching the SiN_x between the two metals. Some manufacturers fabricate AFM cantilevers with such a construction or at least have the option to, but many currently just provide this to enable metallic conductivity of the tip [209], [210]. However,

there are some academic applications of creating a sandwich of metal(s) to minimise thermal bending such as by K. Luo et al. [58] who aimed to reduce the degree of extrinsic stress and strain induced from the temperature change from the metal depositions. Therefore, it is not a completely unfamiliar concept within the AFM community, and manufacturers do have the immediate capability to perform it. However, it is not currently implemented by manufacturers to exclusively reduce thermal bending and has not been attempted for SThM cantilevers or been integrated into its specific, complex fabrication process. To initially explore this, a set of materials were chosen. The larger the material's CTE, the less thickness is required to counteract the Au. However, other properties such as its Young's Modulus and reflectivity are also important. The former has been well articulated in earlier portions of this work, however the latter is also important as the backside metal is the top surface the laser in the optical lever system reflects off. This design actually provides an opportunity to enhance SThM cantilever's laser reflection as the voltage sum that is outputted by most AFM photodetectors is around 2 V. Moreover, a more reflective material should result in less absorption of the laser light by the cantilever. Therefore, less laser induced heating of the tip should occur, a beneficial to SThM's thermal measurements as documented by L. Ramiandrisoa et al. [39]. With this in mind, the key properties for Al (chosen due to deposition capability and known high CTE) and Au are listed in Table 6.4, whereby only the bulk properties are shown due to this early stage exploration.

TABLE 6.4: Potential SThM Backside Metals

Coating Metal	Poisson's Ratio	Young's Modulus (GPa)	CTE (ppm K ⁻¹)
Au	0.45	64.39	15.6
Al	0.34	70.2	23.03

With the properties listed, it can be seen Al has a much greater CTE alongside a relatively similar Young's Modulus to Au. Therefore, a lower thickness should be required to counteract the thermal bending moment induced by the Au. To analyse this, the FDM model was employed with separate Al and Au thickness vs. thermal bend tip vertical deflection studies. The results of which are shown in Fig. 6.6. The trends for both Al and Au demonstrate a clear ability to completely attenuate thermal bend

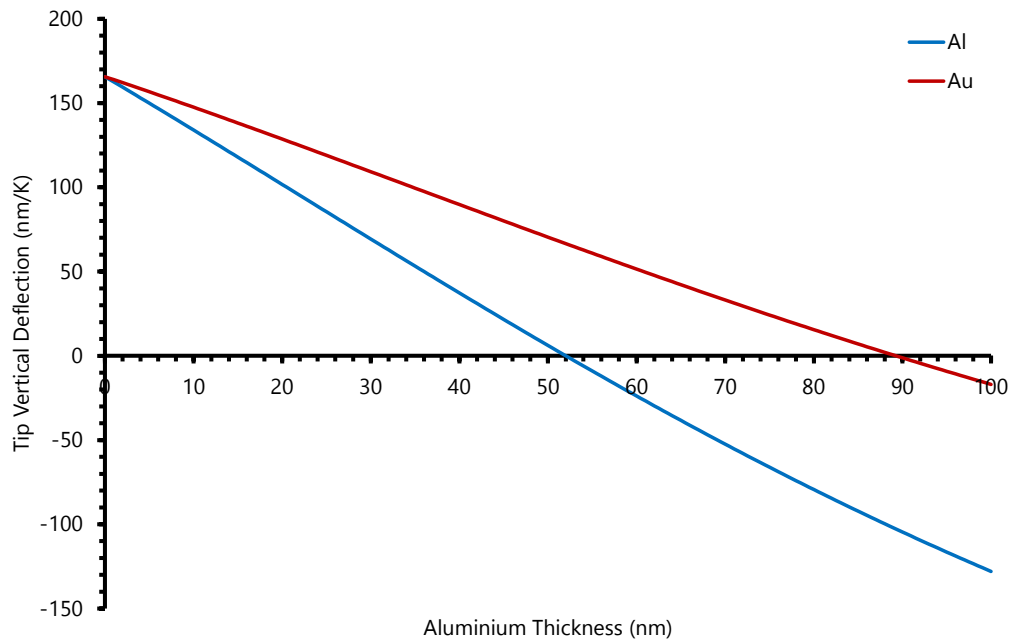


FIGURE 6.6: *FDM - Backside Metal Preliminary Study of Al & Au Thickness vs. Vertical Tip Deflection due to Thermal Bending*

induced deflection. Al appears to provide greater attenuation with a lower thickness of 52 nm for zero tip deflection with 90 nm needed if Au is used instead. However, the above analysis does not output the deflection along the cantilever length which will be variable due to the Au changing width along the SThM cantilever length. Although it should be noted that, as the tip-side Au is no longer required for reflection of the laser, a reduced and more consistent wire width can be easily implemented without any detrimental effect on the SThM's thermal measurement, bringing more consistent longitudinal attenuation. However, in the above, Al's properties are based on bulk values and not those determined from thin films which may dramatically change its ability to induce thermal bending and so counteract the Au. Before proceeding, the potential fabrication of such a solution would only be possible post-release wet etch for SThM probes. This is because of the SiN_x deposition occurring between 700 °C and 800 °C and undertaking this on top of an Al, or even other metal films, may evaporate or recrystallise many metals, cause adhesion and delamination issues, contaminate CVD chambers and may not be compatible with the etching processes required to be performed during probe fabrication. Therefore, access to the back-side of the probe is far easier once the final Si is etched away from the release wet etch. This can be performed individually or to a full wafer. One final point for this potential solution is that

it is based upon balancing the thermal bending moments from the two metals on the same substrate. As a result, variation in the substrate/SiNx thickness and properties is insignificant with only the geometry and material properties of the metals being the dependent factors. These are values which can be well controlled. Overall, it appears to be a realistic and effective potential method of mitigating or eliminating thermal bending.

6.2.2 Chosen Solution - Backside Deposited Metal

From the above exploration, the most viable solution offering the best potential efficacy alongside fabrication simplicity and ease to be included in the current lengthy and complex fabrication process was chosen. This was the Backside Deposited Metal approach. This complete attenuation of thermal bending induced deflection; requires only one additional fabrication process; robust to known fabrication uncertainties (e.g. SiNx thickness); a capability to enhance SThM's laser reflection and so topographic measurement; potentially reduce laser heating of the cantilever and tip to improve thermal measurements and does not require any dramatic changes to the physical dimensions of SThM cantilevers. However, there were two unknowns that could inhibit its credentials as a solution. As deposition of the metal is only possible once the cantilever is free-standing, it is unknown whether this will generate notable residual strain, stress and pre-bend to the cantilever which is undesirable. Moreover, depending on the metal, there may be some unwanted chemical reactions or shorting that could nullify SThM's capability. Specifically, the Pd sensor can overhang at the end of the tip as documented by Y. Zhang et al. [114]. Therefore, it may be possible for backside deposited metal to make physical contact with this. For example, Al and Pd are known to react exothermically upon heating to 650 °C [211]. Although this temperature is very unlikely to be reached in SThM applications, it is something that should be noted. However, there are many positive traits associated with the solution and so at the very least it merit's investigation to shed-light on the stated unknowns. Alongside this solution, it was decided to couple it with a change in the Au wire definition. As mentioned earlier, as the Au is no longer required to reflect the laser, its width can be reduced along with to make it more consistent along its length. This should reduce

the quantity of the required backside metal as well as provide a more consistent attenuation of thermal bending. With this decided, a more comprehensive modelling effort was performed followed by a feasibility study.

6.2.2.1 Modelling

For a more thorough modelling effort, as has been the case throughout this project, a combination of FDM and FEA was applied. However, before these were employed, it was necessary to clearly establish the material properties for the backside coating. Au has already been researched, but the other material in Al needed its properties determined. These are shown below in Table 6.5 whereby the relevant literature has been extracted.

TABLE 6.5: *Relevant Aluminium Mechanical & Thermal Properties*

Property	Reference	Material Thickness (nm)	Details	Magnitude
Poisson's Ratio	[166]	Bulk	NA	0.34
Youngs Modulus	[212]	30 & 50	Sputtered; MEMS Uniaxial Tensile Test	60.2 GPa
	[174]	250-1,150	Sputtered; Magnetostrictive Sensor Strip Technique	55.4 GPa
	[175]	219, 407, 624 & 1,121	Sputtered; Magnetostriction	81.6, 70.4, 52.1 & 53.7 GPa
	[170]	100, 311, 317, 331, 380 & 498	Unknown Deposition Method; Ultra-Fast Pump Probe	47, 55, 58, 54, 65, 47 GPa
	[171]	40	E-beam Evaporated; Laser Based Ultrasound Technique	69 ± 3.45 GPa

	[213]	3,000	E-beam Evaporated; Laser Diffraction on Free-standing Films	57 ± 3 GPa
	[214]	200-1,000	E-beam Evaporated; Micromembrane Deflection Method	65-70 GPa
	[215]	30-500	E-beam Evaporated; Magnetostrictive Sensor	70.4 GPa
	[216]	153	E-beam Evaporated; Microscale Beam Test & Picosecond Ultrasonic Measurement	58 & 60 GPa
Coefficient of Linear Thermal Expansion	[217]	600	Al/0.5%Cu Sputtered; (25–85 °C)	$37.4 \text{ ppm } K^{-1}$
	[218]	300, 500, 1000, 1500 & 1700	Thermal Evaporation; Bilayer Microcantilever Technique (30-90 °C)	18.23, 19.54, 24.28, 28.97 & 29.97 ppm K^{-1}
	[219]	720	Sputtered Al ; X-Ray Based Technique (100 °C)	$22.5 \text{ ppm } K^{-1}$ (21 ppm K^{-1} at 30 °C extrapolating trendline)

From the above literature, the following properties were deduced employing the same method used for previous materials:

- $\nu_{Al} = 0.34$

Very little literature has been produced in determining thin Al film's Poisson's Ratio. Therefore, the bulk value was utilised without further appreciation of the material's thin nature.

- $E_{Al} = 64.58 \text{ GPa}$

Al is more isotropic than Au resulting in any grain orientation having less impact on the determined Young's Modulus. Therefore, this was not needed to be appreciated as much as Au in literature providing a simpler analysis. As a result, averaging of the thermally evaporated Al thin film values was employed.

- $\alpha_{Al} = 18.23 \text{ ppm K}^{-1}$

There was only one piece of literature found that determined the CTE for thermally evaporated (rather than sputtered) thin Al films with even its thinnest film of 300 nm being far greater than would be desired to be deposited for this solution. In alignment with previous deductions of material properties, the most relevant value was then extracted for the thinnest film from the thermally evaporated Al study [218].

With these determined, they were employed in the models. The same thickness vs. tip deflection study, as performed earlier, was executed in the FDM model with the results shown in Fig. 6.7.

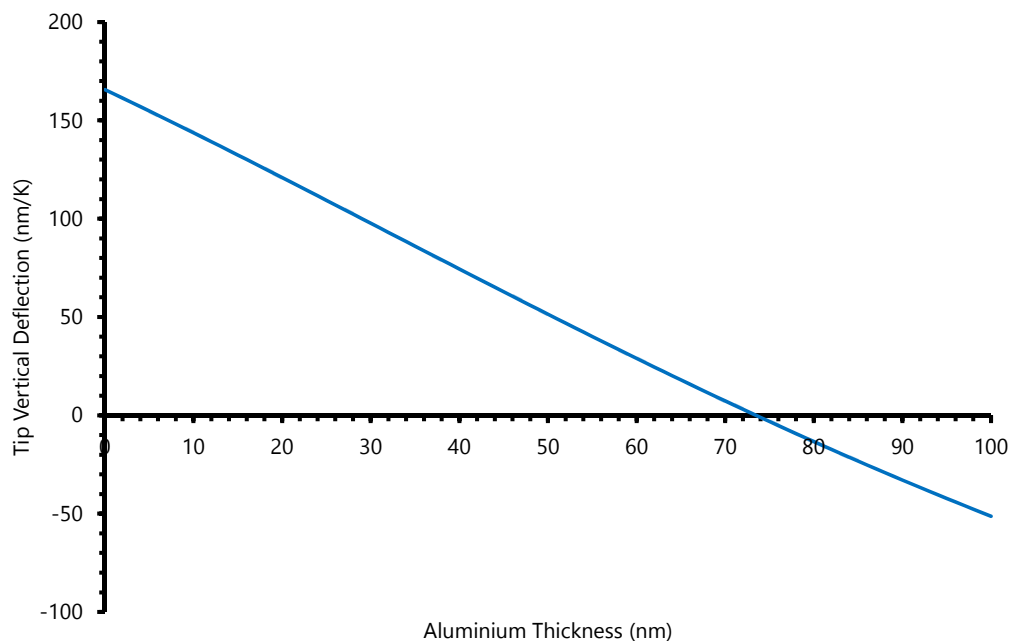


FIGURE 6.7: FDM Model - Backside Metal Study of Al Thickness vs. Vertical Tip Deflection due to Thermal Bending with Updated Material Properties

As expected, with a lower CTE and Young's Modulus, the required thickness of Al for attenuation of thermal bend induced deflection will increase with the model predicting around 73 nm instead of 52 nm for zero tip deflection. However, it should

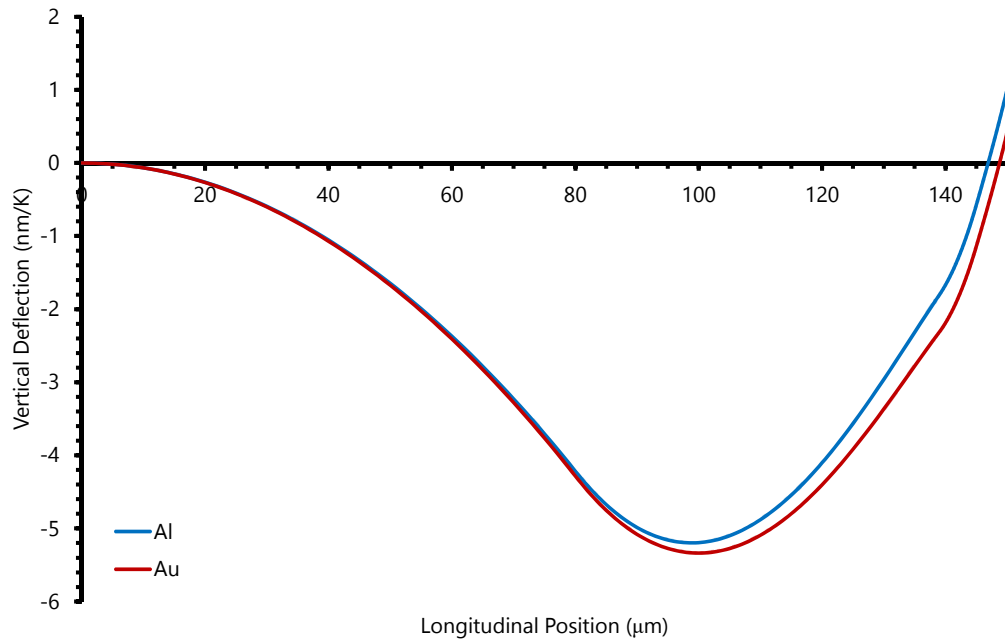


FIGURE 6.8: FDM Model - Thermal Bend Vertical Deflection Profile for 73 & 89 nm Al & Au Backside Coating's Respectively for flat SThM

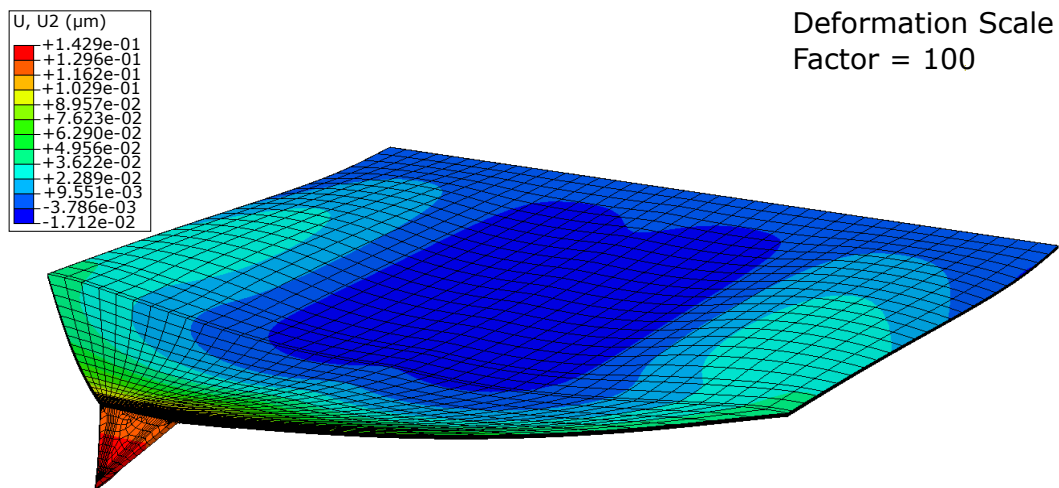


FIGURE 6.9: FEA Model - Al (73nm) SThM Thermal Bending Induced Vertical Deflection from 10 K Temperature Change

be borne in mind that there was actually limited literature found on the CTE for thin Al films deposited by thermal evaporation. Therefore, this value may be a better estimate than the previous bulk value used, but it should only be regarded as an estimate due to this lack of literature. Beyond this, the variable Au width produces an inconsistent thermal bend and hence deflection profile along the cantilever length. This can be seen in Fig. 6.8 for an Al and Au backside thickness of 73 nm and 89 nm respectively, whereby the tip vertical deflection is close to zero. A minimum deflection of -5.4 nm/K was produced which is one 30^{th} of the 166 nm/K determined for an

uncompensated flat SThM cantilever from the FDM Model. This is a massive reduction and provides a great exhibition of this solution's strength. However, the variable bending and deflection is clear along its length. As a result, FEA was subsequently employed due to its more comprehensive ability to determine this alongside explore the lateral behaviour. The first model was a replication of the 73 nm thickness of Al on the backside of a flat SThM cantilever and can be seen in Fig. 6.9. This provided a reference of how the FDM and FEA models compared. The FEA model predicts a more positive tip-deflection of 14 nm/K as opposed to the tip deflection close to zero in Fig. 6.8. To produce a more similar tip deflection in the FEA model, an Al thickness of 81 nm was required. The result of this can be seen in Fig. 6.10 & 6.11. Analysing this, the associated centreline profile shown is comparable and very similar to that seen in Fig. 6.8 with a peak deflection of -5.7 nm/K. Like for the FDM model, this is one 27th of the 155 nm/K generated to the equivalent flat cantilever without backside metallisation from FEA seen in Fig. 4.14. Therefore, it can be concluded that the FDM and FEA models may not produce the exact same deflection for a given Al thickness, but are producing the same relative profiles and reduction along the cantilever. Alongside the longitudinal deflection, the lateral variation should be analysed. From Fig. 6.10, there is a maximum variation of around 3 nm/K laterally across the cantilever. This is less than a fifth of the 17 nm/K seen for the non-backside metallised flat cantilever. Therefore, this shows clearly that this design improves lateral variation in deflection.

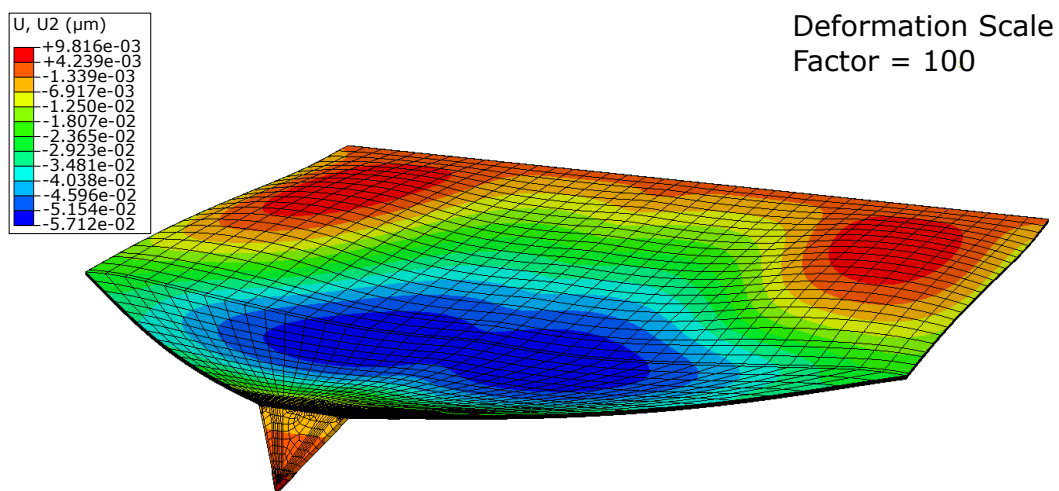


FIGURE 6.10: FEA Model - Al (81nm) SThM Thermal Bending Induced Vertical Deflection from 10 K Temperature Change

Further analysing the longitudinal profile, the significant humped type profile is

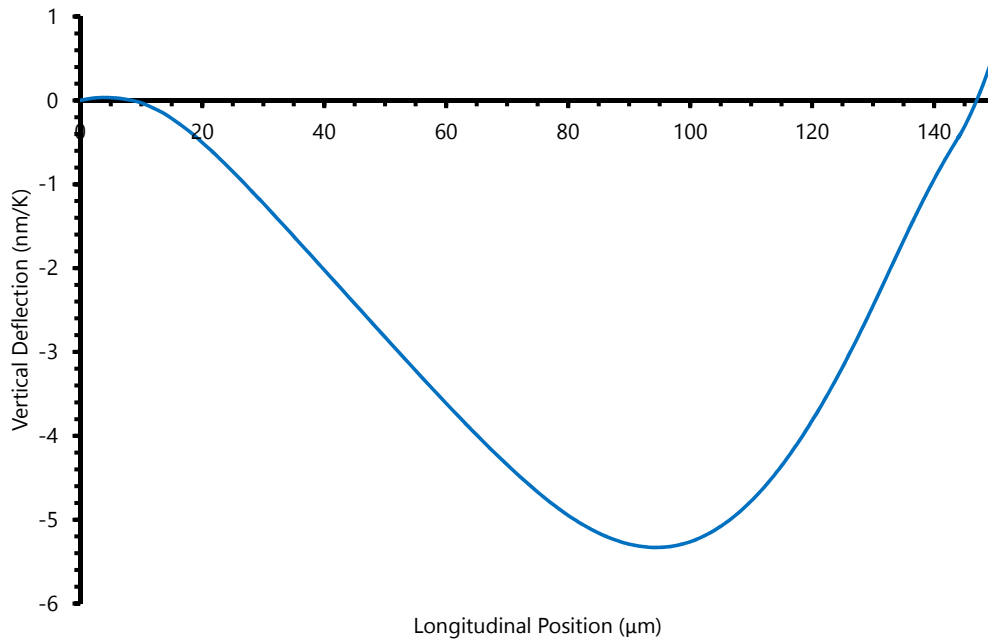


FIGURE 6.11: FEA Model - Al (81 nm) SThM Thermal Bend Induced Centreline Deflection Profile

undesirable with it being dominated by the change in Au width along the length (attributed to the wide section for laser reflection 90 μm along). The latter of which would no longer be needed due to the backside Al reflecting the laser. If the Au width is altered so its width is more consistent along the length, then this will be reduced for a more consistent attenuation or at least a less dramatic humped profile. As a result, a FEA model with no sudden width increase was generated for a comparable tip-deflection to previous models with the resultant profile seen in Fig. 6.12. This utilised 77 nm of Al (4 nm less than the typical SThM Au wire pattern) and showed a far less variable longitudinal profile with a reduction from 5.4 nm/K to 1.5 nm/K in the peak deflection magnitude due to the Au wire's more constant width. However, perfectly consistent attenuation did not occur and so an exploration exercise was performed, altering the widths of the Au coating to produce a more consistent deflection profile for near zero tip deflection. Moreover, as highlighted in Section 6.1, cantilever rotation needs to be similarly zero near the tip-end of the cantilever where the laser is typically positioned. If achievable, it would also be desirable for the OC and IC thermal bend deflection behaviours to additionally align as much as possible. Therefore, a single laser position would provide greatly reduced impact from thermal bending in both. In pursuit of these objectives, an earlier potential solution was exploited. This

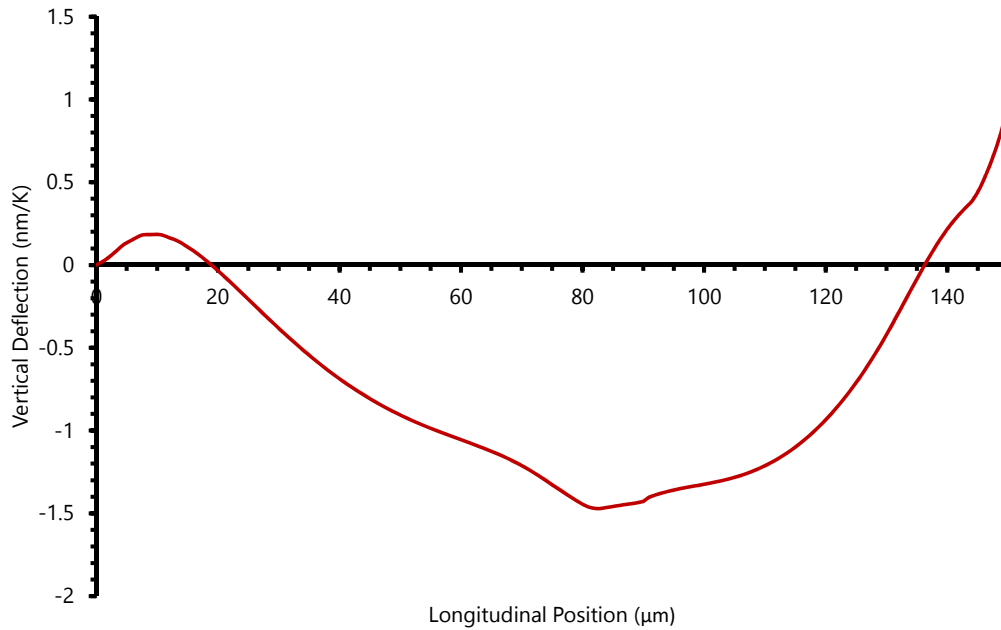
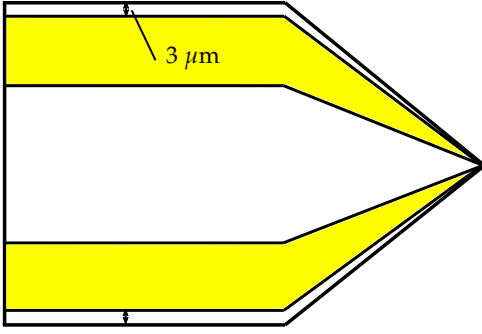
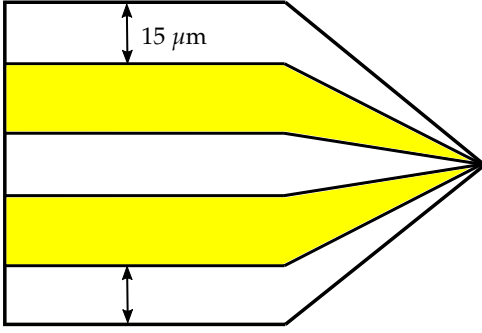
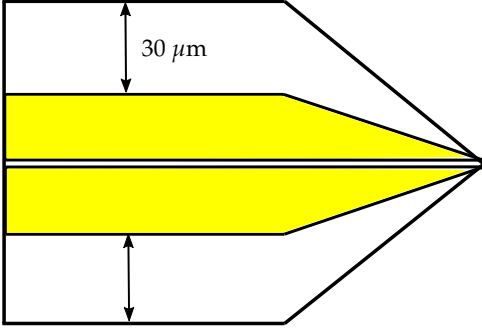
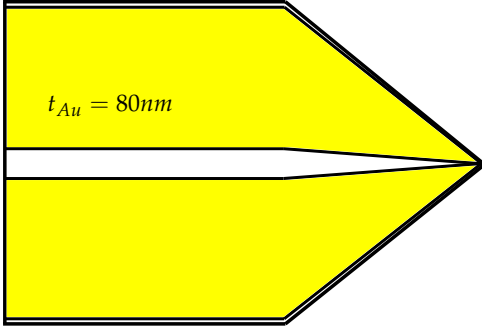


FIGURE 6.12: FEA Model - Al (77nm) SThM Thermal Bend Induced Centreline Deflection Profile with no Wide Mirror Section

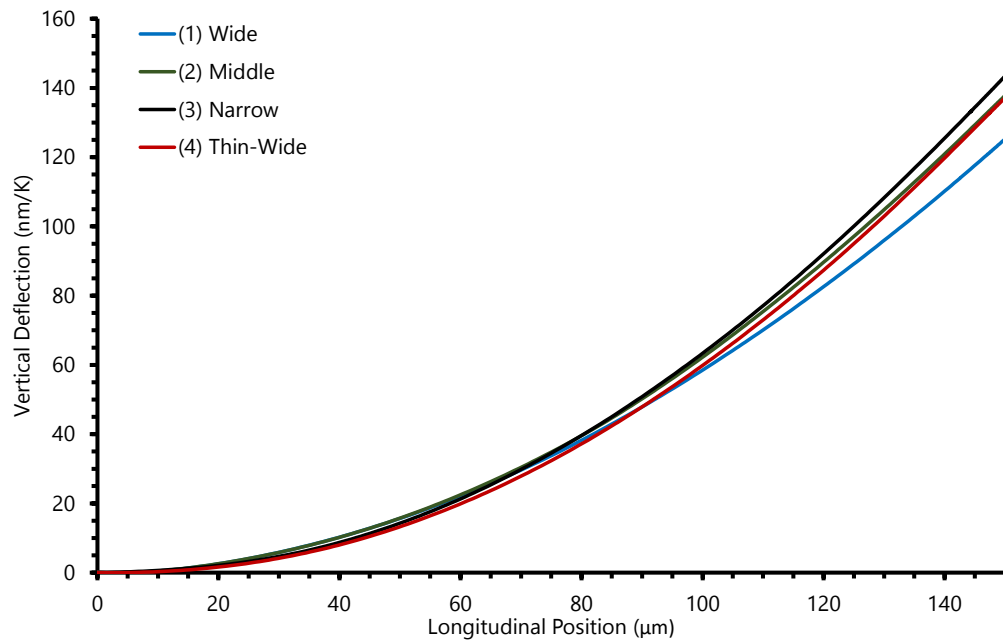
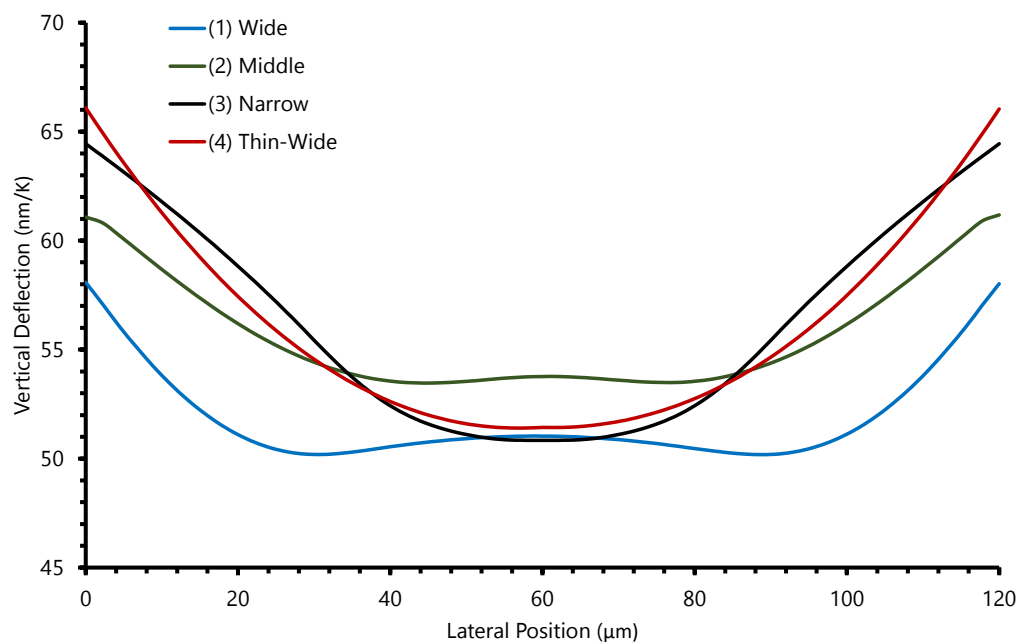
was placing the Au wire location in a wider position closer to the edge as elaborated in Section 6.2.1.3. As indicated from this theoretical study, this should reduce the thermal bending induced deflection from the Au layer and so less Al should be required to counteract this. In addition, along with the goal of producing a consistent deflection behaviour longitudinally, this may also help achieve the same laterally as the Al has a uniform coating and the Au a patterned one. Therefore, altering the Au's lateral placement may aid this. Following on from this, the Au could be thinned and widened so it more closely matches the Al coating for a more even, and equal thermal bend attenuation longitudinally and laterally. Bearing all of these different theoretical factors and design features in mind, a range of designs were constructed and modelled, where the following listed in Table 6.6 were the most important and key ones identified. These were chosen due to showing promise for thermal bend attenuation when combined with a backside Al layer alongside offering Au wires located with wider lateral positions that could have merit, although this needed to be proven experimentally.

One key facet of all the designs seen in Table 6.6 is that a reduction in Au approaching the tip was performed. This was due to models indicating that a reduction would induce a more equal longitudinal vertical deflection from thermal bending. Furthermore, Design 4 has a thinner and wider Au wire. This has been designed to

TABLE 6.6: Final Design Exploration FEA Study

Design No.	Description	Justification	Simplified Graphic
1	Wide Lateral Position of Au (3 μm from Edge)	Less Net Vertical Deflection from thermal bending	
2	Middle Lateral Position of Au (15 μm from Edge)	Less Net Vertical Deflection from thermal bending	
3	Narrow Lateral Position of Au (30 μm from Edge)	Comparison for Design to 2 & 3	
4	Thinner Au ($t_{Au} = 80\text{ nm}$)	Similar to Al Deposition For More Even & Equal Thermal Bend Counteraction	

have a comparable cross-section to the previous design and thus should generate similar electrical-thermal behaviour. This has been verified through simple cross-section calculation and applying R. Lambert's [141] thermal resistive model. The results of

FIGURE 6.13: *New SThM Cantilever Designs - FEA Longitudinal Profiles*FIGURE 6.14: *New SThM Cantilever Designs - FEA Lateral Profiles*

this can be seen in Appendix C. Therefore, with this in mind, FEAs longitudinal and lateral profiles of each design were carried out and are shown in Fig. 6.13 and 6.14 respectively. These show that by implementing a wider Au position, less tip deflection occurs along with less variation laterally. However, the real strength of these designs comes when they are combined the Backside Deposition solution. FEA results images for each design with the appropriate thickness of Al to induce near zero tip deflection

are shown in Fig. 6.15 (all with a Deformation Scale Factor of 1,000) followed by the centreline profiles in Fig. 6.16 for thermal bending when OC and IC.

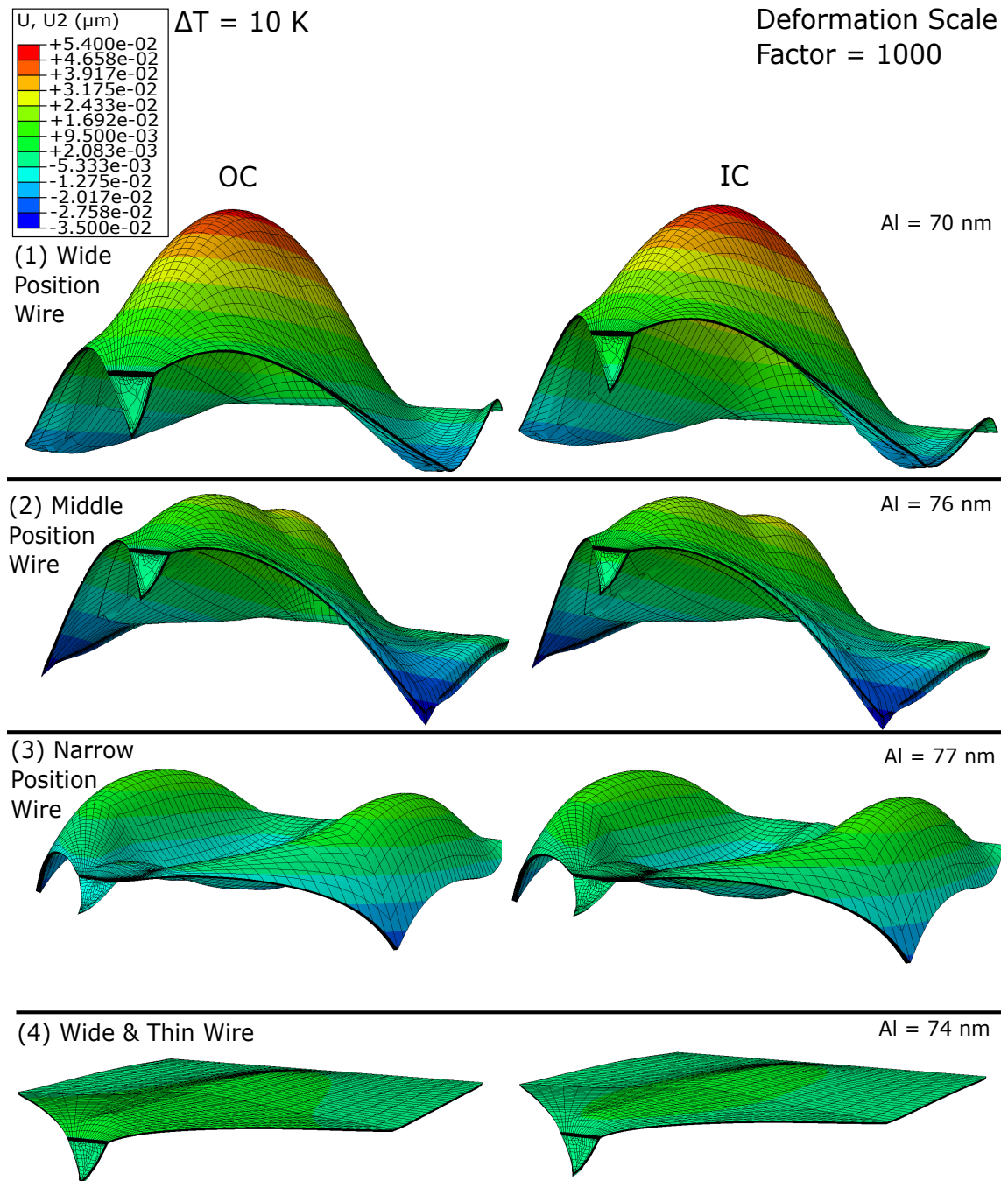
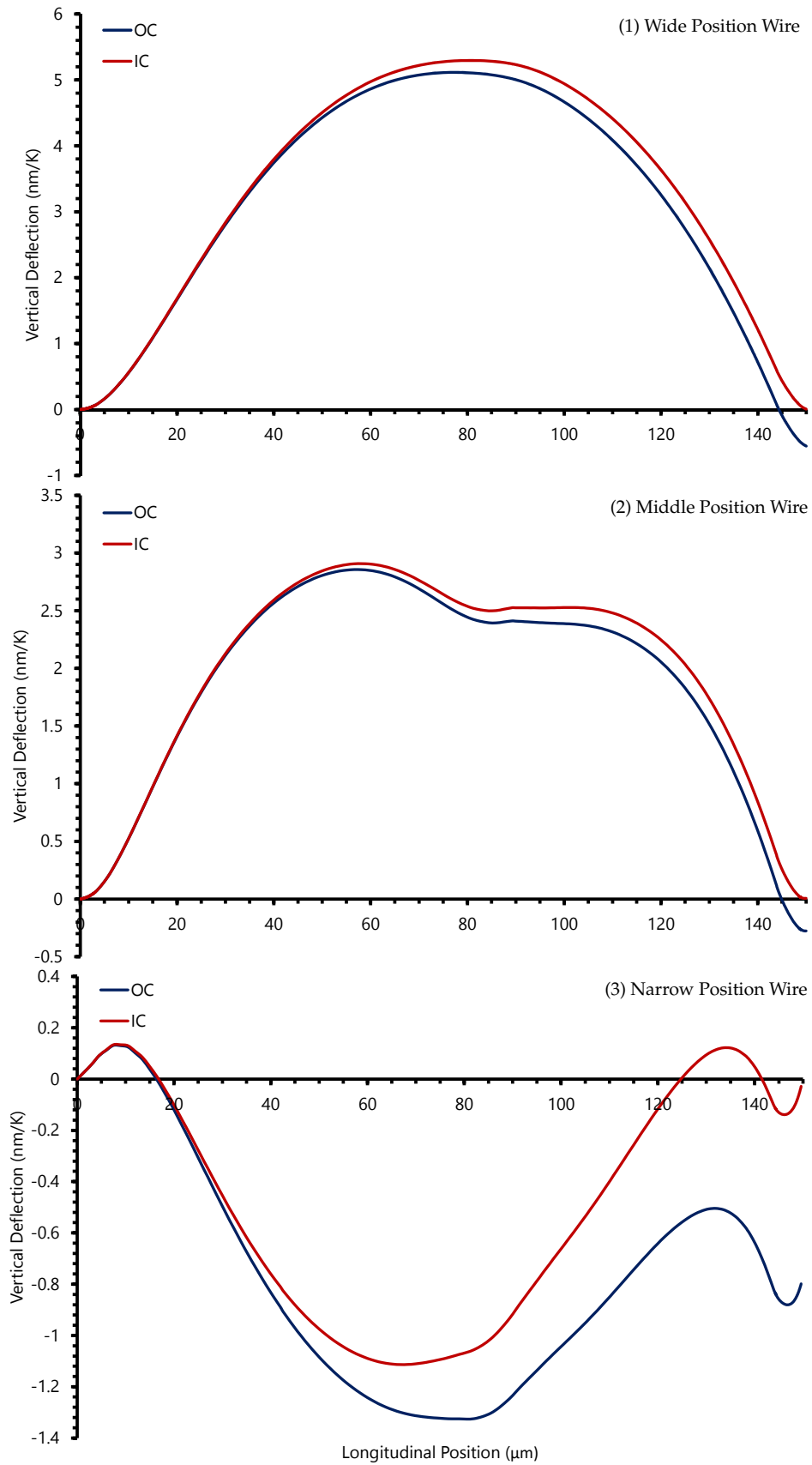


FIGURE 6.15: FEA Wire Study - Thermal Bend (10 K) Outputs Images for OC (left) & IC (right) for Designs (1) Wide Position Wire; (2) Middle Position Wire; (3) Narrow Position Wire; (4) Wide & Thin Wire

Analysing the FEA outputs for the backside metallised models (Fig. 6.15 & 6.16), both the OC and IC thermal bend behaviour are very similar with the OC behaviour being slightly adrift due to not having the exact Al thickness needed to produce the



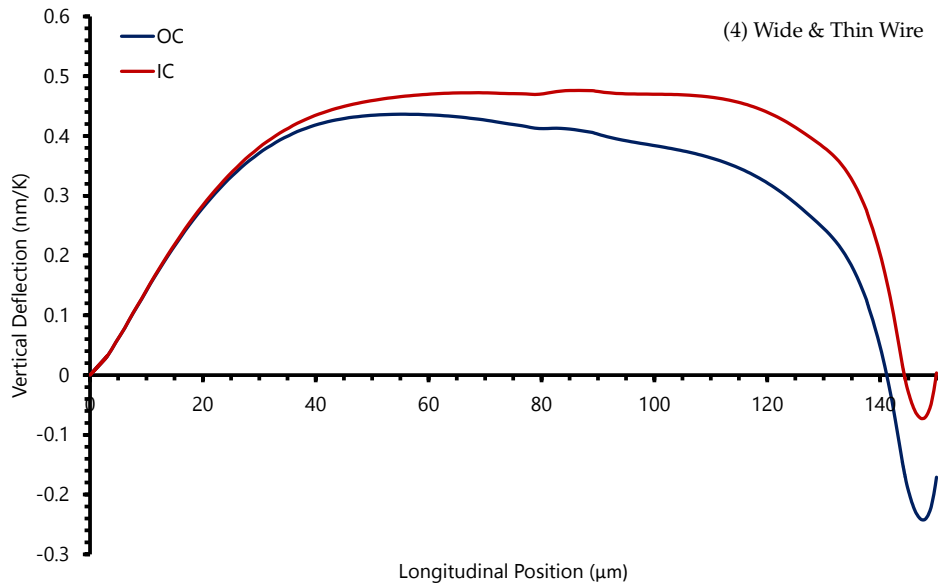


FIGURE 6.16: FEA Wire Study - Thermal Bending Centreline Profiles for Designs (1) Wide Position Wire; (2) Middle Position Wire; (3) Narrow Position Wire; (4) Wide & Thin Wire

zero vertical tip deflection imparted by the tip's Roller BC. The exact Al thickness was not modelled due to it requiring sub-nanometre resolution for the Al thickness that would be unrealistic to achieve using the evaporation techniques available. However, with this in mind, it makes sense that these two scenarios produce near identical behaviour as the only difference between them is the tip's BC of zero vertical deflection, a phenomenon that can be replicated OC if thermal bending is perfectly balanced. Beyond this, each design's produces a different result. For wider lateral Au positioning (Design 1), less Al is required on the backside with 70 nm needed instead of 77 nm for the Narrow design. However, this comes at a cost as the longitudinal and lateral variation is far greater for a wider positioning in contrast to narrow. As a result, there will typically be greater horizontal movement on the photodetector with temperature change. In addition, the optical lever's laser position along the cantilever will produce a variable impact with the typical position near the tip showing relatively pronounced rotation. For a Middle position wire (Design 2), we see a double humped profile whereby a reduction in the deflection range can be seen when compared to the wide wire design. However, this requires a greater Al thickness of 76 nm and still demonstrated a reasonable degree of deflection longitudinally and laterally for vertical deflection. Regarding the Narrow wire design (Design 3), a similar behaviour, but

with a slightly more gradual longitudinal deflection than shown in the comparable FEA model seen in Fig. 6.12. This is thanks to refinement of the Au geometry near the tip. Moreover, it demonstrates less deflection longitudinally and laterally meaning less variable measurement with uncertain laser location. With this said, it does require the upper range of these designs with an Al thickness of 77 nm. The final design explored is the Thin-Wide wire (Design 4), which provided a very good example of thermal bend balancing. Far less vertical deflection was produced overall with the longitudinal and laterally profiles showing significantly less variation than the rest of the designs. The latter of which means that the laser will show less variation with location. Moreover, the profile demonstrates that in the region where the laser would typically be located (i.e. near the tip or 80-140 μm along the cantilever), there is a flat profile resulting in very little rotation that would translate to displacement on the AFM's photodetector. Specifically, this not only means little thermal bending will be registered, but it will more accurately depict the tip's actual deflection approaching zero.

Overall, it seems that each design has its benefits and drawbacks, with the Thin-Wide Au design showing the greatest degree of promise. As a result, it is desirable to explore each design and verify the theoretical findings. However, particular effort was made to fabricate the most promising design in the form of Design 4 with a Thin-Wide Au wire.

6.2.2.2 Feasibility Study

Before committing anything further into the Backside Deposition solution, a feasibility study was executed to provide a more immediate test of the solution's ability to attenuate thermal bending. In addition, this was intended to highlight any further potential benefits or drawbacks. The outcomes of this could then be used to help optimise the final study and prevent lost time, resources and SThM probes. The study involved the deposition of Al with varying thicknesses over a number of SThM cantilevers. Al was selected over Au to perform this as the bulk and thin film properties suggest it is an ideal metal for inducing thermal bending and so counteracting the Au wires on the opposite side of the cantilever. It would also highlight any possibility of the backside Al shorting the Pd tip. With this in mind, five cantilevers were

chosen from the same wafer so that their geometries were as similar as possible for sound comparison. Each had their thermal bend profiles measured before and after metal deposition for sound contrast. The Interferometer and Peltier heater described previously were utilised with the cantilevers placed directly on-top of the Peltier, immediately next to a PT-100 that measured the surface temperature change. The latter was used over the more accurate temperature quantification of SThM's tip due to the challenge and time consuming logistics of obtaining electrical connection and measurement of the probes while allowing them to have the metal deposited post the initial thermal bend quantification. Moreover, as long as the experiment was performed consistently, they would be exposed to the same mechanical and heat transfer conditions and so be comparable. Therefore, this method was appropriate for the scope of this feasibility study. Alongside the thermal bend measurements before and after metal deposition, the probes had their tip resistances measured and their Thermal Tune (i.e. spring constant) data extracted. This was used to confirm no shorting of the tips or resistance changes occurred post metal deposition and provide a gauge for the change in stiffness of the cantilevers respectively. However, the latter measurement is known through L. Avilovas's work [148] to not be an accurate measure, but should be an indicator confirming any degree of mechanical stiffening. Regarding the metal, each cantilever had Al deposited through thermal evaporation as this was the method readily available and utilised for the other metals in SThM manufacture. Plassys IV in the JWNC was employed to perform this, with 20 nm, 40 nm, 60 nm, 80 nm and 100 nm of Al deposited separately on the five chosen cantilevers.

The thermal bend induced deflection profiles before and after metal deposition can be seen in Fig. 6.17. Similar to previous experiments, a total of five locations along the cantilever length had their deflection-temperature gradients measured to produce the respective profiles. The Y-errors were then determined based upon the standard deviation from the linear regression analysis for each point. Alongside these profiles, the tip resistances and Thermal Tune determined Spring Constants can be seen in Table 6.7. Initially analysing this table, the spring constants demonstrate a general trend of increased stiffness with Al deposition and greater thickness. This confirms that some degree of mechanical stiffening is occurring, but as mentioned earlier, the inaccuracy of this value obtained from this measurement is uncertain. Therefore, it should only

TABLE 6.7: Feasibility Study - Spring Constants & Resistances

Probe	Thickness of Al Deposited (nm)	Spring Constant (N/m)		Tip Resistance (Ω)	
		Before	After	Before	After
1	20	0.044	0.082	450	452
2	40	0.118	0.183	462	463
3	60	0.091	0.174	454	454
4	80	0.155	0.244	496	497
5	100	0.135	0.327	494	495

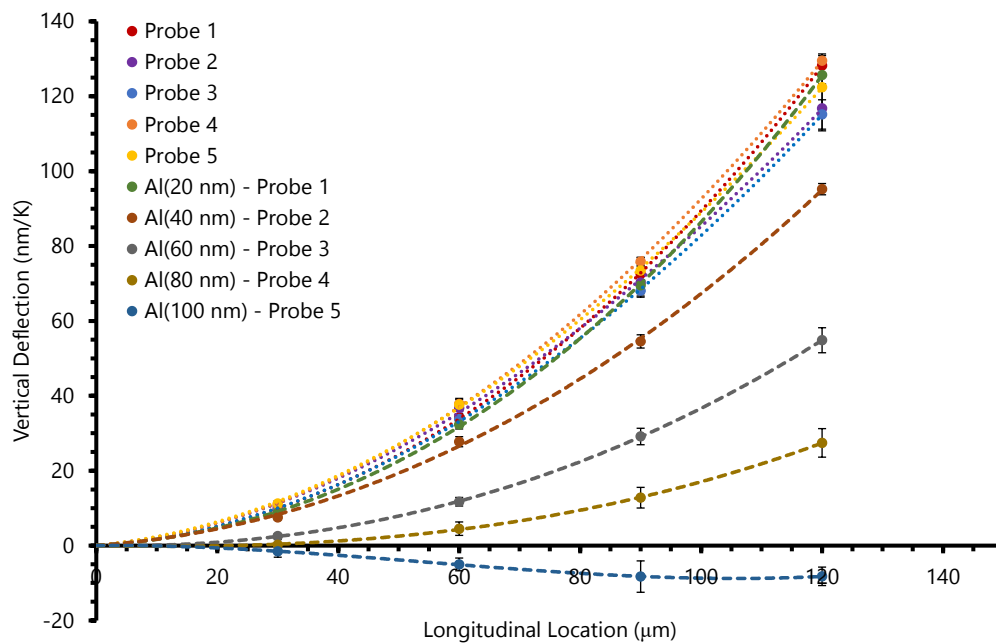


FIGURE 6.17: Preliminary Feasibility Study - Probe Thermal Bending Deflection Profiles

be considered to provide a relative or rough measure in this study and simply confirm thicker Al has caused increased stiffness. Regarding the tip resistances, very little change occurred, with only a uniform resistance increase most likely due to a greater ambient temperature during the post-deposition measurement. This confirms that no shorting of the tip resistor occurred along with no exothermic reaction between Pd and Al that would have destroyed the sensor. Moreover, these resistances were checked periodically over a number of months and no change in these values were observed. Moving towards the profile graph (Fig. 6.17), the deflection profiles have a third order polynomial trendline employed due to the length and width change relation in the

thermal bend equations previously determined. Analysing the pre-deposition profiles, a similar set of profiles were produced. This confirms the experimental method alongside the cantilevers having a similar geometry and properties aiding comparison between them. Post-deposition, the general trend is very apparent: greater Al thickness resulted in more negative vertical deflection. Between 80 nm and 100 nm Al thickness, there is a change in deflection direction with the Al overcoming the Au's temperature change induced deflection. This is greater than the 73 nm & 82 nm thickness theoretically determined by the FDM and FEA respectively based upon the literature defined properties for Al.

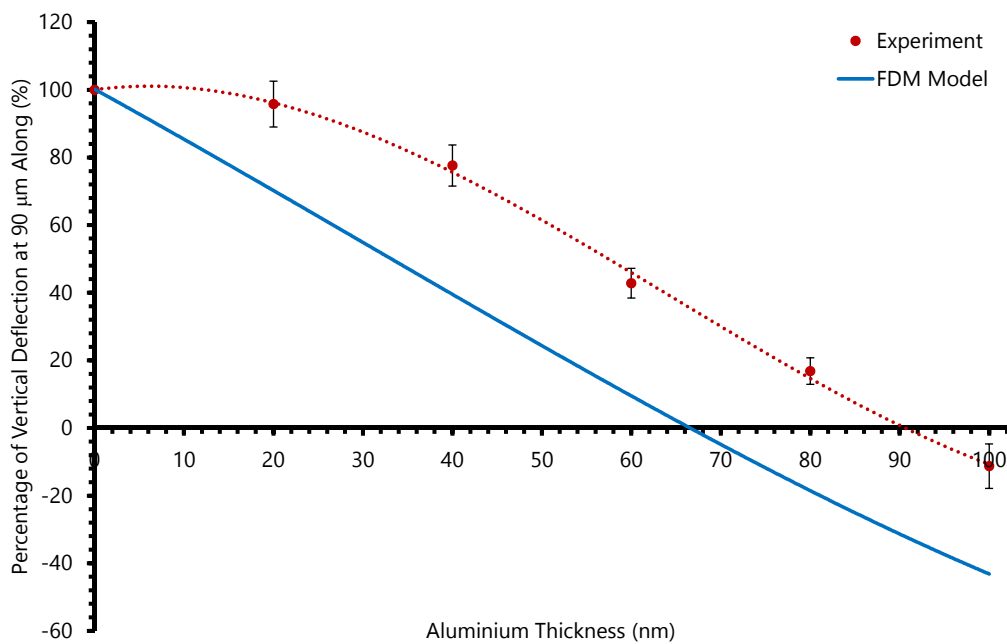


FIGURE 6.18: Feasibility Study - Cantilever Thermal Bending Deflection Percentage Change 90 μm Along

To contrast the thermal bend profiles, the percentage change in the deflection per Kelvin 90 μm along the cantilever (chosen due to the inability to measure tip deflection using the Interferometer) across the five cantilevers can be seen in Fig. 6.18. Based upon the experimental data, a thickness around 92 nm of Al is required to generate zero thermal bend induced deflection. This is greater than the 67 nm predicted by the FDM model for this position along the cantilever. Moreover, the change in deflection for low Al thickness is less than theoretically predicted. However after 40 nm, both generated very similar trends of Al thickness with deflection change. This indicates that the theoretical models are actually predicting the behaviour well, but not for the

low Al thickness's. It has been hypothesised that this is due to thickness related property changes in the Al, specifically either/all of the CTE, Young's Modulus and Poisson's Ratio alongside potentially Aluminium Oxide formation. As demonstrated by the variation between bulk and thin film properties already researched in this project, the former could be a pronounced effect. However, Al also readily reacts with Oxygen to form a passive layer of Aluminium Oxide [220] and at low Al thickness's, it will constitute a greater portion of the total coating. Therefore, if there is any significant Oxygen concentration in the deposition chamber, this may be the case. As a result, it would manifest as a coating with a lower CTE and so a lower reduction in thermal bend induced deflection. This hypothesis can be tested if Oxygen's presence in the chamber can be minimised. This was explored and shall be described later. Before doing this, one potential drawback already highlighted is that the following solution may generate notable residual strain and so stress. This can be analysed by looking at the change in the longitudinal profile at ambient temperature before and after metal deposition. The results of which are shown in Fig. 6.19 for each cantilever.

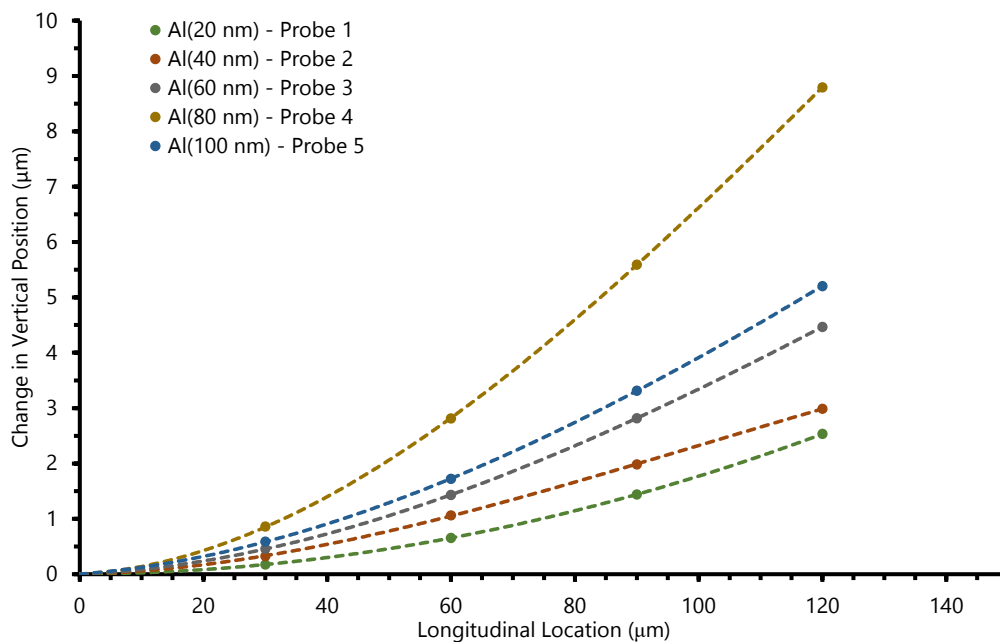


FIGURE 6.19: Feasibility Study - Change in Ambient Profiles/Curvature

Error bars were included, but only two images were extracted at ambient before and after deposition meaning the max-min difference was very low and hard to see for each point. With this in mind, the change in the profiles and so curvature indicate the change in the residual strain and stress [221]. Analysing this, up to 80 nm of

deposited Al, the curvature that correlates with residual strain and stress appears to increase with deposited thickness of Al. However, beyond 80 nm, the 100 nm result suggests a strain decrease. Before analysing this, residual stresses should be clearly defined. These can manifest from two different types of stress: extrinsic and intrinsic [222]. The former has been well documented in literature to have a significant contribution from thermal stresses that arise from CTE mis-match in materials and processing conditions. However, intrinsic stresses are typically generated from non-equilibrium/non-homogeneous formation during the thin film deposition. Phenomena that result from this that have been attributed to intrinsic stresses including voids, impurities, dislocations, grain boundary formation and nucleation [222]. The exact source of residual stress is thus very challenging to determine, especially the intrinsic component.

With the above in mind, when analysing the curvatures a definite trend of Al thickness with increased residual strain and so stress until a critical thickness where this is reversed. One hypothesis for this could be that the change in deflection direction due to temperature change when enough Al is deposited to overcome the Au occurs causing the cantilever to deflect in the opposite direction. As a result, when the cantilever heats up during deposition, it will deflect negatively. This is plausible and indicates that this extrinsic stress may have significant influence on the final structures residual strain and stress. However, it has also been well documented that greater thickness does not always render greater residual stress and strain in a single direction for a number of metal coatings [223]. This has not been explicitly documented for pure Al coatings deposited through thermal evaporation, but is a potential explanation. With this said, formation of Aluminium Oxide could be increasing the residual strain and stress, as highlighted by R. Abermann [224]. However, even this highlights that with greater Oxygen presence and so oxide formation, a peak compressive stress occurred with it eventually changing to produce tensile stress. Although, with the hypothesis of Aluminium Oxide also potentially reducing the deposited layers ability to counteract the Au, it would be generally ideal to limit this to as near zero as possible. Therefore, a study was performed in an attempt to minimise this effect as much as possible and determine whether it renders both enhanced thermal bend reduction with thickness

and residual strain and stress. This was carried out by a chamber-conditioning deposition of 20 nm of Titanium that readily reacts with Oxygen [225] with the sample shutter closed to prevent deposition on the cantilevers. Here, the Titanium deposits around the rest of the chamber and not the sample (termed a dummy deposition in this work) removing any remaining Oxygen in the chamber. A variable set of Al thickness's within the previous experiments 0-100 nm range were deposited employing this deposition method. The percentage change in the thermal bend induced vertical deflection can be seen below in Fig. 6.20 alongside the absolute change in change in Fig. 6.21. Additionally, the residual strain curvatures of each cantilever are shown in Fig. 6.22.

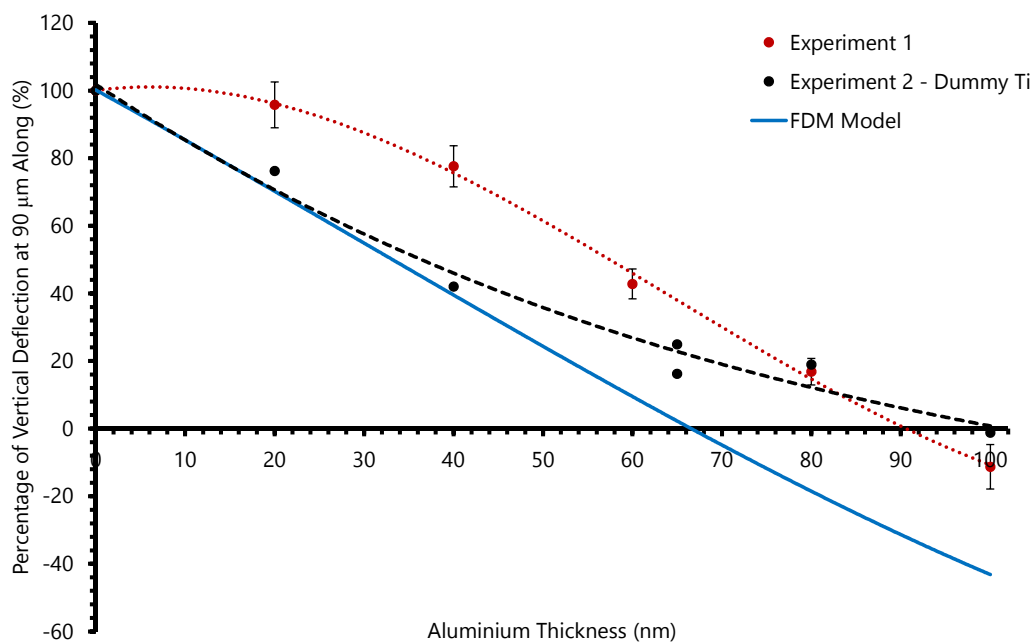


FIGURE 6.20: Feasibility Study - Cantilever Thermal Bending Deflection Percentage Change 90 μm Along With Dummy Ti Data

Analysing Fig. 6.20, there appears to be a greater change in the thermal induced deflection than in the previous experiment for low Al thicknesses with it aligning reasonably well with the theoretical model. However, with greater thickness it converges towards a similar reduction in thermal bending to the previous experiment's data. Initially, the author would hypothesise that with greater thickness in the initial experiment, that it more acts like pure Al which should converge to the result for the

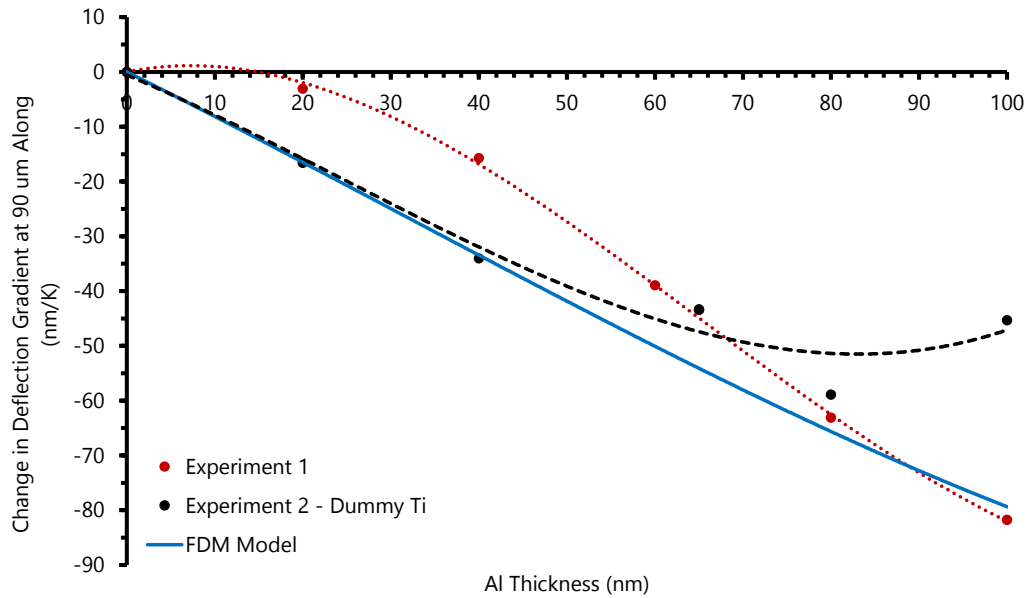


FIGURE 6.21: Feasibility Study - Cantilever Thermal Bend Gradients $90 \mu\text{m}$ Along with Varying Al Thicknesses

dummy Titanium deposition which aligns well with the results. However, with constantly minimal oxide formation in the dummy Titanium data, a more constant reduction in thermal bending would have been expected based on the modelling data. The resultant trendline indicates that perhaps this is not the case, but with only six data points this may not be suffice to fully define the trend. Furthermore, what could be impacting the dummy Titanium data set is that the cantilevers were from different wafers, resulting in slightly different geometries and/or material properties that have generated an inconsistent relationship. Indication of which can be seen with a range of 45 nm/K and 73 nm/K in the thermal bend gradients $90 \mu\text{m}$ along before metallisation. Moreover, the two cantilevers at either extremes of this deflection gradient range exhibit the opposite change in the Al thickness vs. vertical deflection reduction (i.e. increase as opposed to a decrease). This can be seen in Fig. 6.20 between the lower data point for an Al thickness of 65 nm and 80 nm . Therefore, this does indicate that this data set may not be completely comparable contributing notable uncertainty in the results. This is further emphasised if the deflection per Kelvin is graphed for $90 \mu\text{m}$ along the cantilevers, whereby the two cantilevers with the 65 nm of Al deposited show the exact same change in deflection, while the 100 nm shows far less as

seen in Fig. 6.21. The latter is primarily due to the cantilever experiencing the lowest initial thermal bending in the data set and so changing by the least magnitude. This indicates that the SiNx has a notably greater thickness/Young's Modulus and is a reason why the relative percentage change has been graphed in Fig. 6.20 as this aids to remove the substrate as a variable when comparing cantilevers. However, the cantilevers with 65 nm of Al showing the same change in magnitude, but different relative changes indicating that their substrates are very similar but the NiCr-Au wires may be different. Overall, this experiment unfortunately demonstrates some comparability issues between the cantilevers employed and emphasises the requirement for similar cantilevers when performing such a study. However, some indication is given that less oxide formation is occurring at low Al thickness's that may be rendering greater thermal bend reduction in this region. Therefore, it appears that the dummy run of Titanium may be rendering benefits, with the slightly irregular data being primarily due to the variable cantilevers geometry, material properties and/or composition.

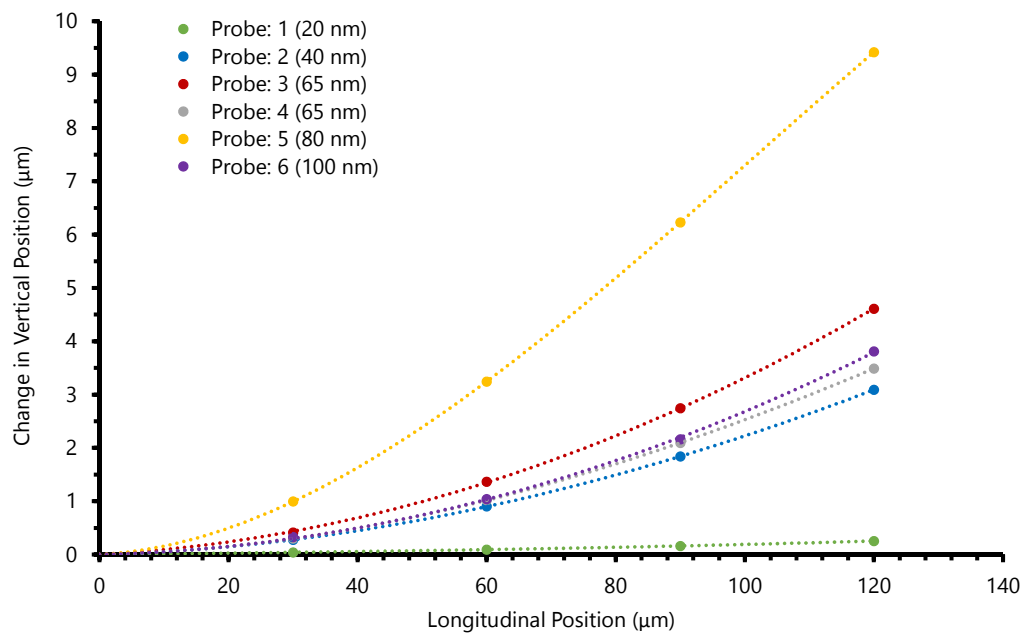


FIGURE 6.22: Feasibility Study - Dummy Ti Cantilever's Change in Ambient Profiles/Curvature

Moving towards the other reason for this specific study, the residual strain/curvature graph of Fig. 6.22 shows a similar picture to that displayed without a Dummy Titanium deposition. Specifically, an increase in the curvature and position with thickness up to 80 nm, whereby the thicker 100 nm deposition generated a decrease. This adds

further evidence to depositions beyond 80 nm of Al producing a shift in the residual strains. One potential hypothesis still being that this is due to the extrinsic/thermal change after a critical magnitude of Al has been deposited. However, this still cannot be verified and could also be due to the known non-linear change in residual strain and stress with thickness. Regarding the absolute residual change with a dummy Ti deposition, apart from the deposition with 80 nm of Al, there appears to be a slight reduction in the resultant residual strain. However, it is hard to decouple this from the known variability in the cantilevers. Overall, the dummy Ti deposition has some indication of limiting oxide formation that may render it more effective, especially at low Al thicknesses. This may translate into reduced residual strain and stress, but this can not be definitively concluded. Although, what can be extracted is that the deposited Al thickness has a clear influence with a reduction in residual strain beyond 80 nm.

With all the above noted, the next step was to employ one of the cantilevers which demonstrated a significant attenuation in thermal bending from the backside Al deposition in an AFM. Even with the significant residual strain imparted from the deposition, it was still possible to obtain a reflection onto the AFM photodetector. The experiment utilised for this was the microheater approach as performed in Section 5.1.2.2. This permitted both the OC and IC thermal bend deflections to be quantified. Moreover, as the normal flat SThM cantilever had already been measured, a direct comparison was possible. Two probes were utilised for this: Probe 5 (Al = 100 nm) from the initial experiment as this demonstrated near complete attenuation and another probe (named Probe 6) with 100 nm of Al using the Dummy Ti run. Two were processed to provide greater confidence in the resultant conclusion and trends as well as to ensure that the Dummy Ti rendered a similar resultant deflection as suggested when approaching this Al thickness. It should be noted that Probe 5 did not have its tip temperature measured during the experiment. Therefore, this employed the previous flat non-backside metallised SThM cantilever's temperature vs microheater power relationship. Hence, to provide additional assurance Probe 6 with the same Al thickness of 100 nm was used with its tip temperature measured. As was performed per Section 5.1.2.2, five laser locations along the cantilever length were chosen with the thermal bend induced deflection gradients determined for both OC and IC thermal induced deflection in accordance to the method previously applied. In addition,

the cantilever was positioned in the same position relative to the microheater as the previous flat SThM cantilever for sound comparison. The results are shown in Fig. 6.23, where a third order polynomial trendline has been employed to simply guide the eye with errors calculated in the typical manner.

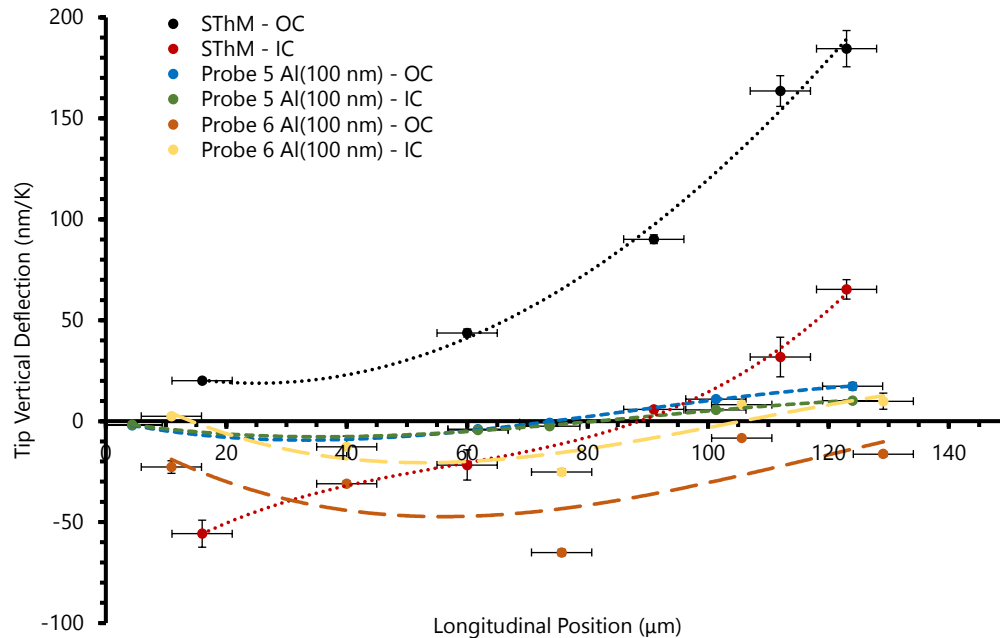


FIGURE 6.23: Feasibility Study - Probe 5 Microheater OC & IC Profiles vs Normal Flat SThM

As can be seen immediately, for both the OC and IC thermal bend profiles, a significant reduction relative to the non-Al SThM cantilever occurred across the whole cantilever length. Analysing the OC profile initially, both Probe 5 and 6 demonstrated significant change in the negative direction in their interpreted tip deflections. For Probe 5 this appears less whereby around $80 \mu\text{m}$ along its length a change in the deflection direction occurred. If this is contrasted to the Interferometer profile in Fig. 6.17 for Probe 5, at around $100 \mu\text{m}$ a POI occurred and so a change in rotation from negative to positive. This is further along the length than that from the AFM's profile, but is a similar position with the same change having happened from negative to positive. However, greater inaccuracy in the AFM laser's longitudinal measurement occurred due to the Al backside coating preventing laser to refract through the SiN_x and onto the Peltier surface that aided the laser location measurements. Moreover, the Optical Profiler experiment employed a uniform temperature change as opposed to the more concentrated microheater one that may be slightly shifted. With this in mind,

their similarity is still apparent, with near zero thermal bend induced deflection being measured at the POI $80\ \mu\text{m}$ along. For Probe 6 a more negative OC deflection occurred indicating that for this cantilever, the 100 nm of Al over-compensated by a reasonable degree. Furthermore, it demonstrated greater variation to its imposed trendline. Although, it is well understood that this trendline will not be able to capture the complexity of this variable temperature distribution alongside the triple-material cantilever construction which may be more convoluting when Al is over-compensating. With this said, towards the free-end the interpreted tip deflection gets more positive which is aligned to all behaviour seen in models and in Probe 5 due to the increase in Au width $80\ \mu\text{m}$ along the cantilever.

Regarding the IC behaviour, Probe 5 shows a very similar profile to the OC situation. This matches the theoretical findings of the FEA Models seen in Fig. 6.16 as when the tip deflection approaches zero the OC and IC begin to align. Comparing this to the non-Al SThM's IC profile, it is greatly reduced with a flatter profile demonstrated. Moreover, this data highlights that 53 % along the cantilever near zero thermal bend interpretation occurs with its Al deposition. This is less expected from the FEA models, but as highlighted previously perhaps the laser location measurement was not as accurate. Furthermore, the flat nature of the profile renders the exact cross-over more likely to vary than if it was steep. Further to the latter point, this flat region effectively makes the laser location wider for a low thermal bend interpretation which is superior to the steeper transition with no Al. Moving onto Probe 6's IC profile, this shows a greater deflection variation than Probe 5's, likely due to the over-compensation of the Al. This deflection is less than when OC due to contact limiting tip displacement along with a change in deflection $108\ \mu\text{m}$ along. This is 72 % along the cantilever which is further along than the non-Al and Probe 5. If this is averaged with Probe 5's POI then it is closer to the expected 60 %. Overall, this data demonstrates a superior profile for both OC and IC thermal bending that can be obtained when depositing a significant thickness of Al. This means that even if the ideal laser position at the POI is not obtained, it will be more insensitive to thermal bending, especially near the tip.

To verify the above translated into improved topographic scans, the same X-X line scan (shown in Fig. 5.13) previously performed was executed for both probes. The results can be seen in Fig. 6.24 & 6.25, with the non-Al SThM cantilever used to provide

contrast.

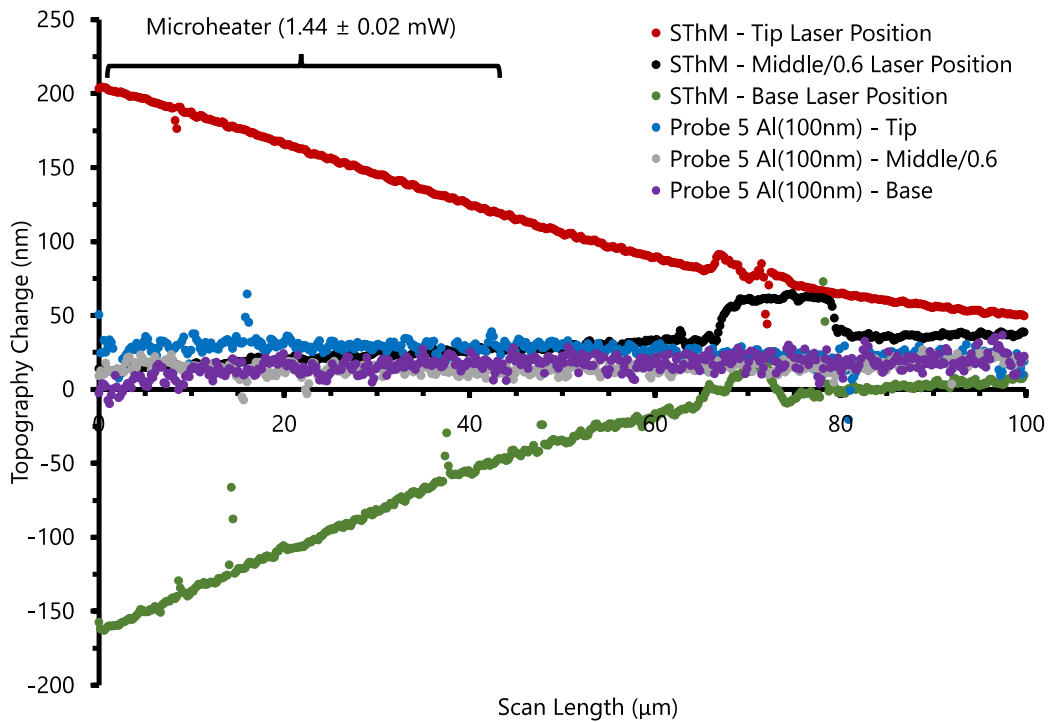


FIGURE 6.24: Feasibility Study - Probe 5 Microheater Line Scan's vs Normal Flat SThM

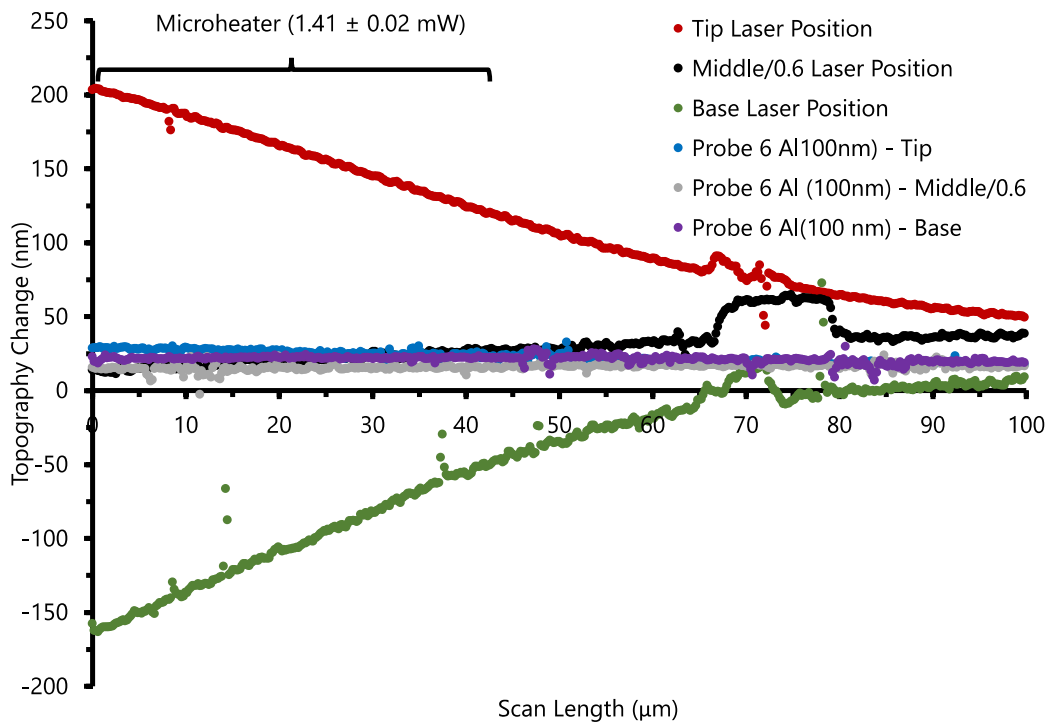


FIGURE 6.25: Feasibility Study - Probe 6 Microheater Line Scan's vs Normal Flat SThM

Analysing these profiles, even with variable laser position, Probe 5 and 6 demonstrated very little variation in topography while approaching the left side where the microheater was located and temperature increase occurred. With both experiencing very similar temperature profiles, they showed only a slight increase in their tip laser positions as the cantilevers moved to the left over the microheater. Both produced a very flat topography for the middle/0.6 laser position while for a base position, Probe 5 experienced a slight decrease while 6 very little. However, they both outputted a very similar topography deviation on the left-side of around 25 nm. This is markedly less than the 360 nm range observed for the non-Al SThM cantilever. This verifies that the IC profile deduced theoretically is translated into a similar topographic output which reiterates the cantilevers pronounced insensitivity to thermal bending.

Overall, the above confirms the ability for backside metal deposition to greatly attenuate Au's induced thermal bending and provides an appreciation of the thickness required for this. Moreover, although not definitive, the data indicates that, specifically for Al, a Dummy Ti deposition prior may render enhanced low thickness performance and potentially reduce residual strain. Therefore, the latter will be performed in the final study. However, significant residual strain still occurred from Al deposition, which would benefit from a more comprehensive study. In addition, investigation into the reduction of the Au so less Al is required, temperature control of the cantilever during deposition, thermal cycling post treatment and employing a different metal for the backside deposition may all be worth exploring. Beyond this, the feasibility study did verify the experimental set-up was capable of producing sound results for analysis that can be employed in any future design study/characterisation.

6.2.3 Design Study

With the Backside Deposition Solution and Au pattern alteration looking very promising from the models and the feasibility study above, a full design study was initiated. This involved fabricating SThM cantilevers with an altered Au pattern that aimed to enhance thermal bend attenuation and reduce the impact of the Au metal as shown by FEA in Section 6.2.2.1. For the latter, less Au is needed as it is no longer required to act as a mirror for the optical lever. This will result in less Au induced thermal bending, meaning a thinner Al film will be required to counteract it. Moreover, changing the

Au pattern may render improvements in the general attenuation across the cantilever width and length. The impact of these alterations on the residual strain and stress is of interest as well. The exact method to fabricate and perform this study is elaborated upon below.

6.2.3.1 Method

The FEA exploration exercise described in Section 6.2.2.1 identified alternative Au patterns which provided some compelling and interesting thermal bend profiles when balanced by Al on the backside of the cantilevers. As a result, these were selected for fabrication and subsequent experimental investigation. All the designs are listed in Table 6.8, with an aerial graphical representation shown in Table 6.6.

TABLE 6.8: *Attenuation Design Study - Different Designs*

Design No.	Description	Wire Width (μm)	NiCr-Au Thickness (nm)	Au Lateral Position from Edge (μm)
1	Wide Wire Position	27	150	3
2	Middle Wire Position	27	150	15
3	Narrow Wire Position	27	150	30
4	Wide & Thin Wire	57	80	1

As a suggested by FEA models, these should all produce different thermal bend behaviours with and without Al depositions. Although with the latter, when the Al approaches the ideal thickness for zero thermal induced tip deflection there are clear differences. This is not only in regard to the Al thickness required, but the subsequent thermal bend profiles both OC and IC. Therefore, this study was aimed to contrast against those results and conclusions, whereby the exceptional promise shown in the FEA's output for Design 4's Thin-Wide construction was identified as a potentially ideal design for future commercial SThM cantilevers. To enable this, multiple cantilevers of each design were fabricated to enable statistically sound conclusions.

Fabrication

As highlighted in Sections 2.4 & 3.3.1, a vast array of fabrication processes are used in the manufacture of commercial SThM devices with the specific process sheet presented in Appendix D. This sheet was followed to produce all the cantilevers fabricated, with Step 62 (EBL definition of the Au wire/pad) and 63 (NiCr-Au metal deposition) being the specific steps required to produce the different Au pattern designs. Furthermore, it should be noted that only a single thickness can be deposited for each EBL definition meaning that a separate definition and deposition needs to occur if there is any thickness variation. This is the case for Design 4 to the others and so this step was performed separately for this probe type. Bearing in mind the previous investigations that provided essential background and insights to the design constraints for SThM probes, the main discussion focus shall be upon Step 62 of the EBL pattern that differentiated each design. These designs were created in Layout-Editor software L-Edit and imported into a format to be written through EBL. This followed the common process flow in the JWNC [139] of exporting L-Edit files into a Graphic Design System (gds) file format; converting these into a fractured pattern file called a Geosoft Project File (gpf) through in-house software called Beamer which allows the EBL tool to write it; importing this fractured pattern into a layout software called c-job for positioning and write parameters to be defined for the wafer in the EBL tool. The L-edit files mirrored the dimensions used in FEA and are shown in Fig. 6.26. These patterns were fractured with a main-field-resolution and beam-step-size of 1 nm and 50 nm respectively. This aligns with what is utilised for commercial SThM probes and was adequate for the Au designs to be written as the features are relatively large and were good enough for sound resolution near the tip region. This file was then exported to the layout software c-job that defined the exact write positioning, alignment markers (pre-markers, global and local) and exposure. Specifically for the latter, a dose of $820 \mu\text{C}/\text{cm}^2$ defined the whole pattern in PMMA resist. However, an additional exposure of $230 \mu\text{C}/\text{cm}^2$ was executed for the Au pattern on the side of the pyramid. The rationale being that the angle of the pyramid results in a reduction in the dose of the beam over this area (simple trigonometry demonstrating this). These parameters resulted in a write frequency lower than the maximum 100 MHz frequency of the EBPG 5200 EBL

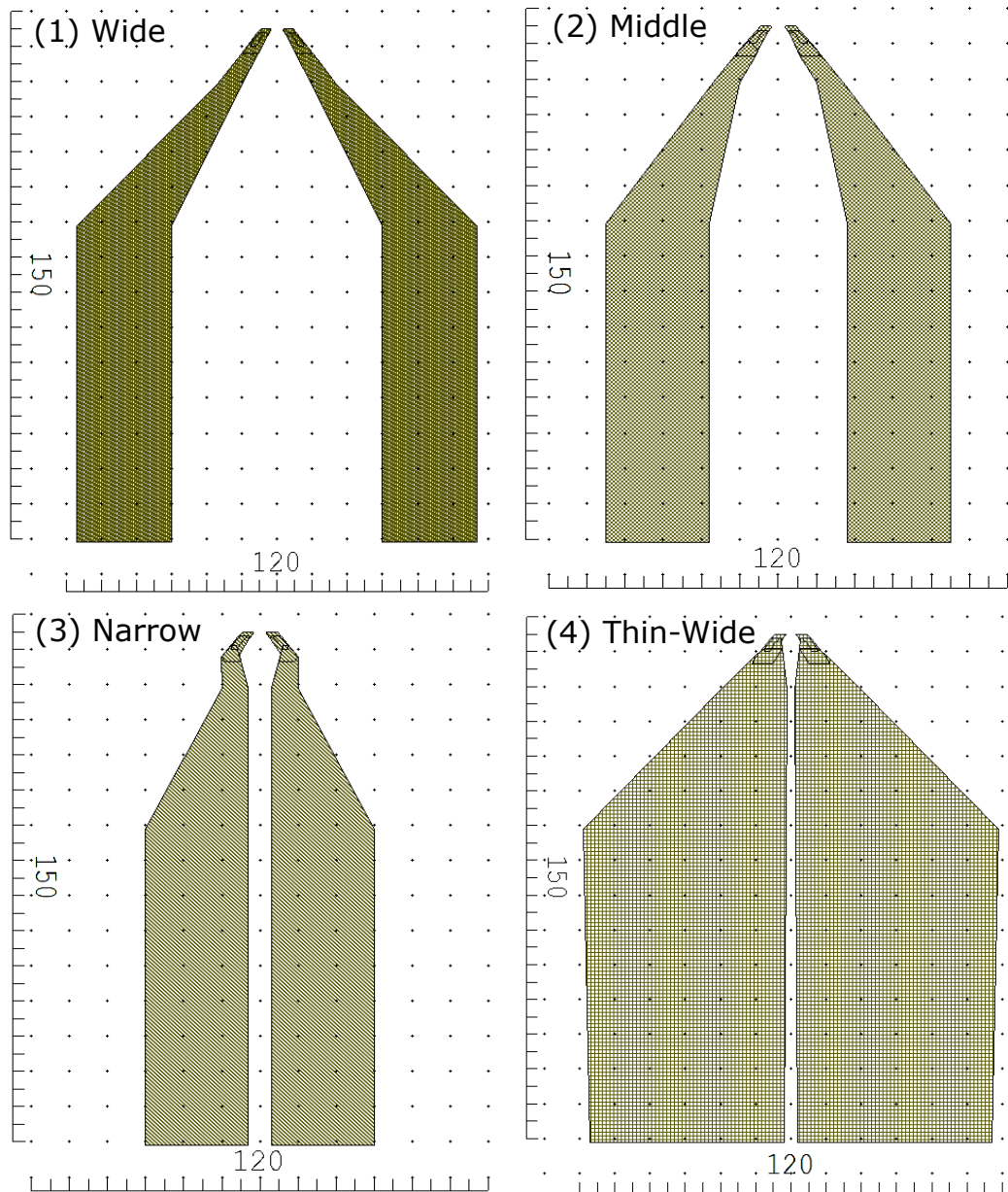


FIGURE 6.26: New SThM Designs L-Edit Images (Dimensions Shown in μm)

tool in the JWNC permitting the patterns to be written. This was then followed by development using MIBK:IPA at 23 °C and deposition of a NiCr adhesion layer and Au in Plassys II to form the wire. As two different NiCr-Au thicknesses were desired with Design 1-3 and 4 requiring 150 nm and 80 nm respectively, these designs had to be written and deposited separately as previously highlighted.

At least 45 probes were written for each design across two wafers to ensure that a sound number of cantilevers of each design was produced. Moreover, each design was

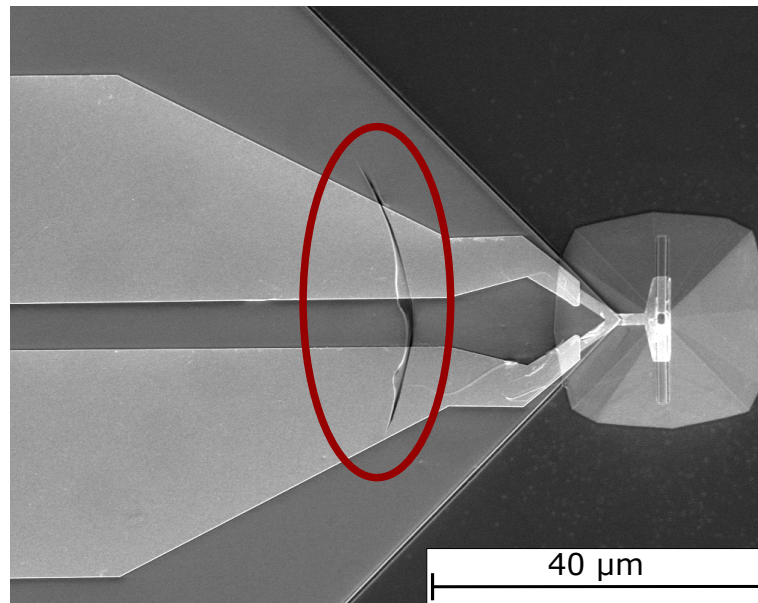


FIGURE 6.27: SEM Image of Narrow Wire Design Post Wire Definition (Step 62) with the Etch Cut Highlighted

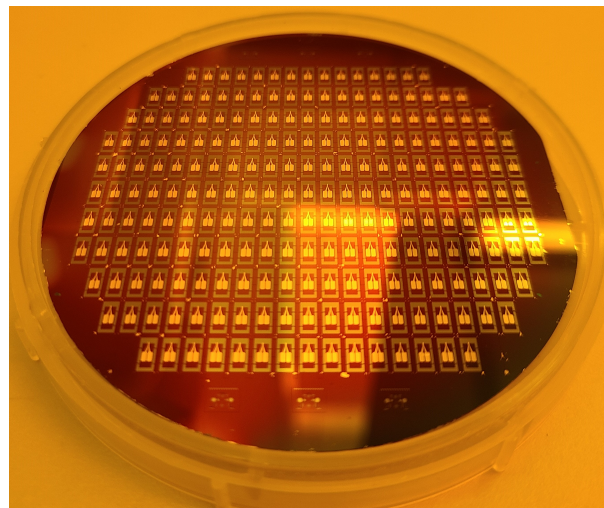


FIGURE 6.28: Image of a 3" SThM Probe Wafer Prior to Release

spread out across the wafer to minimise localised contamination/failure from eliminating a significant number of a single design. This effort was especially required as one of the wafers unfortunately had etch cuts along the SiN_x for many cantilevers as seen in the SEM image obtained in the FEI Nova NanoSem 630 in Fig. 6.27. This occurred due to the cantilever definition between steps 33-48 requiring a combination of EBL and Photolithography. The former defined a pattern for a NiCr hardmask which provided the outer definition of the cantilever (i.e. the border of the cantilever). Photolithography then generated a photoresist pattern that defined the rest of the cantilever (i.e. the internal portion) and the pattern on the main probe chip. The overlap

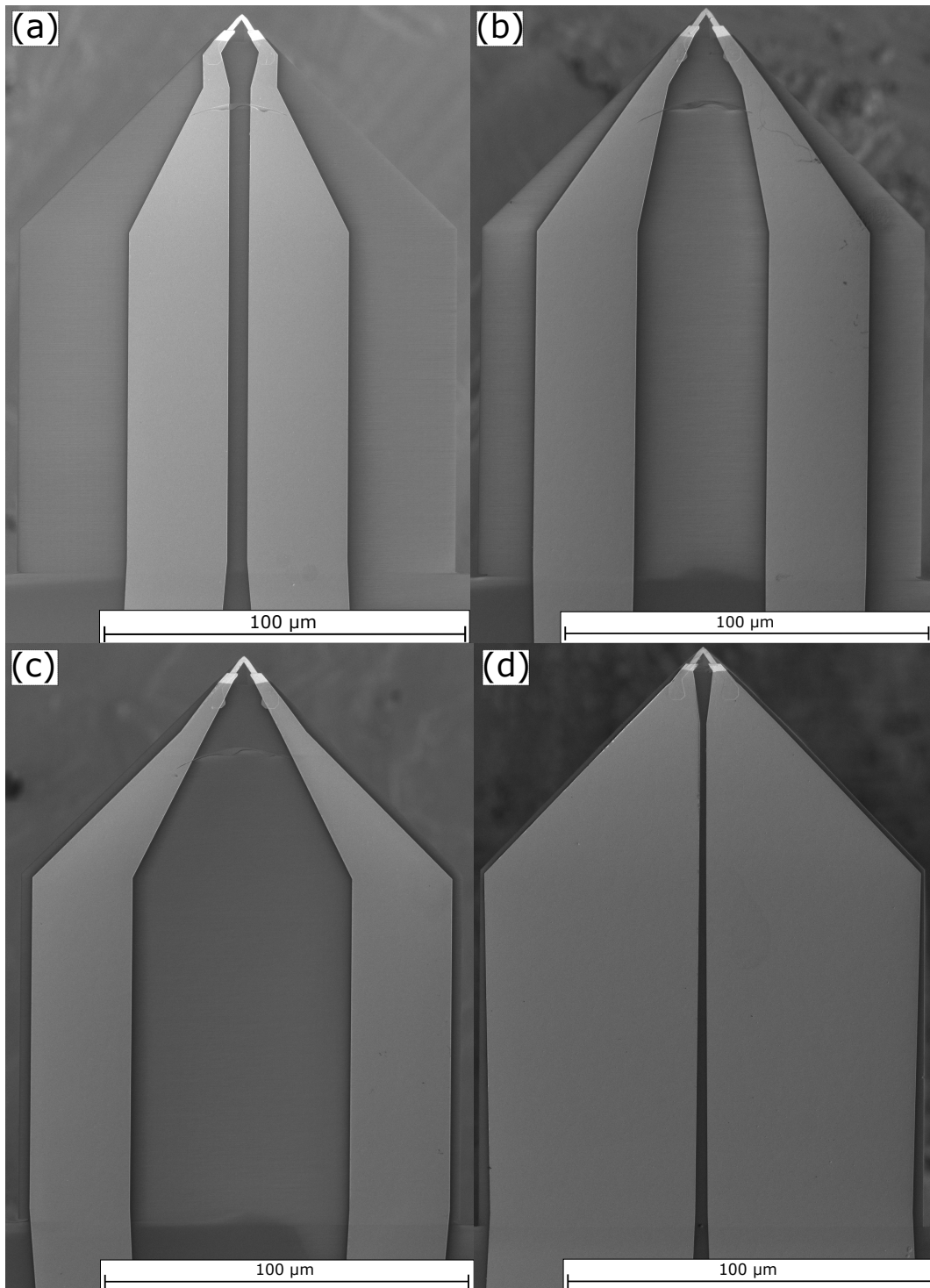


FIGURE 6.29: SEM Images of all SThM Probe Designs Fabricated: (a) Narrow; (b) Middle; (c) Wide; (d) Thin-Wide

of the NiCr hardmask has a fine tolerance less than $10\ \mu\text{m}$ laterally to the EBL defined pattern. Therefore, slight misalignment in either the horizontal axes or rotationally that rendered narrow regions in the cantilever to be exposed and etched through by the RIE CHF_3/O_2 dry etch. This wafer was still employed as the outer mechanical

cantilever structure was still intact and from the base to the etch cut, reasonable cantilever behaviour should still occur. Following the probe process sheet in Appendix D, probes were released from the wafer (see Fig. 6.28 for a visual of a wafer prior to release) utilising a hot TMAH wet etch that removed the Si connecting the probes to the wafer and underneath the SiN_x cantilever. This subsequently left thin SiN_x beams that kept the probes attached to the wafer to be "popped" out. SEM images can be seen of each released wire design in Fig. 6.29. Before proceeding onto experimentation of these cantilevers, it is worth noting that the low stress LPCVD SiN_x deposited at step 23 produced a lower than expected thickness. Instead of it approaching the nominal 400 nm desired, it had an average value of 315 nm and a min-max range of 302.3-337.6 nm respectively. This was not a fundamental problem as it was not thin enough to render the cantilevers susceptible to problems such as delamination or deformation in processes such as the final release etch. However, this notable reduction in thickness relative to standard flat SThM's resulted in lower spring constants and greater deflections due to thermal bending. This was not ideal, but as highlighted already, SiN_x thickness is a known uncertainty and variable, and this provides clear evidence of this. Moreover, as this was already borne in mind as a potential source for variation between cantilevers, the chosen Backside Deposition & Au pattern alteration solution was not affected by this. With this consideration and a number of sound cantilevers for each design fabricated, it was possible to undertake experimentation to ascertain their Mechanical and thermal bend characteristics to contrast them to theoretical models and commercial SThM cantilevers.

Experimentation

The method to which the above cantilever designs were explored experimentally aimed to provide a sound characterisation that could be contrasted to previous experiments alongside that of the models. A time-efficient set of experiments were designed to produce the most useful information for the time required to set-up, perform and analyse them. As a result, the following three experiments were executed.

Experiment Set 1 - OC Thermal Bending Pre-Deposition:

The objective of this experiment was to determine the different thermal bend induced

longitudinal and lateral deflection profiles for each design. This should highlight each design's characteristics and be able to be contrasted to FEA modelling. To induce thermal bending, the same Peltier heater previously used was employed with the deflection and temperature measured using the Interferometer and PT-100 respectively. The latter was used instead of the tip as it was challenging to electrically connect each probe to then disconnect them to permit backside deposition for the subsequent experiment. Furthermore, it is a time consuming process to perform these measurements as bespoke Wheatstone Bridges are required for each cantilever, in-conjunction with the additional time required to find a technique enabling disconnection prior to backside deposition. Moreover, as long as each cantilever is put under the same consistent position and heat transfer conditions they will be completely comparable (as highlighted in previous experiments). To this effect, each SThM probe was placed in the same position immediate to the PT-100 on the Peltier surface. The Peltier input voltage was increased in 0.7 V increments from 0 V to 2.1 V with a settle time of 4 minutes for each increase to enable a steady-state temperature to be reached. Once attained, four Interferometer images were taken alongside the temperature measurement for sound quantification of each.

Experiment Set 2 - OC Thermal Bending Post-Deposition:

The aim for this next experiment set was to demonstrate each design's thermal bend induced deflection profiles post-Al-deposition for a thickness of 55 nm. This would provide further indication of the differences between each design with FEA suggesting that this should be more apparent with significant thermal bend matching between the Au and Al. In addition, the 55 nm thickness was chosen as, from general experimentation, this thickness would provide a good balance to Au's thermal bending across all the different designs. As in the preceding experiment, the Peltier heater was employed with the PT-100 for temperature measurement with the Interferometer used to measure the induced deflection. This was placed in the same position on the Peltier surface as the previous experiment with the same Peltier heater input voltage strategy to ensure a good comparison.

The above two experiments, provide a clear data set to contrast the designs completely for their OC thermal bending deflection profiles. However, although the Interferometer provides an excellent and comprehensive measurement for comparison between the designs and models, it is not ideal for quantifying IC thermal bending. It was desirable to determine this for post-Al deposition in each design with an Al thickness generating near zero tip vertical deflection due to temperature change. Moreover, as the goal was to determine the manifestation of thermal bend in AFM and minimise it, a final experiment was constructed for this cantilever to determine its OC & IC thermal bend profiles in an AFM system. This is detailed below.

Experiment Set 3 - AFM Experiments of Design 4:

This final experiment utilised Design 4's Thin-Wide construction as it demonstrated the most promise theoretically, whereby this experiment aimed to further explore its merits in an AFM and demonstrate its capability as an SThM probe. For this, both the Peltier heater and microheater were employed with the 3100 Dimension AFM to measure their interpreted tip deflections. Dissimilar to the above, the SThM tip was employed for temperature measurement. This provides the most accurate temperature quantification alongside demonstrating the fabricated SThM's functionality. For the first sub-experiment, the Peltier heater was used in the same manner as the previous experiments with the exception that the temperature was acquired from the SThM tip and with the AFM's deflection outputted for a cantilever position 200 μm above the Peltier surface. The latter aimed to provide a similar heat transfer condition to the previous Interferometer experiments. The profile was then constructed from deflection-temperature gradients for multiple laser positions along the cantilever length. Regarding the second sub-experiment employing the microheater, OC and IC profiles were extracted while the cantilever was stationary (like that in Section 5.1.2.2). The cantilever was positioned in a similar manner to previous experiments as well as with the tip making contact with the Si chip and the cantilever body over the microheater. The exact method was replicated as described in Section 5.1.2.2. With this established, a line scan over the microheater was performed with the same X-X line seen in Fig. 5.11 and the subtraction of the heated and unheated scans. For all the above, the best cantilever chosen was vetted through the Interferometer as this provided a quick and

immediate set of deflection profiles due to thermal bending.

6.2.3.2 Results

Experiment Set 1 - OC Thermal Bending Pre-Deposition

Both the longitudinal and lateral profiles were extracted for all four designs to fully exploit the 3D deflection measurement from the Interferometer. The lateral profiles were taken from $90\ \mu\text{m}$ along the cantilevers as this is at the beginning of the taper and so is furthest along the cantilever prior to width reduction. Therefore, this should provide the best SNR to measure any lateral effects for each design. However, the longitudinal profiles should be first explored. These are shown in Fig. 6.30, with trendlines of a second order chosen based on Equation 3.9. X and Y error bars were calculated based upon the pixel size ($\pm 0.32\ \mu\text{m}$) and standard deviation of the determined gradients respectively. The same lateral position was taken for each longitudinal profile to ensure a confident comparison.

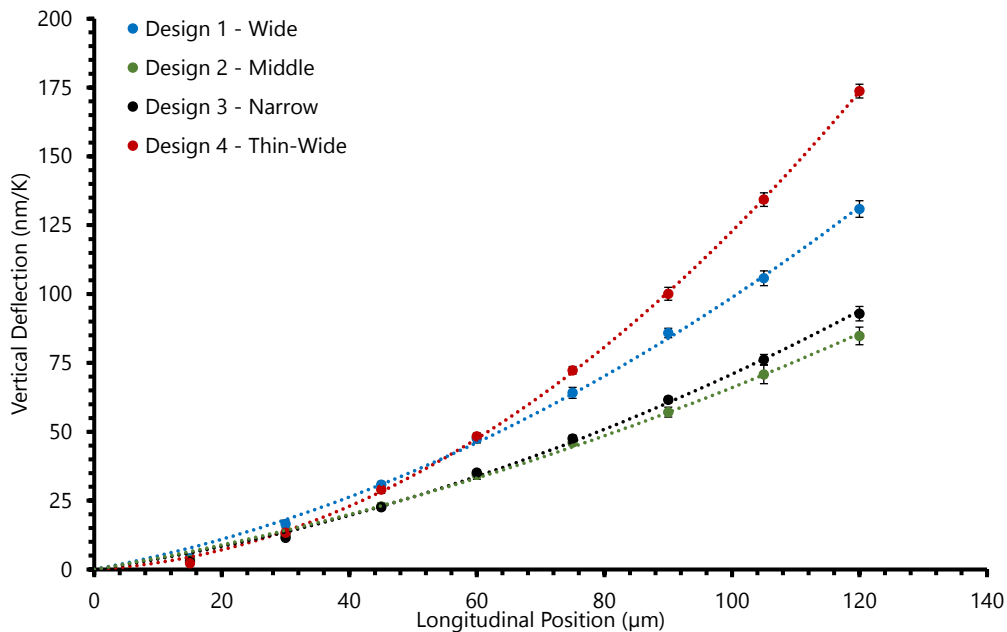


FIGURE 6.30: *Interferometer - Longitudinal Thermal Bend Profiles of New SThM Cantilever Designs*

What jumps out from these Interferometer measured profiles is the similar deflection with temperature change in comparison to a flat SThM design (e.g. $124\ \text{nm/K}$ $120\ \mu\text{m}$ along). This initially suggests that reduced Au has not rendered much improvement, especially for Designs 1-3 which have a similar thickness. However, this

was expected as the lower SiNx thickness averaged 315 nm, while the previous flat SThMs will have a closer thickness to the nominal of 400 nm. Approximately this should render a reduction in spring constant by just under half and so a doubling in deflection for an EF and an increase of 50 % for thermal bend induced deflection according to the FDM Model. Therefore, all cantilevers will be less stiff and so output far greater deflection from thermal bending for the same quantity of Au. With this said, the trendlines demonstrated in FEA as seen in Table 6.3 and Fig. 6.13 were not completely reproduced with wider Au generating greater deflection than the Narrow and Middle coating designs. However, the trend of Au's lateral position to deflection is not in a single direction with the middle position demonstrating the lowest deflection profile. This lack of a clear trend could be partly explained by the variation in the SiNx deposited on the wafer. However, this is hard to know for each cantilever and can not be assumed to fully explain the trend. As a result, this likely highlights a potential issue with the theoretical model's ability to represent the more complex lateral effects upon the final vertical deflection for each cantilever design. Although, these results still mirror the model's conclusion that the Au coating's lateral position does influence the longitudinal profile, albeit an inconclusive trend. Moving towards Design 4's Thin-Wide form, this produced a greater deflection than the other designs. This was not initially expected from the FEA results seen in Fig. 6.13 which demonstrate that it should be comparable to the other designs. Again the SiNx variation could partly explain this. Although, if this is assumed to not be the case, it indicates that the design perhaps is generating greater deflection than predicted from models with it perhaps aligning better with the total cross-section of the Au between designs (Designs 1-3 and 4 showing a maximum of $4.05 \mu\text{m}^2$ and $4.56 \mu\text{m}^2$ respectively). Therefore, a similar conclusion of the trend being unclear, but providing indications that the lateral placement does have an impact on the longitudinal deflection profile. With these points established, the next step was to explore the lateral profiles for each. These can be seen in Fig. 6.31 for $90 \mu\text{m}$ along the cantilevers, whereby the full profiles normalised to temperature change permit appreciation of its potentially more complex form when compared to the longitudinal profiles.

What should be noted before analysis is that due to the probe chip flat reference

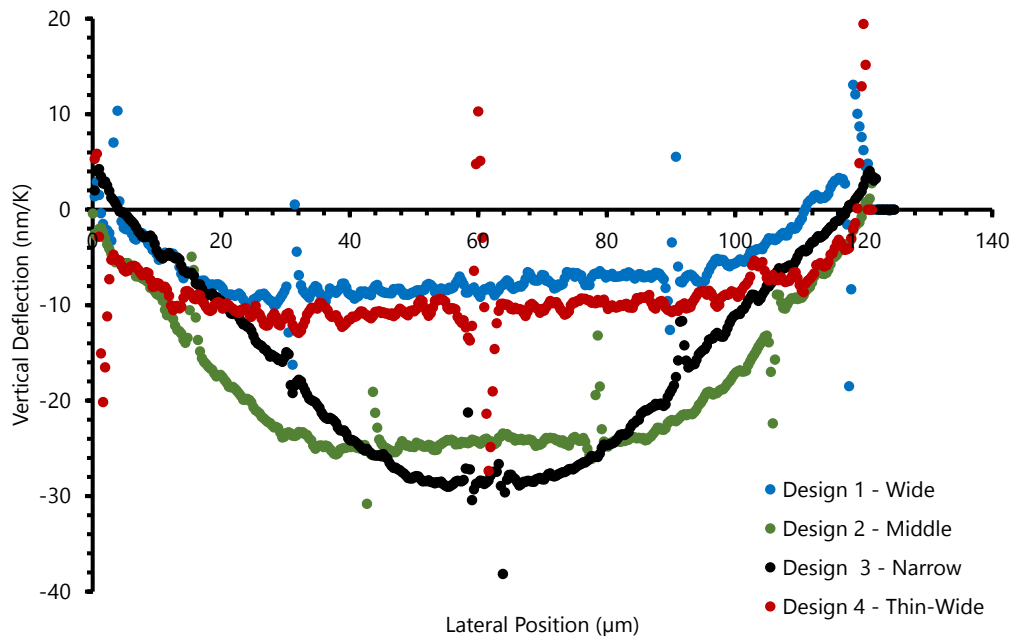


FIGURE 6.31: Interferometer - Lateral Thermal Bend Profiles $90\ \mu\text{m}$ Along New SThM Cantilever Designs

not being able to be utilised, the edges of the structure were taken as the zero. Therefore, these profiles do not provide an absolute output, but a relative one. With this in mind, when comparing to what was expected from FEA as seen in Fig. 6.13, a mixed comparison can be seen. When contrasting Designs 1-3, the profiles show good alignment to FEA whereby the wider Au positioning causes a greater plateauing in the central region and less relative variation. The deflection range for these are greater than depicted in the models that again is most probably associated with their reduced stiffness from the thinner SiN_x. However, Design 4 - Thin-Wide, shows a profile similar to the wide design. This was not predicted by FEA as it generated a profile similar to the narrow design (although a slightly wider plateaued central region). Again, this highlights that the FEA model may not be completely representing the more complex lateral behaviour of these cantilevers. With this said, this experimental result is better than expected as less lateral deflection variation will cause reduced displacement on the horizontal voltage of an AFM's photodetector. Overall, this experiment provided a very interesting comparison to theoretical models and demonstrated that the lateral position of the Au coating appears to have a pronounced impact. However, the trend depicted seems more nuanced than the FEA models suggest.

Experiment Set 2 - OC Thermal Bending Post-Deposition

The next step was to implement the Backside Deposition solution to verify that the reduction in Au in Design's 1-3 does enable less Al to be needed to balance it out. The hope was to also confirm these probes are inherently more thermally insensitive when compared to the normal flat SThM design (this could not be confirmed fully in the previous experiment due to the appreciably lower SiN_x thickness). Furthermore, the result could be contrasted to the FEA models in both the longitudinal and lateral profiles to see if they replicate a similar conclusion made by the previous experiment set. Twenty-six SThM cantilevers had Al deposited on their backside across a range of 50-100 nm in an effort to produce a set of cantilevers generating deflections that approached zero towards their tip. However, during the performance of this study a notable change in the thermal bend behaviour occurred from the deposited Al that caused inconsistent trends of Al thickness vs. thermal bend deflection. This was due to a maintenance on the electron-beam evaporator tool (Plassys IV) mid-way through the study whereby the Al was topped up and the shutter that controls the sample-crucible exposure being serviced. The deposited Al thicknesses were verified with a maximum uncertainty ± 5 nm utilising a stylus profilometer (relatively high uncertainty due to the measurements being performed on the probe chip where contamination was likely due to contact with Gel-Pak during deposition). However, it was strongly suspected that some contamination of the Al crucible occurred during the re-melting causing different resultant thermal bend profiles of the cantilevers (further strengthened as others users highlighted issues with deposited Al). Hence, it was challenging to correctly extrapolate an Al thickness that would render deflections approaching zero as a variable and unclear trend was produced across the deposited cantilevers. As a result, cantilevers with deflections as close to zero as possible were chosen. Designs 1-3 were deposited with the same Al thickness of 55 nm to enable comparison between them and vertical deflections above and below zero across their lengths. For Design 4, 80 nm of Al was deposited. The longitudinal profiles can be seen in Fig. 6.32 with the uncertainties derived in the same manner as Fig. 6.30. Third order polynomials were employed solely to act as a guide for the eye as with deflections around zero and multi-layers interplaying, the resultant profiles will likely be highly ordered.

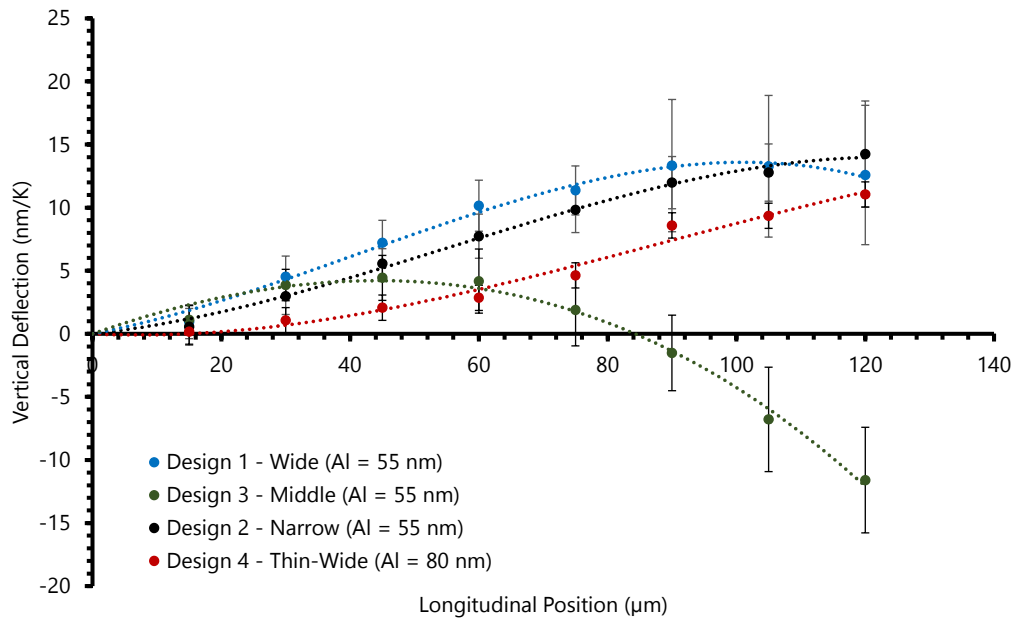


FIGURE 6.32: Interferometer - Longitudinal Thermal Bend Profiles of New SThM Cantilever Designs with Backside Deposition Solution (Al)

Designs 1,2 and 4 exhibited profiles that had not been completely attenuated by the deposited Al (i.e. not thick enough Al). However, with Designs 1-3 having the same Al thickness (55 nm), comparisons can be made between them. All exhibited a notable reduction in deflection compared to their profiles prior to Al metallisation (79-118 nm/K reductions 120 μm along). Design 2 - Middle demonstrated the lowest thermal induced deflection prior to metallisation and so it was logical that it produced the most negative deflection. The deflection along its length was still notably variable, with an initial positive deflection near the base followed by negative near the tip. This confirms the results outputted from FEA alongside the curved/humped profile being downward. Regarding Designs 1 - Wide and 3 - Narrow, both displayed positive profiles with the latter demonstrating a lower rate of change nearer the tip. FEA predicted that the Wide design would tend to curve similarly to the Middle one and signs of this can be seen here, whereby thicker Al would have generated a curve downward in a similar manner. Although not exactly producing tip deflections near zero, these do seem to align with FEA's general trends as seen in Fig. 6.16. For Design 4 - Thin-Wide, a more linear profile can be seen. This is reasonable as the Au is similar to the uniformly deposited Al in contrast to the other designs and so should produce thermal bend profiles more equal and less variable with length. This was indicated by FEA.

However, one aspect that inspired this study was the variation in lateral location of the Au to vertical deflection. Experiment set 1 provided evidence for this, but a definitive conclusion could not be extracted on the exact trend with lateral Au placement. However, this may be indicated by the change in thermal bending of the cantilevers following the Al deposition. Graphs depicting this can be seen in Fig. 6.33 alongside the relative percentage change across each length on the right vertical axis.

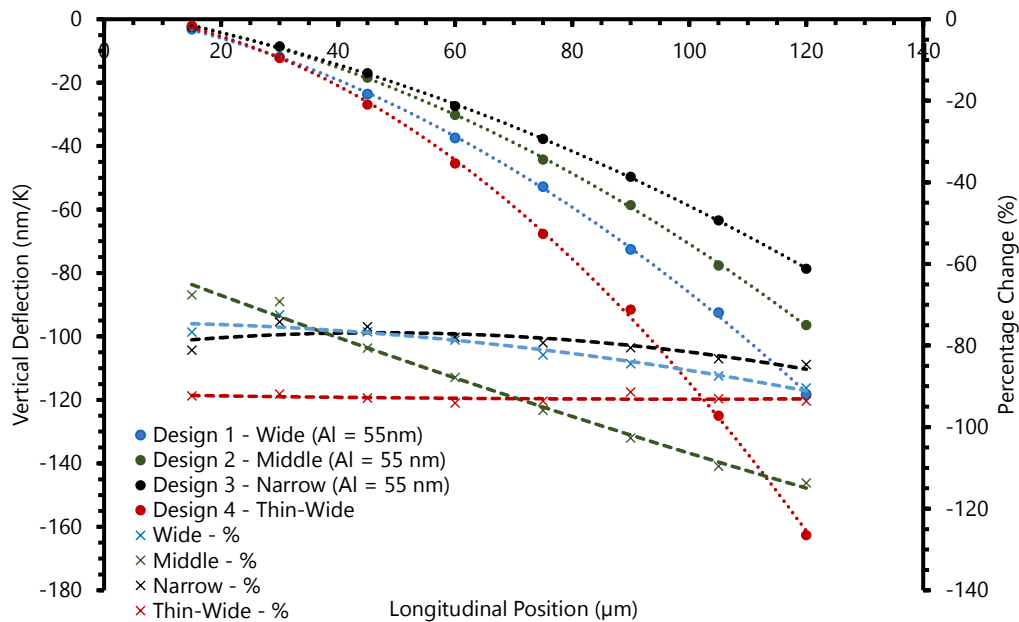


FIGURE 6.33: *Interferometer - Longitudinal Change in Thermal Bend Profiles & Percentage Change of New SThM Cantilever Designs with Backside Deposition Solution (Al)*

Designs 1-3 were the same cantilevers as measured in Experiment set 1 and so provided an accurate depiction of the impact of the Al. However, for Design 4 a different cantilever was used so this may not be as accurate, but should provide a reasonable comparison nonetheless. With this said, there is a clear trend of wider Au placement producing greater reduction in the deflection profile due to the Al. FEA indicated that less Al would be required to counteract for wider Au positions which aligns to these findings. However, this will be partly due to FEA predicting less deflection from the wider Au position which Experiment set 1 did not corroborate. Hence, Au positioning does appear to allow lower Al for the same thermal bend attenuation. For Design 4, a larger change was shown which was due to its thicker Al coating of 80 nm. If the profiles for the percentage change are analysed, Designs 1 and 3 output fairly flat lines while 3 a more negatively trending one. This is likely due to Design 2 being the Middle

one that had the Al over-compensate and so approached a region where it cancelled out the previous second order positive trend. For Design 4, a flat line was produced indicating the Al is counteracting the Au equally. Moving towards the lateral profiles, these were plotted in a similar manner to previously and can be seen in Fig. 6.34.

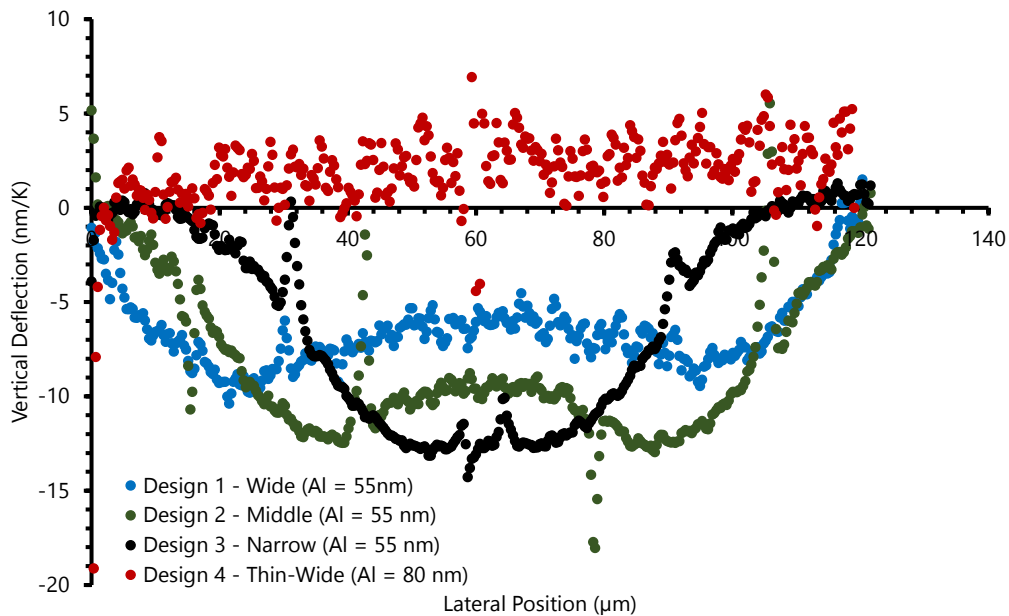


FIGURE 6.34: Interferometer - Lateral Thermal Bend Profiles of New SThM Cantilever Designs with Backside Deposition Solution (Al)

Again, these profiles do not provide absolute magnitudes due to levelling from the edges of the profiles, but the relative shapes can be contrasted. Interestingly, Design 1 - Wide shows a similar maximum change to before metallisation but with a greater arc centrally in the positive direction. This mirrors the previous finding of the design moving towards a profile and deflections upward as opposed to downward when approaching zero deflection. This is additionally seen in Design 2 - Middle, whereby a change in direction has not occurred, but a significant reduction in deflection change by half. This highlights a shift in the positive direction with Al metallisation, but perhaps not as emphatic as the FEA suggested. Design 3 - Narrow looks very similar to FEA's output seen in Fig. 6.15, but a comparable variation in magnitude is seen to the others. This could be explained by an inadequate thickness of Al or highlights that the FEA model has not completely accurately captured the lateral profile. If the latter is true then the benefits of the narrow design having less variation laterally is not the case. Regarding Design 4 - Thin-Wide, a very level profile was demonstrated. This

coincides with the Al balancing the Au evenly and emphatically aligns with FEA's prediction of little lateral variation in vertical deflection (and hence horizontal voltage change on a photodetector). FEA accurately depicted this behaviour which is logical as the Al and Au balance out equally as they are very similar in their coating distribution. Overall, this result set substantiates that the Au coating's lateral position has an impact on thermal bend induced deflection. This correlates in some instances better than others to FEA, indicating that wider Au positioning responds better to backside Al deposition. Moreover, it highlights that Design 4 - Thin-Wide does exhibit ideal characteristics with Au and Al balancing each other very well.

Experiment Set 3 - OC vs. IC Thermal Bending Post-Deposition

The above experiments and analysis provide a thorough characterisation of the thermal bend behaviour for these new cantilever designs. However, it is still beneficial to utilise one of these probe designs in an AFM to demonstrate their capability as SThM cantilevers and susceptibility to thermal bend. Design 4 was chosen for this as both theoretically and experimentally it showed the most promise in its longitudinal and lateral deflection profiles. Specifically, it showed more consistent and less variable profiles upon deposition of the Al that resulted in low thermal bend induced deflection. For example, the lateral profile was the most level of all the designs and the longitudinal showed a relation which looked increasingly more linear with attenuation of Au's induced thermal bending. As a result, the first AFM experiment was to provide an initial contrast to the Peltier experiments performed under the Interferometer. Although, using the cantilever's tip temperature measurement will produce a more accurate quantification than the PT-100 employed in the Interferometer. The experiment was performed in the same manner as described in Section 3.2.2.2. Utilising the TCR calibration measurement a value of $1.67 \times 10^{-3} \text{ K}^{-1}$ was generated which is greater than previous measured values (e.g. $7.33\text{-}8 \times 10^{-4} \text{ K}^{-1}$). This was expected as the commercial cantilevers previously used have two base resistors that are approximately $200 \pm 25 \Omega$ in total that produce a total sensor resistance around $350 \pm 25 \Omega$. As the Thin-Wide cantilever chosen had a tip resistance of 147Ω at ambient, based upon Equation 3.11, the TCR should be just over double which is the case and explains the difference observed. With this established, the resultant thermal bend profile can

be seen in Fig. 6.35, with the profiles for the commercial flat SThM with and without Al deposited are shown for comparison.

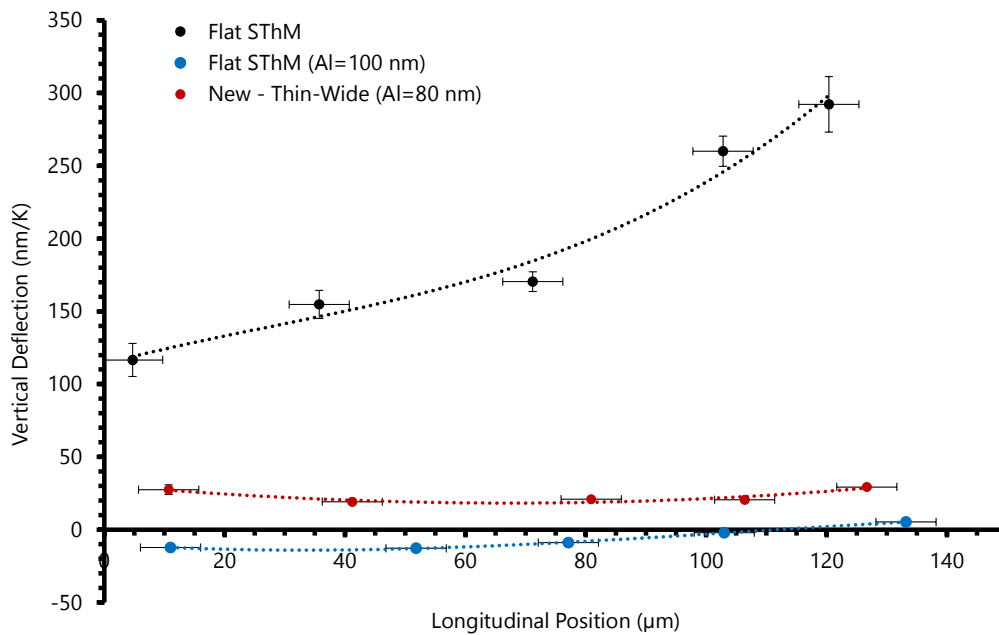


FIGURE 6.35: AFM - Peltier Induced Uniform Temperature Profile of Thin-Wide SThM (Al = 80 nm) Design with Previous SThM Cantilever Comparisons

Analysing this graph, it can be seen that the Al for the previous and new designs show an emphatic improvement relative to the original flat SThM design without any Al. Moreover, comparing the two Al deposited cantilevers some clear differences can also be seen. Firstly, the new design appears to require less Al for a similar effect. This is more significant when it is borne in mind that the new design has a lower SiN_x thickness rendering approximately 50 % greater thermal bend induced deflection. Therefore, it will have produced greater deflection than the original, flat SThM design. Beyond this, a far greater indicator of the new design's merit is clear: a flatter profile. This was seen in the interferometer results, but is very striking in the AFM output. For example the new design demonstrates a thermally induced deflection range of 10 nm/K while the older design with Al outputted 18 nm/K. Hence, the new designs objective to produce a more consistent deflection profile when attenuated with Al has translated into the AFM's output for uniform temperature change. However, it could be argued that the merits of this are relatively minor when compared to the old design and so simply depositing Al provides the vast majority of the attenuation. In contrast to this statement, the new probe will dampen the apparent the benefits with

its stiffness being approximately half and so it is likely with a similar SiN_x thickness and greater Al deposition that an even flatter profile could be achieved. For example, if the SiN_x was nominally 400 nm, the variation would be expected to be 6 nm/K with a greater Al thickness bringing it closer to zero. To further explore this new design, its IC behaviour investigated. As a result, the microheater experiment was performed as described in Section 3.2.3.2. This was carried out in the same manner as previously discussed in Section 5.1.2.2. However, two experiments were performed. This was due to the realisation that for the new design, when IC, there is far less deflection along the cantilever (as shown in Fig. 6.16) in comparison to the other designs due to its well-balanced nature. As a result, the cross-over point (like seen in Fig. 6.23) is harder to define together with the difficulties in ascertaining the optical lever laser's centre spot due to the reflective Al layer. Therefore, multiple measurements were made with these having different laser positions laterally to provide the full range of potential longitudinal profiles. Moreover, as the profile should have lower variation, it is of interest to ascertain the impact of the laser's lateral placement. The results can be seen in Fig. 6.36.

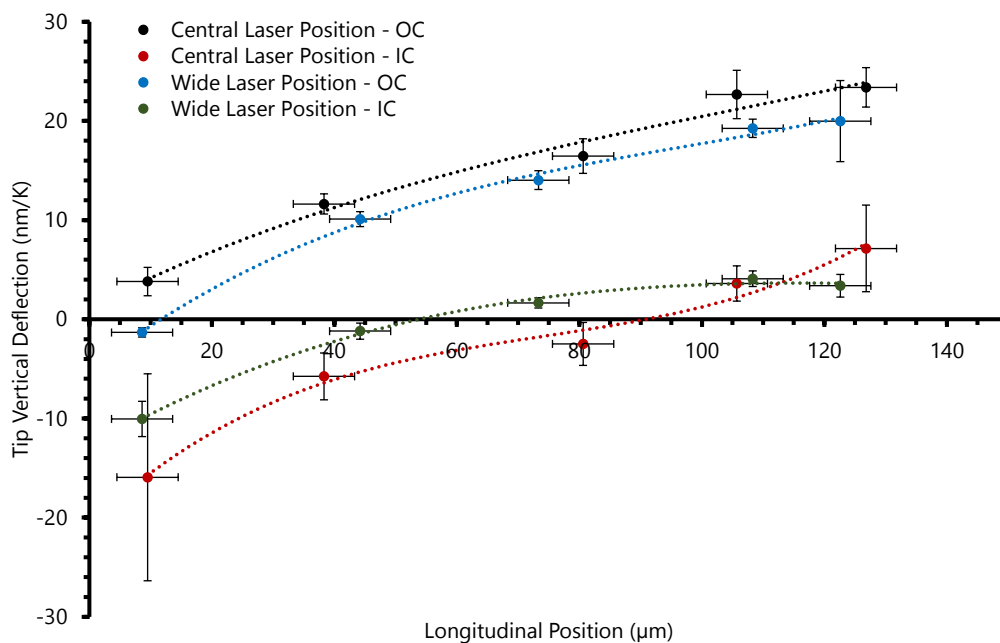


FIGURE 6.36: AFM - Microheater OC vs IC Experiment with Varying Laser Lateral Location on Thin-Wide ($Al = 80\text{ nm}$) Design

Focusing on the IC profiles initially, these show some difference with the more central position being more negative and varying slightly more than the wider laser

position. This appears in agreement with the FEA output seen in Fig. 6.15 showing a slightly greater hump in the central cantilever region. As a result of this and their similarly flat profile, the POI position is different between them. This could be misinterpreted as showing greater variation, but when analysing a range down to 13 nm/K across the length as measured with the wide laser position, this is simply due to the trend being more parallel to the x-axis causing the cross-over to easily shift in conjunction with the challenging longitudinal laser measurement. Furthermore, the OC data reflects the IC data, whereby the wider position shows less deflection. Their shape is similar which is to be expected when the tip is able to displace freely causing fewer non-linear effects. Before moving onto analysing how this translates into topography, it should be explicitly contrasted to previous cantilevers that were evaluated using this experiment. To achieve this, all of the SThM cantilevers which had their IC behaviour deduced using the microheater are shown in Fig. 6.37.

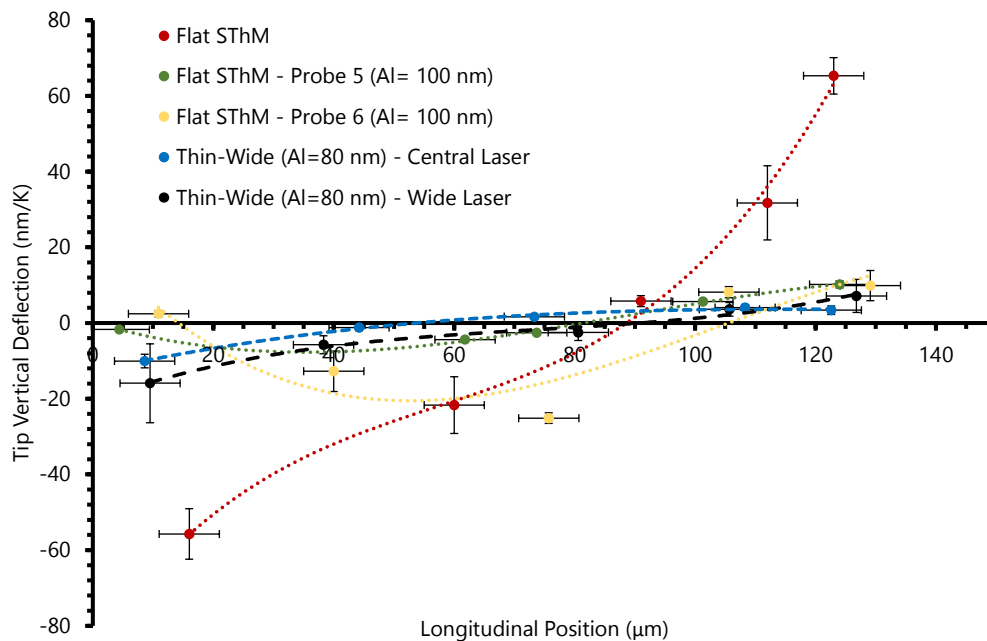


FIGURE 6.37: Microheater IC Experiment - All SThM Cantilever Design Comparison

This graph explicitly highlights the general merit of the Backside Deposition Solution, where the flat SThM cantilever shows a much greater variation across the length relative to all the rest. Contrasting the Al deposited Probes 5 and 6 to that of the Thin-Wide cantilever, it is apparent that the former generally outputs greater variation. Although Probe 5 is well balanced by its Al deposition, it is still evident that

it suffers from its more variable Au patterning with it showing more change in its rate of deflection along its length. For example, from its base it deflects downward and then upward while the Thin-Wide design has a more consistent arc to its profile. This is more evident by contrasting to the less balanced Probe 6 which has a more pronounced variation. Furthermore, the Thin-Wide cantilever is a lot less stiff from its significantly lower SiNx thickness and is notably under-compensated by the Al deposition. Bearing this in mind, its output is very good with the region near the middle-tip, where the optical lever laser is typically focused, showing a very flat profile meaning the rotation is changing little at this point as designed. However, there is one negative in that the base appears to demonstrate greater deflection than Probe 5 or 6. Although it would be ideal to have this flatter, the base is very rarely (if ever) used for laser spot reflection by AFM users. Furthermore, as seen from the FEA output in Fig. 6.16, this Thin-Wide design was expected to rotate by a notable amount immediate to its base, with it plateauing beyond 30 μm , making it such a favourable design. This plateau region then provides the lower thermal bend interpretation in the AFM's optical lever system.

The final experiment to explore the new Thin-Wide design's performance was to quantify its topographic output in a heating scenario. To do this, a line scan of the microheater was executed with the conditions and procedures the same as previously employed in Section 5.1.2.2. The results are demonstrated in Fig. 6.38 with the topography change for the old, flat SThM design overlaid. In addition, it was confirmed through measurement at the cantilever tip that a similar temperature change (approximately 1.5-1.7 K) occurred between each laser position which was very similar to the old, flat SThM's results. Analysing this data, the tip and middle laser positions generated very flat outputs, especially the latter, while base produced topographic change. This aligns well with the stationary microheater experiment above in Fig. 6.36 as the base similarly generated greater interpreted tip deflection while the tip and middle significantly less. The latter two demonstrated variation of 3.8 nm and 0.5 nm from left to right for the tip and middle respectively. This is the lowest measured change in any SThM cantilever, as seen when contrasted to Probe 5 and 6 in Fig.6.24 and 6.25. This is especially good as the Al is not fully counteracting the Au and suggests that

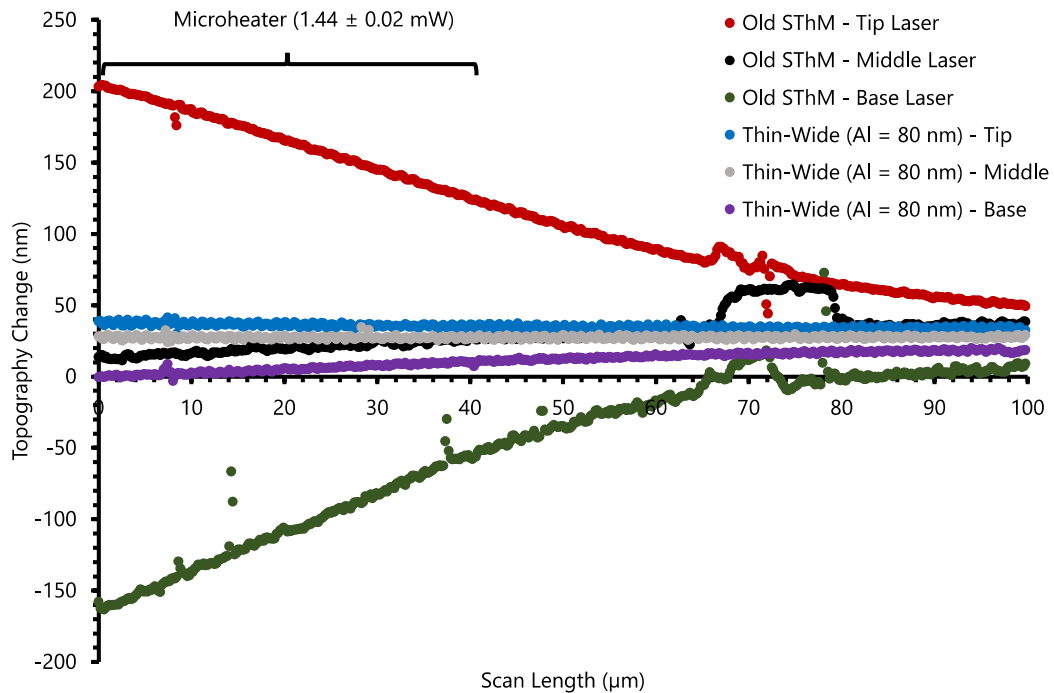


FIGURE 6.38: *Thin-Wide (Al = 80 nm) - Microheater Line Scan Contrast to Old SThM Design Without Al*

this could be improved if the Al was thicker. Regarding the base laser position, its outputted topography produced equal or greater deflections when compared to previous old designs with Al deposited on them. This appears due to the Thin-Wide design and is a potential drawback, although the base is very rarely used by the optical lever due to other issues such as low sensitivity and SNR issues that effect the AFM's topographic measurement in other ways. As a result, the Thin-Wide design appears very good and demonstrates quantifiable improvements when compared to the normal, flat SThM design.

6.2.4 Summary

Before moving on, it is worth summarising these results due to the large number of experiments, data and graphs needed to provide a clear picture of this complex experimental matrix. A wide range of potential solutions to attenuate thermal bending were explored with a backside deposition of metal showing the most promise from initial investigations. In addition, as the Au wires were no longer required to be wide to reflect the optical lever's laser, this was paired with a change of the wire patterning

to reduce the required backside metal thickness and better balance it. Moreover, it provided an opportunity to explore the effects of the Au's lateral position on the resultant thermal bend induced deflection profile longitudinally and laterally. Results demonstrated a general corroboration that Au's lateral location has an impact on vertical deflection in the AFM cantilevers analysed. This did not provide complete agreement with models due to the more complex lateral behaviour and its impact being harder to predict. However, models were a good predictor for most and their core conclusions agree with experimental data that lateral placement has an influence on thermal induced deflection. Alongside these, another design with a thinner and wide Au wire was developed that aimed to mirror the planar deposited backside metal as much as possible. This showed superior longitudinal and lateral profiles from Interferometer deflection measurements when balanced with backside Al metal. Therefore, it was taken forward and employed within an AFM system. These experiments correlated well with relatively flat profiles that showed excellent thermal bend insensitivity that was superior to the previous SThM design that had Al deposited on its backside. Following these findings, the next logical step was to expand this approach and apply the same Backside Deposited Metal solution to non-thermal AFM cantilevers.

6.3 Non-Thermal AFM Cantilevers

Applying all the above knowledge, this section aims to concisely explore and critique non-thermal AFM cantilevers for their effectiveness with the Backside Deposited Metal solution. However, an initial review of the current market solutions should be carried out.

6.3.1 Current Market Solutions

There are cantilevers on the market that are aimed to be more insensitive to Thermal Drift and Bending. The simplest design is a single material cantilever that will produce very little deflection due to temperature change as there is no CTE mis-match between materials. Moreover, there are probes that have metal deposited on either side of the cantilever [209], [210]. This can provide sound and consistent attenuation if the metals are well balanced for equal thermal bending moments from each

side. However, many of these probes were designed with the intention to provide a conductive path to/from the tip and so have not been optimised or fully analysed to show their Thermal Drift and Bending performance. Alongside the above, there are some probes which have reduced coverage of metal such as the MLCT-Bio-DC [56] and all the uniqprobes by NanoSensors [57]. These are based on the idea of less metal generating less thermal bending with only a small section of metal near their tips. Although a sound idea, it lacks an appreciation that at the tip, the cantilever is least stiff and so appreciable thermal bending will likely still occur. An example of this can be seen in Fig. 6.39 which models such a cantilever undergoing 10 K worth of uniform temperature change. It can be seen at the tip that partial Au coverage causes a notable bend downward (around -0.06°). As this is the region the laser is reflecting off and the AFM's optical lever system is measuring, this is not an ideal solution. Moreover, as has been demonstrated in this body of work, the IC thermal bending behaviour will be different to the OC when notable thermal bending occurs.

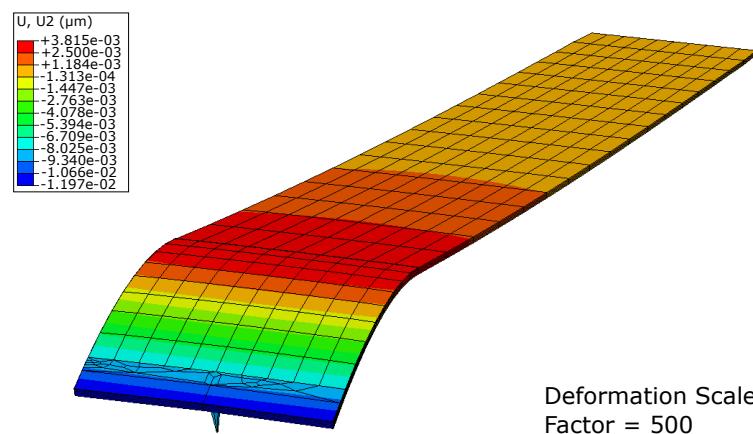


FIGURE 6.39: FEA - Deflection Output for Example of Commercial Solution with Partial Au Coverage Near Tip

A logical solution for both OC and IC could be positioning the Au coating more centrally, especially with the knowledge that when IC the cantilever will generate a similarly humped form seen in all bi-material AFM cantilevers. The modelled result of this scenario can be seen in Fig. 6.40 for the same example structure shown earlier and the same coating dimensions but placed in a central position. By applying the same deformation Scale Factor of 500, it provides a like-for-like comparison to Fig. 6.39. This produces a greater resultant vertical deflection at the cantilever tip due to the imposed thermal bending effectively having a longer lever to translate to the free

end. However, the rotation is less where the Au is located with the centre rotating by -0.04° (approximately a third less). As this is where the laser in the AFM's optical lever system will predominantly reflect off for the tip deflection and force measurement, it should render a lower interpretation of thermal bending. This is a very simple modification and could render appreciably lower thermal bend interpretation. Although, this is at the expense of appreciable absolute tip deflection and so more variable tip forces that result from temperature change. These will not be interpreted by the AFM and so could cause accelerated tip blunting, inconsistent AFM imaging and perhaps loss of contact. Therefore, this is still not an ideal solution. This then leads to either metallisation on both sides of the cantilever or none at all so that both lower AFM interpretation and absolute tip deflection from thermal bending occurs. As some cantilevers require metallisation for functionality and/or for a sound laser reflection, the solution of metallisation on both sides is subsequently explored here. For OC and IC thermal bending on contact mode AFM cantilevers.

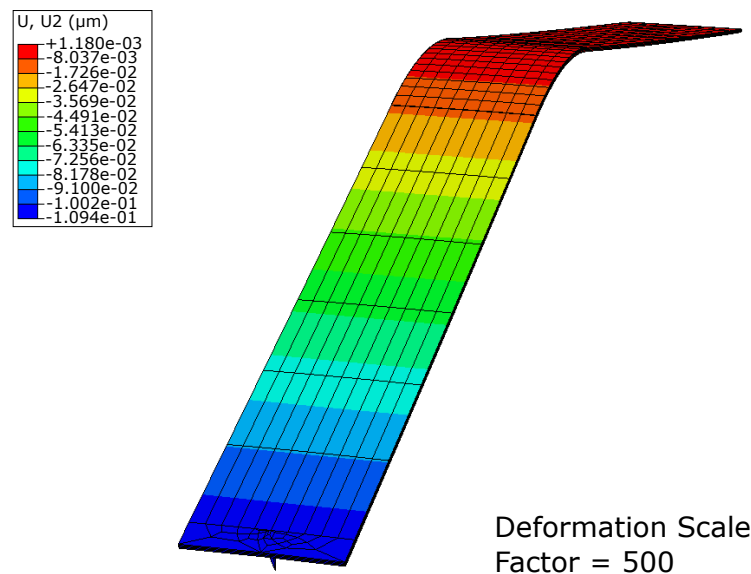


FIGURE 6.40: FEA - Deflection Output for Example of Commercial Solution with Partial Au Coverage Midway Along Cantilever

6.3.2 Backside Deposited Metal Solution

Modelling was first carried out to verify the solution would work for non-thermal AFM cantilevers and highlight any differences that may arise relative to SThM cantilevers. This was also used to aid in the estimation of the required Al thickness to be

deposited on the cantilevers.

6.3.2.1 Modelling

MLCT-B cantilevers were chosen as they have been well characterised in previous models and experiments. Regarding the metal, Al was chosen due to its excellent material properties and demonstrated track-record with SThM cantilevers. In addition, this metal was positioned on the underside/tip-side of the cantilevers in the models due to the native Au being on the topside of the cantilever. The effect of this being highlighted previously in Section 4.2, and means the opposite deflection occurs and the Al will attenuate this in the opposite direction to the SThM cantilevers. With these precursors, the same literature Al values previously defined were employed, with the FEA determining 44 nm of Al to balance MLCT-B's Au coating based upon its nominal thickness. The modelled result of this can be seen in Fig. 6.41. Furthermore, the longitudinal deflection normalised per Kelvin is shown in Fig. 6.42.

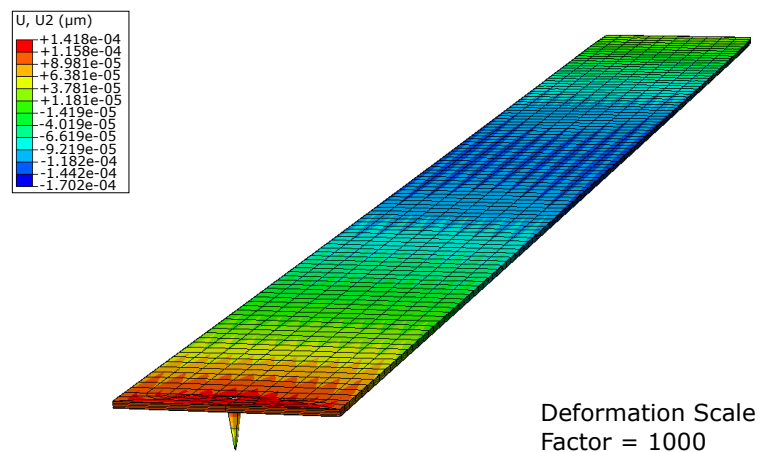


FIGURE 6.41: FEA - Vertical Deflection from 10 K Uniform Temperature Change in MLCT-B Cantilever with 44 nm of Al on the Underside

As it can be seen, negligible deflection occurs along the cantilever length and width due to a near perfect balance between the Au and Al. This is better than has been seen in any previous models due to both the Au and Al coatings being completely planar in their deposition while the previous SThM cantilevers had a patterned Au coating (although made very near planar in the Thin-Wide Design). Moreover, MLCT-B cantilevers are relatively narrow (20 μm) and so they have low deflection variation laterally. This indicates that MLCT-B cantilevers were excellent candidates for the deposition of Al to demonstrate the Backside Deposited Metal solution commercially.

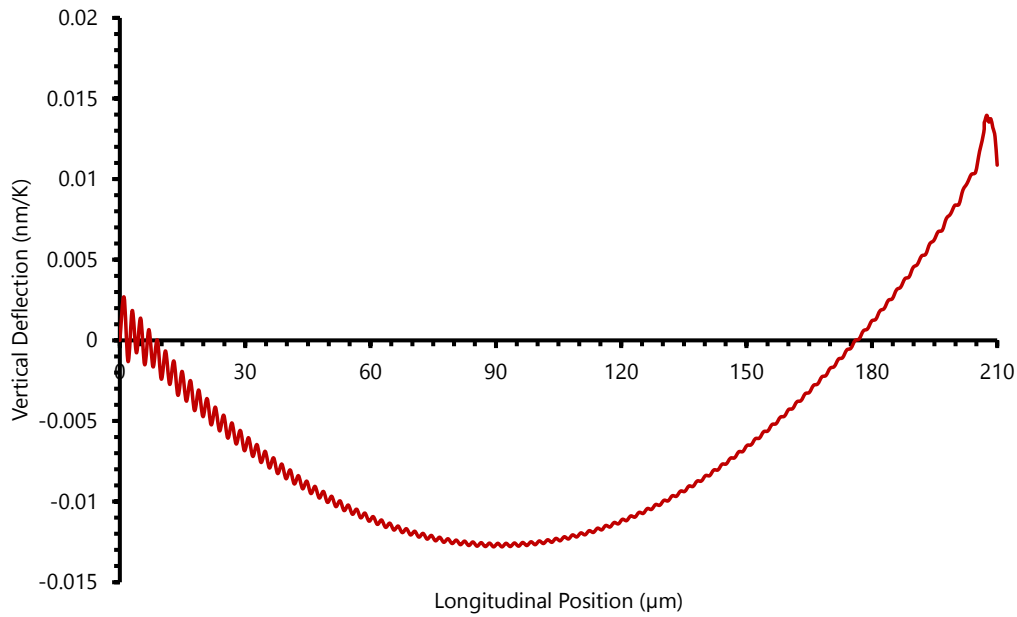


FIGURE 6.42: FEA - Vertical Deflection Centreline Profile Normalised to per Kelvin for MLCT-B Cantilever with 44 nm of Al on the Underside

In addition, the Al thickness of 44 nm provides an indication to what thickness should be required, whereby past experience suggests a greater thickness of around 10 nm will be required. An experimental study was carried out and its results contrasted to the above theoretical models.

6.3.3 Design Study

This study aimed to provide a comparison to the models shown above as well as demonstrate the solutions translation to a commercial AFM cantilever. However, with the previous work for SThM cantilevers providing a lot of data, this study was not as expansive with only the MLCT-B cantilever explored.

6.3.3.1 Method

The approach was a simple one involving depositing multiple Al thicknesses on a number of MLCT-B cantilevers and measuring their thermal bend responses in the Interferometer previous employed with the Peltier heater and PT-100 set-up. This identified which thickness of Al would produce a thermal bend induced profile approaching zero tip deflection. Following this, the cantilever with the best profile was utilised in the Dimension 3100 AFM, in which the Peltier OC, microheater OC vs IC and line

scan experiments were executed in the same way described earlier. As the MLCT-B cantilever does not possess temperature measurement, the Peltier experiment again employed a PT-100. Furthermore, a SThM probe's tip temperature vs. microheater power relation was employed at a number of positions to provide an estimation for the MLCT-B cantilevers temperature change from the microheater and line scans as performed in Section 5.2.2.

6.3.3.2 Results

Employing the method above, an Al thickness of 57 nm generated a deflection profile that approached near zero deflection. The result can be seen in Fig. 6.43 from the Interferometer alongside a MLCT-B cantilever without Al coating for contrast. This emphatically demonstrates a very level profile relative to a MLCT-B cantilever without Al. One aspect to note is that a significant uncertainty occurred in the deflection output. This was due to notable vibration from background work during the experiment in the JWNC facility where the Interferometer tool is installed. However, the gradients obtained relied on 15 separate measurements and so were statistically able to still output a sound overall profile.

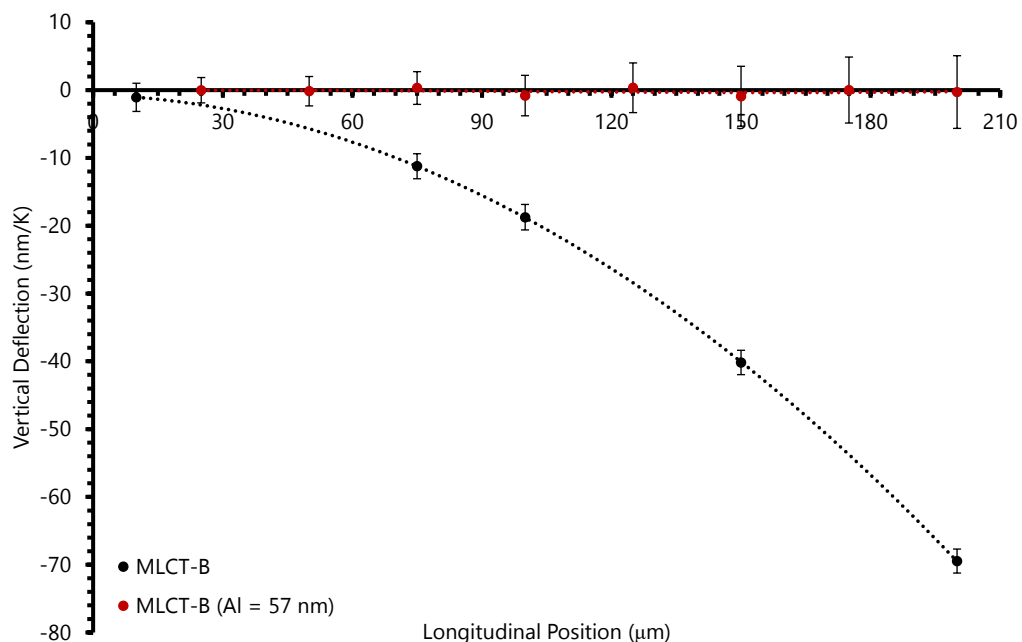


FIGURE 6.43: *Interferometer - MLCT-B Peltier Induced Thermal Bend Profiles*

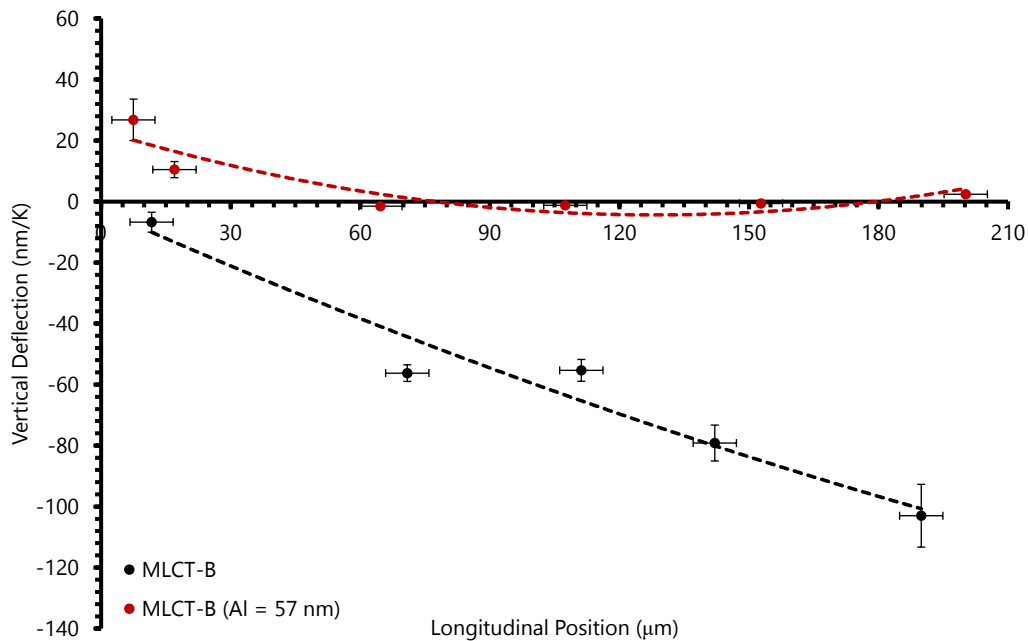


FIGURE 6.44: AFM - MLCT-B Peltier Induced Thermal Bend Profiles

As can be seen in Fig. 6.44, the Interferometer's results were largely mirrored when the cantilever was deployed in the AFM, with an exception for readings taken at its base. Here the InvOLS was very large and resulted in a significant tip deflection for very low rotation. Looking at the other more typical laser locations (i.e. greater than 30 μm along the cantilever), a negligible tip deflection was recorded. Contrasting this to the cantilever without additional Al metallisation demonstrates a stark improvement, with a deflection reduction of up-to 99.3%. This is massive and emphasises this simple solution's effectiveness in-conjunction with the MLCT-B cantilever being able to be well balanced. Moving on to the microheater experiments, this allowed the OC and IC profiles to be compared. The OC profile can be seen in Fig. 6.45 followed by the IC in Fig. 6.46 with a comparison to a normal MLCT-B cantilever's profile.

Starting with the OC profile, it can be seen that a very flat profile was produced similar to that seen in the Peltier experiment with exception to the base. The latter being due to the microheater's low thermal power and the probe chip acting as a heat sink to the cantilever meaning relatively low temperature change occurred near/at the cantilever base. Alongside this, the deflections appear to be slightly positively offset to the uniform temperature change profiles in the Peltier experiment. This will be due to a combination of the microheater's temperature distribution being different and the Al's material properties potentially changing over-time. Pertaining to the latter,

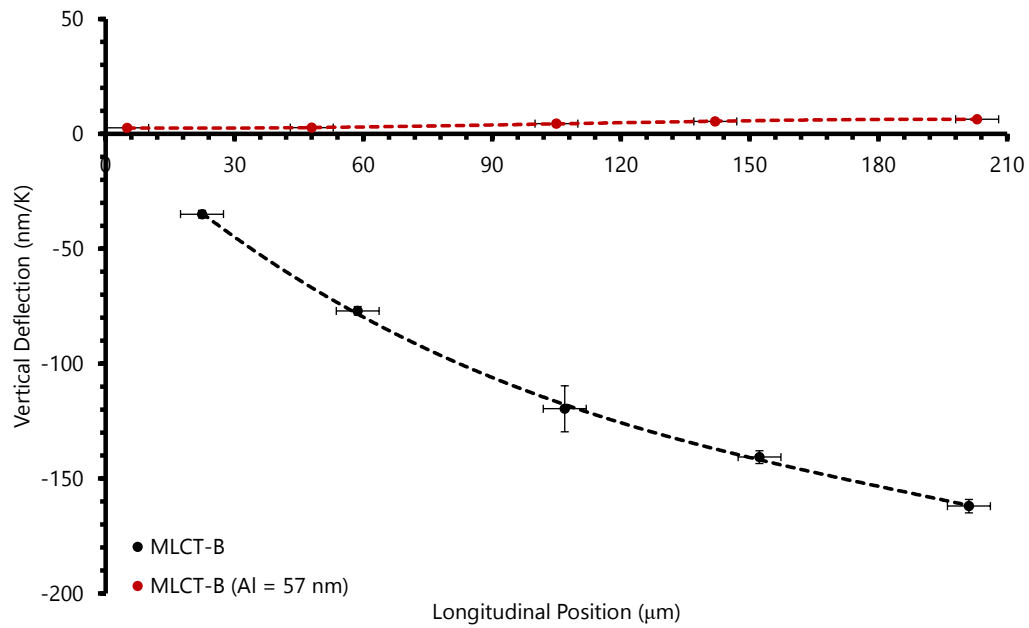


FIGURE 6.45: AFM - MLCT-B Microheater OC Induced Thermal Bend Profiles

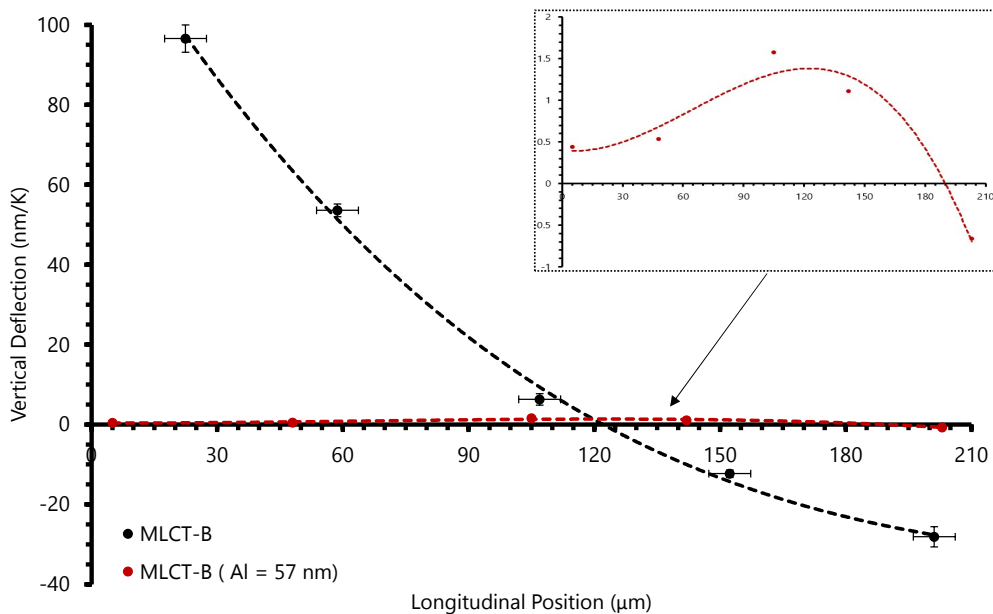


FIGURE 6.46: AFM - MLCT-B Microheater IC Induced Thermal Bend Profiles

this body of work has observed that the Al coatings deposited have changed up-to weeks post deposition. This has manifested in the residual stress and strain changing alongside the thermal bend behaviours which indicate that the mechanical and/or thermal properties have altered. It has been documented that Al films do change over time [224], however this would be expected over a shorter time-scale of up-to

24 hours as opposed to days or even weeks. However, this could be explained by the Al films having a notable contamination that could render an age hardening effect as observed in general Al alloys and first documented back in 1906 by Alfred Wilm [226]. Although, unable to be verified in this work, an exact diagnosis not possible but it was an effect consistently observed in this project for the Al from the Plassys IV tool in the JWNC. With this noted, the net result of the Al on the profiles are still reasonable showing behaviour similar to what would be expected of Al.

Regarding the IC profile, an even lower deflection magnitude across the cantilever's length was observed of 2 nm/K as opposed to 6.4 nm/K when OC. This is logical as the general theme from previous cantilevers is the tip fixation from contact limits deflection. From this data, a less clear profile trend was generated (the trendline being there solely to guide the eye) due to it approaching zero and the reduced SNR causing greater variation. However, what is clear is the pronounced lack of rotation and so interpreted tip deflection across the cantilever, where this could be considered almost negligible. This will translate into lower interpreted tip force and so topography change in AFM scans. Overall, this provides greater confidence in the ability for this and other non-thermal cantilevers to be well attenuated with this Backside Deposited Metal solution. To confirm this translates into improved AFM scans, a line scan was executed as described previously. The result can be seen in Fig. 6.47 with the scans obtained for a normal MLCT-B cantilever provided for contrast.

The result of this is emphatic: flat topographic outputs across all laser positions meaning minimal thermal bending of the cantilever. As highlighted before, MLCT-B's narrow nature with its uniform metal deposition on either side resulted in a very consistent thermal bend balance between the Au and Al. When contrasted to the MLCT-B cantilever without Al, this is distinctly apparent with the base laser position's topography demonstrating a reduction in variation from the far left (heated) to the right (unheated) of 97.5 %. Moreover, a lower offset occurred in the right of the scan which the cantilever's insensitivity will have contributed to. Overall, this provides clear and compelling evidence that this Backside Deposited Metal solution can render an incredibly thermally insensitive cantilever that not only generates lower thermal bend interpretation in AFM's optical lever system, but also suffers from lower absolute deflection of its tip.

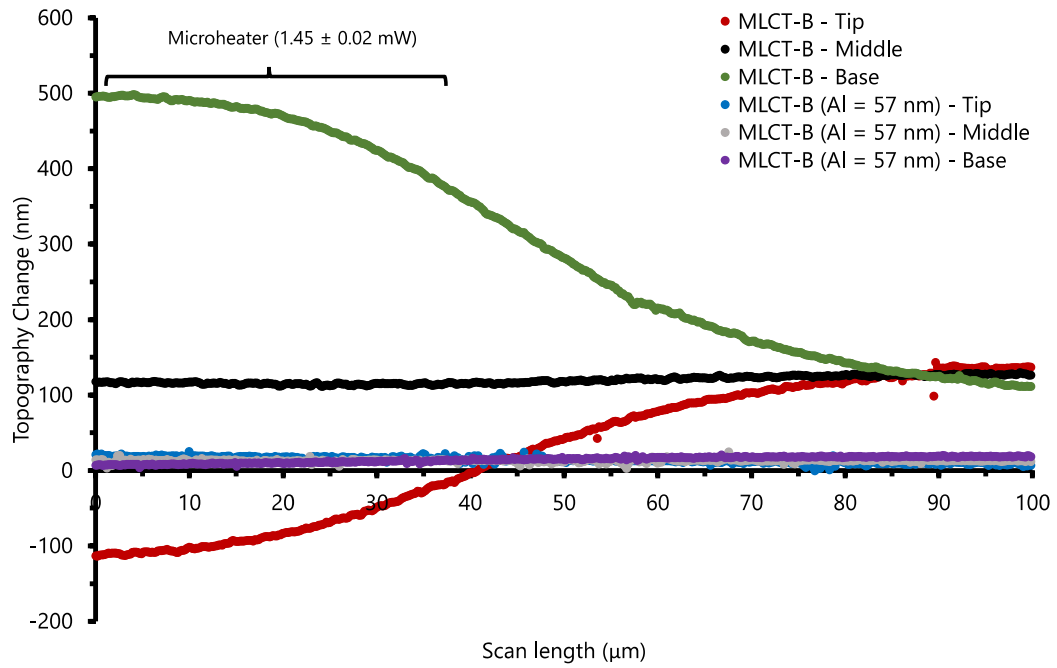


FIGURE 6.47: AFM Line Scan - MLCT-B Topography Change

7. Conclusion & Future Work

7.1 Conclusion

Thermal Drift is a problem most AFM users are familiar with, where common practice is to allow AFMs to warm-up and reach a steady temperature to minimise it prior to measurements. The contribution of the AFM cantilever to Thermal Drift has been acknowledged in the academic and commercial communities, but has not thoroughly been studied. This body of work attempted to shed greater light on this for ubiquitous bi-material AFM cantilevers that exhibit clear thermal bending from temperature change. The first clear conclusion from this work reinforces the basic understanding that the cantilever materials' dissimilar CTE is the primary source of thermal bending. However, through modelling and experimentation, this phenomenon's interpretation within an AFM's common optical lever system is highly variable with longitudinal position of the laser on the cantilever. This results in a signal that is inherently erroneous, differing between systems and even individual experiments using the same AFM. This variable drift occurs both in the deflection measurement and subsequent topography that the AFM feedbacks to the user. The reason for this interpretation is due to the optical lever directly measuring cantilever rotation at the laser spot's position on the cantilever and converting it into tip-deflection through the InvOLS from an EF. The latter is inherently different to thermal bending's induced rotation along the cantilever causing the conversion to be incorrect. Both models and experiments show that this occurs when bi-material cantilevers are out-of-contact and in-contact with a surface. Therefore, when thermal bending occurs, the interpreted tip-deflection should not be initially trusted and quantification of the resultant effect requires reporting of the laser position for clarity and reproduction. Moreover, the latter should ideally be measured

at multiple locations along the cantilever length to quantify the impact that could be inflicted on AFM measurements.

With the above considerations, although both out-of-contact and in-contact have variable and incorrect interpretations of thermal bending, they have very different manifestations of it. When out-of-contact, the AFM's measurement generates rotation and a tip-deflection in the direction towards the lowest CTE material with temperature increase (i.e. typically towards the base material - Si, SiO_x or SiN_x). The impact of this on AFM measurement generally increases when the laser is positioned further towards the tip of the cantilever. With this scenario applying to Tapping and Non-Contact scanning modes, it will cause a movement of their non-oscillated steady-state vertical position and so can cause pronounced, variable artefacts in their deflection and topographic output. Moreover, although not directly explored in this work, temperature change will influence the cantilever's resonant frequency directly and add a further layer of complexity. For in-contact measurements, instead of thermal bending manifesting a deflection increasing towards the tip, it generates a humped deflection profile towards the side that is metallised with temperature increase (i.e. material with higher CTE). This is more akin to bridges with uniformly distributed loads and is due to the surface imparting a mechanical BC that limits the cantilever's tip to displace. The best approximated BC for the tip appears to be a Roller meaning the tip can slide over the surface, but not displace in the vertical regime. Under such a conditions, models and experiments show a lower absolute deflection along the cantilever alongside interpreted tip-deflection by the AFM. Furthermore, as the optical lever directly measures rotation at its laser spot, with the humped profile, both positive and negative deflections and therefore topographic signals can be output. Although varying in drift direction, this also presents an opportunity in the form of a laser position approximately 60 % along the cantilever where the rotation is zero. When the laser is positioned here, negligible interpreted tip-deflection from thermal bending of the cantilever will occur. This work has demonstrated up-to 97.7 % reduction in thermal bending induced topographic artefacts by employing this laser position and hence provides a very effective and immediate solution to mitigate thermal bending when bi-material AFM cantilevers are in-contact. However, a change in tip-force will still

occur due to the inherent erroneous interpretation of it which will produce undesirable differences to the actual tip-force. This can cause inconsistent imaging and may increase the chance of contact loss or tip blunt/sample damage. Therefore, there is still benefit in limiting this thermal bending phenomenon.

In order to minimise thermal bending occurring in the first place, there are multiple solutions. One solution for bi-material AFM cantilevers that provides a simple and effective way to mitigate this is through the deposition of a metal film on the backside of the cantilever. This counteracts the other metal on the cantilever when undergoing thermal bending and so greatly reduces deflection and induced artefacts. With this solution, SThM and non-thermal AFM cantilever exhibit great reductions with up-to 97.5 % reduction in thermal induced topographic artefacts for the equivalent longitudinal laser position during contact scanning. Moreover, demonstration using custom fabricated SThM probes show that even patterned metal coatings can be effectively attenuated whereby the coating can be additionally altered to better match the planar metal film deposited on the backside. This solution additionally has the added benefit of improving both out-of-contact and in-contact scanning methods along with a more accurate measurement of the actual tip-force. The latter being a key improvement over the 60 % laser location solution proposed for in-contact scanning, as this simply mitigates the phenomenon's interpretation rather than the manifestation. However, these solutions can be combined for great reduction in thermal bend induced artefacts, rendering it negligible. As a result, all the benefits of having a metallised AFM cantilever such as increased functionality, higher voltage sum and minimal laser interference can be obtained with low Thermal Drift from the AFM cantilever.

7.2 Future Work

There are multiple direct and indirect avenues that future work could investigate further such as investigating how the out-of-contact deflection combines with the effect of temperature change on AFM cantilever's dynamic component. For example, measuring the out-of-contact deflection and the change in resonance frequency of AFM cantilevers with temperature change and combining these in models and/or experimentation. Moreover, a translation of the laser position along the cantilever in such

modes would be interesting to demonstrate the variation that occurs in the tip's interpreted deflection and topographic output. This could then be followed by the implementation of the Backside Deposited Metal solution to quantify and appreciate the improvement. Another interesting area could be a holistic theoretical and experimental analysis on the influence of the tip, sample and environmental conditions on the tip's mechanical BC and so thermal bend's manifestation. This could provide more appropriate predictions during contact scanning when thermal bending is a pronounced effect under different conditions. Furthermore, thermal bending's interpretation will vary depending on the deflection detection system and so a more theoretical and experimental analysis of this would be worthwhile.

Beyond the above, it would be useful to quantify the overall Thermal Drift in modern AFM tools with and without thermally insensitive cantilevers. This would help elucidate on the cantilever's exact contribution to the general Thermal Drift phenomenon in AFM. More specific to SThM, it would be useful to further qualify both depositing a metal on the opposite side of the cantilever to the Au wires with the new Thin-Wide SThM design fabricated. If a dataset that could predict the ideal metal to be deposited on the opposite side based on what was the total Au-NiCr coating deposited for the wires, then a process could be implemented for high yield production of SThM cantilevers that are insensitive to thermal bending. Furthermore, if a jig was set up to permit easy deposition of metal on multiple SThM cantilevers within the evaporator tools available in the JWNC as well, then this could provide a commercially viable process. Alongside the above, it would be interesting to quantify the effect on the cantilever temperature measurement with SThM cantilevers that displace less with temperature change. One final aspect for SThM cantilevers would be to further explore the groove. Although proven unideal, they are clearly far more complex than standard AFM cantilevers and further experimental work varying groove depth and length would be an interesting study in general, providing contrast with theoretical models.

Appendix A. Supplementary Modelling Work

A.1 FDM Model

A.1.1 Grooved Cantilever's

This demonstrates the equations for the additional grooved cantilever dimensions derived from the NA location equation.

A.1.1.1 Simplified Cross-Section

This simplified cross-section is for vertical side-walls with a single coating.

Groove Depth

From Equation 4.1, we can arrange it into a quadratic equation with h as the variable.

Therefore, applying the quadratic formula we can find h accordingly:

$$h = \frac{-b + \sqrt{b^2 - 4ac}}{2a}$$

$$a = t_s \tag{A.1}$$

$$b = 2\left(\frac{w_s t_s}{c_{rat}} - t_s x_{NA}\right)$$

$$c = w_s t_s \left(\frac{t_s}{2} - x_{NA}\right) + n w_c t_c \left(t_s + \frac{t_c}{2} - x_{NA}\right)$$

Groove Width for a Fixed Overall Width

Through simple rearrangement of x_{NA} equation, the width ratio, c_{rat} is found and so the groove width:

$$c_{rat} = \frac{2hw_s t_s}{w_s t_s \left(x_{NA} - \frac{t_s}{2}\right) + ht_s (2x_{NA} - h) + nw_c t_c \left(x_{NA} - t_s - \frac{t_c}{2}\right)} \quad (A.2)$$

$$w_g = w - s \left(w - \frac{2}{c_{rat}}\right)$$

Overall Width for a Fixed Groove Width

The overall width is found by re-deriving the x_{NA} equation, but instead of linking the groove and wing widths via c_{rat} , they are separate terms. Therefore, we can find the wing width and by simple summation find the overall width:

$$w_w = \frac{\frac{w_g t_s^2}{2} + h^2 t_s + nw_c t_c \left(t_s + \frac{t_c}{2}\right) - x_{NA} (t_s w_g + 2ht_s + nw_c t_c)}{t_s (2x_{NA} - t_s - 2h)} \quad (A.3)$$

$$w_s = 2w_w + w_g$$

Second Moment of Area

The I can be deduced for a fixed NA easily, but requires a more dynamic equation for a variable NA location. As a result, the following equations were derived where each component relates to an area of the grooved cross-section which all sum for the whole cross-section's I:

$$I_1 = \frac{w_g t_s^3}{12} + w_g t_s \left(x_{NA} - \frac{t_s}{2}\right)^2$$

$$I_2 = \frac{2t_s x_{NA}^3}{3}$$

$$I_3 = \frac{w_c t_{below}^3}{12} + w_c t_{below} \left(x_{NA} - t_s - \frac{t_{below}}{2}\right)^2$$

$$I_4 = \frac{w_c t_{above}^3}{12} + w_c t_{above} \left(h + t_s - x_{NA} - \frac{t_{above}}{2}\right)^2 \quad (A.4)$$

$$I_5 = \frac{2t_s (h + t_s - x_{NA})^3}{3}$$

$$I_6 = 2 \left[\frac{(w_w - t_s) t_s^3}{12} + t_s (w_w - t_s) \left(h + \frac{t_s}{2} - x - NA\right)^2 \right]$$

$$I_{Total} = \sum_{i=1}^6 I_i$$

where t_{below} and t_{above} relate to the thickness below and above the NA location.

A.1.1.2 Complex Cross-Section

This more complex cross-section is for angled side-walls with two coatings. These apply the same method for the respective geometry dimensions above in the below.

Groove Depth

$$h = \frac{-b + \sqrt{b^2 - 4ac}}{2a}$$

$$a = t_s \tan \theta_{sw}$$

$$b = \frac{-2w_s t_s}{c_{rat}}$$

$$c = n_{c1} w_{c1} t_{c1} \left(t_s \frac{t_{c1}}{2} - x_{NA} \right) + n_{c2} w_{c2} t_{c2} \left(t_s + t_{c1} + \frac{t_{c2}}{2} - x_{NA} \right) + w_s t_s \left(x_{NA} - \frac{t_s}{2} \right)$$
(A.5)

Groove Width for a Fixed Overall Width

$$c_{rat} = \frac{2w_s t_s h}{w_s t_s \left(x_{NA} - \frac{t_s}{2} \right) + h^2 t_s \tan \theta_{sw} - n_{c1} w_{c1} t_{c1} \left(t_s + \frac{t_{c1}}{2} - x_{NA} \right) - n_{c2} w_{c2} t_{c2} \left(t_s + t_{c1} \frac{t_{c1}}{2} - x_{NA} \right)}$$

$$w_g = w - s \left(w - \frac{2}{c_{rat}} \right)$$
(A.6)

Overall Width for a Fixed Groove Width

$$w_w = \frac{w_g t_s \left(\frac{t_s}{2} - x_{NA} \right) - h t_s \tan \theta_{wl} (h + t_s) + n_{c1} w_{c1} t_{c1} \left(t_s + \frac{t_{c1}}{2} - x_{NA} \right) + n_{c2} w_{c2} t_{c2} \left(t_s + t_{c1} + \frac{t_{c2}}{2} - x_{NA} \right)}{t_s (2x_{NA} - 2h - t_s)}$$
(A.7)

$$w_s = 2w_w + w_g$$

Appendix B. Supplementary Experimental Quantification Work

B.1 PT-100 Equations

Callendar-Van Dusen Equation [227]:

$$\begin{aligned} R(T) &= R(0)[1 + AT + BT^2] && \text{if } 0^\circ\text{C} \leq T < 661^\circ\text{C} \\ R(T) &= R(0)[1 + AT + BT^2 + C(T - 100)T^3] && \text{if } -200^\circ\text{C} < T < 0^\circ\text{C} \end{aligned} \tag{B.1}$$

where $A = 3.9083 \times 10^{-3}$, $B = -5.775 \times 10^{-7}$ and $C = -4.183 \times 10^{-12}$

Appendix C. Supplementary Attenuation Work

C.1 Normal vs. Thin-Wide SThM Cantilever Work

Firstly, a simple cross-section area calculation was performed along sections of the SThM cantilevers with the standard commercial Au geometry (150 nm thickness) vs. that proposed with the new Thin-Wide Au design (80 nm thickness). Fig. C.1 demonstrates this at key positions along the cantilevers lengths where the scale bars below and adjacent to the Au patterns are in microns. As it can be seen, for the section lead-

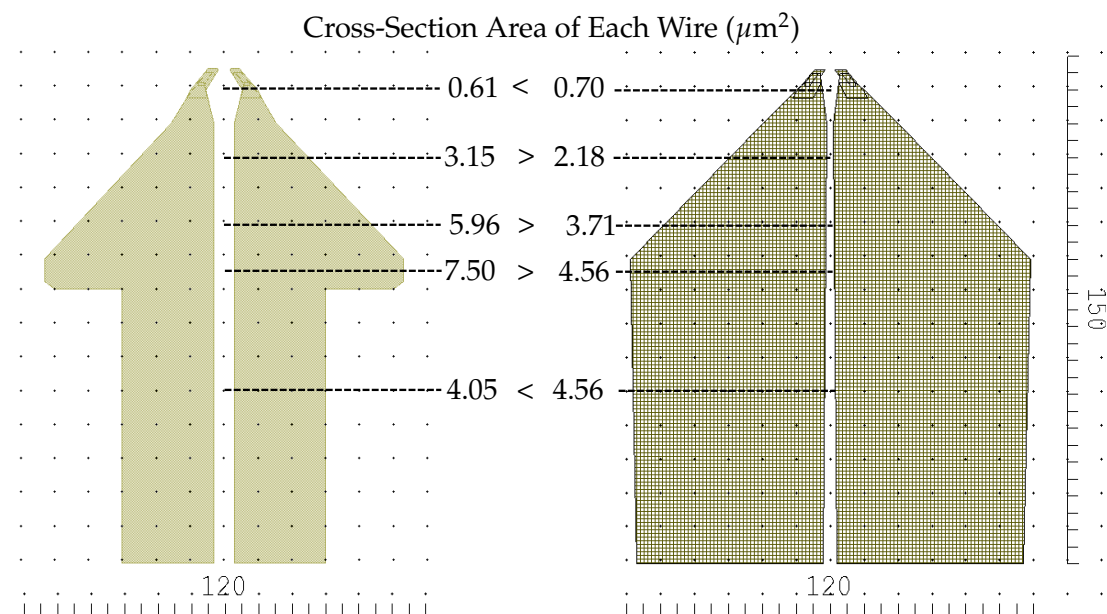


FIGURE C.1: *Normal vs. Thin-Wide SThM Au Designs - Key Cross-Section Areas (μm^2)*

ing up to the width increase of the mirror at 85 μm along, a 80 nm metal thickness has a cross-sectional area that exceeds that of the 150 nm. However, upon this width

increase, it is lower until 140 μm along. As electrons follow the shortest path of least resistance and the wider section is for reflecting the laser, the effect of this lower cross-sectional area on the probes electrical and thermal performance may not be dramatic. To help shed light on this, the thermal-resistive model developed by R. Lambert was employed. The results for which can be seen in Fig. C.2 and C.3 for the thermal resistance and subsequent temperature change from a 0.552 mA current. This predicts that the Thin-Wide design will have similar thermal resistance and temperature profile. However, there is a slight increase in both with an average tip temperature increase of 5 %. With this said, the thermal-resistive model is 1D and does not appreciate the suddenly wide section that theoretically may not contribute much reduction in electron flow resistance. Hence, with this and the difference being relatively low in the thermal-resistive model, the 80 nm thickness was deemed sound electrically and thermally.

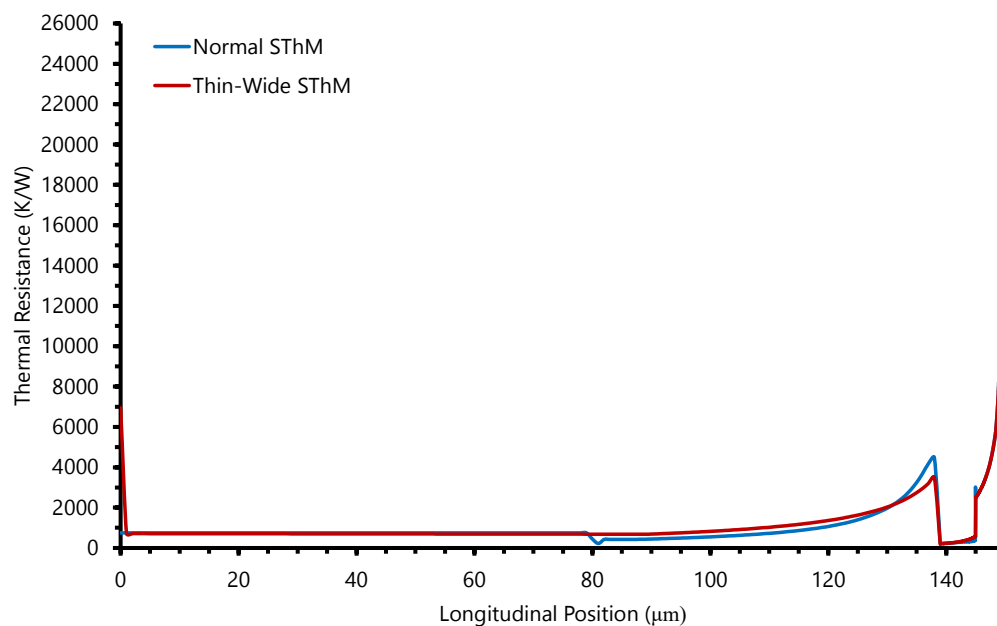


FIGURE C.2: *Thermal-Resistive Model - Thermal Resistance Along Cantilever Graph*

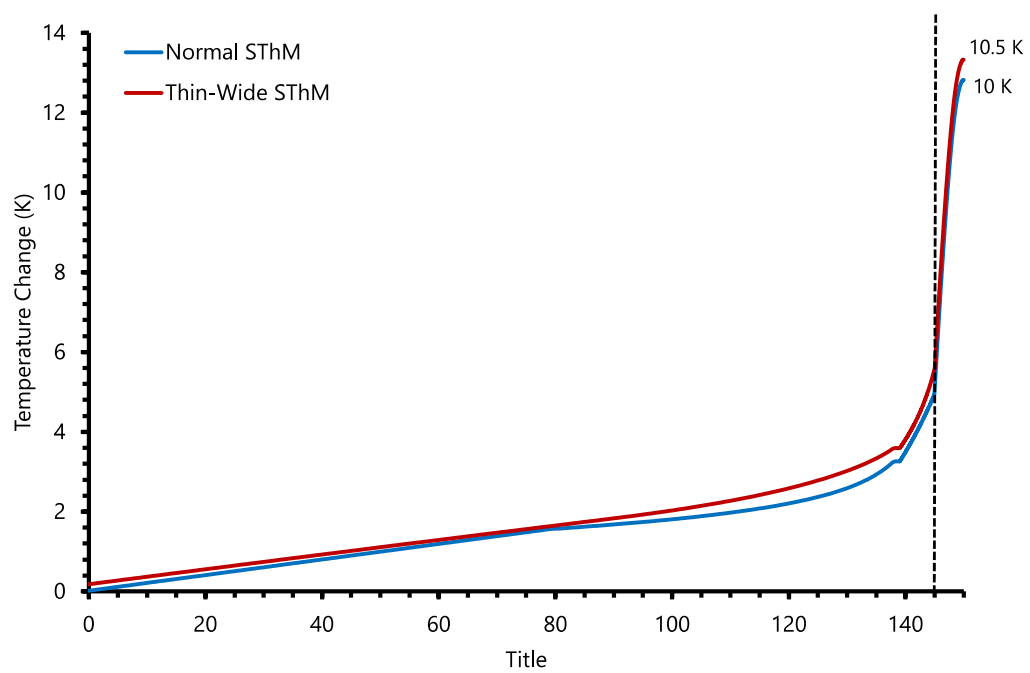


FIGURE C.3: *Thermal-Resistive Model - Temperature Change Along Cantilever Graph*

Appendix D. SThM Fabrication Process Sheet

#		Process Steps
1	Pyramid Level Photolithography	Solvent Clean of a Si/SiO _x /SiN _x 3" Wafer
2		Spin Primer + S1828 on Back Side & Bake
3		Dry Etch - Ash
4		Spin Primer + S1818 on Back Side & Bake
5		Expose on MA6 - Hard Contact
6		Develop
7		Optical Inspection - Pyramid tops
8		Postbake
9	Nitride Dry Etch	Dry Etch - RIE 80+ - C ₂ F ₆
10		Strip Resist
11		Dry Etch - O ₂ Ash
12	Pyramid Etch	HF Dip, KOH Wet etch @ 55°C, Sulphuric Acid Rinse, RO rinse
13		Optical Inspection - Determine Pyramid Height
14	Ribs/Groove (Only if needed!)	Solvent clean, RO rinse, Dry Etch - Ash, Dehydrate
15		Spin - Primer, SPR220-7
16		Softbake - 118 °C for 5 mins, cool gently on hot watchglass. Rehydration delay
17		Expose with ribs mask
18		Develop - Slight agitation
19		Reflow - 140°C 20 mins, cool slowly on hot watch glass, inspect
20		Ribs etch - RIE80+: Part 1: O ₂ , Part 2: CF ₄
21		Strip resist - 10mins, Ultrasonic for 5 mins, acetone, IPA, dry
22		Dektak - Check etch depth
23		Send
24	Back-Side Photolithography	Solvent Clean
25		Spin - Front Side (Pyramids) - AZ4562
26		Spin - Back Side - Primer, S1818
27		Expose - MA6 - Using BSA, Hard Contact
28		Develop
29	Back-Side SiN Etch	Post bake - Oven
30		Dry Etch - RIE80+ (C ₂ F ₆) Strip Resist, IPA rinse

31	E Sic	Dry Etch - Ash
32	BS wet etch	HF Dip, KOH Wet etch @ 105°C, Sulphuric Acid Rinse, RO Rinse Optical Inspection - measure depth.
33	E-beam cantilever definition	Dry Etch - Ash
34		Front (Pyramid) Side: Spin - 8% 2010/9% AR-P632 50k (Bot. #9, Oven bake - 180°C Spin - 4% 2041/4% AR-P649 200k (Bot. #16), Oven bake - 180°C Float coat 1.5% 2041, Oven bake - 180°C (x 4/x6)
35		Cantilever Definition EBL
36		Develop, IPA Rinse Optical Inspection
37		Dry Etch - Ash Evaporate 75nm NiCr, Lift-off
38		SEM Inspection
39		Dry Etch - Ash
40		Dehydration Bake
41	Photolith Cantilevers	Spin - Primer, AZ4562
42		Solvent Loss Time
43		Hotplate Bake
44		Second AZ4562 Spin (repeat above)
45		Delay rehydration
46		Expose - MA6 - Hard Contact
47		Develop - Changing to fresh developer half-way, RO Rinse, Dry Optical Inspection
48		Hardbake
49	Etch Cantilevers	Dry Etch - RIE80+ Interferometer Etch CHF_3 Inspect to ensure etched through at tip. MF319 clean, RO Rinse, Dr
50		Resist Strip Dry Etch - Ash SVC14, IPA Rinse, RO Rinse, Dry, Ash Optical Inspection
51		Chrome Etch, RO Rinse Optical Inspection
52		Short KOH Wet Etch, RO Rinse SEM Inspection - undercut should be visible Nanostrip, RO Rinse, Ash
53	Base Resistors	Spin - 8% 2010/9% AR-P632 50k (Bot. #9, Oven bake Spin - 4% 2041/4% AR-P649 200k (Bot. #16), Oven bake Float coat 1.5% 2041, Oven bake (x 6)
54		Base resistors EBL
55		Develop, IPA rinse, Optical Inspection
56	Tip Resistors	Dry Etch - Ash Evaporate 33nm NiCr 5nm Pt, Lift-off SEM Inspection
57		Solvent Clean, Dry Etch - Ash Spin - 8% 2010/9% AR-P632 50k, Oven bake Spin - 4% 2041/4% AR-P649 200k, Oven bake Float coat 1.5% 2041, Oven bake (x 6)
58		Tip Resistors EBL
59		Develop, IPA rinse, Optical Inspection RIE 80+ - O2- 10 sccm - 10W - 250mT - 30 s (Jump start required)

60		Evaporate 8nm NiCr - 40nm Pd - Plassys IV. Lift-off. No ultrasonic. SEM inspection.
61	Pads	Solvent Clean, Dry Etch - Ash Spin - 8% 2010/9% AR-P632 50k, Oven bake Spin - 4% 2041/4% AR-P649 200k, Oven bake Float coat 1.5% 2041, Oven bake (x 6)
62		Pads EBL
63		Develop , IPA rinse, Optical & SEM Inspection
64		Dry Etch - RIE 80+ (O₂) Evaporate - 8nm NiCr - 145nm Au, Lift-off SEM Inspection, Test Tips electrically, Dry Etch - Ash
65	Release	TMAH Wet Etch @ 80°C Until Centre Probe Floats Away, then etch for further 50-100% Remove Wafer Carefully, Multiple Gentle RO Dips, Blow Dry from Methanol
66		Optical & SEM Inspection, Measure Probes Electrically Pop-out Probes

Text in **Red** were steps that were not performed in the fabrication of the devices in this project

FIGURE D.0: SThM Fabrication Process Sheet

Bibliography

- [1] P. Eaton and P. West, *Atomic Force Microscopy*, First. Oxford University Press, 2010, vol. 1st, ISBN: 978-0-19-957045-4.
- [2] *Kelvin Nanotechnology | Nanofabrication Solutions*, 2018. [Online]. Available: <https://www.kelvinnanotechnology.com/> (visited on 09/05/2018).
- [3] B. Bhushan, *Nanotribology and Nanomechanics*, 1st, B. Bhushan, Ed. Berlin/Heidelberg: Springer-Verlag, 2005, ISBN: 3-540-24267-8. DOI: 10.1007/3-540-28248-3. arXiv: 9809069v1 [arXiv:gr-qc]. [Online]. Available: <http://link.springer.com/10.1007/3-540-28248-3>.
- [4] Bert Voigtländer, *Scanning Probe Microscopy: Atomic Force Microscopy and Scanning Tunneling Microscopy*, B. B. Phaedon Avouris and R. W. Dieter Bimberg, Hiroyuki Sakaki, Klaus von Klitzing, Eds. Springer, 2015, vol. 2015, ISBN: 978-3-662-45239-4. DOI: 978-3-662-45240-0.
- [5] F Peter, A Rüdiger, and R Waser, "Mechanical crosstalk between vertical and lateral piezoresponse force," *Review of Scientific Instruments*, vol. 77, 2006. DOI: 10.1063/1.2176081.
- [6] G. Schmalz, "Über Glatte und Ebenheit als physikalisches und physiologisches problem," *VereinDeutscher Ingenieure*, pp. 1461-1467, 1929.
- [7] R. Young, J. Ward, and F. Scire, "The Topografiner : An Instrument for Measuring Surface Microtopography," *The Review of Scientific Instruments*, vol. 43, no. 7, 1972.
- [8] G. Binnig, H. Rohrer, C. Gerber, and E. Weibel, "Surface studies by scanning tunneling microscopy," *Physical review letters*, vol. 49, no. 1, pp. 57-61, 1982,

- ISSN: 00319007. DOI: 10.1103/PhysRevLett.49.57. [Online]. Available: <http://journals.aps.org/prl/abstract/10.1103/PhysRevLett.49.57>.
- [9] H. Scheel, G. Binnig, and H. Rohrer, "Atomically Flat LPE-Grown Facets Seen by Scanning Tunneling Microscopy," *Journal of Crystal Growth*, vol. 60, pp. 199–202, 1982.
- [10] G. Binnig and H. Rohrer, "Surface imaging by scanning tunneling microscopy," *Ultramicroscopy*, vol. 11, no. 2-3, pp. 157–160, 1983, ISSN: 03043991. DOI: 10.1016/0304-3991(83)90231-0.
- [11] G. Binnig, H. Rohrer, C. Gerber, and E. Weibel, "7 x 7 Reconstruction on Si(111) Resolved in Real Space," *Physical Review Letters*, vol. 50, no. 2, pp. 120–123, 1983.
- [12] G. Binnig and C. F. Quate, "Atomic Force Microscope," *Physical Review Letters*, vol. 56, no. 9, pp. 930–933, 1986. DOI: 10.1201/9781420075250.
- [13] T. R. Albrecht, S. Akamine, T. E. Carver, and C. F. Quate, "Microfabrication of cantilever styli for the atomic force microscope," *Journal of Vacuum Science & Technology A: Vacuum, Surfaces, and Films*, vol. 8, no. 4, pp. 3386–3396, 1990, ISSN: 0734-2101. DOI: 10.1116/1.576520.
- [14] G. Meyer and N. M. Amer, "Erratum: Novel optical approach to atomic force microscopy [Appl. Phys. Lett. **53**, 1045 (1988)]," *Applied Physics Letters*, vol. 53, no. 24, pp. 2400–2402, 1988, ISSN: 0003-6951. DOI: 10.1063/1.100425. [Online]. Available: <http://aip.scitation.org/doi/10.1063/1.100425>.
- [15] Y. Martin, C. C. Williams, and H. K. Wickramasinghe, "Atomic force microscope-force mapping and profiling on a sub 100-Å scale," *Journal of Applied Physics*, vol. 61, no. 10, pp. 4723–4729, 1987, ISSN: 00218979. DOI: 10.1063/1.338807.
- [16] J. E. Stern, B. D. Terris, H. J. Mamin, and D. Rugar, "Deposition and imaging of localized charge on insulator surfaces using a force microscope," *Applied Physics Letters*, vol. 53, no. 26, pp. 2717–2719, 1988, ISSN: 00036951. DOI: 10.1063/1.100162.

- [17] Y. Martin, D. W. Abraham, and H. K. Wickramasinghe, "High-resolution capacitance measurement and potentiometry by force microscopy," *Applied Physics Letters*, vol. 52, no. 13, pp. 1103–1105, 1988, ISSN: 00036951. DOI: 10.1063/1.99224.
- [18] C. C. Williams and H. K. Wickramasinghe, "Scanning thermal profiler," *Microelectronic Engineering*, vol. 5, no. 1-4, pp. 509–513, 1986, ISSN: 01679317. DOI: 10.1016/0167-9317(86)90084-5. arXiv: arXiv:1011.1669v3.
- [19] G. Mills, J. M. Weaver, G. Harris, W. Chen, J. Carrejo, L. Johnson, and B. Rogers, "Detection of subsurface voids using scanning thermal microscopy," *Ultramicroscopy*, vol. 80, no. 1, pp. 7–11, 1999, ISSN: 03043991. DOI: 10.1016/S0304-3991(99)00047-9.
- [20] D. Rugar, H. J. Mamin, and P. Guethner, "Improved fiber-optic interferometer for atomic force microscopy," *Applied Physics Letters*, vol. 55, no. 25, pp. 2588–2590, 1989, ISSN: 00036951. DOI: 10.1063/1.101987.
- [21] A. Ruf, M. Abraham, M. Lacher, K. Mayr, and T. Zetterer, "Miniaturised Fabry Perot AFM Sensor," *International Conference on Solid-State Sensors and Actuators, and Eurosensors IX, Proceedings*, vol. 1, pp. 660–663, 1995.
- [22] H. Edwards, L. Taylor, W. Duncan, and A. J. Melmed, "Fast, high-resolution atomic force microscopy using a quartz tuning fork as actuator and sensor," *Journal of Applied Physics*, vol. 82, no. 3, pp. 980–984, 1997, ISSN: 00218979. DOI: 10.1063/1.365936.
- [23] F. J. Giessibl, "High-speed force sensor for force microscopy and profilometry utilizing a quartz tuning fork," *Applied Physics Letters*, vol. 73, no. 26, pp. 3956–3958, 1998, ISSN: 00036951. DOI: 10.1063/1.122948.
- [24] T. Göddenhenrich, H. Lemke, U. Hartmann, and C. Heiden, "Force microscope with capacitive displacement detection," *Journal of Vacuum Science & Technology A: Vacuum, Surfaces, and Films*, vol. 8, no. 1, pp. 383–387, 1990, ISSN: 0734-2101. DOI: 10.1116/1.576401.

- [25] M. Tortonese, H. Yamada, R. C. Barrett, and C. F. Quate, "Atomic Force Microscopy Using a Piezoresistive Cantilever," in *TRANSDUCERS '91: 1991 International Conference on Solid-State Sensors and Actuators*, San Francisco, CA, USA: IEEE, 1991, pp. 448–451, ISBN: 0-87942-585-7. DOI: 10.1109/SENSOR.1991.148908.
- [26] C. A. Putman, B. G. De Groot, N. F. Van Hulst, and J. Greve, "A detailed analysis of the optical beam deflection technique for use in atomic force microscopy," *Journal of Applied Physics*, vol. 72, no. 1, pp. 6–12, 1992, ISSN: 00218979. DOI: 10.1063/1.352149.
- [27] S. H. Loh and W. J. Cheah, "Optical beam deflection based AFM with integrated hardware and software platform for an undergraduate engineering laboratory," *Applied Sciences (Switzerland)*, vol. 7, no. 3, 2017, ISSN: 20763417. DOI: 10.3390/app7030226.
- [28] T. L. T. Tsang, "Optical levers," Institute for Cosmic Ray Research (ICRR), University of Tokyo, Tokyo, Tech. Rep., 2019, pp. 1–9.
- [29] C. N. Jones and J. Goncalves, "A cost-effective atomic force microscope for undergraduate control laboratories," *IEEE Transactions on Education*, vol. 53, no. 2, pp. 328–334, 2010, ISSN: 00189359. DOI: 10.1109/TE.2009.2021390.
- [30] J. L. Hutter, "Comment on Tilt of Atomic Force Microscopy Cantilevers: Effect on Spring Constant and Adhesion Measurements," *Langmuir*, vol. 21, pp. 2630–2632, 2005, ISSN: 0743-7463. DOI: 10.1021/la047670t.
- [31] J. te Riet, A. J. Katan, C. Rankl, S. W. Stahl, A. M. van Buul, I. Y. Phang, A. Gomez-Casado, P. Schön, J. W. Gerritsen, A. Cambi, A. E. Rowan, G. J. Vancso, P. Jonkheijm, J. Huskens, T. H. Oosterkamp, H. Gaub, P. Hinterdorfer, C. G. Figdor, and S. Speller, "Interlaboratory round robin on cantilever calibration for AFM force spectroscopy," *Ultramicroscopy*, vol. 111, no. 12, pp. 1659–1669, 2011, ISSN: 03043991. DOI: 10.1016/j.ultramicro.2011.09.012.
- [32] A. Gaitas and P. French, "Piezoresistive probe array for high throughput applications," *Procedia Engineering*, vol. 25, pp. 1445–1448, 2011, ISSN: 18777058. DOI: 10.1016/j.proeng.2011.12.357. [Online]. Available: <http://dx.doi.org/10.1016/j.proeng.2011.12.357>.

- [33] J. E. Sader, J. W. M. Chon, P. Mulvaney, J. E. Sader, J. W. M. Chon, and P. Mulvaney, "Calibration of rectangular atomic force microscope cantilevers Calibration of rectangular atomic force microscope cantilevers," vol. 3967, no. 1999, pp. 1–4, 1999. DOI: 10.1063/1.1150021.
- [34] N. A. Burnham, R. J. Colton, and H. M. Pollock, "Interpretation of force curves in force microscopy," *Nanotechnology*, vol. 4, no. 2, pp. 64–80, 1993, ISSN: 09574484. DOI: 10.1088/0957-4484/4/2/002.
- [35] B. Mokaberi and A. A. Requicha, "Towards automatic nanomanipulation: Drift compensation in scanning probe microscopes," *Proceedings - IEEE International Conference on Robotics and Automation*, vol. 2004, no. 1, pp. 416–421, 2004, ISSN: 10504729. DOI: 10.1109/robot.2004.1307185.
- [36] M. Radmacher, J. P. Cleveland, and P. K. Hansma, "Improvement of thermally induced bending of cantilevers used for atomic force microscopy," *Scanning*, vol. 17, no. 2, pp. 117–121, 1995, ISSN: 19328745. DOI: 10.1002/sca.4950170208.
- [37] F Marinello, M Balcon, P Schiavuta, S Carmignato, and E Savio, "Thermal drift study on different commercial scanning probe microscopes during the initial warming-up phase," *Measurement Science and Technology*, vol. 22, pp. 1–8, 2011. DOI: 10.1088/0957-0233/22/9/094016.
- [38] L. A. Wenzler, G. L. Moyes, and T. P. Beebe, "Improvements to atomic force microscopy cantilevers for increased stability," *Review of Scientific Instruments*, vol. 67, no. 12, pp. 4191–4197, 1996. DOI: 10.1063/1.1147568.
- [39] L. Ramiandrisoa, A. Allard, Y. Joumani, B. Hay, and S. Gomés, "A dark mode in scanning thermal microscopy," *Review of Scientific Instruments*, vol. 88, no. 12, 2017, ISSN: 10897623. DOI: 10.1063/1.5002096. [Online]. Available: <https://doi.org/10.1063/1.5002096>.
- [40] J. Spiece, C. Evangeli, K. Lulla, A. Robson, B. Robinson, and O. Kolosov, "Improving accuracy of nanothermal measurements via spatially distributed scanning thermal microscope probes," *Journal of Applied Physics*, vol. 124, no. 1, 2018, ISSN: 10897550. DOI: 10.1063/1.5031085.

- [41] S. Sevim, S. Tolunay, and H. Torun, "Micromachined sample stages to reduce thermal drift in atomic force microscopy," *Microsystem Technologies*, vol. 21, no. 7, pp. 1559–1566, 2015, ISSN: 1432-1858. DOI: 10.1007/s00542-014-2251-3.
- [42] F Marinello, P Bariani, L. D. Chiffre, and E Savio, "Fast technique for AFM vertical drift compensation," *Measurement Science and Technology*, vol. 18, pp. 689–696, 2007. DOI: 10.1088/0957-0233/18/3/019.
- [43] T. I. Z. Hang, Y. I. N. G. Z. Hao, Z. H. T. Ong, and Y. I. F. U. G. Uan, "A novel method to calculate the mechanical properties of cancer cells based on atomic force microscopy," *Acta of Bioengineering and Biomechanics*, vol. 18, no. 1, pp. 19–24, 2016. DOI: 10.5277/ABB-00286-2015-04.
- [44] M. D'Acunto and O. Salvetti, "Pattern Recognition Methods for Thermal Drift Correction in Atomic Force Microscopy Imaging," *Pattern Recognition and Image Analysis*, vol. 21, no. 1, pp. 9–19, 2011, ISSN: 10546618. DOI: 10.1134/S1054661811010056.
- [45] J. E. Krauskopf, M Bartenwerfer, and S Fatikow, "Modeling and compensating thermal drift in time divergent AFM measurements," in *Micro-Nano-Integration; 6. GMM-Workshop*, Duisburg, Germany, 2016, pp. 1–6, ISBN: 978-3-8007-4278-3.
- [46] G. S. Shekhawat, A. Chand, S. Sharma, Verawati, and V. P. Dravid, "High resolution atomic force microscopy imaging of molecular self assembly in liquids using thermal drift corrected cantilevers," *Applied Physics Letters*, vol. 95, 2009. DOI: 10.1063/1.3266519.
- [47] A. Beyder, C. Spagnoli, and F. Sachs, "Reducing probe dependent drift in atomic force microscope with symmetrically supported torsion levers," *Review of Scientific Instruments*, vol. 77, no. 5, 2006, ISSN: 00346748. DOI: 10.1063/1.2202928.
- [48] Z. Schumacher, Y. Miyahara, L. Aeschmann, and P. Grütter, "Improved atomic force microscopy cantilever performance by partial reflective coating," *Beilstein Journal of Nanotechnology*, vol. 6, pp. 1450–1456, 2015. DOI: 10.3762/bjnano.6.150.

- [49] P. S. Dobson, J. M. Weaver, and G. Mills, "New methods for calibrated Scanning Thermal Microscopy (SThM)," *Proceedings of IEEE Sensors*, pp. 708–711, 2007, ISSN: 1930-0395. DOI: 10.1109/ICSENS.2007.4388498.
- [50] M. P. Murrell, M. E. Welland, S. J. O'Shea, T. M. Wong, J. R. Barnes, A. W. McKinnon, M. Heyns, and S. Verhaverbeke, "Spatially resolved electrical measurements of SiO₂ gate oxides using atomic force microscopy," *Applied Physics Letters*, vol. 62, no. 7, pp. 786–788, 1993, ISSN: 00036951. DOI: 10.1063/1.108579.
- [51] M. Nonnenmacher, M. P. O'Boyle, and H. K. Wickramasinghe, "Kelvin probe force microscopy," *Applied Physics Letters*, vol. 58, no. 25, pp. 2921–2923, 1991, ISSN: 00036951. DOI: 10.1063/1.105227.
- [52] M. Dukic, J. D. Adams, and G. E. Fantner, "Piezoresistive AFM cantilevers surpassing standard optical beam deflection in low noise topography imaging," *Scientific Reports*, vol. 5, no. June, pp. 1–11, 2015, ISSN: 20452322. DOI: 10.1038/srep16393.
- [53] S. Timoshenko, "Analysis of Bi-Metal Thermostats," *Journal of the Optical Society of America*, vol. 11, no. 3, pp. 233–255, 1925. DOI: 10.1364/JOSA.11.000233.
- [54] Kanthal, "Kanthal Thermostatic Bimetal Handbook," 2008.
- [55] H. Torun, O. Finkler, and F. L. Degertekin, "Athermalization in atomic force microscope based force spectroscopy using matched microstructure coupling," *Review of Scientific Instruments*, vol. 80, no. 7, pp. 1–3, 2009, ISSN: 00346748. DOI: 10.1063/1.3167276.
- [56] Bruker, "New MLCT-Bio AFM Probes," Bruker Nano Surfaces Division, Tech. Rep., 2015. [Online]. Available: <https://www.brukerafmprobes.com/images/product/specPDF/3945.pdf>.
- [57] N. A. Nanosensors, "Uniqprobe," Nanosensors, Tech. Rep., 2022. [Online]. Available: <https://www.nanosensors.com/uploads/media/files/0001/05/3cfe8ca6ad48a762e2668b7d2b205e3b205dc04c.pdf>.

- [58] K Luo, Z Shi, J Varesi, A Majumdar, K Luo, Z Shi, J Varesi, and A Majumdar, "Sensor nanofabrication , performance , and conduction mechanisms in scanning thermal microscopy Sensor nanofabrication , performance , and conduction mechanisms in scanning thermal microscopy," *Journal of Vacuum Science & Technology B*, vol. 15, no. 2, pp. 349–360, 1997. DOI: 10.1116/1.589319.
- [59] S. Bhuyan, "Designing thermally actuated bimorph as energy harvester," *Energy Harvesting and Systems*, vol. 6, no. 1-2, pp. 29–38, 2020, ISSN: 23298766. DOI: 10.1515/ehs-2019-0002.
- [60] R. A. Coutu, R. S. LaFleur, J. P. Walton, and L. A. Starman, "Thermal Management Using MEMS Bimorph Cantilever Beams," *Experimental Mechanics*, vol. 56, no. 7, pp. 1293–1303, 2016, ISSN: 17412765. DOI: 10.1007/s11340-016-0170-1. [Online]. Available: <http://dx.doi.org/10.1007/s11340-016-0170-1>.
- [61] M. Komeili, A. Ahrabi, and C. Menon, "Resonance vibration of an optical fiber micro-cantilever using electro-thermal actuation," *Mathematical Models in Engineering*, vol. 3, no. 1, pp. 1–16, 2017, ISSN: 2351-5279. DOI: 10.21595/mme.2017.18228.
- [62] T. Lalinský, E. Burian, M. Držík, Š Haščík, Ž Mozolová, and J. Kuzmík, "Thermal actuation of a GaAs cantilever beam," *Journal of Micromechanics and Microengineering*, vol. 10, no. 2, pp. 293–298, 2000, ISSN: 09601317. DOI: 10.1088/0960-1317/10/2/332.
- [63] N. Umeda, "Scanning attractive force microscope using photothermal vibration," *Journal of Vacuum Science & Technology B: Microelectronics and Nanometer Structures*, vol. 9, no. 2, p. 1318, 1991, ISSN: 0734211X. DOI: 10.1116/1.585187.
- [64] R. Pedrak, T. Ivanov, K. Ivanova, T. Gotszalk, N. Abedinov, I. W. Rangelow, K. Edinger, E. Tomerov, T. Schenkel, and P. Hudek, "Micromachined atomic force microscopy sensor with integrated piezoresistive sensor and thermal bimorph actuator for high-speed tapping-mode atomic force microscopy phase-imaging in higher eigenmodes," *Journal of Vacuum Science & Technology B: Microelectronics and Nanometer Structures*, vol. 21, no. 6, p. 3102, 2003, ISSN: 0734211X. DOI: 10.1116/1.1614252.

- [65] T. Ivanov, T. Gotszalk, P. Grabiec, E. Tomerov, and I. W. Rangelow, "Thermally driven micromechanical beam with piezoresistive deflection readout," *Microelectronic Engineering*, vol. 67-68, pp. 550–556, 2003, ISSN: 01679317. DOI: 10.1016/S0167-9317(03)00113-8.
- [66] J. Teng and P. D. Prewett, "Focused ion beam fabrication of thermally actuated bimorph cantilevers," *Sensors and Actuators, A: Physical*, vol. 123-124, no. September 2004, pp. 608–613, 2005, ISSN: 09244247. DOI: 10.1016/j.sna.2005.04.030.
- [67] L. Jiang, R. Cheung, J. Hedley, M. Hassan, A. J. Harris, J. S. Burdess, M. Mehregany, and C. A. Zorman, "SiC cantilever resonators with electrothermal actuation," *Sensors and Actuators, A: Physical*, vol. 128, no. 2, pp. 376–386, 2006, ISSN: 09244247. DOI: 10.1016/j.sna.2006.01.045.
- [68] G. E. Fantner, W. Schumann, R. J. Barbero, A. Deutschinger, V. Todorov, D. S. Gray, A. M. Belcher, I. W. Rangelow, and K. Youcef-Toumi, "Use of self-actuating and self-sensing cantilevers for imaging biological samples in fluid," *Nanotechnology*, vol. 20, no. 43, 2009, ISSN: 09574484. DOI: 10.1088/0957-4484/20/43/434003.
- [69] G. E. Fantner, D. J. Burns, A. M. Belcher, I. W. Rangelow, and K. Youcef-Toumi, "DMCMN: In depth characterization and control of AFM cantilevers with integrated sensing and actuation," *Journal of Dynamic Systems, Measurement and Control, Transactions of the ASME*, vol. 131, no. 6, pp. 1–13, 2009, ISSN: 00220434. DOI: 10.1115/1.4000378.
- [70] S. W. Stahl, E. M. Puchner, and H. E. Gaub, "Photothermal cantilever actuation for fast single-molecule force spectroscopy," *Review of Scientific Instruments*, vol. 80, no. 7, 2009, ISSN: 00346748. DOI: 10.1063/1.3157466.
- [71] V. Pini, B. Tiribilli, C. M. C. Gambi, and M. Vassalli, "Dynamical characterization of vibrating AFM cantilevers forced by photothermal excitation," *Physical Review B - Condensed Matter and Materials Physics*, vol. 81, no. 5, pp. 2–6, 2010, ISSN: 10980121. DOI: 10.1103/PhysRevB.81.054302.
- [72] R. Boubekri, E. Cambril, L. Couraud, L. Bernardi, A. Madouri, D. Martrou, and S. Gauthier, "High frequency 3C-SiC AFM cantilever using thermal actuation

- and metallic piezoresistive detection," *Materials Science Forum*, vol. 711, pp. 80–83, 2012, ISSN: 16629752. DOI: 10.4028/www.scientific.net/MSF.711.80.
- [73] A. Sierakowski, D. Kopiec, W. Majstrzyk, P. Kunicki, P. Janus, R. Dobrowolski, P. Grabiec, I. W. Rangelow, and T. Gotszalk, "Magnetolectric versus thermal actuation characteristics of shear force AFM probes with piezoresistive detection," *Measurement Science and Technology*, vol. 28, no. 3, 2017, ISSN: 13616501. DOI: 10.1088/1361-6501/28/3/034011.
- [74] A. P. Nievergelt, N. Banterle, S. H. Andany, P. Gönczy, and G. E. Fantner, "High-speed photothermal off-resonance atomic force microscopy reveals assembly routes of centriolar scaffold protein SAS-6," *Nature Nanotechnology*, vol. 13, no. 8, pp. 696–701, 2018, ISSN: 17483395. DOI: 10.1038/s41565-018-0149-4. [Online]. Available: <http://dx.doi.org/10.1038/s41565-018-0149-4>.
- [75] A. Setiono, M. Fahrbach, J. Xu, M. Bertke, W. Ombati Nyang'au, G. Hamdana, H. Suryo Wasisto, and E. Peiner, "Phase optimization of thermally actuated piezoresistive resonant MEMS cantilever sensors," *Journal of Sensors and Sensor Systems*, vol. 8, no. 1, pp. 37–48, 2019, ISSN: 2194878X. DOI: 10.5194/jsss-8-37-2019.
- [76] M. Penedo, A. Yurtsever, K. Miyazawa, H. Furusho, K. A. Ishii, and T. Fukuma, "Photothermal excitation efficiency enhancement of cantilevers by electron beam deposition of amorphous carbon thin films," *Scientific Reports*, vol. 10, no. 1, pp. 1–10, 2020, ISSN: 20452322. DOI: 10.1038/s41598-020-74433-x. [Online]. Available: <https://doi.org/10.1038/s41598-020-74433-x>.
- [77] A. Labuda, S. Hohlbauch, M. Kocun, F. T. Limpoco, N. Kirchhofer, B. Ohler, and D. Hurley, "Tapping Mode AFM Imaging in Liquids with blueDrive Photothermal Excitation," *Microscopy Today*, vol. 26, no. 6, pp. 12–17, 2018, ISSN: 1551-9295. DOI: 10.1017/s1551929518001050.
- [78] G. G. Stoney, "The Tension of Metallic Films Deposited by Electrolysis," *Proceedings of the Royal Society A: Mathematical, Physical and Engineering Sciences*, vol. 82, no. 553, pp. 172–175, 1909, ISSN: 1364-5021. DOI: 10.1098/rspa.1909.0021. [Online]. Available: <http://rspa.royalsocietypublishing.org/cgi/doi/10.1098/rspa.1909.0021>.

- [79] W. Riethmuller and W. Benecke, "Thermally Excited Silicon Microactuators," *IEEE Transactions on Electron Devices*, vol. 35, no. 6, pp. 758–763, 1988, ISSN: 15579646. DOI: 10.1109/16.2528.
- [80] W. H. Chu, M. Mehregany, and R. L. Mullen, "Analysis of tip deflection and force of a bimetallic cantilever microactuator," *Journal of Micromechanics and Microengineering*, vol. 3, no. 1, pp. 4–7, 1993, ISSN: 09601317. DOI: 10.1088/0960-1317/3/1/002.
- [81] C. A. Klein, "How accurate are Stoney's equation and recent modifications," *Journal of Applied Physics*, vol. 88, no. 9, pp. 5487–5489, 2000, ISSN: 00218979. DOI: 10.1063/1.1313776.
- [82] C. H. Hsueh, "Modeling of elastic deformation of multilayers due to residual stresses and external bending," *Journal of Applied Physics*, vol. 91, no. 12, pp. 9652–9656, 2002, ISSN: 00218979. DOI: 10.1063/1.1478137.
- [83] M.Zahid and C.Cho, "BIOSTEC: Internation Joint Conference on Biomedical Engineering Systems and Technologies," in *A Study on Bimetallic Effects in Rectangular Microcantilever Biosensors*, Valencia, Spain: INSTICC, 2010, pp. 28–31.
- [84] S. Jouravand, "Design and Simulation of MOEMS Thermal Sensor Based on a Bimetallic Mechanism," *Sensors & Transducers*, vol. 111, no. 12, pp. 38–44, 2009.
- [85] X. Li, W. Y. Shih, I. A. Aksay, and W.-h. Shih, "Electromechanical behavior of PZT-Brass unimorphs," vol. 40, pp. 1733–1740, 1999.
- [86] J. W. Yi, W. Y. Shih, and W. H. Shih, "Effect of length, width, and mode on the mass detection sensitivity of piezoelectric unimorph cantilevers," *Journal of Applied Physics*, vol. 91, no. 3, pp. 1680–1686, 2002, ISSN: 00218979. DOI: 10.1063/1.1427403.
- [87] O. A. Bauchau and J. I. Craig, *Structural Analysis With Application to Aerospace Structures*, G. GLADWELL, Ed., 9. Springer, 2009, vol. 163, ISBN: 9788578110796. arXiv: arXiv:1011.1669v3.
- [88] J. M. Gere, *Mechanics of Materials*, Sixth. Thomson Learning Inc., 2004, p. 913, ISBN: 0071129391. DOI: 10.1016/j.mechmat.2009.01.011. arXiv: arXiv:1011.1669v3. [Online]. Available: <http://www.worldcat.org/isbn/0534553974>.

- [89] E. Oñate, *Structural Analysis with the Finite Element Method Linear Statics*, 1st ed. Springer, Dordrecht, 2013, vol. Volume 2. ISBN: 978-1-4020-8742-4. DOI: doi . org/10.1007/978-1-4020-8743-1.
- [90] S. Sadat, A. Tan, Y. J. Chua, and P. Reddy, "Nanoscale thermometry using point contact thermocouples," *Nano Letters*, vol. 10, no. 7, pp. 2613–2617, 2010, ISSN: 15306984. DOI: 10.1021/nl101354e.
- [91] S. Gomes, A. Assy, and P.-O. Chapuis, *Thermometry at the Nanoscale: Technique and Selected Applications: Section III Non-luminescence-based Thermometry: Chapter 9 - Scanning Thermal Microscopy*, 38th ed., L. D. Carlos and G. Palacio, Eds. Royal Society of Chemistry, 2016, pp. 275–313, ISBN: 9781782622031. DOI: 10.1039/9781782622031-00273.
- [92] S. Gomès, A. Assy, and P. O. Chapuis, "Scanning thermal microscopy: A review," *Physica Status Solidi (A) Applications and Materials Science*, vol. 212, no. 3, pp. 477–494, 2015, ISSN: 18626319. DOI: 10.1002/pssa.201400360.
- [93] J. M. Weaver, L. M. Walpita, and H. K. Wickramasinghe, "Optical absorption microscopy and spectroscopy with nanometre resolution," *Nature*, vol. 342, no. 6251, pp. 783–785, 1989, ISSN: 00280836. DOI: 10.1038/342783a0.
- [94] M. Nonnenmacher and H. K. Wickramasinghe, "Scanning probe microscopy of thermal conductivity and subsurface properties," *Applied Physics Letters*, vol. 61, no. 2, pp. 168–170, 1992, ISSN: 00036951. DOI: 10.1063/1.108207.
- [95] J. Zhou, C. Yu, Q. Hao, D. Kim, and L. Shi, "Nanoscale quantitative thermal imaging of electronic devices," *ASME International Mechanical Engineering Congress and Exposition, Proceedings*, vol. 7, pp. 23–29, 2002, ISSN: 02725673. DOI: 10.1115/IMECE2002-32112.
- [96] A. Pavlov, "Nanoscale measurements of the absolute temperature from the tunneling of the free electron gas," *Applied Physics Letters*, vol. 85, no. 11, pp. 2095–2097, 2004, ISSN: 00036951. DOI: 10.1063/1.1786358.
- [97] G Mills, H Zhou, A Midha, L Donaldson, J. M. R. Weaver, G Mills, H Zhou, A Midha, L Donaldson, and J. M. R. Weaver, "Scanning thermal microscopy

- using batch fabricated thermocouple probes," vol. 2900, no. 1998, pp. 1–4, 1998. DOI: 10.1063/1.121453.
- [98] A Majumdar, "Scanning Thermal," 1999.
- [99] H. Zhou, "Generic scanned-probe microscope sensors by combined micromachining and electron-beam lithography," *Journal of Vacuum Science & Technology B: Microelectronics and Nanometer Structures*, vol. 16, no. 1, p. 54, 1998, ISSN: 0734211X. DOI: 10.1116/1.589835.
- [100] A. Kittel, W. Müller-Hirsch, J. Parisi, S. A. Biehs, D. Reddig, and M. Holthaus, "Near-field heat transfer in a scanning thermal microscope," *Physical Review Letters*, vol. 95, no. 22, pp. 1–4, 2005, ISSN: 00319007. DOI: 10.1103/PhysRevLett.95.224301.
- [101] T. Leinhos, M. Stopka, and E. Oesterschulze, "Micromachined fabrication of Si cantilevers with Schottky diodes integrated in the tip," *Applied Physics A: Materials Science and Processing*, vol. 66, no. SUPPL. 1, pp. 65–69, 1998, ISSN: 09478396. DOI: 10.1007/s003390051101.
- [102] R. Pylkki, P. Moyer, and P. West, "Scanning Near-Field Optical Microscopy and Scanning Thermal Microscopy," *Japanese Journal of Applied Physics*, vol. 33, pp. 3785–3790, 1994. [Online]. Available: <http://iopscience.iop.org/1347-4065/33/6S/3785>.
- [103] M. I. Lutwyche, M. Despont, U. Drechsler, U. Dürig, W. Häberle, H. Rothuizen, R. Stutz, R. Widmer, G. K. Binnig, and P. Vettiger, "Highly parallel data storage system based on scanning probe arrays," *Applied Physics Letters*, vol. 77, no. 20, pp. 3299–3301, 2000, ISSN: 00036951. DOI: 10.1063/1.1326486.
- [104] L. Aigouy, G. Tessier, M. Mortier, and B. Charlot, "Scanning thermal imaging of microelectronic circuits with a fluorescent nanoprobe," *Applied Physics Letters*, vol. 87, no. 18, pp. 1–3, 2005, ISSN: 00036951. DOI: 10.1063/1.2123384.
- [105] B. Samson, L. Aigouy, P. Löw, C. Bergaud, B. J. Kim, and M. Mortier, "Ac thermal imaging of nanoheaters using a scanning fluorescent probe," *Applied Physics Letters*, vol. 92, no. 2, 2008, ISSN: 00036951. DOI: 10.1063/1.2832673.

- [106] J. Varesi and A. Majumdar, "Scanning Joule expansion microscopy at nanometer scales," *Applied Physics Letters*, vol. 72, no. 1, pp. 37–39, 1998, ISSN: 00036951. DOI: 10.1063/1.120638.
- [107] A. Dazzi, R. Prazeres, F. Glotin, and J. M. Ortega, "Local infrared microspectroscopy with subwavelength spatial resolution with an atomic force microscope tip used as a photothermal sensor," *Optics Letters*, vol. 30, no. 18, p. 2388, 2005, ISSN: 0146-9592. DOI: 10.1364/ol.30.002388.
- [108] J. Lai, T. Perazzo, Z. Shi, and A. Majumdar, "Optimization and performance of high-resolution micro-optomechanical thermal sensors," *Sensors and Actuators, A: Physical*, vol. 58, no. 2, pp. 113–119, 1997, ISSN: 09244247. DOI: 10.1016/S0924-4247(96)01401-X.
- [109] G. Wielgoszewski and T. Gotszalk, *Chapter Four – Scanning Thermal Microscopy (SThM): How to Map Temperature and Thermal Properties at the Nanoscale*. 2015, vol. 190, pp. 177–221, ISBN: 9780128023808. DOI: 10.1016/bs.aiep.2015.03.011.
- [110] Y. Zhang, W. Zhu, F. Hui, M. Lanza, T. Borca-Tasciuc, and M. Muñoz Rojo, "A Review on Principles and Applications of Scanning Thermal Microscopy (SThM)," *Advanced Functional Materials*, vol. 1900892, 2019, ISSN: 16163028. DOI: 10.1002/adfm.201900892.
- [111] A. Majumdar, J. P. Carrejo, and J. Lai, "Thermal imaging using the atomic force microscope," *Applied Physics Letters*, vol. 62, no. 20, pp. 2501–2503, 1993, ISSN: 00036951. DOI: 10.1063/1.109335.
- [112] B. Gotsmann, M. A. Lantz, A. Knoll, and U. Durig, *Nanotechnology: Volume 6: Nanoprobes: 4 - Nanoscale Thermal and Mechanical Interactions Studies using Heatable Probes*, H. Fuchs, Ed. Wiley-VCH, 2009, p. 121, ISBN: 3527317333.
- [113] Y. Ge, "Quantitative measurement using scanning thermal microscopy," Ph.D. dissertation, University of Glasgow, 2016, pp. 0–244.
- [114] Y. Zhang, P. S. Dobson, and J. M. R. Weaver, "High temperature imaging using a thermally compensated cantilever resistive probe for scanning thermal

- microscopy," *Journal of Vacuum Science & Technology B, Nanotechnology and Microelectronics: Materials, Processing, Measurement, and Phenomena*, vol. 30, no. 1, pp. 1–5, 2012, ISSN: 2166-2746. DOI: 10.1116/1.3664328. [Online]. Available: <http://avs.scitation.org/doi/10.1116/1.3664328>.
- [115] S. Sadat, A. Tan, Y. J. Chua, and P. Reddy, "Nanoscale thermometry using point contact thermocouples," *Nano Letters*, vol. 10, no. 7, pp. 2613–2617, 2010, ISSN: 15306984. DOI: 10.1021/nl101354e.
- [116] P. Janus, D. Szmigiel, M. Weisheit, G. Wielgoszewski, Y. Ritz, P. Grabiec, M. Hecker, T. Gotszalk, P. Sulecki, and E. Zschech, "Novel SThM nanoprobe for thermal properties investigation of micro- and nanoelectronic devices," *Microelectronic Engineering*, vol. 87, no. 5-8, pp. 1370–1374, 2010, ISSN: 01679317. DOI: 10.1016/j.mee.2009.11.178. [Online]. Available: <http://dx.doi.org/10.1016/j.mee.2009.11.178>.
- [117] B. Yang, M. Lenczner, S. Cogan, F. Menges, H. Riel, B. Gotsmann, P. Janus, and G. Boetch, "Modelling, simulation and optimization for a SThM nanoprobe," *2014 15th International Conference on Thermal, Mechanical and Multi-Physics Simulation and Experiments in Microelectronics and Microsystems, EuroSimE 2014*, 2014. DOI: 10.1109/EuroSimE.2014.6813869.
- [118] M. Lenczner, B. Yang, A. Bontempi, D. Teyssieux, S. Cogan, P. Janus, B. Köhler, and N. Ratier, "A SThM probe optimization and its time-space multi-scale modeling," *Mechatronics*, 2016, ISSN: 09574158. DOI: 10.1016/j.mechatronics.2016.05.010.
- [119] M. Świątkowski, A. Wojtuś, G. Wielgoszewski, M. Rudek, T. Piasecki, G. Józwiak, and T. Gotszalk, "A low-noise measurement system for scanning thermal microscopy resistive nanoprobe based on a transformer ratio-arm bridge," *Measurement Science and Technology*, vol. 29, no. 4, 2018, ISSN: 13616501. DOI: 10.1088/1361-6501/aa9d10.

- [120] P. Klapetek, J. Martinek, P. Grolich, M. Valtr, and N. Jeet, "Graphics cards based topography artefacts simulations in Scanning Thermal Microscopy," *International Journal of Heat and Mass Transfer*, vol. 108, pp. 841–850, 2017, ISSN: 0017-9310. DOI: 10.1016/j.ijheatmasstransfer.2016.12.036. [Online]. Available: <http://dx.doi.org/10.1016/j.ijheatmasstransfer.2016.12.036>.
- [121] P. S. Dobson, G. Mills, and J. M. Weaver, "Microfabricated temperature standard based on Johnson noise measurement for the calibration of micro- and nano-thermometers," *Review of Scientific Instruments*, vol. 76, no. 5, 2005, ISSN: 00346748. DOI: 10.1063/1.1899463.
- [122] Marc J. Madou, *Fundamentals of Microfabrication - The Science of Miniturization*, Second. Boca Raton: CRC Press LLC, 2002, ISBN: 9781315274225. DOI: [doi.org/10.1201/9781482274004](http://dx.doi.org/10.1201/9781482274004).
- [123] S. Franssila, *Introduction to Microfabrication*. John Wiley & Sons, Limited, 2004, ISBN: 9780470749838. DOI: 10.1002/9781119990413.
- [124] H. H. Gatzen, V. Saile, and J. Leuthold, *Micro and Nanofabrication - Tools and Processes*. Springer, 2015, ISBN: 9783662443941. DOI: 10.1007/978-3-662-44395-8.
- [125] Y. Zhang, P. S. Dobson, and J. M. Weaver, "Batch fabricated dual cantilever resistive probe for scanning thermal microscopy," *Microelectronic Engineering*, vol. 88, no. 8, pp. 2435–2438, 2011, ISSN: 01679317. DOI: 10.1016/j.mee.2011.02.040. [Online]. Available: <http://dx.doi.org/10.1016/j.mee.2011.02.040>.
- [126] R. Dey, "Nanofabrication and its application in atomic force microscopy (AFM)," Doctor of Philosophy, University of Waterloo, 2015.
- [127] H. Zhou, G. Mills, B. K. Chong, A. Midha, L. Donaldson, and J. M. R. Weaver, "Recent progress in the functionalization of atomic force microscope probes using electron-beam nanolithography," *Journal of Vacuum Science & Technology A: Vacuum, Surfaces, and Films*, vol. 17, no. 4, pp. 2233–2239, 1999, ISSN: 0734-2101. DOI: 10.1116/1.581753.

- [128] H. Zhou, A. Midha, L. Bruchhaus, G. Mills, L. Donaldson, and J. M. R. Weaver, "Novel scanning near-field optical microscopy/atomic force microscope probes by combined micromachining and electron-beam nanolithography," *Journal of Vacuum Science & Technology B: Microelectronics and Nanometer Structures*, vol. 17, no. 5, p. 1954, 1999, ISSN: 0734211X. DOI: 10.1116/1.590855.
- [129] P. S. Dobson, J. M. Weaver, D. P. Burt, M. N. Holder, N. R. Wilson, P. R. Unwin, and J. V. Macpherson, "Electron beam lithographically-defined scanning electrochemical-atomic force microscopy probes: Fabrication method and application to high resolution imaging on heterogeneously active surfaces," *Physical Chemistry Chemical Physics*, vol. 8, no. 33, pp. 3909–3914, 2006, ISSN: 14639076. DOI: 10.1039/b605828k.
- [130] B. K. Chong, H. Zhou, G. Mills, L. Donaldson, and J. M. R. Weaver, "Scanning Hall probe microscopy on an atomic force microscope tip," *Journal of Vacuum Science & Technology A: Vacuum, Surfaces, and Films*, vol. 19, no. 4, pp. 1769–1772, 2001, ISSN: 0734-2101. DOI: 10.1116/1.1379324.
- [131] W. W. Hu, K. Sarveswaran, M. Lieberman, and G. H. Bernstein, "Sub-10 nm electron beam lithography using cold development of poly(methylmethacrylate)," *Journal of Vacuum Science & Technology B: Microelectronics and Nanometer Structures*, vol. 22, no. 4, p. 1711, 2004, ISSN: 0734211X. DOI: 10.1116/1.1763897.
- [132] P. Rai-Choudhury, *Handbook of Microlithography, Micromachining, and Microfabrication. Volume 1: Microlithography*. Spie Optical Engineering Press, 1997, ISBN: 9781510607965. DOI: 10.1117/3.2265070.
- [133] M. Zhao, T. Xu, B. Chen, and J. Niu, "Technology of alignment mark in electron beam lithography," *7th International Symposium on Advanced Optical Manufacturing and Testing Technologies: Smart Structures and Materials for Manufacturing and Testing*, vol. 9285, no. January, p. 92850C, 2014, ISSN: 1996756X. DOI: 10.1117/12.2068112.
- [134] S. Thoms, D. S. Macintyre, K. E. Docherty, and J. M. Weaver, "Alignment verification for electron beam lithography," *Microelectronic Engineering*, vol. 123, pp. 9–12, 2014, ISSN: 01679317. DOI: 10.1016/j.mee.2014.02.005. [Online]. Available: <http://dx.doi.org/10.1016/j.mee.2014.02.005>.

- [135] G. S. May and C. J. Spanos, *Fundamentals of Semiconductor Manufacturing and Process Control*. A John Wiley & Sons, Inc., 2006, ISBN: 9780471784067.
- [136] M. Elwenspoek and R. Wiegerink, "Silicon Micromachining," in *Mechanical Microsensors. Microtechnology and MEMS*, Springer, Berlin, Heidelberg, 2001, ch. 3, pp. 24–58. DOI: 10.1007/978-3-662-04321-9_3.
- [137] Marc J. Madou, *Fundamentals of Microfabrication*. CRC Press, 1997.
- [138] K. Nojiri, *Dry Etching Technology for Semiconductors*. Springer, 2015, p. 611, ISBN: 978-3-319-10294-8. DOI: 10.1007/978-3-319-10295-5.
- [139] University of Glasgow, *James Watt Nanofabrication Centre*. [Online]. Available: <http://jwnc.eng.gla.ac.uk/> (visited on 05/28/2021).
- [140] S. Tönnerberg, "Optimisation and characterisation of LPCVD silicon nitride thin film growth," *Master Thesis*, 2006. [Online]. Available: <http://publications.lib.chalmers.se/records/fulltext/18906.pdf>.
- [141] R. Lambert, "Design, Fabrication and Characterisation of Thermally Optimised Novel SThM Probes," Ph.D. dissertation, University of Glasgow, 2019, pp. 0–392.
- [142] C. W. M. McKay, "Modification of Scanning Thermal Microscopy Probes to Reduce the Effects of Air Conduction," *Masters Thesis*, University of Glasgow, 2018, pp. 0–48.
- [143] R. S. Gates and M. G. Reitsma, "Precise atomic force microscope cantilever spring constant calibration using a reference cantilever array," *Review of Scientific Instruments*, vol. 78, no. 8, pp. 129–131, 2007, ISSN: 00346748. DOI: 10.1063/1.2764372.
- [144] Z. C. Ying, M. G. Reitsma, and R. S. Gates, "Direct measurement of cantilever spring constants and correction for cantilever irregularities using an instrumented indenter," *Review of Scientific Instruments*, vol. 78, no. 6, pp. 1–7, 2007, ISSN: 00346748. DOI: 10.1063/1.2747095.
- [145] J. Putnam, M. Damircheli, and B. Eslami, "Effects of laser spot positioning with optical beam deflection method on tapping mode and bimodal AFM," *Journal of Multi-Body Dynamics*, 2020. DOI: 10.1177/1464419320951343.

- [146] J. Bausells, "Piezoresistive cantilevers for nanomechanical sensing," *Microelectronic Engineering*, vol. 145, pp. 9–20, 2015, ISSN: 01679317. DOI: 10.1016/j.mee.2015.02.010. [Online]. Available: <http://dx.doi.org/10.1016/j.mee.2015.02.010>.
- [147] M. A. Poggi, A. W. McFarland, J. S. Colton, and L. A. Bottomley, "A method for calculating the spring constant of atomic force microscopy cantilevers with a nonrectangular cross section," *Analytical Chemistry*, vol. 77, no. 4, pp. 1192–1195, 2005, ISSN: 00032700. DOI: 10.1021/ac048828h.
- [148] L. Avilovas, "Micro Electro-Mechanical System Design, Fabrication and Application for Atomic Force Microscopy Probe Elasticity Characterisation," Ph.D. dissertation, University of Glasgow, 2021.
- [149] E. Q. Sun, "Shear Locking and Hourglassing in MSC Nastran , ABAQUS , and ANSYS Shear Locking," *MSc Software Users Meeting*, pp. 1–9, 2006.
- [150] J. H. Dellinger, "The temperature coefficient of resistance of copper," *Journal of the Franklin Institute*, vol. 170, no. 3, pp. 213–216, 1910, ISSN: 00160032. DOI: 10.1016/S0016-0032(10)90872-7.
- [151] Y. G. GUREVICH and J. E. VELAZQUEZ-PEREZ, "Peltier Effect in Semiconductors," *Wiley Encyclopedia of Electrical and Electronics Engineering*, no. April, pp. 1–21, 2014. DOI: 10.1002/047134608x.w8206.
- [152] M. Novak, "VXI Universal Surface Measurements for 3D Optical Microscopes," *Bruker, Application Notes*, pp. 1–5, 2013. [Online]. Available: https://mbns.bruker.com/acton/attachment/9063/f-09b6/0/-/-/-/-/AN554-VXI.pdf{_}blank.
- [153] P. S. Dobson, G Mills, and J. M. Weaver, "Microfabricated temperature standard based on Johnson noise measurement for the calibration of micro- and nano-thermometers," *Review of Scientific Instruments*, vol. 76, no. 5, 2005. DOI: 10.1063/1.1899463.
- [154] H. Zhou, B. K. Chong, P. Stopford, G. Mills, A. Midha, L. Donaldson, and J. M. R. Weaver, "Lithographically defined nano and micro sensors using "float coating" of resist and electron beam lithography," *Journal of Vacuum Science &*

- Technology B: Microelectronics and Nanometer Structures*, vol. 18, no. 6, p. 3594, 2000, ISSN: 0734211X. DOI: 10.1116/1.1321271. [Online]. Available: <http://scitation.aip.org/content/avs/journal/jvstb/18/6/10.1116/1.1321271>.
- [155] Bruker, *VITA - SThM*, 2021. [Online]. Available: <https://www.brukerafmprobes.com/c-205-vita-sthm.aspx> (visited on 07/30/2021).
- [156] H. A. Tinoco, J. Holzer, T. Pikálek, Z. Buchta, J. Lazar, A. Chlupová, T. Kruml, and P. Hutař, "Determination of elastic parameters of Si₃N₄ thin films by means of a numerical approach and bulge tests," *Thin Solid Films*, vol. 672, no. December 2018, pp. 66–74, 2019, ISSN: 00406090. DOI: 10.1016/j.tsf.2018.12.039. [Online]. Available: <https://doi.org/10.1016/j.tsf.2018.12.039>.
- [157] P. Martins, C. Malhaire, S. Brida, and D. Barbier, "On the determination of Poisson's ratio of stressed monolayer and bilayer submicron thick films," *Microsystem Technologies*, vol. 15, no. 9, pp. 1343–1348, 2009, ISSN: 09467076. DOI: 10.1007/s00542-009-0822-5.
- [158] J. J. Vlassak and W. D. Nix, "A new bulge test technique for the determination of Young's modulus and Poisson's ratio of thin films," *Journal of Materials Research*, vol. 7, no. 12, pp. 3242–3249, 1992, ISSN: 20445326. DOI: 10.1557/JMR.1992.3242.
- [159] B. A. Walmsley, Y. Liu, X. Z. Hu, M. B. Bush, J. M. Dell, and L. Faraone, "Poisson's ratio of low-temperature PECVD silicon nitride thin films," *Journal of Microelectromechanical Systems*, vol. 16, no. 3, pp. 622–627, 2007, ISSN: 10577157. DOI: 10.1109/JMEMS.2007.893518.
- [160] H. O. Pierson, *Handbook of Chemical Vapor Deposition*, Second Edi, R. F. Bunshah, G. E. McGuire, and S. M. Rossnagel, Eds. New York: Noyes Publications, 1999, ISBN: 0815514328.
- [161] J. F. Shackelford and W. Alexander, *Materials Science and Engineering Handbook*, Third Edit. New York: CRC Press LLC, 2001, ISBN: 0849326966. DOI: 10.1126/science.232.4757.1485.
- [162] D. Faurie, P. O. Renault, E. Le Bourhis, and P. Goudeau, "Study of texture effect on elastic properties of Au thin films by X-ray diffraction and in situ tensile

- testing," *Acta Materialia*, vol. 54, no. 17, pp. 4503–4513, 2006, ISSN: 13596454. DOI: 10.1016/j.actamat.2006.05.036.
- [163] B. Arrazat, V. Mandrillon, K. Inal, M. Vincent, and C. Poulain, "Microstructure evolution of gold thin films under spherical indentation for micro switch contact applications," *Journal of Materials Science*, vol. 46, no. 18, pp. 6111–6117, 2011, ISSN: 00222461. DOI: 10.1007/s10853-011-5575-8.
- [164] B. Merle, "Mechanical properties of thin films studied by bulge testing," Ph.D. dissertation, FAU University, 2013, p. 148, ISBN: 9783944057088.
- [165] C. E. Software, *Nickel-Chromium Alloys*, Cambridge, UK, 2019.
- [166] H. Warlimont and W. Martienssen, *Handbook Materials Data*, Second. Springer, 2018, ISBN: 9783319697413. DOI: <https://doi.org/10.1007/978-3-319-69743-7>.
- [167] P. Morin, G. Raymond, D. Benoit, P. Maury, and R. Beneyton, "A comparison of the mechanical stability of silicon nitride films deposited with various techniques," *Applied Surface Science*, vol. 260, pp. 69–72, 2012, ISSN: 01694332. DOI: 10.1016/j.apsusc.2012.04.003. [Online]. Available: <http://dx.doi.org/10.1016/j.apsusc.2012.04.003>.
- [168] K. B. Gavan, H. J. R. Westra, E. W. J. M. V. D. Drift, W. J. Venstra, and H. S. J. V. D. Zant, "Size-dependent effective Young's modulus of silicon nitride cantilevers," vol. 233108, no. November 2018, pp. 1–4, 2009. DOI: 10.1063/1.3152772.
- [169] Y. Hwangbo, J. M. Park, W. L. Brown, J. H. Goo, H. J. Lee, and S. Hyun, "Effect of deposition conditions on thermo-mechanical properties of free standing silicon-rich silicon nitride thin film," *Microelectronic Engineering*, vol. 95, pp. 34–41, 2012, ISSN: 01679317. DOI: 10.1016/j.mee.2012.03.003. [Online]. Available: <http://dx.doi.org/10.1016/j.mee.2012.03.003>.
- [170] F. Zhang, S. Krishnaswamy, and C. M. Lilley, "Photoacoustic evaluation of the mechanical properties of aluminum / silicon nitride double-layer thin films," *AIP Conference Proceedings*, vol. 820 II, pp. 1098–1104, 2006, ISSN: 0094243X. DOI: 10.1063/1.2184647.

- [171] D. M. Profunser, J. Vollmann, and J. Dual, "Determination of the material properties of microstructures by laser based ultrasound," *Ultrasonics*, vol. 42, no. 1-9, pp. 641–646, 2004, ISSN: 0041624X. DOI: 10.1016/j.ultras.2004.01.049.
- [172] H. D. Espinosa and B. C. Prorok, "Size effects on the mechanical behavior of gold thin films," *Journal of Materials Science*, vol. 38, no. 20, pp. 4125–4128, 2003. DOI: <https://doi.org/10.1023/A:1026321404286>.
- [173] C. Birleanu, M. Pustan, V. Merie, R. Müller, R. Voicu, A. Baracu, and S. Craciun, "Temperature effect on the mechanical properties of gold nano films with different thickness," *IOP Conference Series: Materials Science and Engineering*, vol. 147, no. 1, 2016, ISSN: 1757899X. DOI: 10.1088/1757-899X/147/1/012021.
- [174] C. Liang and B. C. Prorok, "Measuring the thin film elastic modulus with a magnetostrictive sensor," *Journal of Micromechanics and Microengineering*, vol. 17, no. 4, pp. 709–716, 2007, ISSN: 09601317. DOI: 10.1088/0960-1317/17/4/006.
- [175] H. M. Zhou, F. Li, Q. Ye, J. X. Zhao, Z. L. Xia, Y. Tang, and J. Wei, "Young's modulus measurement of thin films by resonant frequency method using magnetostrictive resonator," *Computers, Materials and Continua*, vol. 13, no. 3, pp. 235–248, 2010, ISSN: 15462218. DOI: 10.3970/cmcc.2009.013.235.
- [176] M. C. Salvadori, I. G. Brown, A. R. Vaz, L. L. Melo, and M. Cattani, "Measurement of the elastic modulus of nanostructured gold and platinum thin films," *Physical Review B - Condensed Matter and Materials Physics*, vol. 67, no. 15, pp. 1–5, 2003, ISSN: 1550235X. DOI: 10.1103/PhysRevB.67.153404.
- [177] W. D. Nix, "Mechanical properties of thin films," *The Minerals, Metals & Materials Society - Metallurgical Transactions A*, vol. 20A, pp. 2217–2245, 1989, ISSN: 00846600. DOI: 10.1146/annurev.ms.20.080190.002135.
- [178] V. K. Pamula, A. Jog, and R. B. Fair, "Mechanical property measurement of thin-film gold using thermally actuated bimetallic cantilever beams," *2001 International Conference on Modeling and Simulation of Microsystems - MSM 2001*, pp. 410–413, 2001.
- [179] Y. H. Huh, D. I. Kim, D. J. Kim, H. M. Lee, and J. H. Park, "Dependency of micro-mechanical properties of gold thin films on grain size," *Engineering*

- Against Fracture - Proceedings of the 1st Conference*, pp. 339–346, 2009. DOI: 10 . 1007/978-1-4020-9402-6_27.
- [180] C. W. Baek, J. M. Kim, Y. K. Kim, J. H. Kim, H. J. Lee, and S. W. Han, “Mechanical characterization of gold thin films based on strip bending and nanoindentation test for MEMS/NEMS applications,” *Sensors and Materials*, vol. 17, no. 5, pp. 277–288, 2005, ISSN: 09144935.
- [181] E. Le Bourhis, D. Faurie, B. Girault, P. Goudeau, P. O. Renault, P. Villain, and F. Badawi, “Mechanical properties of thin films and nanometric multilayers using tensile testing and synchrotron X-ray diffraction,” *Plasma Processes and Polymers*, vol. 4, no. 3, pp. 311–317, 2007, ISSN: 16128850. DOI: 10 . 1002/ppap . 200600094.
- [182] K. Du, X. Pang, C. Chen, and A. A. Volinsky, “Mechanical properties of evaporated gold films. hard substrate effect correction,” *Materials Research Society Symposium Proceedings*, vol. 1086, pp. 98–103, 2008, ISSN: 02729172. DOI: 10 . 1557/proc - 1086 - u08 - 41.
- [183] C. Birleanu and M. Pustan, “The effect of film thickness on the tribomechanical properties of the chrome-gold thin film,” *Symposium on Design, Test, Integration and Packaging of MEMS/MOEMS, DTIP 2016*, 2016. DOI: 10 . 1109/DTIP . 2016 . 7514857.
- [184] S. U. Jen and T. C. Wu, “Young’s modulus and hardness of Pd thin films,” *Thin Solid Films*, vol. 492, no. 1-2, pp. 166–172, 2005, ISSN: 00406090. DOI: 10 . 1016/ j . tsf . 2005 . 06 . 048.
- [185] A. Kaushik, H. Kahn, and A. H. Heuer, “Wafer-level mechanical characterization of silicon nitride MEMS,” *Journal of Microelectromechanical Systems*, vol. 14, no. 2, pp. 359–367, 2005, ISSN: 10577157. DOI: 10 . 1109/JMEMS . 2004 . 839315.
- [186] G. Carlotti, P. Colpani, D. Piccolo, S. Santucci, V. Senez, G. Socino, and L. Verdini, “Measurement of the elastic and viscoelastic properties of dielectric films used in microelectronics,” *Thin Solid Films*, vol. 414, no. 1, pp. 99–104, 2002, ISSN: 00406090. DOI: 10 . 1016/S0040 - 6090 (02)00430 - 3.

- [187] C.-L. Tien and T.-W. Lin, "Thermal expansion coefficient and thermomechanical properties of SiN_x thin films prepared by plasma-enhanced chemical vapor deposition," *Applied Optics*, vol. 51, no. 30, p. 7229, 2012, ISSN: 1559-128X. DOI: 10.1364/ao.51.007229.
- [188] L. Wang, R. W. Snidle, and L. Gu, "Rolling contact silicon nitride bearing technology: A review of recent research," *Wear*, vol. 246, no. 1-2, pp. 159–173, 2000, ISSN: 00431648. DOI: 10.1016/S0043-1648(00)00504-4.
- [189] J. H. Jou, C. N. Liao, and K. W. Jou, "A method for the determination of gold thin film's mechanical properties," *Thin Solid Films*, vol. 238, no. 1, pp. 70–72, 1994, ISSN: 00406090. DOI: 10.1016/0040-6090(94)90650-5.
- [190] A. I. Oliva, J. M. Lugo, R. A. Gurubel-Gonzalez, R. J. Centeno, J. E. Corona, and F. Avilés, "Temperature coefficient of resistance and thermal expansion coefficient of 10-nm thick gold films," *Thin Solid Films*, vol. 623, pp. 84–89, 2017, ISSN: 00406090. DOI: 10.1016/j.tsf.2016.12.028.
- [191] A. E. Mag-Isa, B. Jang, J. H. Kim, H. J. Lee, and C. S. Oh, "Coefficient of thermal expansion measurements for freestanding nanocrystalline ultra-thin gold films," *International Journal of Precision Engineering and Manufacturing*, vol. 15, no. 1, pp. 105–110, 2014, ISSN: 22347593. DOI: 10.1007/s12541-013-0311-8.
- [192] F. Avilés, O. Ceh, and A. I. Oliva, "Physical properties of AU and AL thin films measured by resistive heating," *Surface Review and Letters*, vol. 12, no. 1, pp. 101–106, 2005, ISSN: 0218625X. DOI: 10.1142/S0218625X05006834.
- [193] T. C. Hodge, S. ann Bidstrup-Allen, and P. A. Kohl, "Stresses in Thin Film Metallization," *IEEE Transaction on Components, Packaging, and Manufacturing Technology - Part A*, vol. 20, no. 2, pp. 241–250, 1997. DOI: 10.1109/95.588580.
- [194] Y. Ge, "Quantitative Measurement Using Scanning Thermal Microscopy," Ph.D. dissertation, University of Glasgow, 2016, p. 244. DOI: <http://theses.gla.ac.uk/id/eprint/7474>.
- [195] Park Systems, "AFM Probe Selection Guide," Park Systems, Tech. Rep., 2018.

- [196] A. Instruments, *SThM Probes*. [Online]. Available: <https://www.anasysinstruments.com/products/thermal-probes-tips-afm-sthm/{\#}:{~}:text=SThMProbes{\%}3A{\&}text=Theyarebatchfabricatedprobes,theapexofthetip.> (visited on 05/03/2021).
- [197] Bruker, *VITA-DM-GLA-1*. [Online]. Available: <https://www.brukerafmprobes.com/p-3707-vita-dm-gla-1.aspx> (visited on 05/03/2021).
- [198] R. S. Gates and M. G. Reitsma, "Precise atomic force microscope cantilever spring constant calibration using a reference cantilever array," *Review of Scientific Instruments*, vol. 78, no. 8, pp. 7–10, 2007, ISSN: 00346748. DOI: 10.1063/1.2764372.
- [199] L. Yang, Y. S. Tu, and H. L. Tan, "Influence of atomic force microscope (AFM) probe shape on adhesion force measured in humidity environment," *Applied Mathematics and Mechanics (English Edition)*, vol. 35, no. 5, pp. 567–574, 2014, ISSN: 02534827. DOI: 10.1007/s10483-014-1813-7.
- [200] M. Munz, "Force calibration in lateral force microscopy: a review of the experimental methods," *Journal of Physics D: Applied Physics*, vol. 43, no. 6, p. 063 001, 2010, ISSN: 0022-3727. DOI: 10.1088/0022-3727/43/6/063001. [Online]. Available: <http://stacks.iop.org/0022-3727/43/i=6/a=063001?key=crossref.b38dfbef811bdb081fc8e31bb13495d2>.
- [201] C. E. Software, *Silicon Nitride*, Cambridge, UK, 2019.
- [202] C. E.-P. Software, *Gold*, Cambridge, UK, 2019.
- [203] C. E. Software, *Palladium*, Cambridge, UK, 2019.
- [204] Bruker, *MLCT*, 2021. [Online]. Available: <https://www.brukerafmprobes.com/p-3444-mlct.aspx> (visited on 03/23/2021).
- [205] Nanoworld, *Pyrex-Nitride Probe – Diving Board Cantilevers*, 2021. [Online]. Available: <https://www.nanoworld.com/pyrex-nitride-rectangular-silicon-nitride-cantilever-afm-tip-pnp-db>.
- [206] C. E. Software, *Silica (quartz fused)*, Cambridge, UK, 2019.
- [207] C. E.-P. Software, *Tungsten Alloys*, Cambridge, UK, 2019.

- [208] M. Jolley, "Applications of tetramethylammonium hydroxide (TMAH) as a post tungsten CMP cleaning mixture," *Solid State Phenomena*, vol. 65-66, pp. 105–108, 1999, ISSN: 16629779. DOI: 10.4028/www.scientific.net/SSP.65-66.105.
- [209] Nanosensors, *A TEC-FMAu*, 2021. [Online]. Available: <https://www.nanosensors.com/advanced-tip-at-the-end-of-the-cantilever-force-modulation-mode-au-coating-afm-tip-A TEC-FMAu>.
- [210] N. I. Technologies, "Nanoworld® SPM and AFM probes," Tech. Rep., 2021.
- [211] A. K. Snell, "Exothermic Fuse Wire," *Platinum Metals Review*, vol. 4, no. 3, pp. 85–85, 1960, ISSN: 0032-1400.
- [212] M. A. Haque and M. T. A. Saif, "Mechanical behavior of 30 – 50 nm thick aluminum films under uniaxial tension," *Scripta Materialia*, vol. 47, pp. 863–867, 2002. DOI: doi.org/10.1016/S1359-6462(02)00306-8.
- [213] H. Huang and F. Spaepen, "Tensile testing of free-standing Cu, Ag and Al thin films and Ag/Cu multilayers," *Acta Materialia*, vol. 48, no. 12, pp. 3261–3269, 2000, ISSN: 13596454. DOI: 10.1016/S1359-6454(00)00128-2.
- [214] H. D. Espinosa, B. C. Prorok, and B. Peng, "Plasticity size effects in free-standing submicron polycrystalline FCC films subjected to pure tension," *Journal of the Mechanics and Physics of Solids*, vol. 52, no. 3, pp. 667–689, 2004, ISSN: 00225096. DOI: 10.1016/j.jmps.2003.07.001.
- [215] S. Schmidt and C. A. Grimes, "Characterization of nano-dimensional thin-film elastic moduli using magnetoelastic sensors," *Sensors and Actuators, A: Physical*, vol. 94, no. 3, pp. 189–196, 2001, ISSN: 09244247. DOI: 10.1016/S0924-4247(01)00708-7.
- [216] S. Lee, Y. Y. Kim, and Y. Cho, "A Comparative Study on the Elastic Characteristics of an Aluminum Thin-Film Using Laser Optical Measurement Techniques," *Coatings*, vol. 7, no. 143, 2017. DOI: doi:10.3390/coatings7090143.
- [217] R. M. Pocratsky and M. P. de Boer, "Determination of thin film coefficient of thermal expansion and residual strain from freestanding fixed–fixed beams," *Journal of Vacuum Science & Technology B, Nanotechnology and Microelectronics: Materials, Processing, Measurement, and Phenomena*, vol. 32, no. 6, p. 062001,

- 2014, ISSN: 2166-2746. DOI: 10.1116/1.4896761. [Online]. Available: <http://dx.doi.org/10.1116/1.4896761>.
- [218] W. Fang and C. Y. Lo, "On the thermal expansion coefficients of thin films," *Sensors and Actuators, A: Physical*, vol. 84, no. 3, pp. 310–314, 2000, ISSN: 09244247. DOI: 10.1016/S0924-4247(00)00311-3.
- [219] O. Kraft and W. D. Nix, "Measurement of the lattice thermal expansion coefficients of thin metal films on substrates," *Journal of Applied Physics*, vol. 83, no. 6, pp. 3035–3038, 1998, ISSN: 00218979. DOI: 10.1063/1.367118.
- [220] B. A. Shaw and R. G. Kelly, "What is corrosion?" *Electrochemical Society Interface*, vol. 15, no. 1, pp. 24–26, 2006, ISSN: 10648208. DOI: 10.1149/2.f06061if.
- [221] J. H. Zhao, Y. Du, M. Morgen, and P. S. Ho, "Simultaneous measurement of Young's modulus, poisson ratio, and coefficient of thermal expansion of thin films on substrates," *Journal of Applied Physics*, vol. 87, no. 3, pp. 1575–1577, 2000, ISSN: 00218979. DOI: 10.1063/1.372054.
- [222] M. N. Ghasemi Nejjhad, C. Pan, and H. Feng, "Intrinsic strain modeling and residual stress analysis for thin-film processing of layered structures," *Journal of Electronic Packaging, Transactions of the ASME*, vol. 125, no. 1, pp. 4–17, 2003, ISSN: 10437398. DOI: 10.1115/1.1512295.
- [223] A. L. Del Vecchio and F. Spaepen, "The effect of deposition rate on the intrinsic stress in copper and silver thin films," *Journal of Applied Physics*, vol. 101, no. 6, 2007, ISSN: 00218979. DOI: 10.1063/1.2712150.
- [224] R. Abermann, "Internal stress of vapour-deposited aluminium films: Effect of O₂ and water vapour present during film deposition," *Thin Solid Films*, vol. 186, no. 2, pp. 233–240, 1990, ISSN: 00406090. DOI: 10.1016/0040-6090(90)90145-4.
- [225] P. Walker and W. H. Tarn, *Handbook of Metal Etchants*. CRC Press LLC, 1991, ISBN: 0849336236.
- [226] I. J. Polmear, "Aluminium alloys - A century of age hardening," *Materials Forum*, vol. 28, pp. 1–14, 2004, ISSN: 08832900.
- [227] J. Wu, "A Basic Guide to RTD Measurements," *Texas Instruments Incorporated*, no. June, pp. 1–42, 2018.